

EVALUATION OF NONDESTRUCTIVE TECHNOLOGIES TO ASSESS
PRESENCE AND EXTENT OF DELAMINATION OF HOT
MIX ASPHALT AIRFIELD PAVEMENTS

MANUEL CELAYA

Department of Civil Engineering

APPROVED:

Soheil Nazarian, Ph.D., Chair

Cesar J. Carrasco, Ph.D

Carlos Martin Chang-Albitres, Ph.D

Jose Espiritu Nolasco, Ph.D.

Patricia D. Witherspoon, Ph.D.
Dean of the Graduate School

Copyright ©

By

Manuel Celaya

2011

DEDICATION

To my beloved Angelica.....

To my parents, Manuel and Pilar.....

To my sisters Ana and Natalia and my nephew Maxi

EVALUATION OF NONDESTRUCTIVE TECHNOLOGIES TO ASSESS
PRESENCE AND EXTENT OF DELAMINATION OF HOT
MIX ASPHALT AIRFIELD PAVEMENTS

by

MANUEL CELAYA, MSCE, EIT

DISSERTATION

Presented to the Faculty of the Graduate School of

The University of Texas at El Paso

in Partial Fulfillment

of the Requirements

for the Degree of

DOCTOR OF PHILOSOPHY

Department of Civil Engineering

THE UNIVERSITY OF TEXAS AT EL PASO

May, 2011

UMI Number: 3457746

All rights reserved

INFORMATION TO ALL USERS

The quality of this reproduction is dependent on the quality of the copy submitted.

In the unlikely event that the author did not send a complete manuscript and there are missing pages, these will be noted. Also, if material had to be removed, a note will indicate the deletion.



UMI 3457746

Copyright 2011 by ProQuest LLC.

All rights reserved. This edition of the work is protected against unauthorized copying under Title 17, United States Code.



ProQuest LLC.
789 East Eisenhower Parkway
P.O. Box 1346
Ann Arbor, MI 48106 - 1346

ACKNOWLEDGEMENTS

I am grateful to all of the people who helped and guided me throughout the years. Without their support this project could not have been completed.

My mentor and friend, Dr. Soheil Nazarian, provided continuous guidance and support throughout my career at UTEP. I continue to have the opportunity to work with him and have access to his knowledge and research experience. I thank him for his invaluable counseling and friendship.

I also want to thank my committee members, Dr. Cesar Carrasco, Dr. Carlos Chang, and Dr. Jose Espiritu. Each has provided me with great help and assistance in their area of expertise. As colleagues, I continue to enjoy learning from them and working with them.

Extended thanks go to Dr. Carlos Ferregut and Dr. Roberto Osegueda for their valuable advice and continuous support. I also would like to extend my thanks to my colleagues at the Center for Transportation Infrastructure Systems (CTIS), Imad Abdallah, Deren Yuan, Jose Garibay, Sergio Rocha, Cesar Tirado, and Veronica Anaya. I enjoy working with them every day. Dante Mejia, Selcan Ertem, Carlos Solis, Hector and Jose Luis Hernandez and Tania Ramirez, played a large role in the completion and success of this research study.

I would like to acknowledge the funders of my study, the Asphalt Pavement Technology Program (AAPTP), especially, the Project Manager Mr. Monte Symons. My appreciation is also extended to Ms. Joanna Ambroz and Mr. Stewart Craig of Portland International Airport and Mr. Robert Pellan, Mr. Ben Barrett, and Mr. Tom Pyle of Boston Logan International Airport. .

Last and most important, I want to thank my beloved girlfriend Angelica and all my family for their love, support, and encouragement.

ABSTRACT

Sufficient bonding between the hot mix asphalt layers is essential to ensure the desired structural capacity of a pavement. Delamination or debonding problems are particularly more severe on airfield pavements, due to higher traffic loads applied by aircrafts. Further progression of delamination may result in stripping of the lower layers due to the intrusion of moisture or may develop other dangerous distresses such as foreign object debris. The existing nondestructive testing procedures and equipment that have the potential to address the problem were identified and their effectiveness and potential for success were evaluated. The Ground Penetrating Radar, Falling Weight Deflectometer, Thermography, Sonic/Seismic Methods and Impulse Response were evaluated on a controlled pavement section that was specifically constructed with various levels and depths of debonding and two airfields. Most technologies can detect severe delamination successfully. Even though not perfect, the impulse response method (with a site specific temperature adjustment) and ultrasonic surface wave method are the most promising methods for detecting debonded sections.

SUMMARY OF FINDINGS

In this study, the existing NDT procedures and equipment that have the potential to detect the debonding and delamination of hot mix asphalt (HMA) layers were identified and their effectiveness and potential for success were evaluated. Based on literature survey and analyses of the technical and practical strength and concerns, the methods considered for evaluation are summarized in Table I.

Table I – Methods Considered for Evaluation in This Study

Method / Device									
Electro-magnetic	Impulse			Vibration		Seismic/Sonic			Thermal
Air-launched and Ground-Coupled Ground Penetrating Radar (GPR)	Falling Weight Deflectometer (FWD)	Light Weight Deflectometer (LWD)	Impulse Response (IR)	Stiffness Gauge (SG)	High Frequency Sweep (HFS)	Impact Echo (IE)	Ultrasonic Surface Waves (USW)	Ultrasound (US)	Thermal Imaging (TI)

For a rigorous experimental evaluation of these methods, a 130 ft by 9 ft pavement section containing ten distinct sections was constructed with known sizes (from 6 in. by 6 in. to 4 ft by 4ft), depths (2.5 in. and 5 in.), severity (partial-debonding, full-debonding and severe delamination), surface mix (fine and coarse mixes) and climatic condition (cool and hot). Based on an initial evaluation, the feasible technologies were narrowed down to the methods shown in Table II.

The technical and practical parameters that most likely affect the successful detection of delamination with NDT methods include the accuracy, reproducibility, detectability threshold, speed of data collection, speed of data analysis, and the sophistication of data analysis.

Table II – Methods Found Feasible from Phase I Field Study

Electromagnetic	Impulse		Seismic/Sonic
Ground-Coupled Ground Penetrating Radar (GPR)	Falling Weight Deflectometer (FWD)	Impulse Response (IR)	Ultrasonic Surface Waves (USW)

The *accuracy* was judged by correlating the response of the NDT methods to the degree of debonding induced in the sections. The *reproducibility* associated with different test procedures was quantified by conducting triplicate tests with each NDT device. The *detectability threshold* was assessed by the percent of defects identified as a function of size, depth and severity. The *speed of data collection* was judged based on the time needed to set up and test time per point. The time to complete the analysis of the raw data for each methodology was used to assess the *speed of analysis*. The *sophistication of data analysis* was estimated by asking personnel with different levels of experience (an expert, a person that is familiar with the method and a new user that was just trained) to conduct the analysis. The parameters described above were given relative weights as shown in Table III to determine an overall ranking for different methods.

The rankings of the methods are shown in Table IV. None of the methods could find all of the debonded areas. However, some methods performed better for some certain application. Table V demonstrates the best applications of each method. Based on the outcome of the study, the following statements can be made:

- The impulse-response method could detect about 59% of the debonded areas with the majority of defects detected were the fully-debonded areas (both shallow and deep).
- The USW method as implemented in the PSPA could detect 53% of the debonded areas.

PSPA could detect the shallow debonding (both partial and full) the best.

Table III – Weight Factors of Parameters Used in Evaluation of Methods

Evaluation Category	Relative Weight
Accuracy	0.35
Reproducibility	0.20
Detectability Threshold	0.20
Speed of Data Collection	0.15
Speed of Data Analysis	0.05
Sophistication of Data Analysis	0.05
Total	1.00

Table IV – Ranking of Most Feasible Methods

Method \ Parameter	Accuracy	Reproducibility	Detectability Threshold	Speed of Data Collection	Speed of Data Analysis	Sophistication of Data Analysis	Ranking
	Weight Factor						
	0.35	0.2	0.2	0.15	0.05	0.05	
PSPA Ultrasonic Surface waves	3	3	3	3	3	3	2
FWD Modulus	2	3	1	3	3	3	3
Impulse Response Flexibility	4	5	3	3	3	3	1
Ground Coupled GPR	1	5	1	5	1	1	4

Table V – Recommended Best Applications for Most Feasible Methods

Defect Type		Detection Ranking			
Depth	Bonding	PSPA	IR	FWD (Def.)	GPR
Deep	Fully Debonded		√		
	Partially Debonded		?		
Shallow	Fully Debonded	√	√	√	√
	Partially Debonded	√			
Severe Delamination		√	√	√	√

- The FWD could detect about 46% of the debonded areas (primarily full debonding) based on the backcalculation of the modulus of the HMA layer.
- GPR could detect 33% of the debonded areas, primarily when talcum powder or clay was used as the debonding agent. GPR could be used as a qualitatively method to identify severely debonded areas, especially in the presence of moisture.

The evaluation of the technologies was carried out both in the cool weather and hot weather. Almost all methods either performed equally well or better in the cool weather. One major practical recommendation of this study is that the IR, FWD and USW methods require temperature adjustments for their success. Approximate temperature adjustment relationships exist for the USW and FWD methods. However, for the IR a site specific temperature adjustment protocol may be needed.

The feasible methods recommended by this study can be significantly improved by implementing more sophisticated yet practical analysis schemes.

TABLE OF CONTENTS

ACKNOWLEDGEMENTS.....	V
ABSTRACT	VI
SUMMARY OF FINDINGS.....	VII
LIST OF FIGURES.....	XVI
LIST OF TABLES.....	XXVI
CHAPTER 1 – INTRODUCTION.....	1
CHAPTER 2 – DELAMINATION OF HMA AIRPORT PAVEMENTS	5
CHAPTER 3 – METHODS FOR DETECTING DELAMINATION OF HMA.....	17
Electromagnetic Methods.....	18
Ground Penetrating Radar.....	18
Impulse Methods.....	20
Falling Weight Deflectometer (FWD)	20
Light Weight Deflectometer (LWD).....	21
Impulse Response (IR) Method	21
Vibration Methods	22
Stiffness Gauge.....	22
High Frequency Sweep	22
Sonic/Ultrasonic/Seismic Methods	22
Impact Echo	22
Ultrasonic Surface Waves.....	22
Ultrasound.....	23
Thermal Methods	23
Infrared Thermography	23
Assessment of Methods for Detecting Delamination.....	24
Detectability Extent	25
Detectability Threshold.....	25

Speed of Data Collection and Coverage.....	26
Speed of Data Analysis	26
Expertise Needed for Data Processing and Data Interpretation	26
Availability of Equipment.....	26
Reliability of Equipment.....	26
Past Experience with the Method for Detecting Delamination of HMA.....	28
Ability to Implement Procedures without Specialists	28
CHAPTER 4 – CONSTRUCTION OF CONTROL PAVEMENT SECTION	32
Laboratory Tests to Determine Suitability of Debonding Agents.....	32
Construction of Test Section.....	36
CHAPTER 5 – PRELIMINARY EVALUATION OF NDT METHODS.....	42
Location of Test Points	42
Sonic/Ultrasonic Seismic Methods	42
Impact-Echo (IE) and Ultrasonic Surface Waves (USW).....	42
Ultrasonic Surface Waves (USW) Results	44
Impact-Echo (IE) Results.....	49
Ultrasonic (US).....	51
Impulse Methods.....	55
Falling Weight Deflectometer (FWD)	55
Light Weight Deflectometer (LWD).....	57
Impulse Response (IR).....	60
Vibration Methods	64
Stiffness Gauge.....	64
High Frequency Sweep	65
Infrared Camera	68
Electromagnetic Methods.....	69
Simulation of 3D Ground Penetrating Radar	76
Coring Results.....	78
CHAPTER 6 – VERIFICATION TESTS OF SELECTED NDT METHODS ON CONTROLLED STUDY	81

Location of Test Points	81
Ultrasonic Surface Wave (USW) Method.....	82
Falling Weight Deflectometer (FWD)	92
Impulse Response	100
Thermal Methods	104
Ground Coupled GPR.....	106
CHAPTER 7 – FIELD INVESTIGATION OF SELECTED NDT METHODS	109
Portland International Airport Site.....	109
Test Results	113
Section A5	113
Section C6.....	116
South Ramp Section.....	118
Sections E4	121
Boston Logan International Airport Site.....	125
Test Results	128
Section 1	128
Section 2	132
CHAPTER 8 – EVALUATION OF NDT METHODS FOR DETECTING DELAMINATION OF HMA	135
Accuracy	135
Reproducibility.....	138
Detectability Threshold.....	140
Speed of Data Collection	142
Speed of Data Analysis	143
Sophistication of Data Analysis	144
Overall Ranking of Candidate NDT Methods.....	144
CHAPTER 9 – SUMMARY, CONCLUSIONS AND RECOMMENDATIONS	147
Summary	147

Conclusions.....	149
Recommendations.....	150
REFERENCES.....	152
APPENDIX A – NDT METHODS FOR DELAMINATION DETECTION.....	159
Electromagnetic Methods.....	159
Ground Penetrating Radar.....	159
Impulse Methods.....	165
Falling Weight Deflectometer (FWD).....	166
Light Weight Deflectometer (LWD).....	171
Impulse Response Method.....	171
Vibration Methods.....	179
Stiffness Gauge.....	179
High Frequency Sweep.....	180
Sonic/Ultrasonic Seismic Methods.....	182
Impact Echo.....	182
SASW.....	185
IE-SASW.....	188
Ultrasound.....	191
Thermal Methods.....	193
Infrared Thermography.....	193
APPENDIX B – JOB MIX FORMULAE.....	199
APPENDIX C – CONSTRUCTION DETAILS OF CONTROLLED STUDY.....	201
Schematic of Delamination on Controlled Study.....	201
Subgrade Preparation and Construction of Asphalt Base.....	203
Construction of Asphalt Pavement.....	206
APPENDIX E – COMPLETE NDT RESULTS OF EXTENDED TESTS ON SMALL SCALE STUDY.....	227

APPENDIX F – ADDITIONAL NDT RESULTS ON PORTLAND AND BOSTON INTERNATIONAL AIRPORTS.....	254
APPENDIX G – COMPLETE NDT RESULTS FOR DETECTABILITY STUDY	266
CURRICULUM VITAE.....	267

LIST OF FIGURES

Figure 1.1 – Slippage Failure due to Loss of Bond at Nagoya Airport	2
Figure 1.2 – Slippage at High-Speed Taxiway (“Curved” Grooves Indicate Slippage).....	2
Figure 1.3 – Typical Slippage Failure.....	3
Figure 2.1 – Collars Designed for Testing Samples in Shear (Mohammad et al., 2002)	9
Figure 2.2 – Shearing Setup developed at FDOT (Sholar et al., 2004)	15
Figure 4.1 – Preparation of Laboratory Specimens and Specimens Ready for Shear Tests.....	33
Figure 4.2 – Schematic of Shear Apparatus.....	34
Figure 4.3 – Detail of Asphalt Sample Placement on Shear Device	35
Figure 4.4 – Test Output from Shear Device	35
Figure 4.5 – Location of Asphalt Section at UTEP Facilities.....	37
Figure 4.6 – Schematic of Controlled Section	37
Figure 4.7 – Typical Layout for Partially and Fully Debonded Areas	38
Figure 4.8 – PSPA Results after Second Day of Construction.....	40
Figure 4.9 – PSPA Results for Top Lift after Completion of Construction	40
Figure 4.10 – Variation of Percentage of Marshall Density on Controlled Study.....	41
Figure 5.1 – Location of Test Points for a Given Section	43
Figure 5.2 – PSPA Detail.....	43
Figure 5.3 – Time Records Results with PSPA on Controlled Study.....	44
Figure 5.4 – Dispersion Curve Results with PSPA on Controlled Study	45
Figure 5.5 – Statistical Analysis of PSPA Modulus on Controlled Study.....	46
Figure 5.6 – Overall Modulus Results (Top View) on Controlled Study.....	47
Figure 5.7 – Dispersion Curve Results for 5 Lines (Cross Section).....	48

Figure 5.8 – IE Results with PSPA on Controlled Study	49
Figure 5.9 – Example of IE Results with PSPA on Controlled Study (Cross Section)	50
Figure 5.10 – Ultrasonic Linear Array System Used in Preliminary Evaluations.....	51
Figure 5.11 – 3D reconstructed Results of Line Measurements.....	52
Figure 5.12 – Examples of Images on Intact and Severely Debonded Sections.....	53
Figure 5.13 – Examples of Images on Sections with Shallow and Deep Debonding.....	54
Figure 5.14 – Field Reconstructed Results from Line Measurements on Section 3.....	55
Figure 5.15 – Falling Weight Deflectometer on Controlled Study.....	56
Figure 5.16 – Deflection Examples from FWD on Controlled Study	56
Figure 5.17 – Statistical Analysis of FWD Deflection on Controlled Study.....	57
Figure 5.18 – FWD Moduli Results on Controlled Study	58
Figure 5.19 – Light Weight Deflectometer on Controlled Study	59
Figure 5.20 – Deflection Examples from LWD on Controlled Study	59
Figure 5.21 – Statistical Analysis of LWD Deflections on Controlled Study	60
Figure 5.22 – Impulse Response Test Setup.....	61
Figure 5.23 – IR Examples on Controlled Study.....	62
Figure 5.24 – Statistical Analysis of Voltage Amplitude Ratio of IR on Controlled Study.....	63
Figure 5.25 – FFT Results from IR Examples on Controlled Study	63
Figure 5.26 – Statistical Analysis of FFT Amplitude Ratio of IR on Controlled Study	64
Figure 5.27 – Stiffness Gauge on Controlled Study	65
Figure 5.28 – Statistical Analysis of SSG Modulus on Controlled Study	66
Figure 5.29 – High Frequency Sweep Test Setup.....	67
Figure 5.30 – High Frequency Sweep Examples on Controlled Study	67

Figure 5.31 – Infrared Camera on Controlled Study	68
Figure 5.32 – Infrared Camera Results on Severe Debonded Area	69
Figure 5.33 – Infrared Camera Results on Controlled Study.....	70
Figure 5.34 – Air Launched (Left) and Ground Coupled (Right) GPR Units	70
Figure 5.35 – Raw Linescan around the Severe Debonded Area with Air-launched GPR	71
Figure 5.36 – O-scopes for Intact and Severe Debonded Locations with Air-launched GPR.....	72
Figure 5.37 – Processed Linescans with Air-launched GPR on Controlled Study.....	73
Figure 5.38 – Linescan around the Severe Debonded Area with Ground-coupled GPR	74
Figure 5.39 – O-scopes for Intact and Severe Debonded Locations with Ground-coupled	74
Figure 5.40 – Linescans with Ground-coupled GPR on Controlled Study.....	75
Figure 5.41 – 3D Displays of Transition Section at Different Depths.....	77
Figure 5.42 – 3D Displays of Section 3 at Different Depths	78
Figure 5.43 – 3D Displays of Section 5 at Different Depths	78
Figure 5.44 – Coring Operations on Controlled Study	79
Figure 6.1 – Location of Test Points for a Given Section	82
Figure 6.2 – Contour Maps of PSPA Modulus from Extended Tests in Cool Weather	83
Figure 6.3 – Contour Maps of PSPA Modulus from Extended Tests in Hot Weather	84
Figure 6.4 – Temperature Influence of PSPA Modulus	85
Figure 6.5 – Temperature-Adjusted Contour Maps of PSPA Modulus in Cool Weather	86
Figure 6.6 – Temperature-Adjusted Contour Maps of PSPA Modulus in Hot Weather	87
Figure 6.7 – Temperature-Adjusted Contour Maps of PSPA Modulus in Cool Weather based on Revised Statistical Criteria.....	88

Figure 6.8 – Temperature-Adjusted Contour Maps of PSPA Modulus in hot Weather based on Revised Statistical Criteria.....	89
Figure 6.9 – Modulus Contour Plot of Top 2.5 in. from Cool Weather Tests.....	89
Figure 6.10 – Dispersion Curve Contour Plots for Cool Weather.....	90
Figure 6.11 – Contour Maps of FWD Deflection in Cool Weather based on Revised Statistical Criteria.....	92
Figure 6.12 – Contour Maps of FWD Deflection in Hot Weather based on Revised Statistical Criteria.....	93
Figure 6.13 – Temperature Influence on FWD Deflection.....	94
Figure 6.14 – Temperature-Adjusted Contour Maps of FWD Deflection in Cool Weather based on Revised Statistical Criteria.....	95
Figure 6.15 – Temperature-Adjusted Contour Maps of FWD Deflection in Hot Weather based on Revised Statistical Criteria.....	96
Figure 6.16 – Contour Maps of FWD Moduli in Cool Weather based on Revised Statistical Criteria.....	97
Figure 6.17 – Contour Maps of FWD Moduli in Hot Weather based on Revised Statistical Criteria.....	98
Figure 6.18 – Temperature Influence of FWD Modulus on Controlled Study.....	98
Figure 6.19 – Temperature-Adjusted Contour Maps of FWD Moduli in Cool Weather based on Revised Statistical Criteria.....	99
Figure 6.20 – Temperature-Adjusted Contour Maps of FWD Moduli in Hot Weather based on Revised Statistical Criteria.....	100

Figure 6.21 – Contour Maps of IR Flexibility in Cool Weather based on Revised Statistical Criteria	101
Figure 6.22 – Contour Maps of IR Flexibility in Hot Weather based on Revised Statistical Criteria	102
Figure 6.23 – Influence of Temperature on IR Flexibility.....	102
Figure 6.24 – Temperature-Adjusted Contour Maps of IR Flexibility in Cool Weather based on Revised Statistical Criteria.....	103
Figure 6.25 – Temperature-Adjusted Contour Maps of IR Flexibility in Cool Weather based on Revised Statistical Criteria.....	104
Figure 6.26 – Infrared Camera on Controlled Study	105
Figure 6.27 – Infrared Camera Results on Transition Area.....	105
Figure 6.28 – Processed Linescans with Ground-Coupled GPR from Extended Tests.....	107
Figure 7.1 – Schematic of PDX and Location of Test Sections	109
Figure 7.2 – Location of Section A5 and Test Layout.....	110
Figure 7.3 – Location of Section C6 and Test Layout.....	111
Figure 7.4 – Location of South Ramp Section and Test Layout.....	111
Figure 7.5 – Damaged and Intact Areas on South Ramp Section.....	112
Figure 7.6 – Location of Sections 1 and 2 of E4 and Test Layout	112
Figure 7.7 – Post-processed GPR Linescans on Section A5	114
Figure 7.8 – NDT Results on Section A5	115
Figure 7.9 – Post-processed GPR Linescans of Line 1 on Section C6.....	116
Figure 7.10 – NDT Results on Section C6	117
Figure 7.11 – Core C10 Stripped at 5 inches from Section C6.....	118

Figure 7.12 – Post-processed GPR Linescans of Line 1 on South Ramp Section.....	118
Figure 7.13 – NDT Results on South Ramp Section	119
Figure 7.14 – Cores Retrieved from South Ramp Section.....	120
Figure 7.15 – Post-processed GPR Linescans on Line 1 of Sections 1 and 2 of E4.....	121
Figure 7.16 – PSPA Modulus (ksi) on Sections 1 and 2 of E4.....	122
Figure 7.17 – IR Results (FFT Ratios) on Sections 1 and 2 of E4	122
Figure 7.18 – FWD Deflection Results (mils) on Sections 1 and 2 of E4.....	123
Figure 7.19 – FWD Modulus Results (ksi) on Sections 1 and 2 of E4.....	123
Figure 7.20 – Cores Retrieved from Sections 1 and 2 of E4	125
Figure 7.21 – Schematic of BOS and Location of Test Sections.....	126
Figure 7.22 – Location of Section 1 and Test Layout.....	126
Figure 7.23 – Surface Cracking and Areas with Different Surface Pavement on Section 1	127
Figure 7.24 – Location of Section 2.....	127
Figure 7.25 – Field Picture of Section 1	128
Figure 7.26 – Post-processed GPR Linescans on Section 1	129
Figure 7.27 – PSPA Modulus (ksi) on Section 1	130
Figure 7.28 – IR Results on Section 1	130
Figure 7.29 – Cores Retrieved from Section 1	131
Figure 7.30 – PSPA and IR Results on Section 2.....	132
Figure 7.31 – Cores Retrieved from Section 2	133
Figure 8.1 – Overall Probability of Detection of NDT Methods.....	141
Figure A.1 – Equipment Setup for Air Launched (Left) and Ground Coupled (Right) GPR Units.....	159

Figure A.2 – Principle of GPR for Pavement Layer Thickness Evaluation	160
Figure A.3 – Reflections Due to Air-filled Delamination in Asphalt (Smith and Scullion, 1993)	163
Figure A.4 – Reflection Coefficient Due to Air-filled and Water-filled Delamination (from Smith and Scullion, 1993).....	164
Figure A.5 – Radar Profile and Core Retrieved Showing Asphalt Delamination (GBG Australia).....	165
Figure A.6 – Trailer Mounted FWD	166
Figure A.7 – Typical Deflection Basin Measured From FWD.....	167
Figure A.8 – Effect of Slip/TFR Correlation (Gomba, 2004).....	169
Figure A.9 – Light Weight Deflectometer	171
Figure A.10 – Impulse Hammer Test Setup	172
Figure A.11 – Example of IRH Signals for Intact and Delaminated Slabs (CTL, www.ctlgroup.com)	173
Figure A.12 – Time Histories of Input and Output Signals for Debonded (a) and Bonded (b) Surfacing (Kruncheva et al., 2004).....	174
Figure A.13 – Magnitude of TFE versus Frequency for Bonded and Debonded Surfacing (Kruncheva et al., 2004)	176
Figure A.14 – Typical Debonded (Left) and Bonded (Right) Time Histories (Sangiorgi et al., 2003)	178
Figure A.15 – Box Counting Fractal Dimension	178
Figure A.16 – Box Counting Fractal Dimension for a Bonded Location.....	178
Figure A.17 – Soil Stiffness Gauge (SSG) or GeoGauge™	179

Figure A.18 – Electromagnetic/Piezoelectric Shaker System	181
Figure A.19 – Typical Blocked Forced Output	181
Figure A.20 – Typical Impact Echo Test System.....	183
Figure A.21 – Schematic of Impact Echo Method	183
Figure A.22 – Typical Intact and Damaged-Location Dispersion Curves and Variation in Modulus with Depth for Cores after Being Saw cut (a) Intact Location and (b) Damaged Location. (Hammons et al., 2005).....	187
Figure A.23 – Portable Seismic Pavement Analyzer.....	189
Figure A.24 – Typical Records from PSPA.....	190
Figure A.25 – Delamination Detection by Ultrasonic Echo Method.....	192
Figure A.26 – A1040 POLYGON Ultrasonic Device	192
Figure A.27 – Real Time Tomographic Imaging of an Internal Structure of a Concrete Specimen.....	193
Figure A.28 – Infrared Survey Vehicle.....	194
Figure A.29 – Example Image of Thermal Analysis (Daytime Condition) (from Tsubokawa et al., 2007)	196
Figure A.30 – Thermographs Showing Defects on Asphalt Runway (Moropoulou et al., 2002).....	196
Figure A.31 – Low-temperature Areas Generally Match the Debonded Areas Found by IE. (Tsubokawa et al., 2007).....	197
Figure C.1 – Layout of Delamination on Coarse Mix Sections.....	201
Figure C.2 – Layout of Delamination on Fine Mix Sections.....	202
Figure C.3 – Layout of Delamination on Transition Sections.....	202

Figure C.4 – Preparation of Subgrade.....	203
Figure C.5 – Construction of Asphalt Base	204
Figure C.6 – Construction of Debonding Sections on Asphalt Base (Deep Debonding).....	205
Figure C.7 – Installation of Thermocouple on Asphalt Base.....	206
Figure C.8 – HMA Delivery to the Site.....	207
Figure C.9 – Construction of Bottom Layer of HMA	208
Figure C.10 – Construction of Top Layer of HMA	208
Figure C.11 – Construction of Additional Debonding on Transition Section	209
Figure E.1 – Overall Modulus Results (Top View) on Small Scale Study. Hot Weather Results.....	239
Figure E.2 – Dispersion Curve Results for 10 Lines of Extended Testing (Cross Section and Cool Weather).....	240
Figure E.3 – Dispersion Curve Results for 10 Lines of Extended Testing (Cross Section and Hot Weather).....	242
Figure E.4 – IE Results with PSPA on Extended Tests of Small Scale Study (Cool Weather) ..	244
Figure E.5 – IE Results with PSPA on Extended Tests of Small Scale Study (Hot Weather) ...	246
Figure F.1 – Dispersion Curves for Section A5.....	254
Figure F.2 – Post-processed GPR Linescans on Section C6	255
Figure F.3 – Dispersion Curves for Section C6.....	256
Figure F.4 – Post-processed GPR Linescans on South Ramp Section	257
Figure F.5 – Dispersion Curves for South Ramp Section.....	258
Figure F.6 – Post-processed GPR Linescans on Section 1 of E4	259
Figure F.7 – Post-processed GPR Linescans on Section 2 of E4	260

Figure F.8 – Dispersion Curves for Section 1 of E4.....	261
Figure F.9 – Dispersion Curves for Section 2 of E4.....	262
Figure F.10 – Post-processed GPR Linescans on Selected Cores of Section 1	263
Figure F.11 – Dispersion Curves for Section 1.....	264

LIST OF TABLES

Table 3.1 – List of Feasible Technologies for Detecting Delamination of HMA Layers	19
Table 3.2 – Advantages, Disadvantages and Potential Use of Feasible Methods	27
Table 3.3 – Evaluation of NDT Methods.....	29
Table 4.1 – Shear Strengths (in psi) for Laboratory Prepared Specimens.....	36
Table 4.2 – Summary of Debonding Agents Considered for the Controlled Study	36
Table 4.3 – Characteristics of Sections Used in This Study	39
Table 5.1 – List of NDT Technologies Used on the Controlled Study.....	42
Table 5.2 – Criteria Used to Analyze Moduli on Controlled Study	46
Table 5.3 – Frequency (KHz) at Maximum Amplitude Measured with High Frequency Sweep at Selected Locations of Controlled Study.....	68
Table 5.4 – Summary of Shear Strength Results (psi) for Cores Retrieved	80
Table 6.1 – List of NDT Technologies Used on Extended Tests on Controlled Study	81
Table 6.2 – Revised Criteria Used to Analyze Moduli.....	87
Table 7.1 – Comparison of Core Condition with NDT Results on Section A5.....	113
Table 7.2 – Comparison of Core Condition with NDT Results on Section C6.....	116
Table 7.3 – Comparison of Core Condition with NDT Results on South Ramp Section.....	120
Table 7.4 – Comparison of Core Condition with NDT Results on Sections 1 and 2 of E4.....	124
Table 7.5 – Comparison of Core Conditions with NDT Results on Section 1	131
Table 7.6 – Comparison of Core Conditions with NDT Results on Section 2	134
Table 8.1 – Criteria Used to Evaluate NDT Accuracy	135
Table 8.2 – Ranking of Probability of Success of NDT Methods to Detect Delamination.....	137
Table 8.3 – Ranking Criteria for Accuracy of Different Methods.....	138

Table 8.4 – Reproducibility of NDT Methods.....	139
Table 8.5 – Ranking of Detectability Threshold.....	142
Table 8.6 – Ranking of Speed of Data Collection	143
Table 8.7 – Ranking of Speed of Data Analysis and Interpretation	143
Table 8.8 – Ranking of Sophistication of Data Analysis Needed and Difficulties Found	144
Table 8.9 – Utility Weights for Selection of NDT Methods.....	145
Table 8.10 – Final Ranking of Feasible NDT Methods.....	146
Table C.1 – NDG Density Results after Completion of Controlled Study.....	209
Table C.2 – Percentage of Marshall Density Obtained with NDG after Completion of Controlled Study	209
Table C.3 – PSPA Results after Second Day of Construction (Lifts 1 and 2 Combined)	210
Table C.4 – PSPA Results after Second Day of Construction (Top Lift).....	210
Table C.5 – PSPA Results after Completion of Construction (3 Lifts Combined)	211
Table C.6 – PSPA Results after Completion of Construction (Top Lift).....	211
Table D.1 – PSPA Results on Small Scale Study (3 Lifts Combined). Coarse Mix	212
Table D.2 – PSPA Results on Small Scale Study (3 Lifts Combined). Fine Mix and Transition	213
Table D.3 – PSPA Results on Small Scale Study (Top Lift). Coarse Mix.....	214
Table D.4 – PSPA Results on Small Scale Study (Top Lift). Fine Mix and Transition.....	215
Table D.5 – FWD Results on Small Scale Study	216
Table D.6 – LWD Results on Small Scale Study. Coarse Mix.....	217
Table D.7 – LWD Results on Small Scale Study. Fine Mix and Transition	218
Table D.8 – IR Results (Voltage) on Small Scale Study. Coarse Mix	219

Table D.9 – IR Results (Voltage) on Small Scale Study. Fine Mix and Transition	220
Table D.10 – IR Results (FFT) on Small Scale Study. Coarse Mix	221
Table D.11 – IR Results (FFT) on Small Scale Study. Fine Mix and Transition.....	222
Table D.12 – Geogauge Results on Small Scale Study. Coarse Mix	223
Table D.13 – Geogauge Results on Small Scale Study. Fine Mix and Transition	224
Table D.14 – Shear Strength Results (psi) for Cores Retrieved at 2 ft from Start from Small Scale Study.....	225
Table D.15 – Shear Strength Results (psi) for Cores Retrieved at 7 ft from Start from Small Scale Study.....	226
Table E.1 – PSPA Results on Small Scale Study (3 Lifts Combined). Fine Mix and Transition (Cool Weather)	227
Table E.2 – PSPA Results on Small Scale Study (3 Lifts Combined). Coarse Mix (Cool Weather).....	229
Table E.3 – PSPA Results on Small Scale Study (Top Lift). Fine Mix and Transition (Cool Weather).....	230
Table E.4 – PSPA Results on Small Scale Study (Top Lift). Coarse Mix (Cool Weather)	232
Table E.5 – PSPA Results on Small Scale Study (3 Lifts Combined). Fine Mix and Transition (Hot Weather).....	233
Table E.6 – PSPA Results on Small Scale Study (3 Lifts Combined). Coarse Mix (Hot Weather).....	235
Table E.7 – PSPA Results on Small Scale Study (Top Lift). Fine Mix and Transition (Hot Weather).....	236
Table E.8 – PSPA Results on Small Scale Study (Top Lift). Coarse Mix (Hot Weather)	238

Table E.9 – FFT Ratios of Impulse Response on Small Scale Study. Fine Mix and Transition (Cool Weather).....	248
Table E.10 – FFT Ratios of Impulse Response on Small Scale Study. Coarse Mix (Cool Weather).....	250
Table E.11 – FFT Ratios of Impulse Response on Small Scale Study. Fine Mix and Transition (Hot Weather).....	251
Table E.12 – FFT Ratios of Impulse Response on Small Scale Study. Coarse Mix (Hot Weather).....	253
Table G.1 – Probability of Success of NDT Methods to Detect Different Levels and Sizes of Delamination.....	266

CHAPTER 1 – INTRODUCTION

To achieve the desired bearing capacity of a pavement structure and, as a result, a longer service life, sufficient bonding between the pavement layers is essential. Other than a reduction in the structural bearing capacity, a poor bond and the subsequent delamination or debonding between the surfacing layers reduces the serviceability and pavement performance. If delamination goes undetected, it can ultimately result in the peeling away of thin overlays from the surface of the roadway.

Delamination or debonding problems are particularly more severe on airfield pavements, due to higher traffic loads applied by aircrafts. Especially, the situation is more critical on runways at the high-speed taxiway exits, where airplanes brake and turn (Bognacki et al., 2007), or on areas under large horizontal load of aircraft at takeoff, creating slippage due to inadequate bonding between the top layer and the layer below. In severe cases, it can lead to runway closures (Tsubokawa et al., 2007). As an example, Figure 1.1 shows a case of asphalt delamination that occurred due to loss of bond between the surface and binder courses for a runway constructed only one year before the incident. In this case, the thickness of the surface course that suffered delamination was 2 in., the slippage area was 12 ft wide and 25 ft long, and the runway had to be closed for repairs.

Some other studies have found that the cause of airport delamination can be attributed to intersection of multiple-traffic paths on runways and large shear forces caused by pivoting wheels (Carroll and Dempsey, 2007). Delamination problems in airfield pavements are often preceded by slippage failures that can be detected by the presence of curved grooves on the surface, as illustrated in Figure 1.2, (Bognacki et al., 2007) or half-moon-shaped cracks having two ends pointed away from the direction of traffic, as detailed in Figure 1.3 (Shahin, 2005).



Figure 1.1 – Slippage Failure due to Loss of Bond at Nagoya Airport (from Tsubokawa et al., 2007)



Figure 1.2 – Slippage at High-Speed Taxiway (“Curved” Grooves Indicate Slippage, Bognacki et al., 2007)

These debonding and slippage problems can be aggravated with aggregate with inadequate aggregate interlock used in the asphalt pavement or insufficient amount of tack coat between layers (Bognacki et al., 2007).

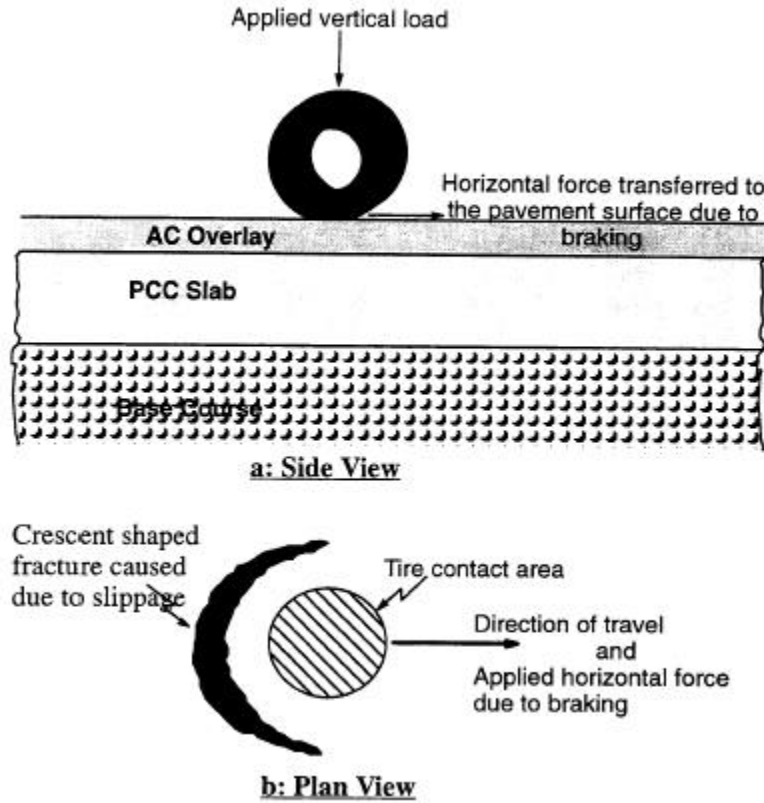


Figure 1.3 – Typical Slippage Failure (from Kulkarni, 2004)

Besides the risk of damage to the aircrafts because of foreign object debris (FOD), the delaminated layers and their associated cracks require recurrent maintenance activities, and may lead to premature need for major rehabilitation of the airfields. If undetected, the progression of delamination may result in stripping of the lower layers due to the intrusion of moisture.

The objective of this study was to provide a comprehensive procedure and guidance to estimate the presence and extent of hot mix asphalt (HMA) delamination in airport pavements. To that end, nondestructive procedures capable of locating areas of delamination were identified, tested and conclusions on their applicability were drawn.

Common conditions of past instances of major damage to airport HMA pavements resulting from delamination are identified, and the key indicators that may be used to identify potential areas of delamination are discussed in Chapter 2. The existing nondestructive test

(NDT) procedures and/or equipment that have been used or have the potential to address the problem are identified and their effectiveness and potential for success are evaluated in Chapter 3. The more effective methods are then more critically studied.

Chapter 4 details the construction of a control pavement section with different types, severity and depths of debonding and Chapter 5 contains the preliminary evaluation of several NDT methods on the control section. Chapter 6 describes the verification tests of selected NDT methods on the same control section.

The results from field investigation of selected NDT methods at two actual airfields are presented in Chapter 7. Chapter 8 includes the evaluation of NDT methods based on results obtained from the control section and the recommendation of most promising methods for detecting delamination of HMA. Finally, Chapter 9 presents the summary and conclusions of this study.

CHAPTER 2 – DELAMINATION OF HMA AIRPORT PAVEMENTS

Three modes of debonding or delamination can occur: 1) delamination between two layers/lifts of HMA, 2) debonding between HMA overlay and portland cement concrete (PCC) slab, and 3) debonding between base and HMA. All three modes impact the structural and functional performance of the airfields. However, the most critical ones are the shallow delamination of two HMA layers and debonding of thin HMA overlays over PCC slabs.

The lack of interface bonding may lead to several premature distresses of which slippage, cracking, delamination and distortion are most prominent. In most cases, delamination occurs either at high temperature or very high loads (especially horizontal loads) or a combination of the two when there is a poor bond between the surface and binder courses. Therefore, special attention has to be given to areas where horizontal loads are the largest such as frequent braking and accelerating zones, sharp curves or at the intersection of multiple-traffic paths.

Manifestation of delamination and its detrimental effects are perhaps more severe on airfield pavements, due to higher loads applied by aircrafts. The situation is most critical on runways at the high-speed taxiway exits, where airplanes brake and turn (Bognacki et al., 2007). In areas under large horizontal loads where aircrafts turn or break or takeoff, slippage due to inadequate bonding between the different lifts of the surface layer are also of particular concern (Tsubokawa et al., 2007). Delamination may also occur at the intersection of multiple-traffic paths on runways where large shear forces are exerted by pivoting wheels (Carroll and Dempsey, 2007). Jet blasts can particularly complicate the problem by converting fragments of the delaminated layer into foreign object debris (FOD).

Some construction practices in airfield industry may also aggravate the occurrence of delamination defects. For example, smoothness criteria and its tight tolerance required by the

FAA drive contractors into constructing pavements with multiple thinner lifts rather than fewer thicker lifts. Multiple layers may not act as one solid unit under shear forces and are therefore, more delamination susceptible. On the other hand, such defects could be avoided by treating and cleaning the surfaces of dust and debris and applying sufficient amount of tack coat prior to placing the overlay. Other factors such as leakage of jet turbine fluids and exhausts on the airfield pavements are considered responsible for delamination problems on military airports (Department of the Air Force, 2002, Newman, and Shoenberger, 2002).

Asphalt layer thickness plays a key role in preventing delamination. Increasing layer thickness reduces the interfacial shear stress, due to vertical and horizontal loads (Kulkarni, 2004). Even though the presence of a delaminated layer at any depth is undesirable, Hammons et al. (2005) have shown that under truck traffic, the delamination or even stripping deeper than 8 in. impacts the performance of the pavement less significantly, and the risk of surface distress is small (Hammons et al., 2005). As such, the focus of delamination detection should be on layers close to the surface (say the top 5 in.).

Other experimental studies have shown that the interface properties depend more seriously on the type of materials in contact, rather than on the amount of the applied tack coat and the interface condition (Kruncheva et al., 2006). In that study it was suggested that the interface bond should be described by introducing a vertical shear reaction modulus (against uplifting of the asphalt layer) as well as the horizontal shear reaction modulus.

Generally speaking, for the pavement to be structurally and functionally sound, a proper interface bonding between the upper and lower HMA layers is necessary. The Asphalt Institute MS-16 manual indicates that slippage cracks result from a lack of bond between the surface and the layer beneath. Distortion, a result of asphalt layer instability, can take a number of different

forms such as shoving, pushing, corrugation or rutting. Corrugation is a form of plastic movement typified by ripples across the asphalt surface which occurs usually at intersections where there is acceleration or deceleration of vehicles. This distress is a functional failure of the pavement and can affect the ride quality and safety. The development of slippage cracks, crescent or half-moon shaped, is also a result of poor interfacial bond. In this distress, under the shearing action of the traffic, the asphalt mix moves laterally away from the rest of the surface. Some reasons for a lack of bonding between the asphalt layers are:

- Poor condition of the old pavement - presence of dust, oil, rubber, dirt, water or any other non-adhesive materials;
- Application of excessive, inadequate or non-uniform tack coat;
- Highly polished aggregate on existing surface which may be water sensitive and/or use of tack coat that may not be compatible with the polished aggregates;
- Use of mixture having a high sand content, especially with rounded particles;
- Use of improper construction technique and lack of proper degree of compaction of the HMA layer.

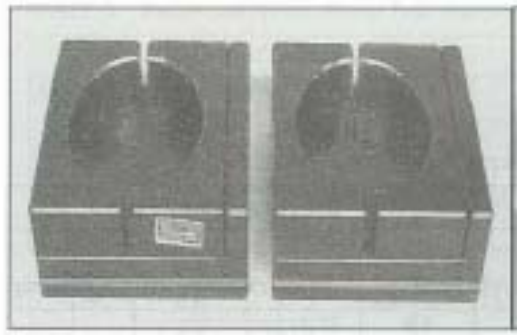
In summary, the debonding or delamination could be caused by any one or a combination of any of the factors listed above. In addition to the above criteria, the following factors may contribute to the delamination: (a) improper consideration of temperature and field conditions, (b) excessive load repetitions and vehicular accelerations and, (c) very thin surface layer thickness. In practice, most of the delamination distresses can be attributed to either improper construction techniques or choice of inappropriate tack coat. Pertinent research conducted in the area of HMA concrete delamination is briefly described below.

Mohammad et al (2002) measured the influence of different tack coats on the interface shear strength of adjacent layers. They conducted a load-controlled, simple shear test by shearing the specimens at interface. Lateral confinement was provided by a collar (Figure 2.1) that ensured the failure was at interface and nowhere else. The specimens were manufactured in three steps:

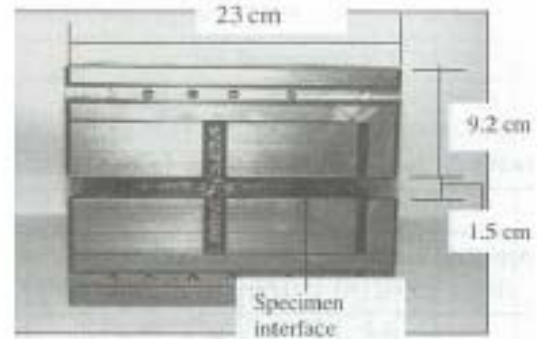
- Compact the 'bottom' part of the specimen in a Superpave gyratory compactor
- After cooling, apply the tack coat at the specified rate
- Insert the 'bottom' specimen in the gyratory mold, pour loose asphalt mix over the tack coat, and compact.

The target air void content for each of the bottom and top specimens was 6%. Each of those specimens was tested in a SST machine at a loading rate of 50 lb/min until failure. The testing was conducted at temperatures of 25°C and 55°C. It was observed that CRS-2P emulsion performed better than PG64-22, PG76-22M, SS-1, SS-1H, and CSS-1h. In addition, for each of the tack coats, an optimum rate of application that gave the highest shear strength was determined. The study demonstrated that even under the most optimal performance of tack coat, the maximum strength attained is only 83% of monolithic mixture strength, implying that interfaces potentially cause slip planes.

Shahin et al (1986) discussed the effect of layer slippage on the performance of asphalt pavements. Using BISAR (Bituminous Structures Analysis in Roads) and the French Shell model (Bonnaure et al., 1980) for analysis, various scenarios were evaluated about the fatigue life of a typical airfield pavement. The pavement section analyzed had a 2-inch thick overlay



(a) Collars to provide lateral confinement



(b) Assembled collars with specimen inside

Figure 2.1 – Collars Designed for Testing Samples in Shear (Mohammad et al., 2002)

over a 4-inch thick HMA surface course. The criteria for failure considered were the tensile stress at the bottom of the asphalt layers (overlay and the original surface course) and the vertical compressive strain on the subgrade. Shahin et al. (1986) made the following observations:

- Only a small amount of slippage is sufficient to produce strains in the pavement that approach those of the free slippage case.
- The tensile stress at the bottom of the overlay causes a compressive stress to develop on the upper surface of the asphalt surface layer. This causes a relative movement of points on the either side of the interface. This distortion further weakens the bond between the asphalt layers, allowing more slippage leading to higher strains.
- The subgrade strains increase with increasing slippage. Because two thinner layers are not as stiff as a single layer of the same overall thickness, the compressive vertical strain on the subgrade increases.
- Further, under the action of horizontal loads, the horizontal strains for no friction are much higher than those with full friction.

The principal normal tensile strains, developed by the horizontal loads along the back edge of the contact area, are of the same magnitude and cause progressive failure along the rear

edge. This tensile failure would cause slippage cracks in the overlay. If the overlay is not properly bonded to the underlying layers, the overlay moves resulting in opening of the cracks. These cracks are crescent shaped. In order to fix these cracks, either the existing layer needs to be removed and re-paved or a thicker well-bonded overlay should be placed on the existing overlay. In addition to strong interlayer bonding, the authors suggested an overlay stiffness of at least 500 ksi.

A research to evaluate the adhesion between asphalt mixes was conducted by Uzan (1976) and Uzan et al. (1978) using the Goodman's constitutive law:

$$\tau = K \times \Delta u \quad (2.1)$$

where τ is the shear stress at interface, Δu the relative horizontal displacement of the two faces at the interface, and K is the horizontal interface reaction modulus.

The analysis was carried out using the BISAR program for a test section at different levels of adhesion. It was observed that for a perfectly smooth interface ($K=0$) the tensile radial strain at the bottom of the uppermost layer was higher than for the perfectly rough interface. The top of the second layer also changed to compressive strain when K approached zero. Further, even an adherence of 90% provides results that were close to a smooth condition as described in Shahin et al. (1986). Direct shear tests were performed on the layered asphalt concrete specimens with shearing along the tack coat at different temperatures, vertical pressures and rates of application of tack coat. The following three components that contribute to the interface shear strength were identified:

- Adhesion, represented by the tensile properties of the slip plane.
- Friction, from roughness of the two faces.

- Interlocking, from the penetration of aggregates into the voids of the other layer. The interlocking component depends on the texture of the surfaces in contact and properties of the asphalt mix.

It was suggested that measurement of the adhesion component, which is indicated by rupture of the bond between layers in the bitumen or mastic phase, could be done by a tensile test (the interlocking effect would be absent for pure tension.).

The following factors largely influenced the interface shear strength:

- Temperature: The effect of higher temperatures is more dominant while testing in tension than in compression. With increasing vertical pressures, the interlocking component becomes more dominant than the adhesion component.
- Tack Coat Rate: The tack coat usually functions in the following two ways:
 - Fills voids on the surface.
 - Increases the interface film thickness or gets absorbed in the adjacent layers.

The filling of voids on the surface of the mixes increases the contact area and consequently the adhesion. However, excessive film thickness decreases the adhesion and aggregate interlock. Very low tack coat rate could result in the loss of adhesion component. Hence, it is required that the tack coat be applied at an optimum rate.

- Rate of Deformation: The rate of shear deformation is an important factor in controlling the strength and deformation ability of the interface. Generally, with increasing the rate of deformation, the magnitude of stress developed increases.

A common method for measuring the bond strength of asphalt cores is the pull-off test (Tschegg et al., 1995). For this test, a 4-in.-diameter core is drilled from the top surface down through the overlay, through the interface, and about 2 in. into the base layer. A Steel plate is

glued to the top surface of the core. The core is then pulled off with a tension machine in the axial direction of the base layer. The maximum load is registered during the pull-off test. This is a simple test method but gives only the adhesive tensile strength with large scatter in the results. The reasons for the scatter in the results are: eccentricity of load, small core diameter and large aggregate size, notches at the surface of the cores by drilling or burst out aggregates, stress concentrations, uncontrolled temperature, and indentation effects owing to rough surfaces. In addition, the test was useless if the tensile strength of the mix was lower than the interface bond strength.

To avoid such drawbacks, a 'Wedge Splitting Test' was developed (Tschegg et al., 1995). In that test, a block of asphalt concrete was made to crack along a predetermined joint at a steady rate. The splitting was done by a wedge that was located in a groove between the two blocks of asphalt. The force and the displacements were recorded during the crack propagation until complete separation of the specimen took place. Based on the shape of the force-displacement curve, a differentiation between brittle and ductile behavior was possible. It was found that with increasing temperature, the plastic behavior of the asphalt increased. There was a decrease in the peak loads with an increase in the temperature. At low temperatures, it was found that the relationship between the force and the crack opening displacement was linear. However, this test could not distinguish between the two different types of tack coats used for that study.

Ameri-Gaznon et al (1990) evaluated the octahedral shear stress (OSS) and the octahedral shear stress ratio (OSR) for different pavement sections. In particular, the OSR and the rut resistance in an asphalt concrete pavement (ACP) overlay were evaluated based on the overlay thickness, interlayer bonding and horizontal surface shear. The properties of the bituminous materials were evaluated using the triaxial test. The cohesion, c , and the angle of internal

friction, ϕ , were determined at 104°F at a loading rate of 4 in./min. The modified ILLIPAVE finite element computer program was used to calculate the OSR's within ACP layers. In the absence of the interlayer bond, the overlay acted independently of the rest of the pavement system allowing greater relative movement in between the two asphalt layers. This reduced the confining stress causing larger OSS in the overlay.

They found that a 4-inch thick overlay was the most critical one when there was free slippage. With increase in the bonding, the critical thickness increased to 6 in. For a complete bond, the stress levels were the highest at the mid height of the ACP overlay. With the loss of bond, the critical stress shifts to the bottom of the surface layer. The stress levels were far more critical than when a complete bond exists. Typically, with increasing the stiffness, it is expected that the shear stresses would decrease. For a poor interlayer bond, the trends were the opposite. The authors also found that the horizontal surface shear force doubled the OSS induced in the ACP overlay for full bond as compared to the no-bond conditions.

Hachiya and Sato (1997) conducted a three-step study. The first step consisted of analyzing the airport runway and taxiway using BISAR to calculate the interface shear stresses and strains. The results showed that shear stresses at interfaces depended on surface layer thickness (thinner layers producing higher shear stresses) and horizontal force on the surface. An increase in the horizontal force, in form of acceleration and braking, caused an increase in the interfacial shear stresses. The pavement failure was caused by interlayer separation due to increased shear and tensile cracking at the bottom of the top layer. Construction of thicker lifts can help reduce the interlayer shear stresses.

In the second step, laboratory tests were conducted on asphalt concrete specimens and emulsions. Asphalt specimens were tested in shear and tension at various temperatures in a

strain-controlled mode. The interfaces were hot jointed, cold jointed, tack coated (0.088 gal/yd²) and monolithic. Tack coated joints performed better than cold joints but not as well as hot joints or monolithic construction. The interlayer shear strength was dependent on the type of the tack coat used (modified emulsions worked best), rate of application, curing time, and temperature.

In the third part, three sections were constructed and subjected to loading by an assembly similar to aircraft landing gear. The top layer in each of the sections was of the same thickness but constructed differently. The first section was constructed in three lifts, the second in two lifts, and for the third in a single lift. It was observed that the section constructed in a single lift rutted more than the other two. The section least likely to rut was the one with three lifts. Overall, it was suggested to use higher lift thicknesses and modified emulsions to reduce the interlayer slippage on airport pavements.

West et al. (2006) includes a comprehensive synthesis of the different tests developed by researchers around the globe to measure the bond strength between HMA layers. The various devices evaluated in that study fall into three major categories: shear strength tests [ASTRA (Italy), FDOT method (Florida), LPDS method (Swiss), Japan method, Superpave Shear Tester, Leutner test (Germany)], tensile strength tests (ATACKER, Austrian method, Canadian MTQ method) and torsion strength tests (ATACKER).

Eedula and Tandon (2006) used a simple shear device similar to ASTRA Shear Box Apparatus for laboratory evaluation of bond strength in recovered cores. The rate of loading, normal pressure, and temperature have been studied and optimized for measuring bond strength. Sholar et al. (2004) investigated the effect of different tack coat application rates, curing time, types of aggregates, rates of shear and moisture on the interfacial bond strength of composite asphalt specimens. A device, shown in Figure 2.2, was developed to test the specimens in shear.

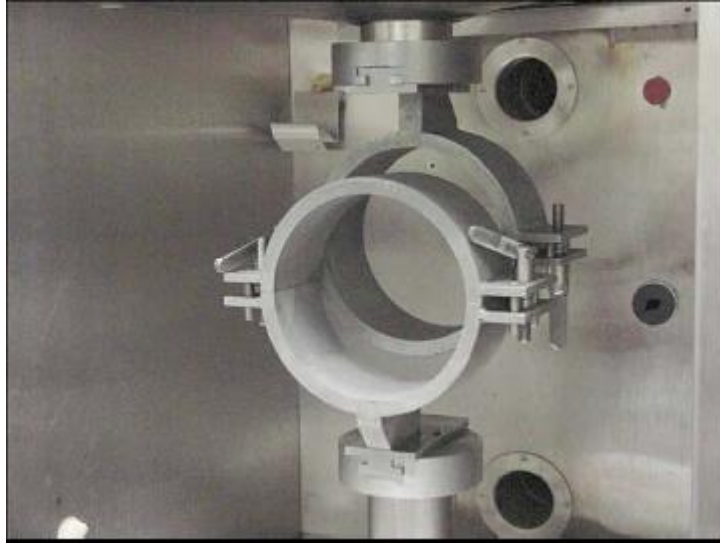


Figure 2.2 – Shearing Setup developed at FDOT (Sholar et al., 2004)

The device was mounted in a temperature controlled MTS test chamber. The shear strengths of composite samples were measured at constant strain rates. The shear strength of the interface was directly related to the rate of shear and inversely to the test temperature. It was observed that exposure of tack coat to moisture, prior to paving a new overlay, caused reduction in the interfacial shear strength. This emphasizes the need to have proper curing of tack coats before paving a new layer. Further, coarser gradations (19.0 mm) performed significantly better than finer (12.5 mm) gradations in terms of shear strengths. In addition, milling of the existing pavement surface before applying tack coat significantly increased the bond strength of the interface in shear. Increasing the rate of application of tack coat caused a marginal increase in the shear strength of the interface.

Mukhtar and Dempsey (1996) conducted tests to evaluate the shear strength of HMA-PCC interface. PCC specimens 2 in. in diameter by 2 in height were cast and cured for a period of 28 days. Subsequently, a tack coat was applied at one of the surfaces and the PCC specimen was inserted in the mold having 2-inch internal diameter. Loose asphalt mix was compacted to a density of 147 pcf in three 1-in. thick lifts. A vertical confining load of 79 psi was applied to

simulate the field condition corresponding to a 2.5-inch thick HMA overlay over PCC. The specimens were then sheared at interface in a strain-controlled mode at the rate of 1, 30 and 300 in./min. The testing was carried out at of 0, 20, 40, 60, 80 and 100 °F. It was observed that, regardless of the testing temperature and shearing rate, monolithic HMA specimens had higher shear strength than specimens jointed at the interface. The shear strength of the interface increased with higher rate of shear and lowering of temperature. Analysis performed by the authors indicated maximum shear stresses below the wheel.

CHAPTER 3 – METHODS FOR DETECTING DELAMINATION OF HMA

The desirable method should ideally detect the onset of delamination as soon as possible, as opposed to detecting the problems in its advanced stages. Therefore, an appropriate practical nondestructive tool capable of detecting the potential of delamination or debonding during or shortly after construction is very desirable. Under well executed construction practices, the bond strength between two adjacent layers increases for some time after placement because of the curing of the tack coat. The time to reach the ultimate bond strength is also affected by a number of environmental parameters (such as ambient temperature).

The most common use of the equipment is most likely for the evaluation of the existing pavements, sometimes with unknown construction documentation, for forensic purposes. In this case, the desirable NDT equipment should ideally be able to cover a large area of the airfield in a rapid manner, and should be able to detect the onset of delamination when it is extended over a small area.

A number of NDT technologies have been developed that can be potentially employed for the detection of delamination within HMA layers. Most of these technologies have been used extensively for detecting the delamination in PCC slabs rather than HMA layers. The detection of delamination in PCC is much more straightforward than in the HMA. Some of the difficulties in directly applying successful technologies used for identifying PCC delamination arise from the following:

- concrete slabs are typically placed in thicker lifts than HMA layers,
- the cement paste generates an almost homogenous layer as opposed to the HMA that is essentially a particulate matter (especially for coarser mixes such as SMA),

- the tack coat at the interface of successive HMA layer may act as a weak bonding agent, complicating the detection of debonding,
- changes in temperature play a key role in the measured mechanical properties of HMA layers as well as the adhesion characteristics of tack coat that will affect the results of some of the NDT test.

Table 3.1 contains a list of the NDT technologies which have the potential to detect delamination within HMA layers. The following section provides an overview of these candidate NDT techniques and brief discussion on their advantages, disadvantages, and possible limitations when used for detection of delamination within HMA. More detailed information on these technologies is given in Appendix A. It is recommended that the readers review Appendix A to become familiar with the methods and terminologies discussed below.

The methods can be categorized into five broad groups of Electromagnetic, Impulse, Vibration, Seismic/Sonic and Thermal. A brief description of each method is provided next.

Electromagnetic Methods

Ground Penetrating Radar

The application of GPR in detecting delamination has been found to be questionable. Even at frequencies of 1 to 2 GHz, the GPR wavelengths in asphalt are too long to resolve the thin delamination. Numerical modeling of the GPR signals for the case of delaminated asphalt was carried out by Smith and Scullion (1993). The results indicated that the detection of an air-filled delamination of 0.2 in. or larger water-filled delamination of 0.1 in. and larger at a minimum depth of 2 in. may be detected using a 2.5 GHz GPR antenna. The maximum speed for data acquisition suggested was 10 mph.

Table 3.1 – List of Feasible Technologies for Detecting Delamination of HMA Layers

Method	Device	Advantages	Concerns
Electro-magnetic	GPR	Rapid test, provides full areal coverage	Cannot directly detect delamination even at 1 or 2 GHz
Impulse	FWD	Available and well understood, rapid test	Impulse duration too long to focus on top thin layers, variability in thickness and modulus of sublayers may mask the detection of delamination
	LWD	Easier to perform tests than FWD	
	Impulse Response	Have been successful to detect different levels of debonding in HMA, rapid test, needed components are readily available	Even though automated analysis available, automated equipment is not available
Vibration	Stiffness Gauge	Input load is controlled, equipment available	Coupling to HMA problematic, load is too light, frequency range is too low
	High-frequency Sweep	Reasonably priced equipment is available for other applications	Automation may be required, has not been used on HMA
Seismic/Sonic	Impact-Echo	Proven technology for detection of delamination in concrete, automated equipment is available	Limited use for detecting HMA delamination, coupling of energy to coarser mixes
	SASW	automated equipment is available, feasibility has been shown in HMA	Coupling of energy to coarser mixes, thinner top layers
	Ultrasound	Proven technology for detection of delamination in concrete, automated equipment is available	Has not been used on HMA, frequency content may be too high that interact with coarse aggregates
Thermal	Thermography	Rapid test, provides full areal coverage, automated equipment and interpretation	Highly dependent on environmental conditions such as wind speed, ambient temperature, and sunlight, can only be used to detect very shallow delamination

Based on other field investigations, the GPR survey may provide useful information which may indicate delamination between asphalt layers. For example, the much larger amplitudes in GPR radargrams mark the location of delaminated zones.

Impulse Methods

Falling Weight Deflectometer (FWD)

A number of studies have been carried out to assess the suitability of the FWD for assessing the delamination of HMA layers. Intuitively, higher deflections are expected, if poor bond between asphalt layers exists. A new backcalculation process for assessing the bond condition between the HMA layers using FWD deflections has shown some promising results (Al Hakim, 1998). The backcalculated parameter in that process is a parameter called the interface stiffness (see Appendix A for definition). In the same study, the backcalculated interface stiffness from FWD deflection basins was found not to be successful for assessing of bond condition between thin HMA layers.

Other studies have compared the slippage susceptibility at asphalt interfaces with FWD measurements. A Tack Coat Failure Ratio (TFR) was defined as the ratio of the moduli of the HMA layers above and below the debonded interface measured from FWD. TFR compared well with the slippage susceptibility at the interfaces as defined in Gomba (2004). However, given the uncertainty in backcalculating the moduli of thin HMA layers, this observation may need further evaluation.

Other approaches have been carried out based on the “area” concept (a deflection basin curvature index), that calculates the overall composite modulus of the entire pavement structure (Hammonds et al., 2005). This process is described in Appendix A. The approach can be used

effectively to approximate the relative stiffness of the uppermost bound layer(s) in a pavement for comparative purposes. However, this is an empirical approach and has not been calibrated with FWD measurements.

Light Weight Deflectometer (LWD)

After an extensive review of the literature, no cases have been found that the LWD was used for detecting delamination. In general, the LWD is likely not suitable for the detection of delamination in real world applications because of the long duration of impulse and the limitations of sensor locations.

Impulse Response (IR) Method

In principle, the IR method is very similar to the LWD tests. The main difference is the higher ranges of frequencies excited in the IR method (several kilohertz for IR vs. less than 100 Hz for LWD). The IR method has shown promise as a quantitative and qualitative tool to obtain information about the interface bond between HMA interfaces. In the IR method, the bond condition is estimated from a parameter defined as Transfer Function Estimate (TFE). This parameter is obtained from the variation of the ratio of deflection measured with a geophone or an accelerometer and measured load imparted to the pavement with frequency. Different TFE values were attributed to different bonding condition (Kruncheva et al., 2005).

Other approaches have focused on the fractal theory as a quantitative indicator of bond conditions. As reflected in Appendix A, in these studies it was feasible to determine ranges from well bonded areas to de-bonded areas of asphalt pavements (Sangiorgi et al., 2003). However, the differences in the values between the bonded and debonded conditions for pavements with thin structures are small.

Vibration Methods

Stiffness Gauge

The stiffness gauge imparts very small energy in the range of 100 to 200 Hz. Since the stiffness gauge is optimized for low-stiffness geo-materials, neither the force level nor the frequency range seems adequate for detecting delamination. A French study (Lepert et al., 1992) has shown that this technique may not be effective even when used in controlled experimental study test sections with different interface conditions

High Frequency Sweep

The high-intensity, high-frequency vibration generated by high frequency sweep devices primarily excites the pavement layer on top the delaminated layer. The resulting variation in stiffness with frequency for this method may be used to detect delamination but this method has not been proved in the field. This method has not been implemented for the detection of HMA delamination before.

Sonic/Ultrasonic/Seismic Methods

Impact Echo

This method has been effective in the detection of HMA delamination deeper than 4 in. (Armitage et al., 2000). When delamination occurs at depths less than 4 in., it is still possible to detect the existence of the delamination; however, no information regarding the depth to the delaminated layer can be drawn. A detailed description of the method is provided in Appendix A.

Ultrasonic Surface Waves

This method can be use not only to detect delamination but also identify the approximate depth of the debonded layers. In this method, the variation in the velocity with wavelength is

measured to generate a so-called dispersion curve (see Appendix A). The wavelength at which the phase velocity is no longer constant is closely related to the thickness of the top layer (Nazarian et al., 1997). For two layers with similar modulus bonded together, the variation in modulus with wavelength is more or less constant. However, when the two layers are debonded, the modulus will decrease significantly with wavelength below the interface of the two layers. This method has been successfully used in some forensic studies to detect HMA stripping (Hammons et al., 2005).

Some devices can automatically conduct the IE and SASW tests simultaneously and in a rapid manner.

Ultrasound

This method consists of generating a short ultrasonic impulse by a transmitting transducer, and recording the response through the material with up to 56 receivers. The depth of the defect is determined on the basis of the travel time of the impulse and the ultrasonic wave velocity. This method has proven to be effective in flaw detection mainly in concrete material (Garbacz and Garboczi, 2003). However, no research has been carried out to detect asphalt delamination.

Thermal Methods

Infrared Thermography

Infrared thermography (IR) is a diagnostic NDE method which relates changes in surface temperature of a material to subsurface or internal flaws. On existing pavements, the IR technology can be used to relate local temperature gradients to the presence of shallow subsurface flaws in HMA. It is believed that the trapped air in a delamination or cracked zone acts as an insulator blocking the heat transfer between the HMA lifts above and below the

delaminated interface. Consequently, the surface of the pavement over the delaminated area exhibits a temperature gradient (negative at night and positive during the day) with respect to its surrounding fully bonded area (Moropoulou et al., 2002). This method depends on environment and climate conditions and daytime.

Some promising results in terms of detecting shallow delamination (2 to 3 in.) in HMA using IR are reported by Tsubokawa et al. (2007). However, some unfavorable results are also reported by Hammons et al. (2005). No information regarding depth at which delamination occurs can be obtained with this method.

Assessment of Methods for Detecting Delamination

A number of parameters should be assessed to ensure that the methods can detect the delamination of HMA layers in an accurate, repeatable and practical manner. The factors considered in this study consist of the following:

- Detectability threshold
- Speed of data collection and coverage
- Speed of data analysis and interpretation
- Availability of commercial equipment
- Expertise needed for data processing and data interpretation
- Equipment reliability
- Past experience with the method for detecting delamination of HMA
- Ability to implement procedures without Specialists

The assessment of these factors for the NDT methods included in Table 3.1 is summarized in Table 3.2 and the rationale beyond this assessment is described below.

Detectability Extent

The detectability extent is defined as the planar extent of debonding that should occur before they can be detected by the method. Two levels of detectability extent are used (localized and extensive). “Localized debonding” refers to small areas (say less than 3 ft in dimensions) where “extensive debonding” refers to when a large area of the airfield is debonded. Intuitively, the methods that can detect the smaller defects are more desirable. However, this factor should be viewed in conjunction with the detectability threshold and whether the data is collected continuously or the tests are spot tests as discussed below.

In general, the Vibration and Seismic/ Sonic methods are capable of detecting smaller defected areas since they are localized tests. Depending on the speed of operation, the GPR can also detect localized defects.

Detectability Threshold

The detectability threshold is defined as the stage at which the delamination can be detected by the method. Two levels of detectability threshold are used (onset and advanced). The onset of delamination is defined as when the two layers are debonded but they are still in contact, whereas the advanced stage is defined as when the two layers are significantly separated due to the intrusion of moisture or the deterioration of the HMA layers at the boundary of the layers.

Impulse response, Impact Echo and SASW methods require only separation of the layers to detect the debonding. GPR at least theoretically requires either 0.2 in. of separation between the adjacent layers to detect the separation of the reflected waves from the top and bottom of the separated layers.

Speed of Data Collection and Coverage

The GPR and thermography method collect data in a continuous manner, whereas the other methods are all spot measurements. The rates of production of the methods that collect data at discrete points are similar and between 25 to 40 points/hr.

Speed of Data Analysis

The data analysis is defined as processing the raw data collected by the device into either a single parameter or a graphical output. For almost all methods, the data analysis is quite rapid and in most cases the results are available for inspection in the field.

Expertise Needed for Data Processing and Data Interpretation

Data processing and interpretation is defined as locating the locations of debonded areas from the analyzed data. This includes filtering the analyzed data and delineating the anomalies detected into the debonding of the layers.

None of the methods are currently perceived to be easy to interpret without adequate training. The GPR and the Impulse Response methods may require higher levels of expertise than the others for this purpose.

Availability of Equipment

For almost all methods, off-the-shelf equipment is available that can be purchased.

Reliability of Equipment

The reliability of the equipment is defined as the ruggedness of the equipment in terms of day-to-day production and the feasibility of using the equipment under different environmental and real-world conditions. Most of the devices proposed in Table 3.2 have been evaluated for reliability of the operation, and for the most part demonstrated their reliability. The

Table 3.2 – Advantages, Disadvantages and Potential Use of Feasible Methods

Method	Device	Equipment Limitations and Capabilities							Past Experience	Ability to implement procedures/equipment without Specialists
		Detectability Extent	Detectability Threshold	Speed of Data Collection and Area Coverage	Speed of Data Analysis	Availability and accessibility of equipment	Expertise Needed for Data Processing and Interpretation	Equipment Reliability		
Electro-magnetic	GPR	Small	Advanced	Rapid/Continuous	Slow	Commercially Available	High	High	Mixed Results	Medium
Impulse	FWD	Extensive	Advanced	5 min./point	Rapid	Commercially Available	High	High	Mixed Results	Medium
	LWD	Small		2 min./point	Rapid	Commercially Available	Unknown	Medium	None	Medium
	Impulse Response	Small	Onset	2 min./point	Rapid	Commercially Available	High	High	Some	High
Vibration	Stiffness Gauge	Unknown	Unknown	2 min./point	Unknown	Commercially Available	Unknown	High	None	Unknown
	High-frequency Sweep	Unknown	Onset	Unknown	Unknown	Research Stage	Unknown	Unknown	None	Unknown
Seismic/Sonic	Impact-Echo	Small	Onset	2 min./point	Rapid	Commercially Available	Medium	High	Some	High
	SASW	Small	Advanced	2 min./point	Rapid	Commercially Available	Medium	High	Some	High
	Ultrasound	Unknown	Unknown	2 min./point	Unknown	Commercially Available	Unknown	High	None	Unknown
Thermal	Thermography	Extensive	Advanced	Rapid/Continuous	Rapid	Commercially Available	Medium	Medium	Mixed Results	Low

thermography has been ranked medium because favorable environmental conditions are needed for its use.

Past Experience with the Method for Detecting Delamination of HMA

Based on the literature survey and the experience of the research team, the outcome of past experience of organizations that have attempted these tests are summarized to either “mixed results,” “some,” and “none.” “Mixed results” refers to the cases when different organizations have reported both favorable and unfavorable experience with detecting debonding of HMA for a given method. “Some” refers that the experience with the method has been positive but the number of studies are limited to draw a definite conclusion. A number of methods ranked as “None” signifies that they have never been used to detect delamination of HMA layers.

Ability to Implement Procedures without Specialists

The ability of utilizing these methods by technicians routinely without the need for specialists is also considered. This factor is important for organizations that prefer not to outsource their pavement evaluation program. For the most part, the data collection can be carried out by the technicians. However, the data interpretations may need different levels of expertise. The thermography requires specialized equipment and interpretations that, at least in the near future may require specialists for data collection and analysis. The GPR still requires experts to interpret the data. The methods with the highest chance of being implemented in-house are the impulse response, impact-echo and SASW. However, even these methods require appropriate training for a conscientious technician or engineer.

Based on the qualitative information provided in Table 3.2, the methods were ranked in a quantitative manner as shown in Table 3.3. The ranking is based on a utility analysis considering

Table 3.3 – Evaluation of NDT Methods

Method	Device	Evaluation Category							Total	Categorizing Methods by Tier
		Applicability to Delamination Detection and Limitations/ Restrictions of Test Equipment	Accuracy and Repeatability of Test Results	Equipment State of Development	Time Required for Data Analysis	Production Rate, Time Required for Testing	Initial Cost and Maintenance/ Operational Cost of Test Equipment	Data Collection Guidelines and Data Presentation		
Utility Weight		0.25	0.25	0.1	0.15	0.1	0.1	0.05	1.00	
Electro-magnetic	GPR	3	3	5	5	5	1	5	3.6	1
Impulse	FWD	1	3	5	3	3	3	3	2.7	2
	LWD	1	3	3	3	3	5	3	2.7	2
	Impulse Response	3	5	3	5	3	3	3	3.8	1
Vibration	Stiffness Gauge	1	1	3	3	3	5	1	2.1	3
	High-frequency Sweep	3	1	3	3	3	3	3	2.5	3
Seismic/ Sonic	Impact-Echo	3	5	5	5	3	3	3	4.0	1
	SASW	3	5	5	5	3	3	3	4.0	1
	Ultrasound	3	3	3	3	3	3	3	3.0	2
Thermal	Thermography	3	3	5	3	5	1	3	3.2	2

several parameters with different weighting factors. The following parameters were selected for ranking in the order of importance:

1. Applicability to Delamination Detection and Limitations/Restrictions of Test Equipment
2. Accuracy and Repeatability of Test Results
3. Time Required for Data Analysis
4. Equipment State of Development
5. Production Rate
6. Time Required for Testing
7. Initial Equipment Cost and Maintenance/Operational Cost of Test Equipment
8. Data Collection Guidelines and Data Presentation

The first two parameters were given higher weights of 0.25 out of 1 since they are the most important factors in deciding whether a method is appropriate or not. Time required for analysis was weighted slightly higher than other parameters since the timely delivery of results deemed important. The data collection guidelines and data presentation is rather important but they were not deemed as important as other practical items enumerated under items 4 through 7.

Each of the eight criteria listed above was ranked either 1 (low), 3 (average) or 5 (high). The weighted averages of the individual rankings were used to categorize the methods into the following three tiers:

- Tier 1, which includes GPR, Impulse Response, Impact echo and SASW, seems to have the best chance to provide a practical solution to the detection of delamination. Based on the research team's experience and others, these four tests may have the highest probability of success.

- Tier 2, which consists of Ultrasound, thermography and FWD/LWD, are either not used before or has not always proven effective.
- Tier 3 methods consist of the stiffness gauge and high-frequency sweep. These methods have not been used for the delamination detection before and the research team has concerns with their probability of success.

Based on this analysis, the focus of evaluation was shifted on the tier 1, and to lesser extend tier 2 and tier 3 methods.

CHAPTER 4 – CONSTRUCTION OF CONTROL PAVEMENT SECTION

The construction of a pavement section to evaluate all NDT methods is detailed in this chapter. Several laboratory tests that were conducted to identify and evaluate debonding agents are described first. Then, the construction of the pavement section is detailed. Three levels of debonding between two layers of HMA, ranging from bonded to partially-bonded to fully-debonded, were replicated. In addition, a case of extremely severe debonding of HMA was also reproduced.

Laboratory Tests to Determine Suitability of Debonding Agents

Two local HMA mixes that met the Federal Aviation Administration (FAA) specifications were considered. One mix met the requirements of Item P-401 (Plant Mix Bituminous Pavements) and the other Item P-403 (Base, Leveling or Surface Course). The job mix formulas of these two mixes are included in Appendix B.

To establish the suitability of different materials to be used as debonding agents, a series of laboratory tests were conducted. Kruntcheva et al. (2004) recommended clay slurry and talcum powder to reproduce partial and full debonding between two lifts, respectively. In addition to these agents, grease and thin paper soaked in motor oil were considered. A tack coat in compliance with Item P-603 at a rate of 0.14 g/yd^2 (0.7 lit/m^2) was also used as control bonding agent. Direct shear tests were performed to assess the bond strength.

The process of preparation of the specimens is shown in Figure 4.1. After several iterations, the following steps were followed:

- Compacting a bottom lift using a gyratory compactor to a relative density of about 90%
- Applying a bonding agent (Figures 4.1a and 4.1b)

- Compacting the top lift using 75 blows of a Marshall Hammer according to ASTM D6926-04 (Figure 4.1c)

The specimens were approximately 4 in. (100 mm) in diameter and 4.2 in. (105 mm) in height (Figure 4.1d).

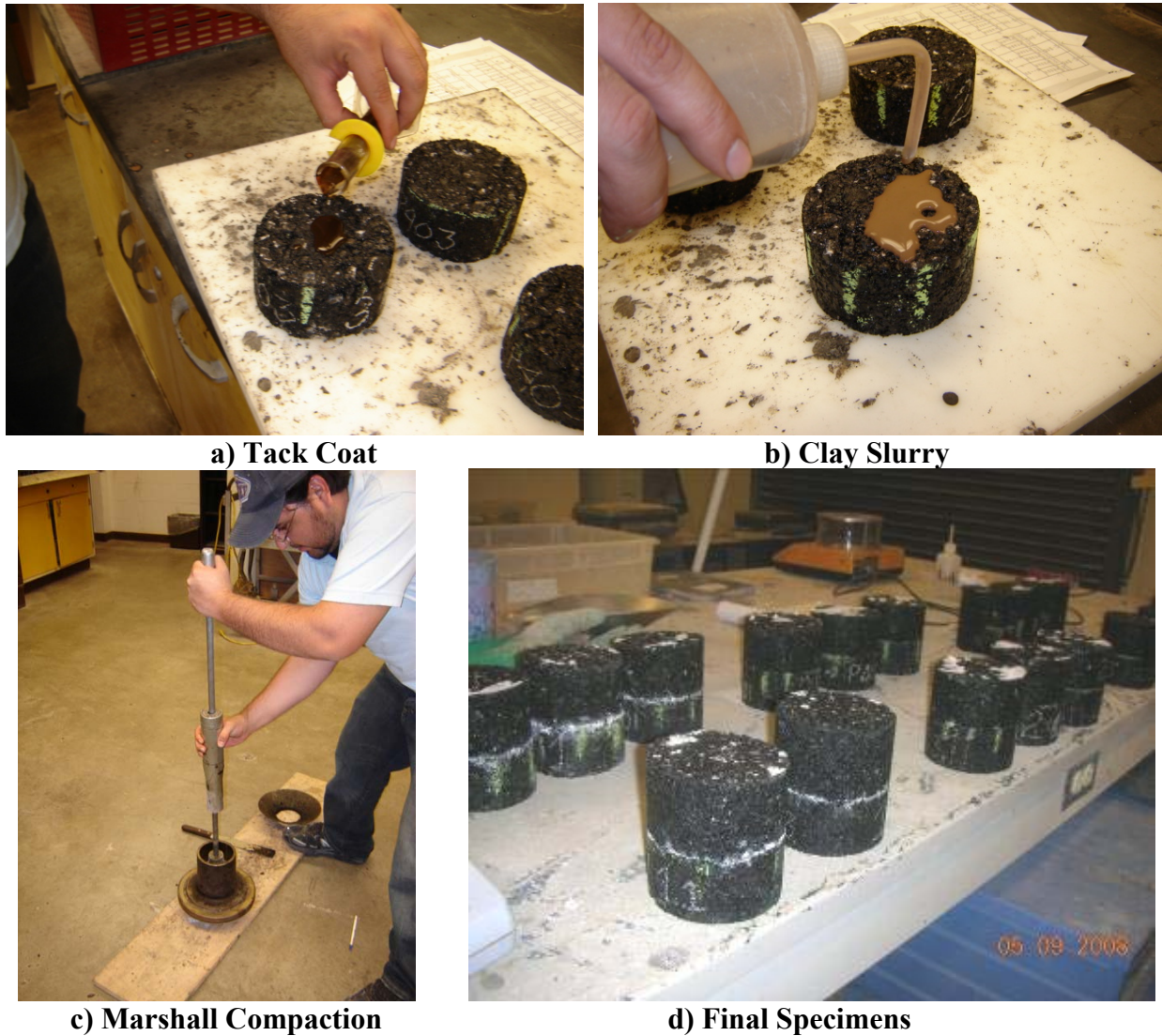


Figure 4.1 – Preparation of Laboratory Specimens and Specimens Ready for Shear Tests

The shear device used in this study is shown in Figure 4.2. The bottom lift of the specimen was trimmed so the interface between the top and bottom lifts of the specimen precisely matched with the interface of the top and bottom plates of the direct shear device. The

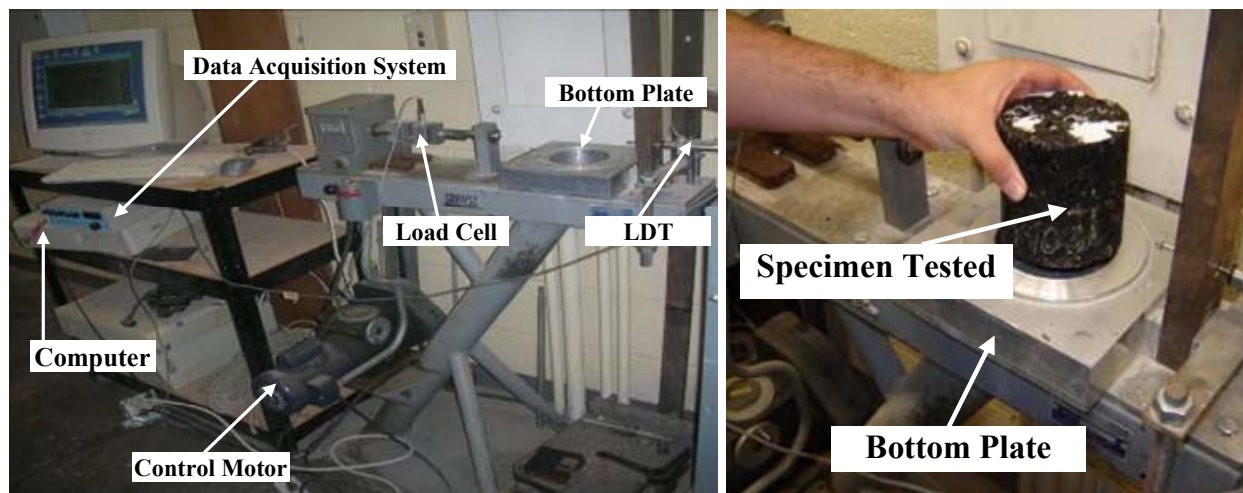


Figure 4.2 – Schematic of Shear Apparatus

specimen was sheared at a constant rate of 0.05 in./min (1.3 mm/min, see Figure 4.3) after a vertical load of 50 lbs was applied to the specimen. All tests were conducted at laboratory temperature of 72°F (22°C). A load cell attached to the system measured the load applied at any moment, while a linear displacement transducer (LDT) measured the displacement between the top and bottom lifts. Figure 4.4 illustrates typical shear forces measured with tack coat and talcum powder as bonding agents. The shear strength is simply the maximum force measured divided by the area of the specimen. The shear strengths measured for each bonding agent are presented in Table 4.1. Two sets of specimens were prepared. One set consisted of the P-403 mix as the bottom lift and the P-401 mix as the top lift. The other set comprised of two lifts of the P-401 mix. Three to seven replicate specimens were prepared for each debonding agent. For both sets of specimens, the highest bond strengths were associated with the tack coat (about 33 psi, 220 kPa), and the lowest with a thin paper soaked in motor oil (about 5 psi, 35 kPa). The coefficients of variation (COVs) of the results are rather high for most bonding agents. Aside from experimental errors, the shear resistance from aggregate interaction might explain the high COVs of these results.

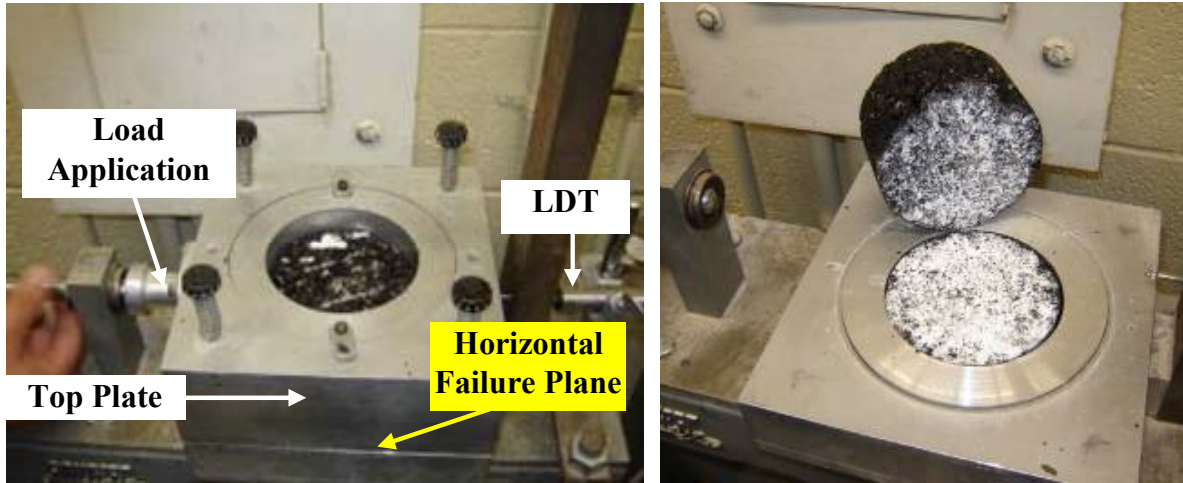


Figure 4.3 – Detail of Asphalt Sample Placement on Shear Device

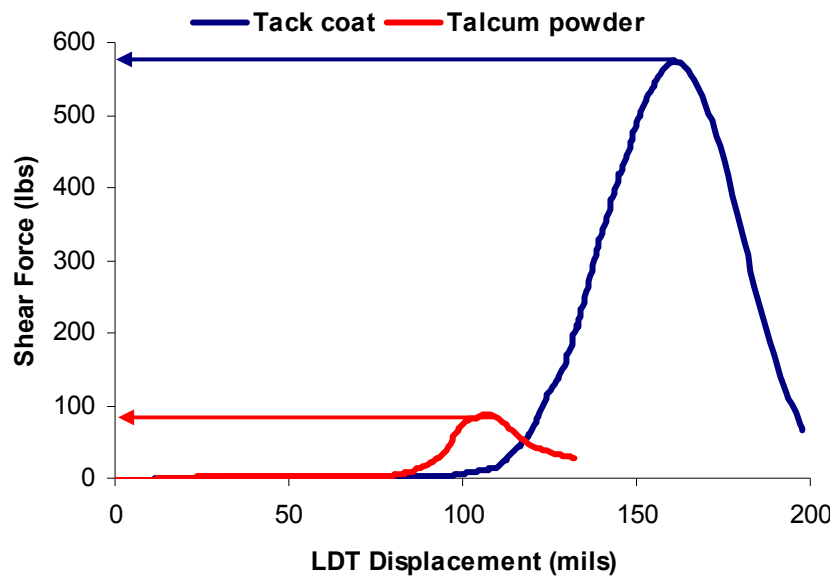


Figure 4.4 – Test Output from Shear Device

The debonding agents used in the construction of the pavement section are summarized in Table 4.2. In addition to the proposed materials, a severe debonding was reproduced by placing a piece of thick corrugated cardboard in selected areas.

Table 4.1 – Shear Strengths (in psi) for Laboratory Prepared Specimens

Sample Condition	P-401/P-401 Mixes					P-403/P-401 Mixes			
	Tack Coat	Talcum Powder	Clay Slurry	Grease	Paper Soaked in Motor Oil	Tack Coat	Talcum Powder	Clay Slurry	Paper Soaked in Motor Oil
Average*	35	20	22	19	5	32	17	27	5
COV	36%	51%	75%	19%	34%	24%	5%	19%	47%

* of three to seven specimens

Table 4.2 – Summary of Debonding Agents Considered for the Controlled Study

Partial Debonding	Full Debonding	Control Bonding	Severe Debonding
Clay Slurry	Paper Soaked in Motor Oil	Regular Amount of Tack Coat as per FAA Item P-603	Cardboard between Layers
Talcum Powder			
Grease			

Construction of Test Section

Details on the construction of the test section can be found in Appendix C. Ten different sections were constructed in a vacant lot within UTEP property, as shown in Figure 4.5. The final layout of the sections is depicted in Figure 4.6. Each section was 9 ft long (2.7 m) by 10 ft (3 m) wide. Three transition zones were incorporated [a 10 ft (3 m) section before Section 1, a 15 ft (4.6 m) section between Sections 5 and 6 and a 10 ft (3 m) section beyond Section 10] to minimize the variability of the laid down mix during construction.

The nominal pavement cross-section for all sections consisted of a prepared sandy-silt subgrade and about 8 in. (200 mm) of HMA placed in three lifts. The first two lifts of the HMA were the same for all sections. The bottom lift consisted of about 3 in. (75 mm) of a P-403 mix

and the middle lift 2.5 in. (63 mm) of a P-401 mix. The top lift of Sections 1 through 5 consisted of a coarse mix (P-403 mix) and Sections 6 through 10 a fine mix (P-401 mix).



Figure 4.5 – Location of Asphalt Section at UTEP Facilities

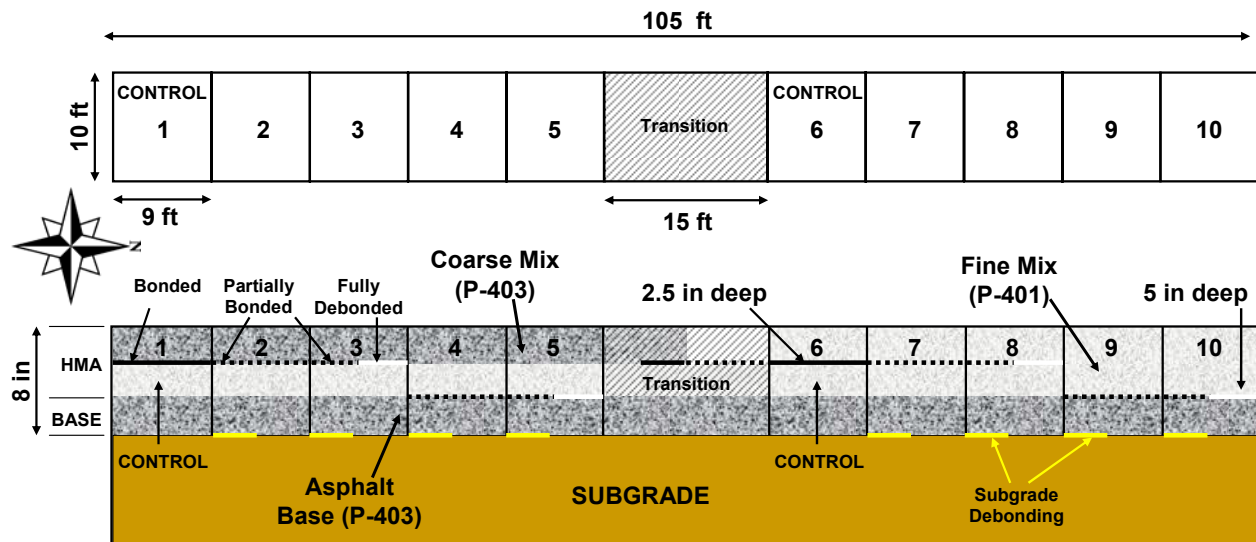


Figure 4.6 – Schematic of Controlled Section

A typical plan view of each section is depicted in Figure 4.7. The characteristics of the sections are summarized in Table 4.3. In general, a 4 ft (1.2 m) by 9 ft (3 m) area for each

section was debonded. In addition, smaller debonded areas were constructed to test the detectability threshold of the methods.

Details measurements for each point are included in Appendix C. Seismic moduli obtained with the PSPA on top of the second lift are presented in Figure 4.8. The surface temperature (T) was measured with a laser gun. The values presented were converted to a reference temperature of 77°F using (Li and Nazarian, 1994):

$$Modulus_{77F} = \frac{Modulus_T}{(-0.00307 * T + 1.2627)} \quad (4.1)$$

The average PSPA modulus (converted to the reference temperature) of the second lift was 1733 ksi (12 GPa) and the average composite modulus of the first and second lift was 1791 ksi (12.3 GPa). The same points were tested 24 hr after the completion of the third lift (see Figure 4.9). The average modulus of the top lift was 2047 ksi (14 GPa) and the average composite modulus of the three lifts was 1753 ksi (12 GPa).

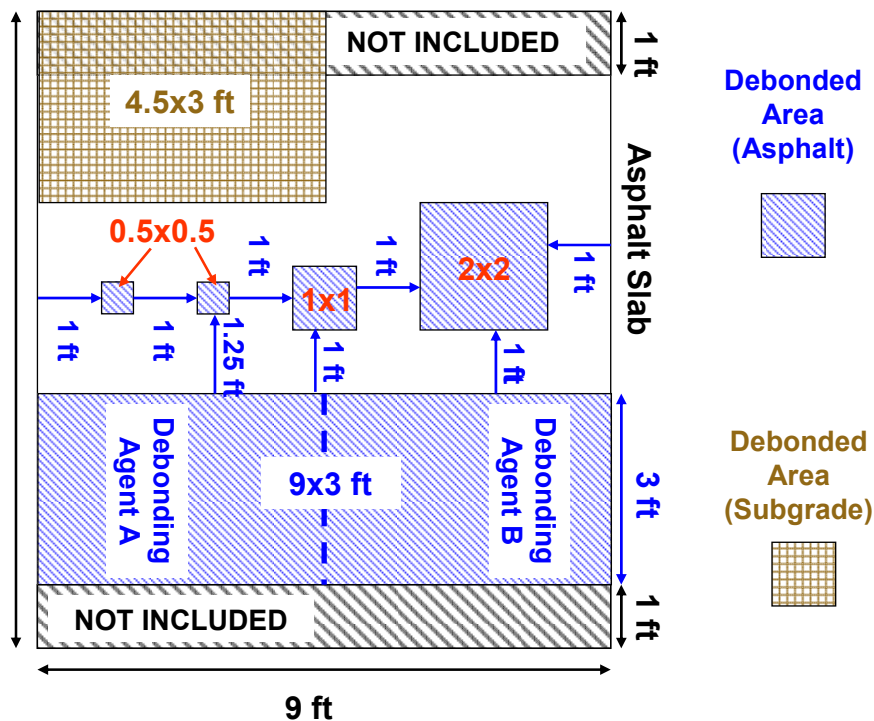


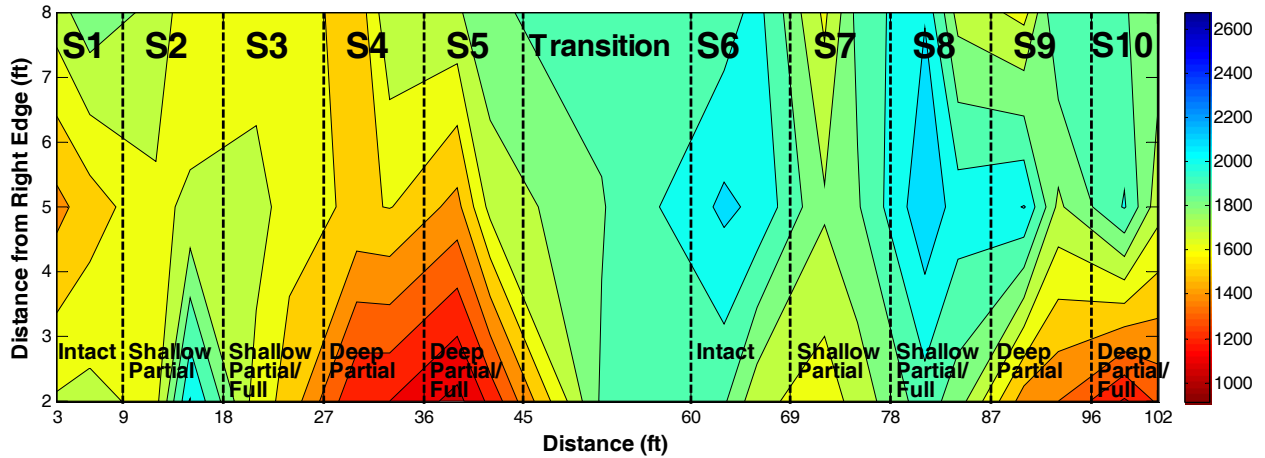
Figure 4.7 – Typical Layout for Partially and Fully Debonded Areas

Table 4.3 – Characteristics of Sections Used in This Study

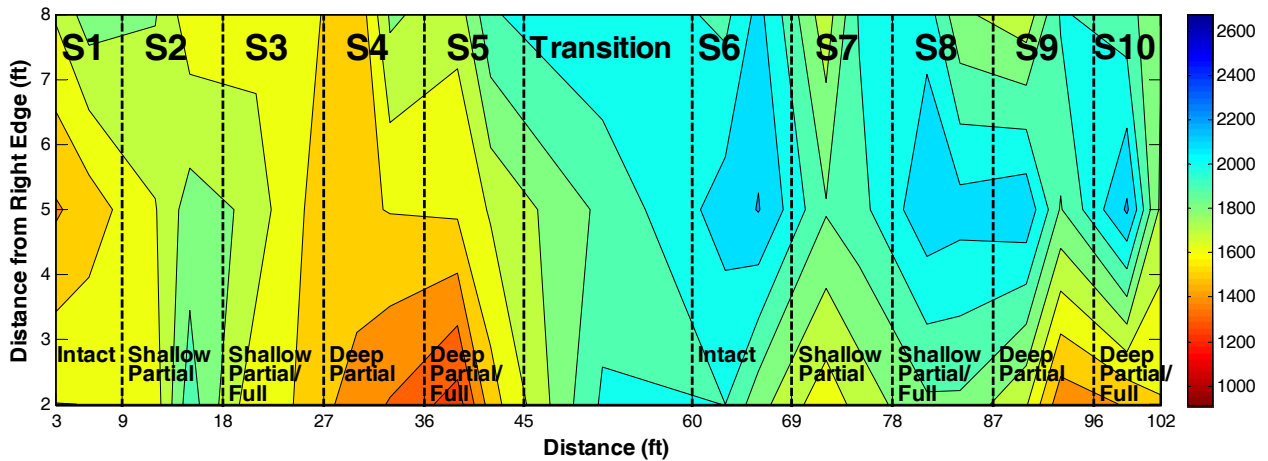
Section	Surface Mix	Designation	Debonding Agent				
			Tack Coat	Grease (Agent A)	Clay Slurry (Agent B)	Talcum Powder (Agent A)	Paper with Oil (Agent B)
1	Coarse Mix	Control	✓				
2		Shallow Partially-Debonded		✓	✓		
3		Shallow Fully-Debonded				✓*	✓
4		Deep Partially-Debonded		✓	✓		
5		Deep Fully-Debonded				✓*	✓
6	Fine Mix	Control	✓				
7		Shallow Partially-Debonded		✓	✓		
8		Shallow Fully-Debonded				✓*	✓
9		Deep Partially-Debonded		✓	✓		
10		Deep Fully-Debonded				✓*	✓

* Partially-Debonded

The nuclear density gauge (NDG) was used at 33 locations on the surface of the HMA. The variation in the relative density along the section is in Figure 4.10. Densities measured with the NDG are detailed in Appendix C. The average relative density was about 95%.



a) Lifts 1 and 2 Combined



b) Second Lift

Figure 4.8 – PSPA Results after Second Day of Construction

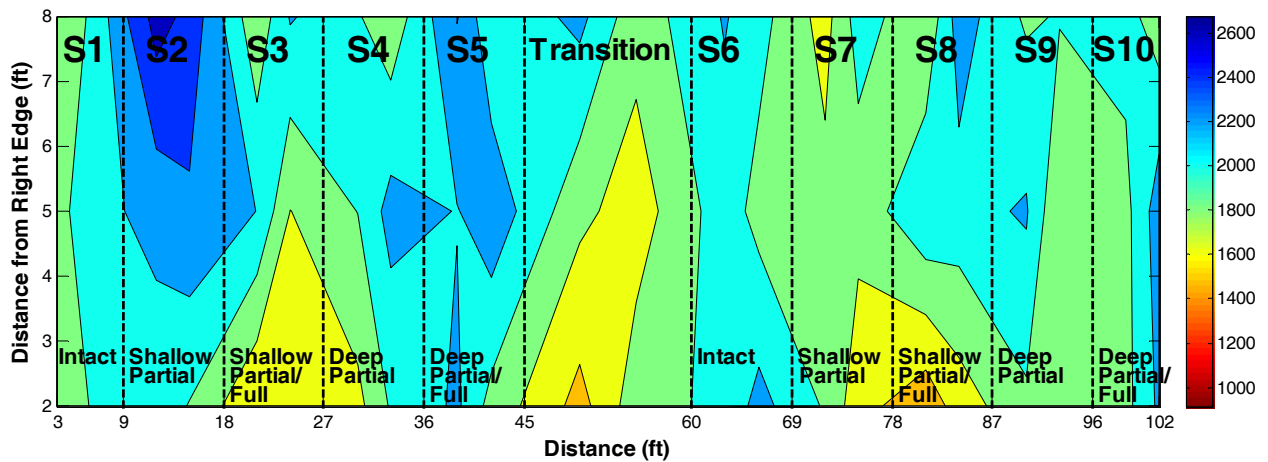


Figure 4.9 – PSPA Results for Top Lift after Completion of Construction

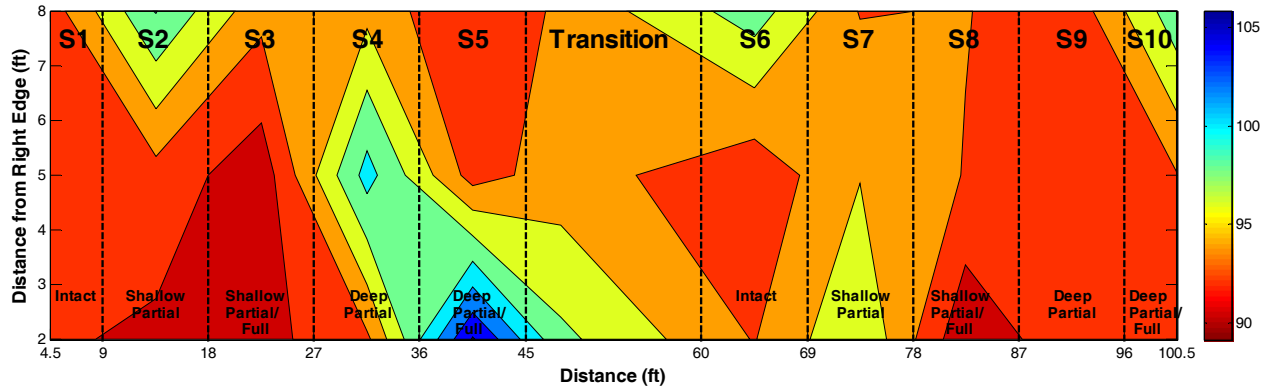


Figure 4.10 – Variation of Percentage of Marshall Density on Controlled Study

CHAPTER 5 – PRELIMINARY EVALUATION OF NDT METHODS

The preliminary evaluation with several NDT methods on the control pavement section is included in this chapter. Table 5.1 contains a list of NDT technologies employed for the detection of debonding within HMA layers. These NDT methods are extensively described in Appendix A. As such, only the results with each one will be presented in this chapter.

Table 5.1 – List of NDT Technologies Used on the Controlled Study

Method / Device									
Electro-magnetic	Impulse			Vibration		Seismic/Sonic			Thermal
Ground Penetrating Radar (GPR)	Falling Weight Deflectometer (FWD)	Light Weight Deflectometer (LWD)	Impulse Response (IR)	Stiffness Gauge (SG)	High Frequency Sweep (HFS)	Impact Echo (IE)	Ultrasonic Surface Waves (USW)	Ultrasound (US)	Thermal Imaging (TI)

Location of Test Points

As shown in Figure 5.1, 25 points were evaluated on every section. The transversal spacing between lines varied, but the longitudinal spacing was fixed at 2 ft (0.6 m). The same number of lines was maintained on the transition section (between Sections 5 and 6). The number of points was increased to 8 with the same spacing. Preliminary core locations are also included in the figure.

Sonic/Ultrasonic Seismic Methods

Impact-Echo (IE) and Ultrasonic Surface Waves (USW)

A Portable Seismic Pavement Analyzer (PSPA) was used to conduct these two tests simultaneously. As shown in Figure 5.2, the PSPA consists of an automatic source and two receivers. A test and the field analysis would take about 15 seconds.

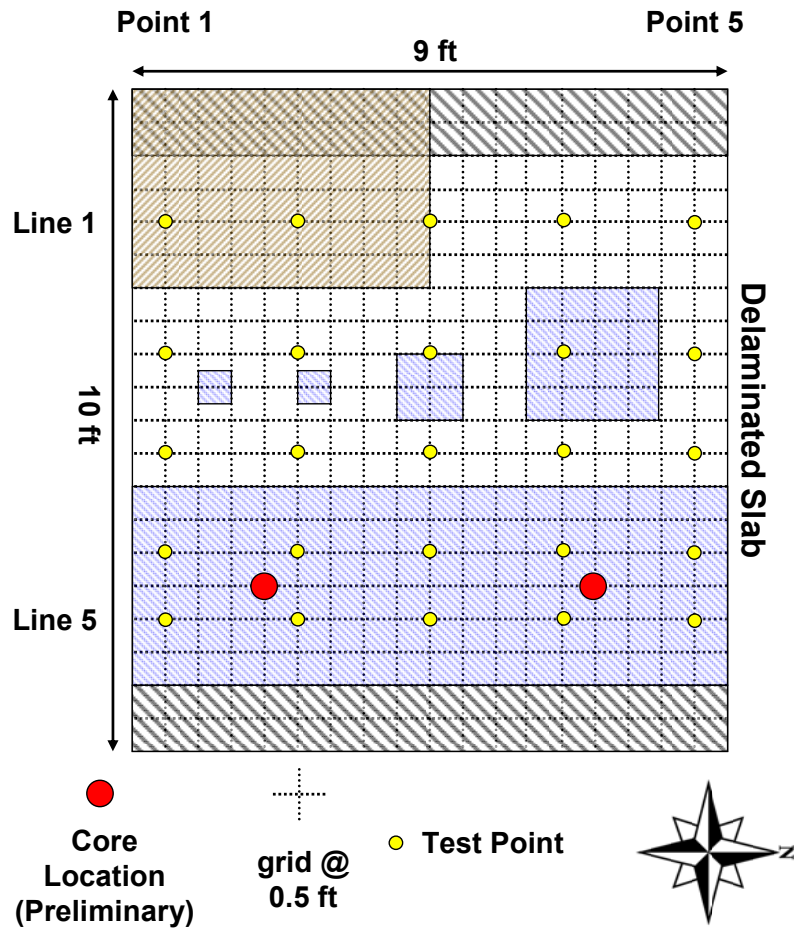


Figure 5.1 – Location of Test Points for a Given Section

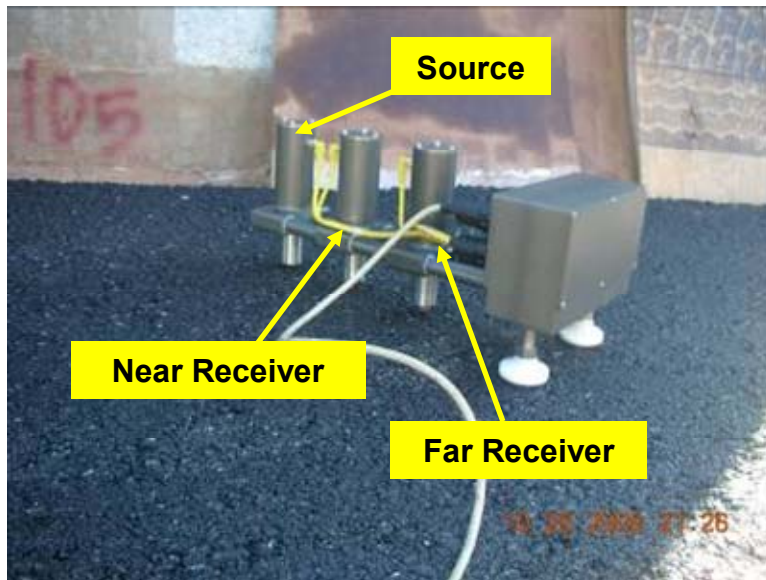


Figure 5.2 – PSPA Detail

Examples of typical voltage outputs of the three PSPA sensors as seen by the operator in the field are shown in Figure 5.3 for an intact and a severely debonded area. The time records from the two receivers (the black and green traces) are appreciably different from the two tests. The pulses are wider for the debonded record, and the minima of the two records from the intact areas are closer to one another than the ones from the damaged area.

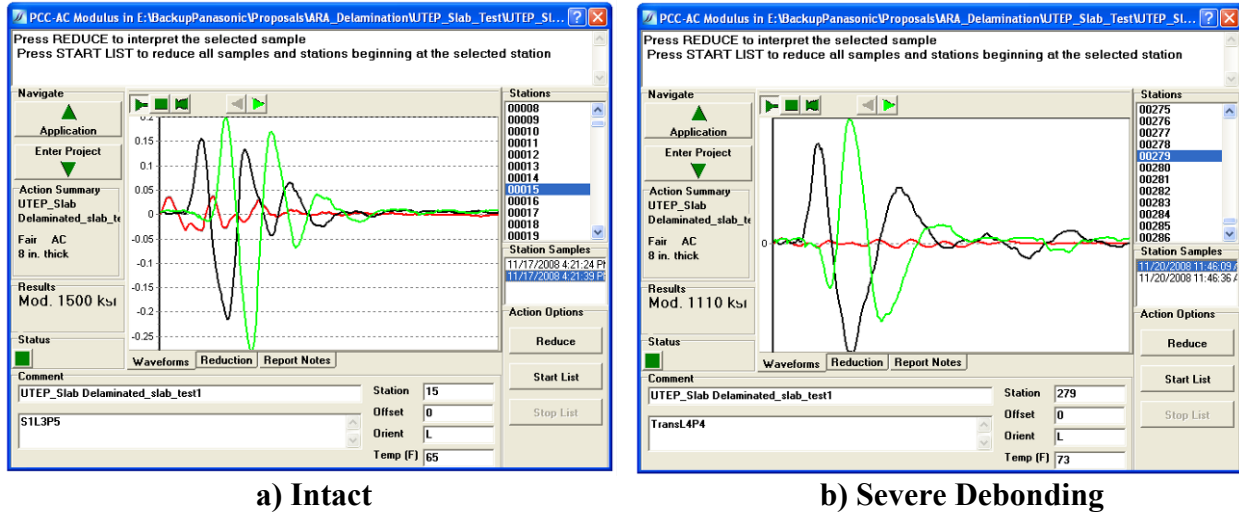
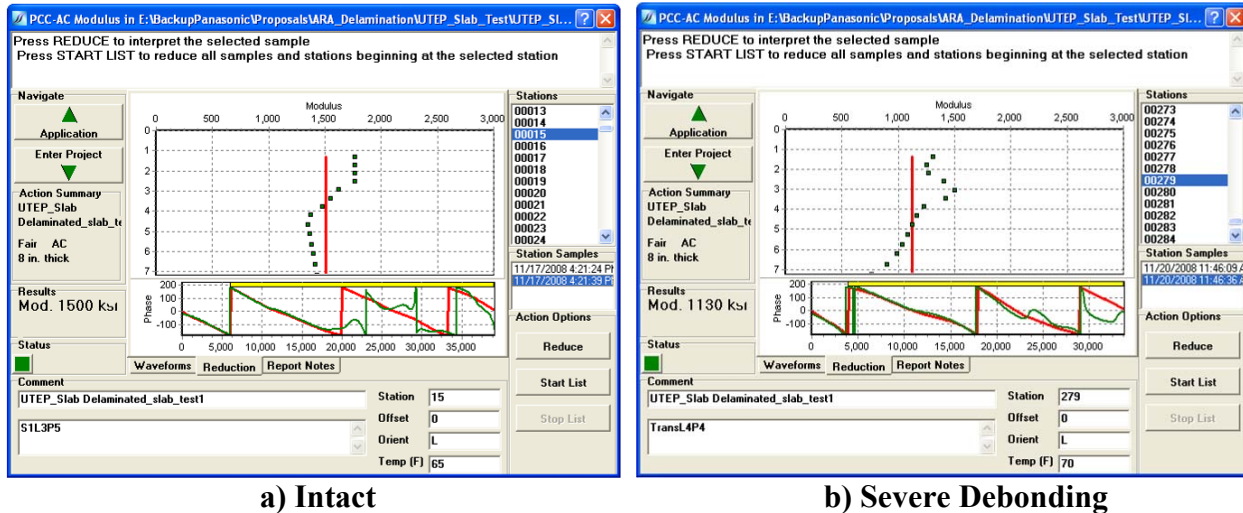


Figure 5.3 – Time Records Results with PSPA on Controlled Study

Ultrasonic Surface Waves (USW) Results

The USW analysis page as seen by the operator in the field is shown in Figure 5.4 for the time records shown in Figure 5.3. The top graphs demonstrate the variation in modulus with wavelength (called dispersion curves). The dispersion curve for the intact area is fairly uniform; whereas for the damaged point a sharp decrease in modulus below a wavelength of 2.5 in. (63 mm, the location of the damage) is evident.

The vertical red lines in the graphs demonstrate the average moduli of the HMA layer from close to surface (1 in., 25 mm) to 8 in. (200 mm, nominal thickness of the layer). As reflected in the left hand side of the two graphs, these average moduli are about 1500 ksi (10 GPa) for the intact and 1130 ksi (7.8 GPa) for the damaged areas.

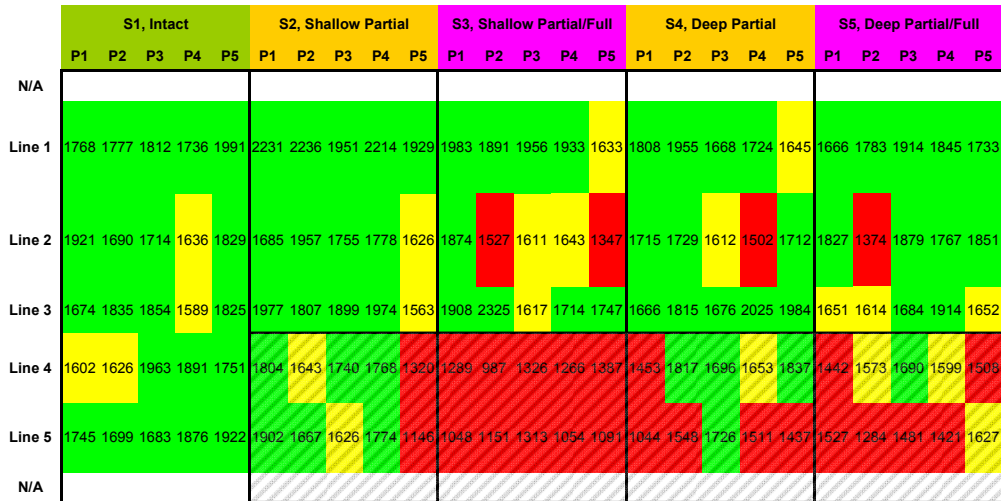


a) Intact **b) Severe Debonding**

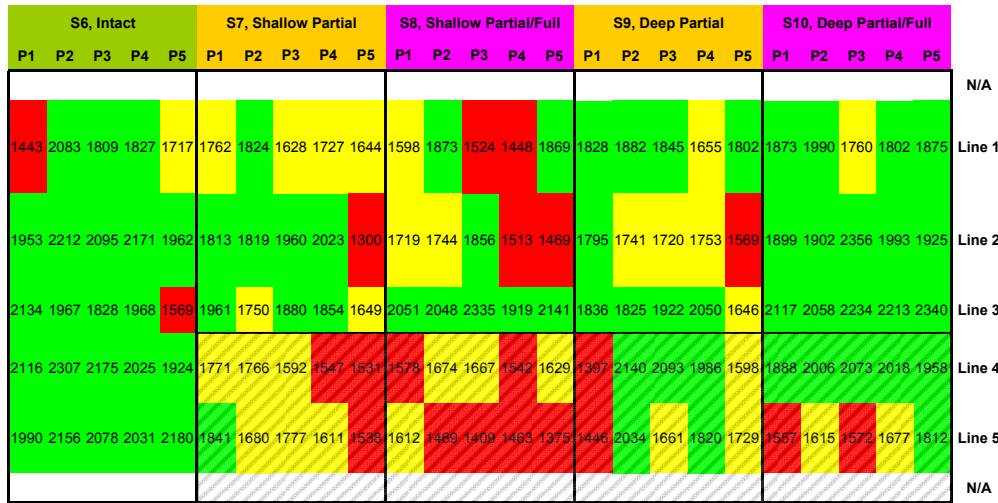
Figure 5.4 – Dispersion Curve Results with PSPA on Controlled Study

The variation in the average moduli along the ten sections is shown in Figure 5.5. Moduli were adjusted for temperature using Equation 4.1. For the benefit of the readers, the figure is color-coded. The definition of each color is included in Table 5.2. The average and standard deviation of each control section (1 and 6) were used as reference. In Figure 5.5a that corresponds to the coarse surface mix, an area from the right hand side of Section 2 until the end of Section 5 generally exhibits lower moduli as anticipated. However, parts of Sections 2 and 4, both located on partially debonded sections, exhibit normal moduli. Similar trends are observed for the fine surface HMA sections (Figure 5.5b). However, in these sections the deep debonding is not as well defined as for the similar sections with coarse surface HMA.

The average moduli for the top 2.5 in. (63 mm) of the ten sections are shown in Figure 5.6a. Some indication of debonding is observed on the prepared damaged areas, particularly for Sections 3 and 5 (coarse mixes). On the sections prepared with fine mix, the reduction of modulus is smaller on the debonded areas. For the transition area, similar findings are obtained as detailed in Appendix D. When the overall thickness of 8 in. (200 mm) was considered, the



a) Sections 1 to 5



b) Sections 6 to 10

Figure 5.5 – Statistical Analysis of PSPA Modulus on Controlled Study

Table 5.2 – Criteria Used to Analyze Moduli on Controlled Study

Color Code	Modulus Value	Interpretation
Green	$E > E_{\text{control}} - \sigma_{\text{control}}$	Measured modulus is similar or higher than modulus from control section
Yellow	$E_{\text{control}} - \sigma_{\text{control}} > E > E_{\text{control}} - 2 \sigma_{\text{control}}$	Measured modulus is somewhat less than control modulus
Red	$E < E_{\text{control}} - 2 \sigma_{\text{control}}$	Measured modulus is substantially less than control modulus

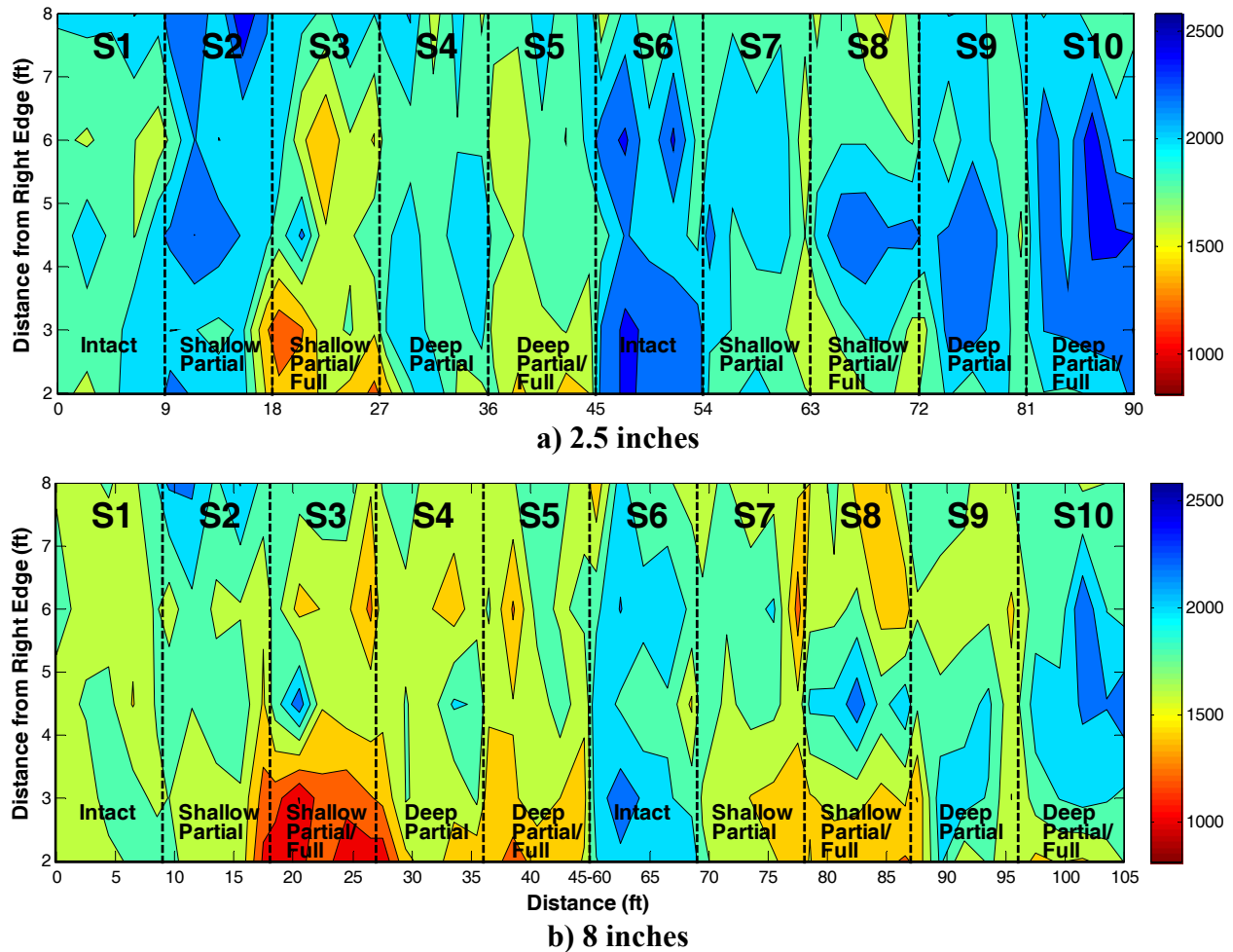


Figure 5.6 – Overall Modulus Results (Top View) on Controlled Study

indication of debonding on the prepared areas is more evident, as detailed in Figure 5.6b. This demonstrates that the USW analysis might be able to identify delaminated areas.

Detailed dispersion curves are presented in Figure 5.7 for the 5 lines and for the 10 sections. Prepared debonded areas are also depicted in the figures. A reduction in modulus can be observed in most sections except section 9. This demonstrates that the USW method might be able to identify delaminated areas.

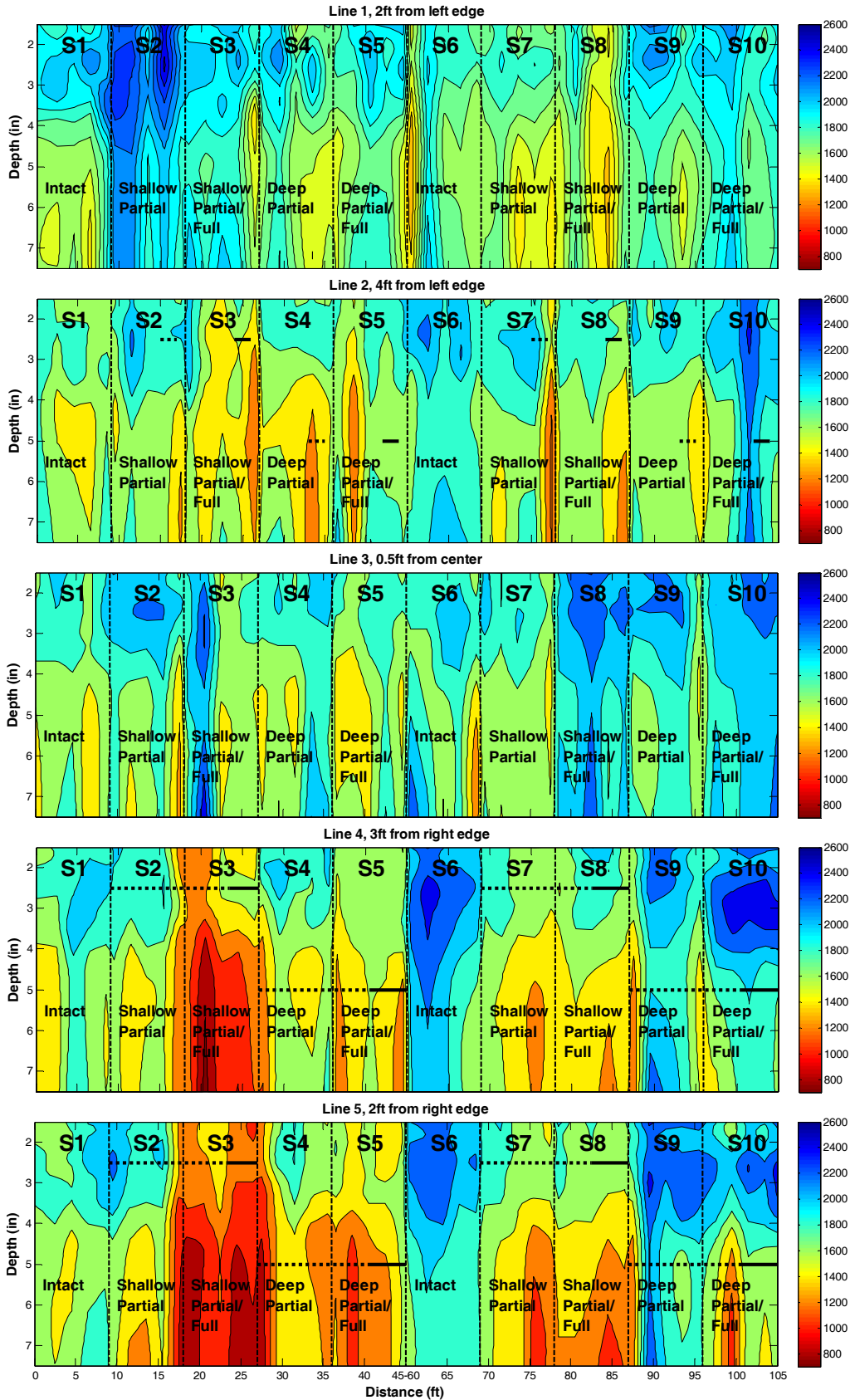


Figure 5.7 – Dispersion Curve Results for 5 Lines (Cross Section)

Impact-Echo (IE) Results

The IE method is based on detecting the resonance frequency of the standing wave reflecting from the bottom and the top of a pavement layer. The IE results are illustrated in Figure 5.8 for intact and severely debonded locations. The normalized amplitude of the frequency response on the PSPA receiver closer to the source was used. To obtain the frequency response, a Fast Fourier Transform (FFT) algorithm was applied to the time records from PSPA. For the case of the intact location, only a peak around 6800 Hz dominates the frequency spectrum. For the case of severe debonding, there is a shift to a lower frequency because a flexural (drum like) mode dominates the frequency response of the incident wave on the asphalt.

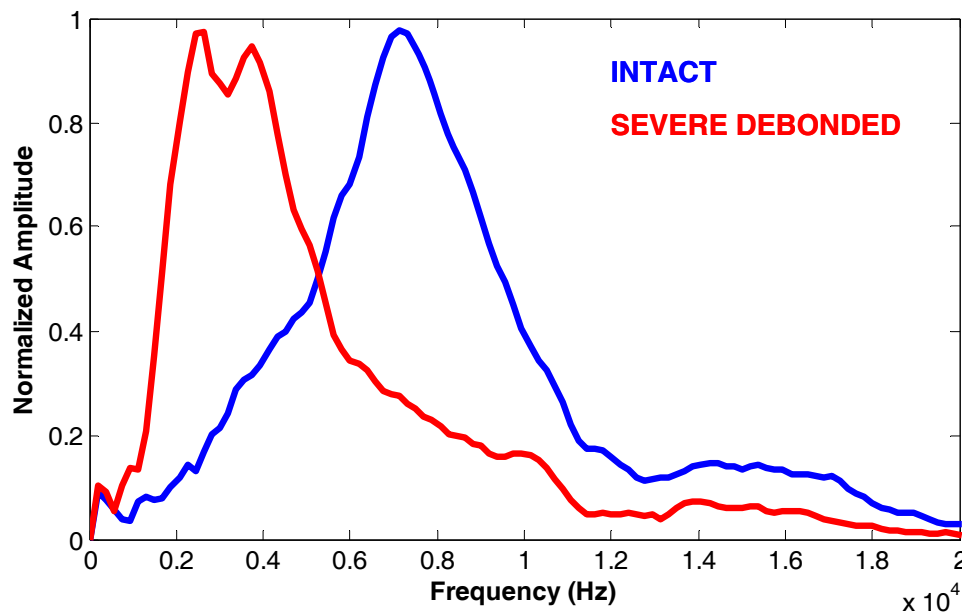


Figure 5.8 – IE Results with PSPA on Controlled Study

The contour maps of amplitude spectra are presented in Figure 5.9. On the intact section, all points show a predominant resonant frequency. Even though signs of debonding can be observed for some of the shallow fully-debonded area, the delineation of partially debonded areas from intact area seems difficult. Perhaps with more advanced analysis, this method can be

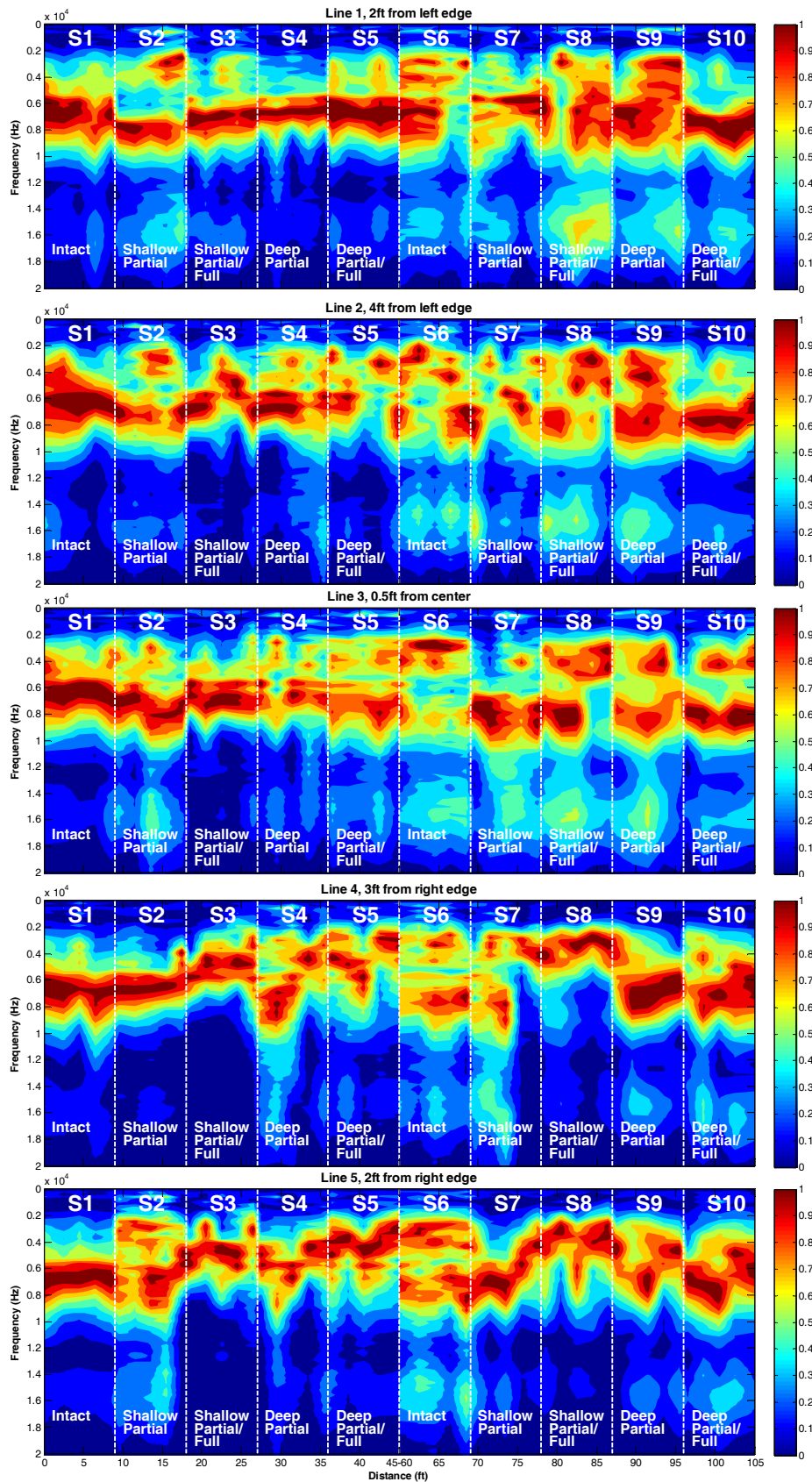


Figure 5.9 – Example of IE Results with PSPA on Controlled Study (Cross Section)

improved for day-to-day use. However, with the current state of the practice, the method may not be as reliable.

Ultrasonic (US)

An ultrasonic low frequency tomography (a.k.a. MIRA) is a low frequency ultrasonic linear array system developed by Acsys (in cooperation with BAM) especially for accelerated concrete inspection. This device is a multi-sensor ultrasonic echo (pulse echo) system, which uses the synthetic aperture focusing technique (SAFT) to provide nearly real-time images of the internal structure of the test object.

MIRA (Figure 5.10) consists of 10 measuring units, each including 4 low-frequency broadband (20-100 KHz) shear transducers with the nominal operation frequency of 50 KHz, polarized perpendicular to the length of the array. Each measuring unit includes also the electronics needed for generating, receiving, and digitizing the signals. The ten measuring units, which form the array, are packaged in the box. The data acquisition is controlled by a laptop computer and the connection between the array and the laptop is wireless.

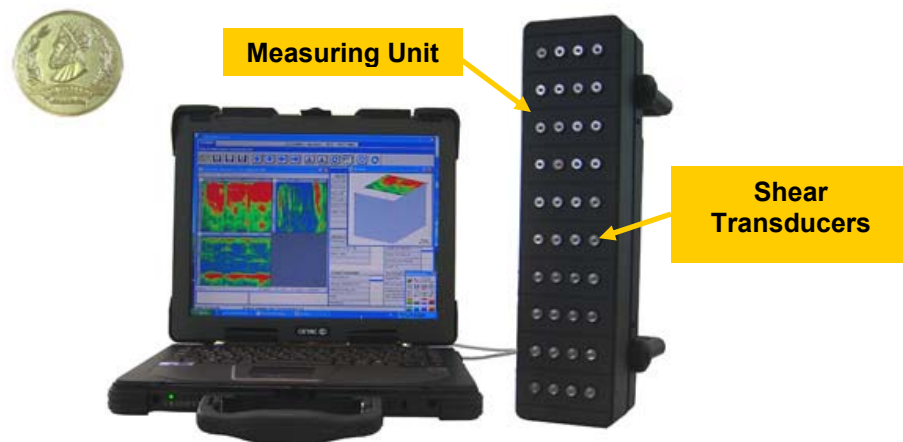


Figure 5.10 – Ultrasonic Linear Array System Used in Preliminary Evaluations

At every test point, a complete “sweep” is carried out (i.e., the first unit acts as the transmitter and all others as receivers, then the second unit acts as the transmitter and the others

record the signals, and this process continues). After one full sweep is completed in less than one second, the data is transferred to the computer, the image is reconstructed using the SAFT algorithm and displayed on the laptop screen (B-Scan). The data measured along a line can be combined into one data set and displayed as B-, C-, and D-scans (Figure 5.11).

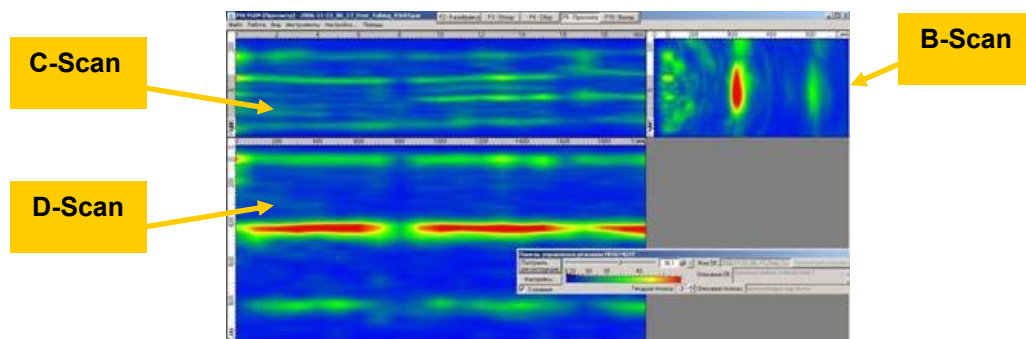
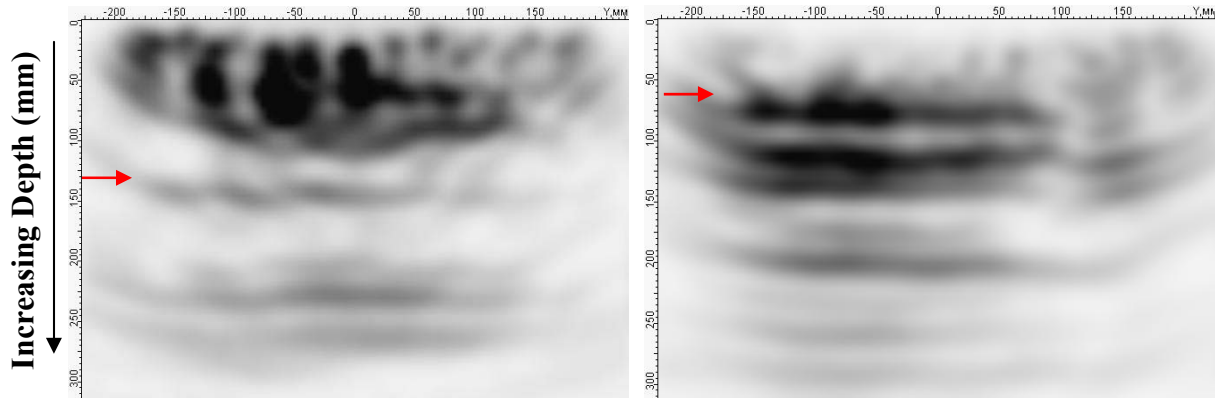


Figure 5.11 – 3D reconstructed Results of Line Measurements

Examples of B-Scans as seen immediately by the operator in the field on sections with no debonding (Section 6) and severe shallow debonding (transition section) are shown in Figure 5.12. The two B-scans are different. The first horizontal interface recognized in the B-Scan of the intact section is at a depth of about 5 in. (125 mm), which corresponds to the thickness of the top two HMA layers. As expected, the reflection from this interface is not very strong. Two other deep faint interfaces are also recognizable in this figure: one appears to be the multiple of the first reflecting interface and the other one might indicate the base-subgrade interface, although the latter interface is expected to appear at a depth of 8 in. (200 mm). This difference may be due to the inaccuracies in measuring the wave velocity during the calibration phase. A strong shallow interface is observed on the severely debonded section (Figure 5.12b). The interface appears at a depth of about 3 in. (75 mm), deeper than the expected 2.5 in. (64 mm, (marked by the red arrow). Multiple reflections are also observed in this figure; the first one particularly strong.



(a) Intact

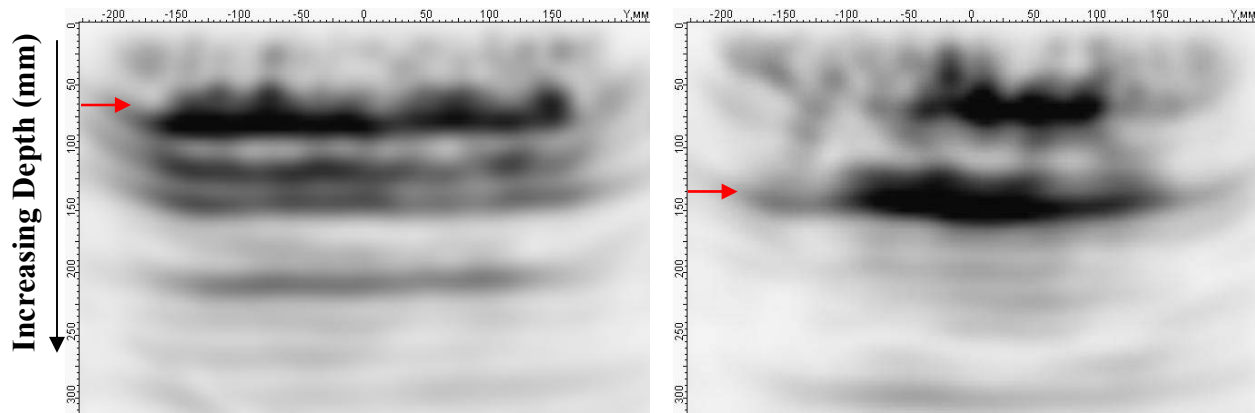
(b) Severe Debonding

Figure 5.12 – Examples of Images on Intact and Severely Debonded Sections

Two more field B-scans were obtained taken on shallow and deep fully debonded zones as shown in Figure 5.13. The image from the shallow and fully debonded section (Figure 5.13a) is similar to the severely debonded image (Figure 5.12b). The B-scan for the deep debonded section is rather different and features a very strong reflection at about 5 in. (130 mm) depth, where the debonding is expected. No more reflecting layers are present beyond this strong reflecting layer. A very faint multiple is present at about 11 in. (280 mm).

The test sections were designed and constructed such that they closely reflect the construction practices used for building actual runways. This consideration has resulted in an unavoidable symmetry in the structure of these sections. This built-in symmetry makes it difficult to distinguish, for example between the multiple reflections from a shallow delamination (at 5 in. and 7.5 in.) and direct reflections from the second and third structural interfaces at 5 in. and 8 in., respectively. More sophisticated post-processing algorithms may be used to remove multiples and differentiate different interfaces.

Ambiguities in interpretation of the results can be greatly reduced if instead of point measurements, line measurements are taken. Line measurements enable a 3-D reconstruction



(a) Shallow Fully Debonded

(b) Deep Fully Debonded

Figure 5.13 – Examples of Images on Sections with Shallow and Deep Debonding

and viewing of the results in the form of interrelated B-scans, C-scans, and D-scans. This will greatly facilitate the field interpretation of the results. However, line measurements require measurements at relatively small intervals of 4 in. (100 mm) which may make the field testing longer. Moreover, the data collection is sometimes challenging because of the difficulties in achieving the required coupling at certain positioning of the device, required to complete one line of measurements or a ‘band’.

An example of a reconstructed band (without any additional post-processing) taken on Section 3 is shown in Figure 5.14. The C- and D-scans represent the field reconstructed results from a series of measurements taken at 4 in. (100 mm) steps along a 10 ft (3 m) long line and a 1.5 ft- (450 mm) wide band. The C-scan is taken at a depth of 3 in. (or 75 mm). The extent of built-in shallow fully debonded sections is marked with red. Despite the occasional difficulties with coupling (due to the HMA roughness), the debonded zones are distinguishable in the C-scan. The results of point and line measurements indicate that the ultrasonic measurements may be used to locate the debonded interfaces within HMA.

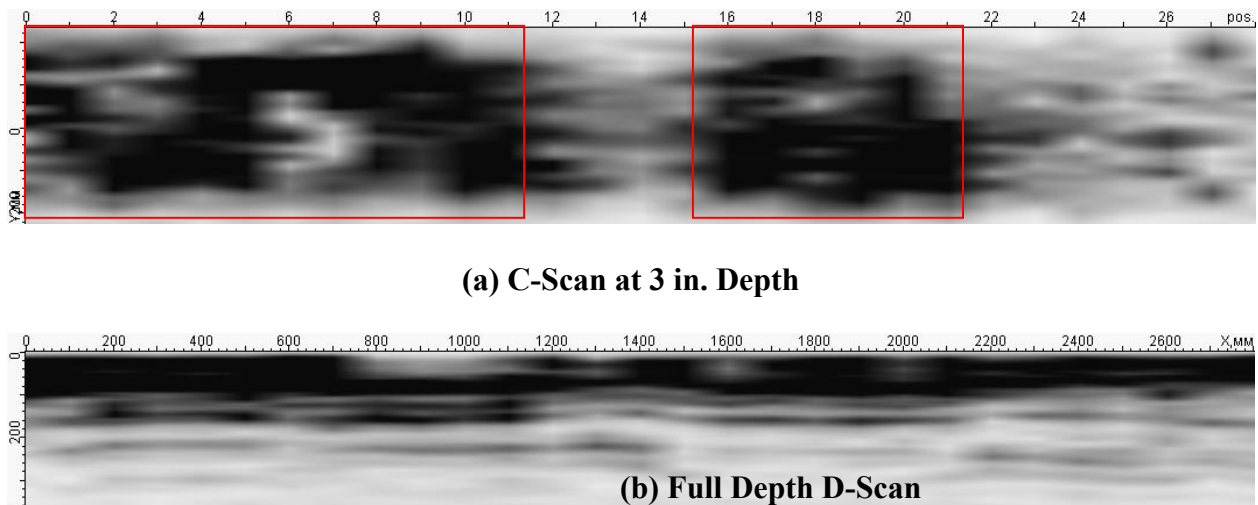


Figure 5.14 – Field Reconstructed Results from Line Measurements on Section 3

Impulse Methods

Falling Weight Deflectometer (FWD)

The FWD used on this study consisted of an impact loading mechanism and a set of seven geophones to measure vertical surface displacements. The entire system is trailer mounted as shown in Figure 5.15a. The first geophone (or SD1) was located right underneath the load and each of the other geophones was placed at 1 ft (300 mm) intervals (see Figure 5.15b). The loading device consisted of a 12 in. (300 mm) diameter load plate (Figure 5.15b) and an equivalent load of about 6,000 lbs (27 kN) was applied on the asphalt section at selected locations. A total of 90 points were considered in the preliminary study. Only Lines 1, 3 and 5 and Points 1, 3 and 5 of each section (see Figure 5.1 for details) were evaluated. Each test consisted of a setting drop, followed by three additional drops. The average vertical displacement of the last three drops measured with each geophone was used for every test location.

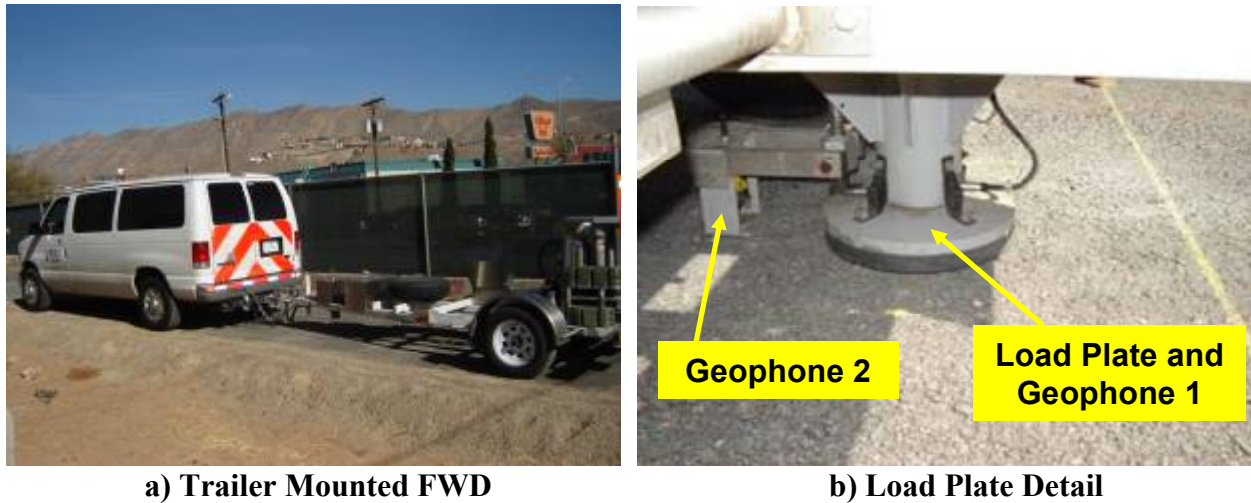


Figure 5.15 – Falling Weight Deflectometer on Controlled Study

Deflections measured for the seven geophones at an intact and the severely debonded locations are shown in Figure 5.16. Deflections of Geophones 1 and 2 (labeled as SD1 and SD2) are considerably greater at the severe debonded location. For the other five geophones, differences between intact and deboned deflections are small.

The variation in the deflection along the ten sections is shown in Figure 5.17. The color code criteria presented in Table 5.2 were used. In this case because higher deflections correspond to less stiff material, standard deviations were added instead of subtracted.

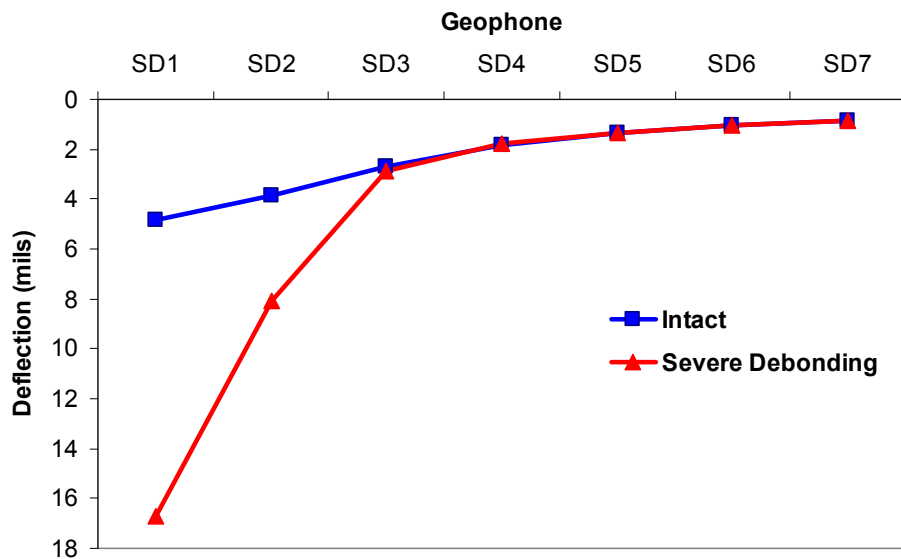


Figure 5.16 – Deflection Examples from FWD on Controlled Study

	S1, Intact			S2, Shallow Partial			S3 Shallow Partial/Full			S4, Deep Partial			S5, Deep Partial/Full		
	P1	P3	P5	P1	P3	P5	P1	P3	P5	P1	P3	P5	P1	P3	P5
N/A															
Line 1	4.9	4.6	4.7	5.6	5.7	5.2	5.4	5.5	4.7	5.0	4.1	3.9	4.2	4.1	4.5
Line 3	5.1	5.0	5.1	5.6	6.0	5.7	5.6	6.3	6.8	5.9	5.3	4.7	4.7	5.1	5.2
Line 5	7.0	6.7	5.9	6.9	6.9	7.6	8.9	10.0	11.6	8.1	6.3	7.0	7.4	7.6	6.7
N/A															

a) Sections 1 to 5

	S6, Intact			S7, Shallow Partial			S8, Shallow Partial/Full			S9, Deep Partial			S10, Deep Partial/Full		
	P1	P3	P5	P1	P3	P5	P1	P3	P5	P1	P3	P5	P1	P3	P5
N/A															
Line 1	5.2	5.7	5.6	5.5	5.2	5.2	5.5	5.3	5.1	5.2	4.4	4.9	5.3	5.5	5.0
Line 3	5.0	4.9	5.2	5.3	6.5	6.4	5.7	5.5	6.8	4.8	4.8	5.4	5.1	5.1	5.1
Line 5	5.2	5.8	5.3	5.7	5.7	6.0	5.6	6.4	8.2	5.6	6.7	7.3	9.3	9.8	8.7
N/A															

b) Sections 6 to 10

Figure 5.17 – Statistical Analysis of FWD Deflection on Controlled Study

As reflected in Figure 5.17, the deflections correspond to the debonding quite well. These deflections were converted to modulus using MODULUS 6.0 (Liu and Scullion, 2001). A 2-layer analysis that considered the entire asphalt thickness (8 in., 200 mm) and a subgrade was used. Asphalt moduli obtained with MODULUS are shown on Figure 5.18. In general, the FWD did quite well in detecting debonding. The only concern is perhaps the number of intact locations that are identified as inferior, especially on Sections 7 and 8.

Light Weight Deflectometer (LWD)

The LWD operates on a similar principle as the FWD, consisting of an impact loading mechanism and a geophone to measure deflections. The LWD used in this study is illustrated in

	S1, Intact			S2, Shallow Partial			S3 Shallow Partial/Full			S4, Deep Partial			S5, Deep Partial/Full		
	P1	P3	P5	P1	P3	P5	P1	P3	P5	P1	P3	P5	P1	P3	P5
N/A															
Line 1	1093	1289	1306	812	757	916	918	783	1091	912	1375	1606	1273	1279	1008
Line 3	989	1080	1108	877	749	846	870	672	524	763	920	1184	1081	871	786
Line 5	692	769	1046	675	660	493	328	244	195	408	741	527	374	346	487
N/A															

a) Sections 1 to 5

	S6, Intact			S7, Shallow Partial			S8 Shallow Partial/Full			S9, Deep Partial			S10, Deep Partial/Full		
	P1	P3	P5	P1	P3	P5	P1	P3	P5	P1	P3	P5	P1	P3	P5
N/A															
Line 1	876	749	804	856	862	784	697	749	849	759	1085	898	835	741	990
Line 3	927	1073	946	903	282	451	598	628	380	856	881	689	876	899	914
Line 5	869	619	815	685	619	489	495	357	228	692	458	409	285	252	307
N/A															

b) Sections 6 to 10

Figure 5.18 – FWD Moduli Results on Controlled Study

Figure 5.19. The device consisted of about 22 pound (100 N) load and a load plate of 8 in. (200 mm) diameter. A sensor underneath the load plate measured the deflection of the load plate during testing. The device also provides the material stiffness based on the deflection measured. For every test the load was raised about 20 in. (500 mm) and dropped to obtain an equivalent load of 1,600 lbs (7 kN). The average deflection and stiffness of three drops after a seating load are reported.

Deflections time-histories measured on the intact and severe debonded locations are shown in Figure 5.20. On the debonded location, maximum deflection (about 15 mils, 380 microns) was approximately 3 times larger than the intact location (5 mils, 125 microns). The debonded location was also replicated to study repeatability of the system. However,

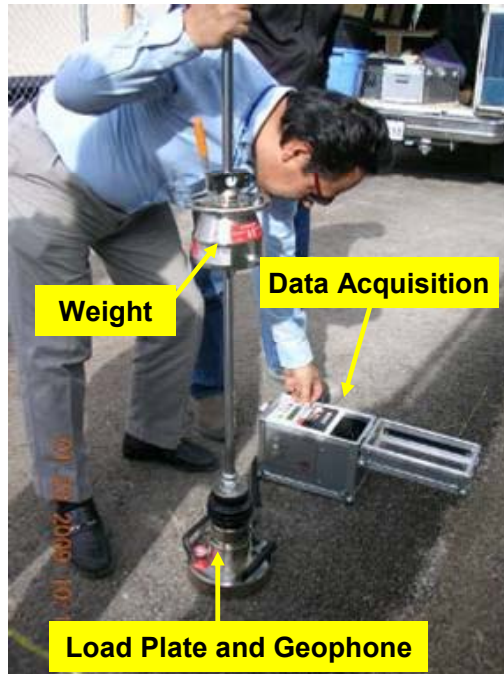


Figure 5.19 – Light Weight Deflectometer on Controlled Study

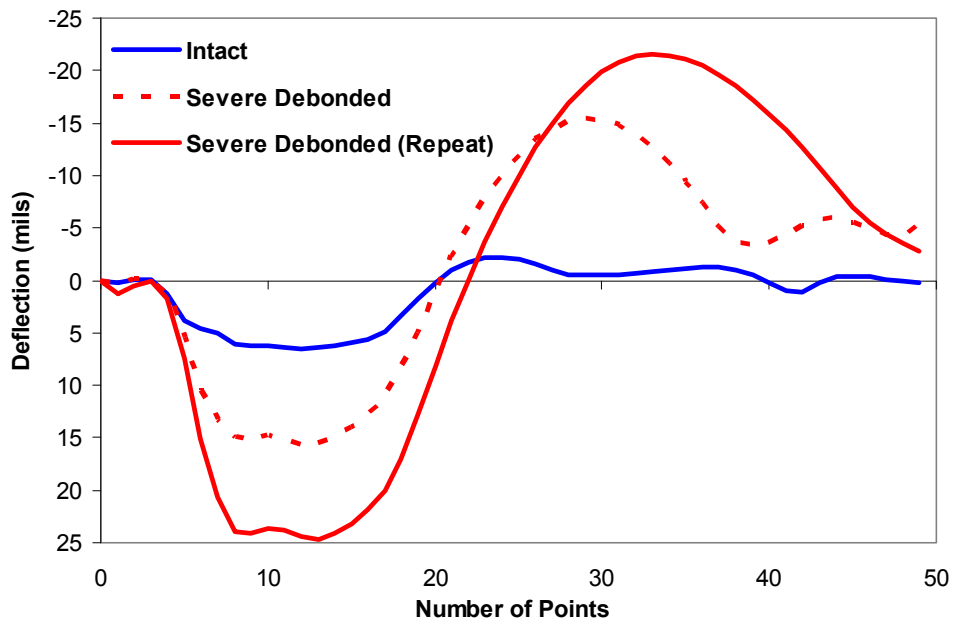


Figure 5.20 – Deflection Examples from LWD on Controlled Study

considerable differences were observed as judged by the maximum deflections measured of 15 and 25 mils for the same location.

The average deflections for the ten sections are shown in Figure 5.21. The LWD did not provide any indication of debonding for almost all debonded area, since higher deflections did not correspond to delaminated areas. However, a number of intact areas yielded higher deflections. Based on this study, it seems that the LWD may not be suitable for detecting debonding.

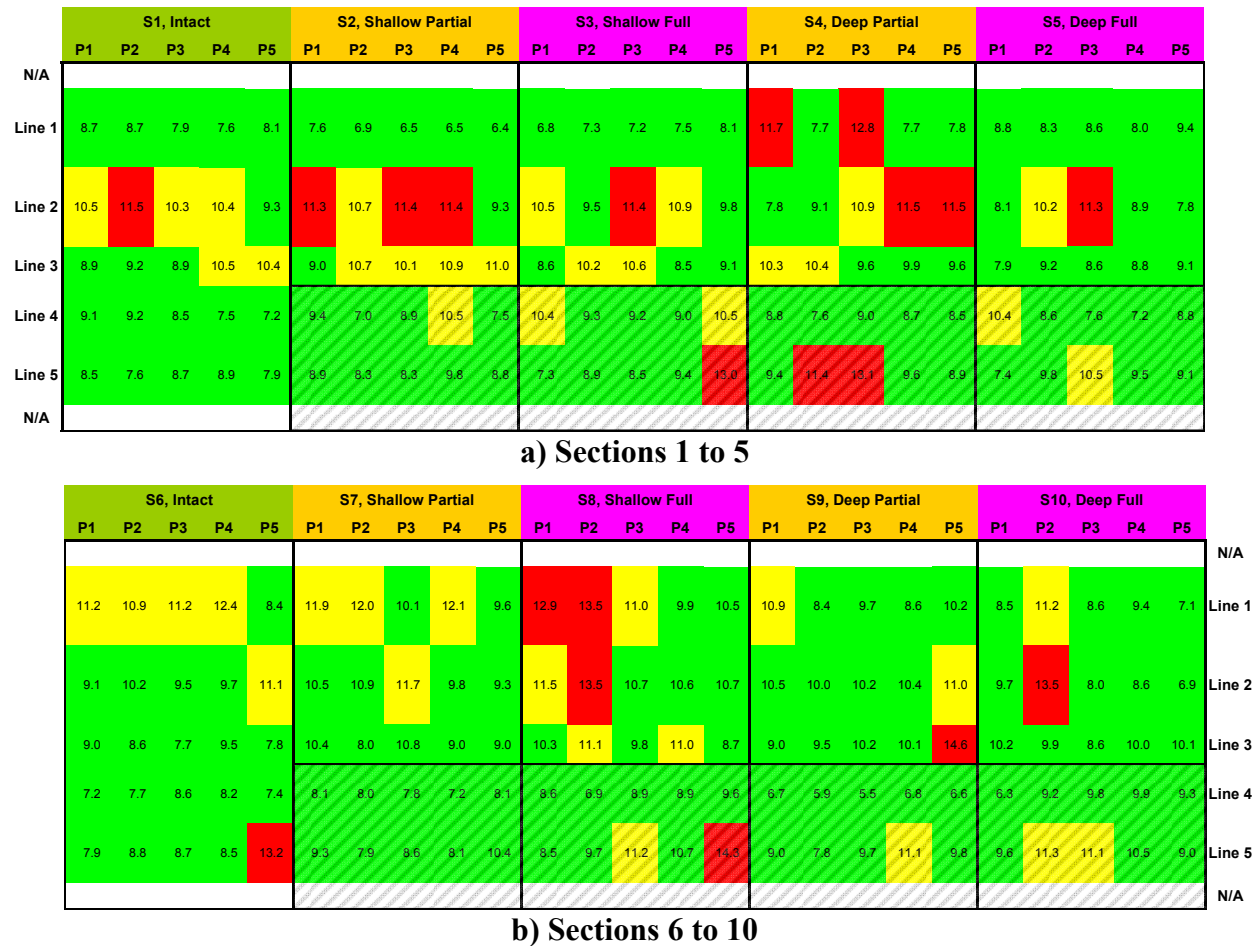


Figure 5.21 – Statistical Analysis of LWD Deflections on Controlled Study

Impulse Response (IR)

The basic operating principle of the impulse response method is to apply an impulsive loading to the pavement surface with a hammer and to measure the vertical displacement using a geophone. If structural distresses are present in the form of loss of adhesion between pavement

layers, this is reflected in the dynamic response of the pavement structure. The response is usually measured in terms of voltage amplitude of the geophone.

The equipment used in this study is shown in Figure 5.22. A 10-lb (45 N) hammer instrumented with a load cell and a 4.5-Hz geophone were used. Both the hammer and the receiver were connected to a portable field computer for data acquisition and storage. The time

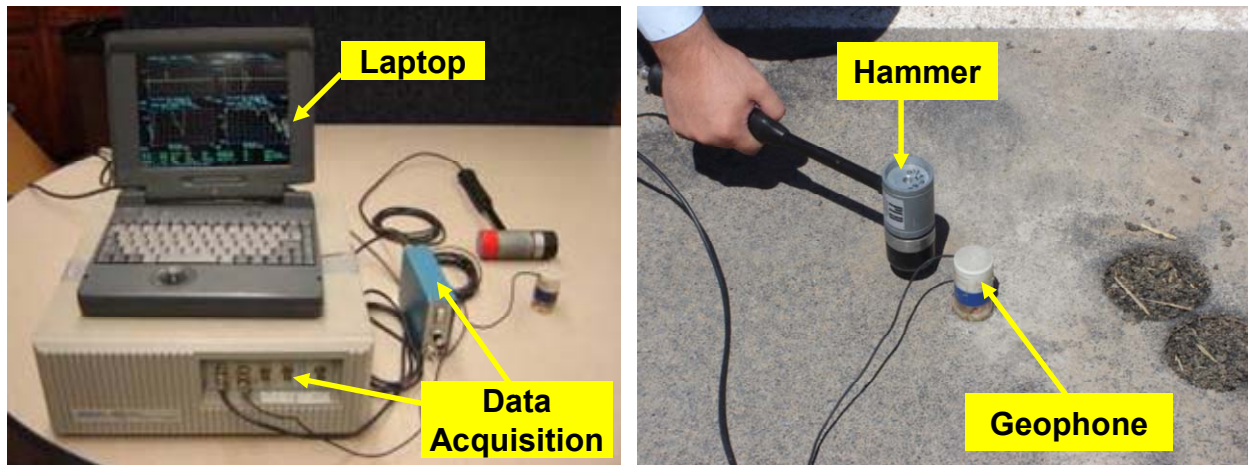


Figure 5.22 – Impulse Response Test Setup

needed to carry out one test, is about 30 seconds. The equivalent load applied by the hammer was kept constant and was around 2,500 lbs (11 kN).

An example of two test results on a sound and severely debonded area are shown in Figure 5.23. The voltage amplitude of the geophone for the severe debonded area was around three to four times as large as compared to the intact location, while the amplitude of the load remained similar. The pulse was also much wider for the debonded record. The ratio between the load cell and geophone amplitudes was used in this study first because of its simplicity. Smaller ratio corresponds to greater flexibility of the section and therefore debonded locations.

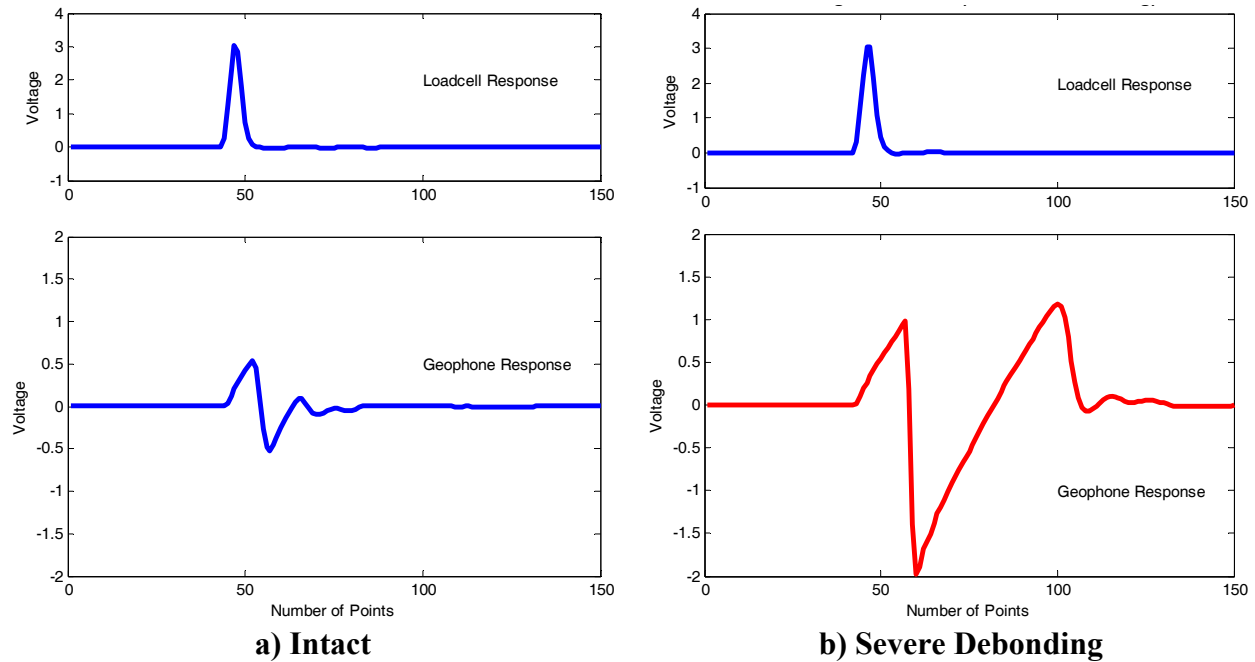
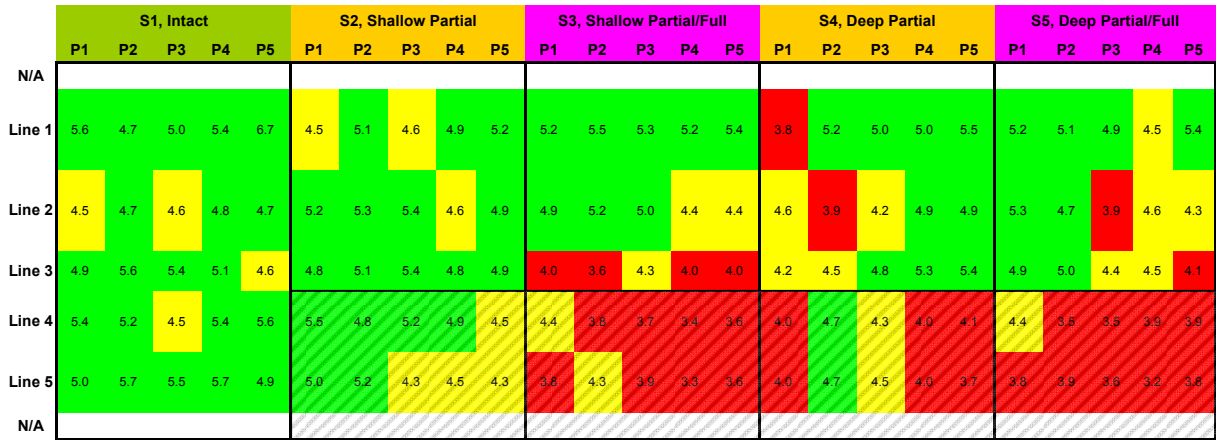


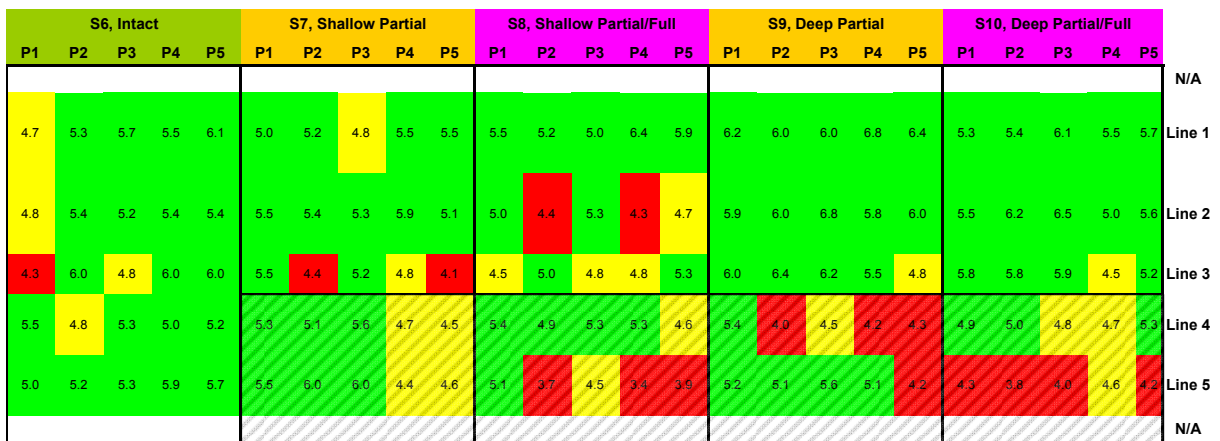
Figure 5.23 – IR Examples on Controlled Study

Results are summarized and color-coded in Figure 5.24. Most of the fully debonded areas along lines 4 and 5 were identified on the coarse mix and only a few on the fine mix, mostly on line 5. Some partially debonded areas showed indication of marginally less stiff (marked as yellow), but some were found to be intact (green) or substantially less stiff (red). For the case of the intact locations (line 1 and sections 1 and 6), the majority of the points were categorized as intact.

A more appropriate but slightly more complicated analysis consisted of determining the frequency responses using a FFT algorithm. The frequency responses for the intact and severe debonding cases are presented in Figure 5.25. The amplitude spectra for the loads were similar. However, a significant difference was found when the geophone responses were compared. For the intact location the amplitude presented a dominant frequency of about 300 Hz with amplitude of 4.5 and for the severe debonded the frequency was erratic and the maximum amplitude was close to 30. The ratio of the maximum values of the FFT amplitude was used to compare the

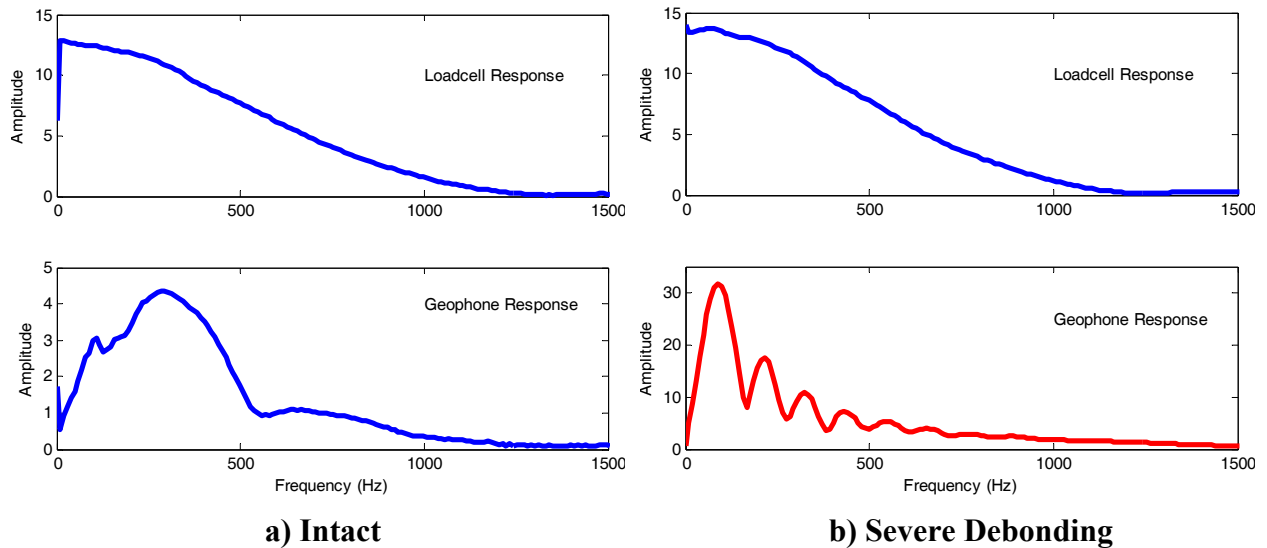


a) Sections 1 to 5



b) Sections 6 to 10

Figure 5.24 – Statistical Analysis of Voltage Amplitude Ratio of IR on Controlled Study



a) Intact

b) Severe Debonding

Figure 5.25 – FFT Results from IR Examples on Controlled Study

results as color-coded in Figure 5.26. In this case most of the fully debonded points were identified for both mixes. The partial debonding did not show as much sensitivity similar to the voltage ratio described earlier. Most of the intact locations were identified as intact. Once again, the IR method seems promising for the detection of debonding.

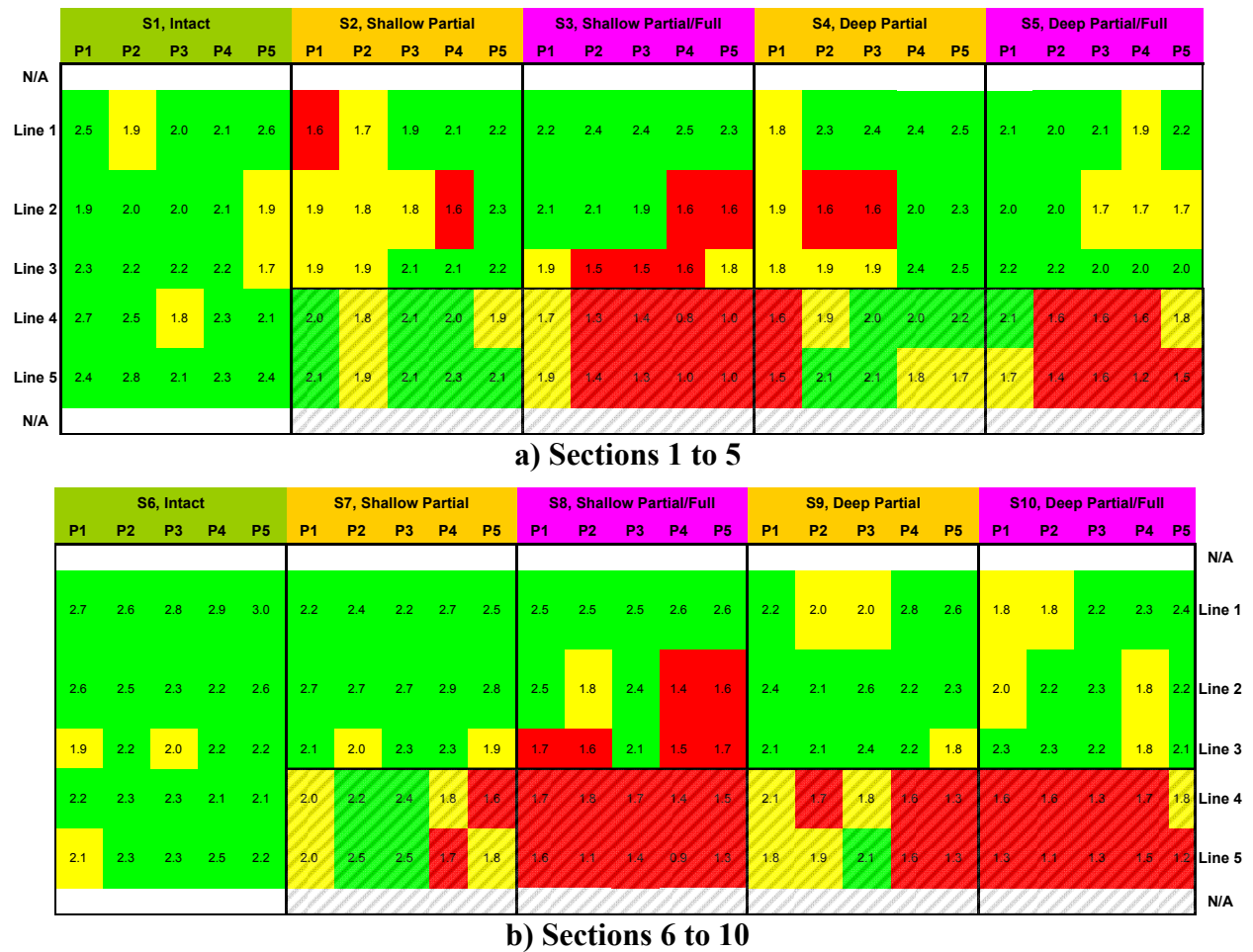


Figure 5.26 – Statistical Analysis of FFT Amplitude Ratio of IR on Controlled Study

Vibration Methods

Stiffness Gauge

The soil stiffness gauge (SSG) used in this study is depicted in Figure 5.27. The SSG is a 11 in. (280 mm) in diameter and 10 in. (250 mm) in height portable cylinder with a 4.5 in. (114 mm) outer diameter and 3.5 in. (89 mm) inner diameter ring-shaped foot extending from the

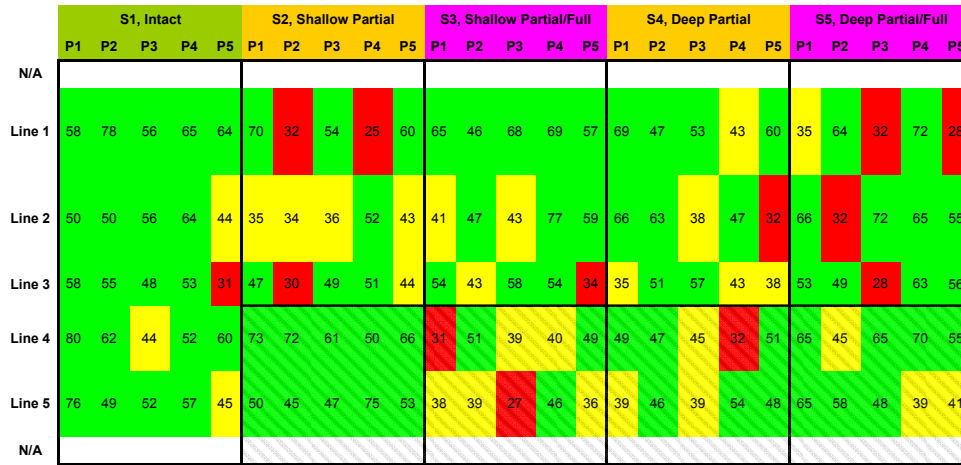


Figure 5.27 – Stiffness Gauge on Controlled Study

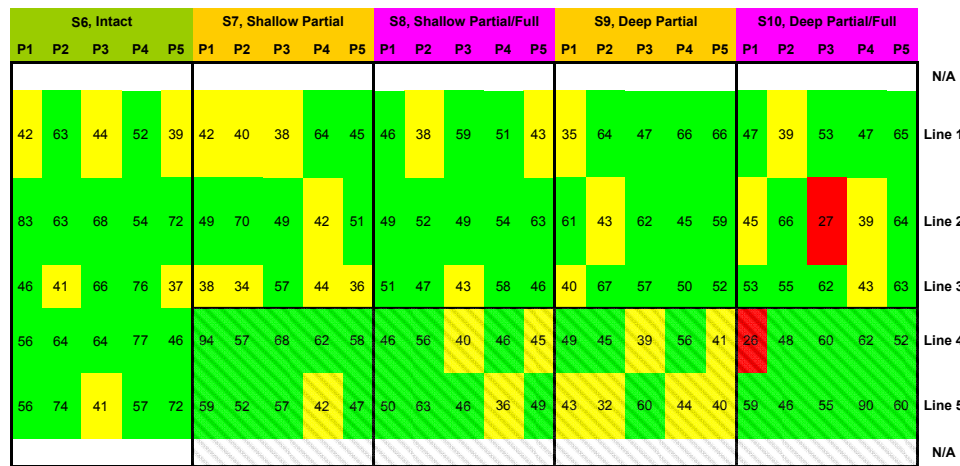
bottom of the device and it weighs approximately 22 lbs (100 N). The stiffness gauge vibrates the material in the range of frequencies of 100 Hz to 200 Hz using small load amplitudes. The variation in stiffness (displacement/load) with frequency (called stiffness spectrum) is used to measure the modulus of the material. To collect a point the SSG is carefully placed on the point of interest and the operator starts the sequence. The SSG typically requires one minute to carry out a measurement. Stiffness obtained on these points ranged from 99 to 420 klbf/in. (17 to 73 MN/m). The SGC stiffnesses for the ten sections are shown in Figure 5.28. Details can be found in Appendix D. The minimum value was obtained on the severe debonded area and the maximum was measured on the debonded area of Section 7 (shallow and full debonding). Similar to LWD, the SSG did not provide reasonable indication of the debonding areas.

High Frequency Sweep

This method uses a high-frequency, hand-held electromagnetic/piezoelectric shaker, which can be used to impart steady state swept vibration at high-frequencies and at high energy. The high-intensity, high-frequency vibration primarily excites the pavement layer. Such



a) Sections 1 to 5



b) Sections 6 to 10

Figure 5.28 – Statistical Analysis of SSG Modulus on Controlled Study

vibrations can be detected by the built-in accelerometer of the shaker. The stiffness spectra from this device can be used to detect the delaminated layer similar to the IR method.

The setup used in this study is shown in Figure 5.29. A dynamic signal analyzer was used to generate a sweep from frequencies of 0 to 20 kHz. The signal was amplified with a signal amplifier and then sent to the shaker. The frequency response between the accelerometer and the load cell inside the shaker was measured and recorded with the analyzer. An example of two tests obtained on a sound and severely debonded areas are shown in Figure 5.30. The frequency corresponding to the maximum amplitude in both cases was similar and around 5 kHz.

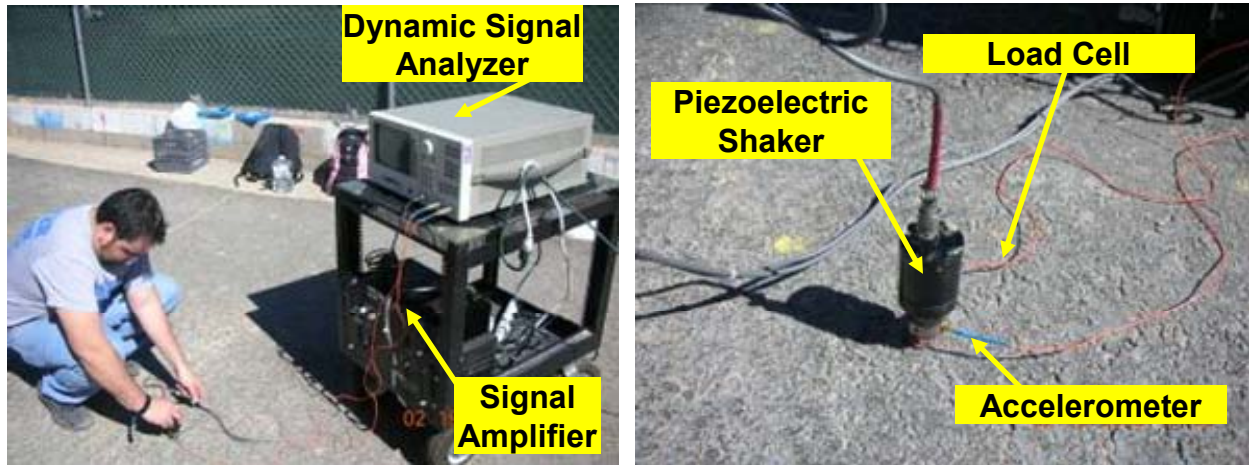


Figure 5.29 – High Frequency Sweep Test Setup

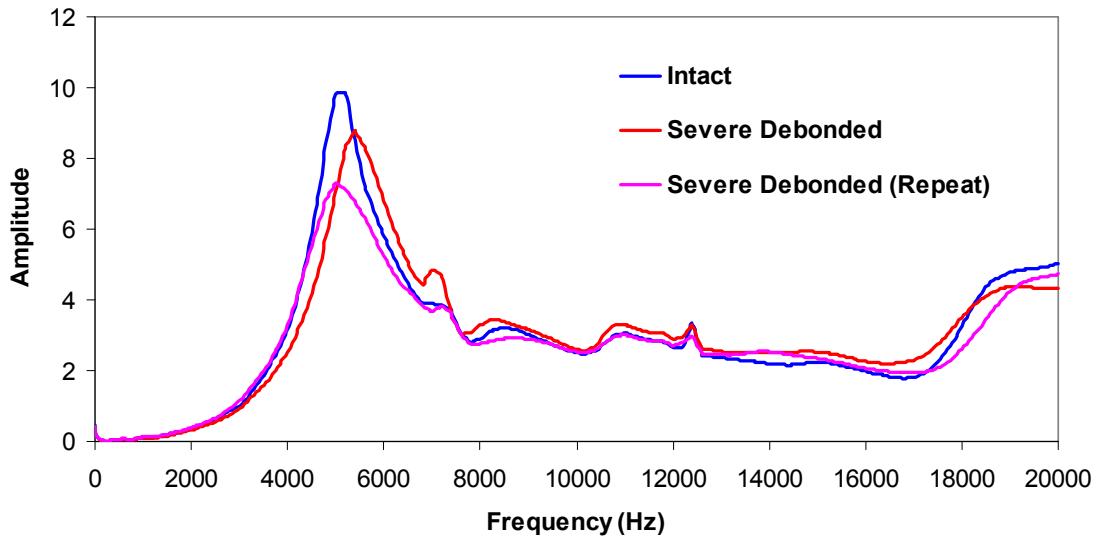


Figure 5.30 – High Frequency Sweep Examples on Controlled Study

Since the time to collect one point required around 5 minutes, only 3 points (P1, P3 and P5) of Line 5 on the first 5 slabs were initially collected. Results are summarized in Table 5.3. The frequencies at the maximum amplitude as well as the maximum amplitudes of the frequency response were very similar for all points and no significant differences among fully- and partially-debonded areas and bonded areas were found. This method also does not seem very feasible.

Table 5.3 – Frequency (KHz) at Maximum Amplitude Measured with High Frequency Sweep at Selected Locations of Controlled Study

Parameters Measured	Section 1			Section 2			Section 3			Section 4			Section 5		
	P1	P3	P5	P1	P3	P5	P1	P3	P5	P1	P3	P5	P1	P3	P5
Frequency at Max. Amplitude	5.1	5.0	5.0	5.1	5.3	5.6	4.7	5.2	5.7	5.1	5.1	5.1	5.0	4.9	5.3
Maximum Amplitude (Volts)	8.8	9.5	10.1	9.0	8.9	7.8	7.5	9.1	7.8	8.9	10.1	9.0	7.4	8.7	9.0

Thermal Methods

Infrared Camera

An InfraCAM™ SD from FLIR systems was used to evaluate the thermal method as shown in Figure 5.31. The camera collects thermal images of a surface area of approximately 2 ft by 2 ft (0.6 m by 0.6 mm) when the camera is used at a height of approximately 4 ft (1.2 m) from the surface. The camera operates on a range of temperatures from 14°F to 660°F (-10°C to 350°C). The operator aims a laser pointer to the surface of the pavement and collects and stores an image of 240x240 pixels. The time needed to collect and store an image is typically 20 seconds.



Figure 5.31 – Infrared Camera on Controlled Study

A combined image around the severely deboned area is shown in Figure 5.32. A passive source (sunlight) was used to create the temperature differentials on the surface of the HMA. The hotter areas (depicted in white) correspond to the area on top of the severe debonding. The same procedure was applied to collect the data on the 10 sections. A total of 25 pictures were obtained on each section at the predetermined locations. Results are presented in Figure 5.33. Only the severely debonded area within the transition zone was clearly detected by the infrared camera. The results of this method were not very encouraging. A more sensitive thermal camera may provide more reasonable results.

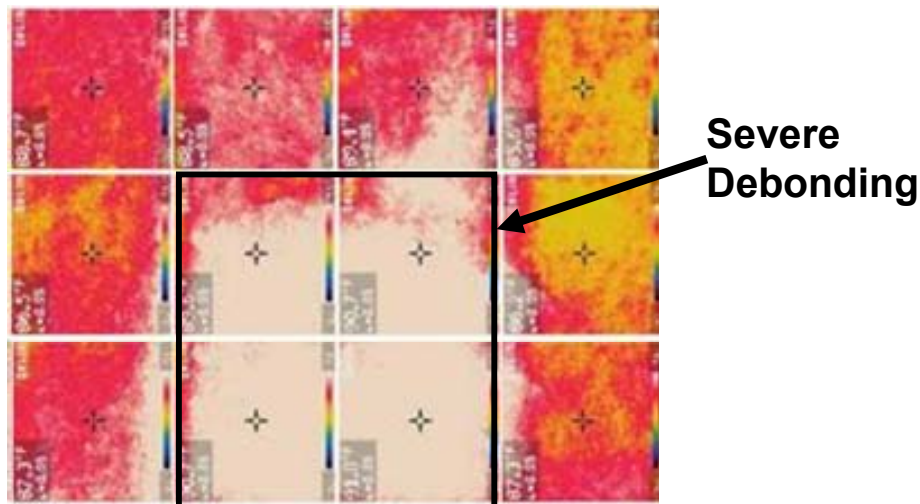


Figure 5.32 – Infrared Camera Results on Severe Debonded Area

Electromagnetic Methods

Ground Penetrating Radar (GPR) is a geophysical nondestructive technique that uses electromagnetic pulses to test, characterize, or detect subsurface materials based on changes in electromagnetic properties of the subsurface layers. Typical equipment setups for GPR surveys are shown in Figure 5.34 for air-launched and ground coupled systems.

GPR emits short electromagnetic pulses radiated through an antenna and receives the reflected signals from the pavement layers. These waveforms are digitized and interpreted by

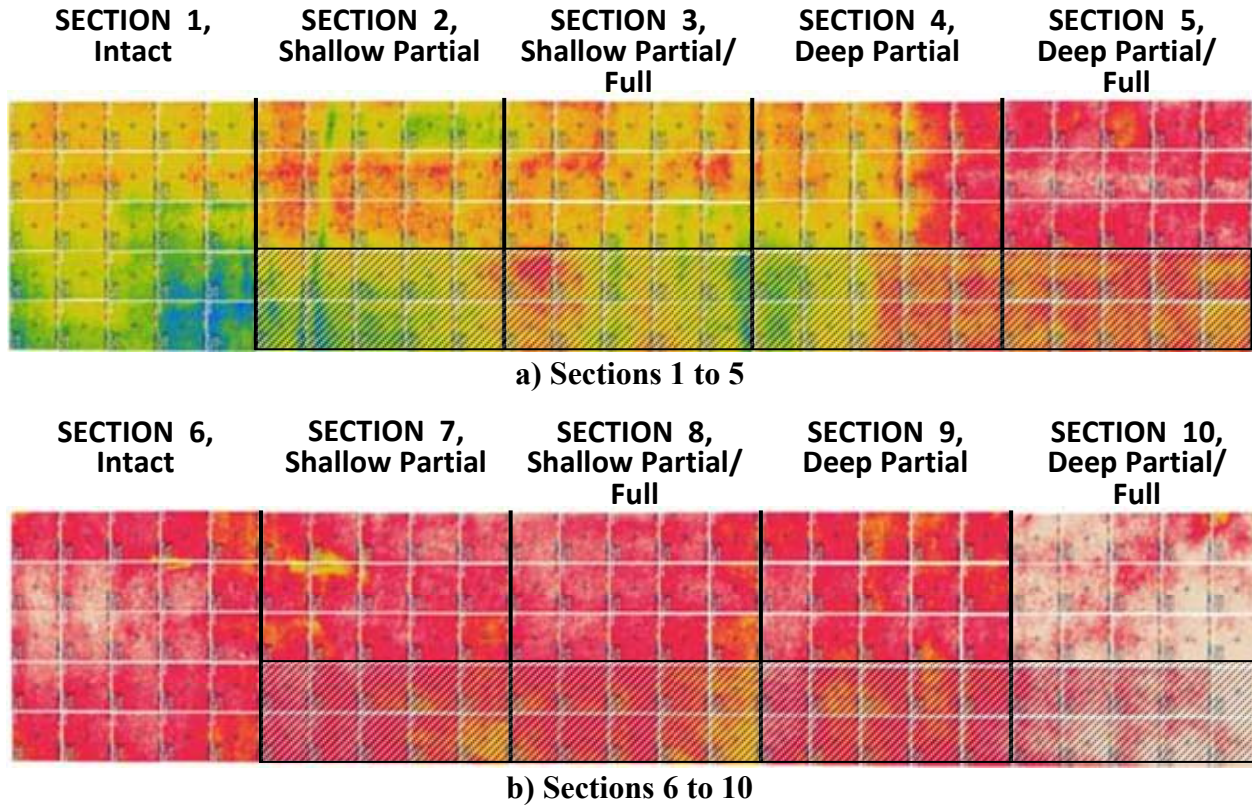


Figure 5.33 – Infrared Camera Results on Controlled Study



Figure 5.34 – Air Launched (Left) and Ground Coupled (Right) GPR Units

computing the amplitude and arrival times from each main reflection. The reflections of these waves at interfaces and objects within the material are analyzed to determine the location or depth of these interfaces.

The air-launched GPR used was a Geophysical Survey Systems Inc. (GSSI) SIR-20 (SIRveyor) 2-GHz antenna (Model 4105) mounted on a supporting beam retrofitted to the back of a van. The system comprised of two-channel data acquisition unit controlled by a laptop computer. The system was also connected to a survey wheel for measuring distance. Lines 1 to 5 were initially investigated with the air-launched system. On average five minutes were necessary to complete an entire line.

A typical raw linescan of an area around the severe debonding is shown in Figure 5.35. The horizontal axis relates to distance measured from the start point (ft) and the vertical axis indicates time measured (nanoseconds). The linescan comprises of different individual waveforms or O-scopes. Examples of typical O-scopes for an intact and a severely debonded area are shown in Figure 5.36. There is a small peak corresponding to the reflection from the debonding.

The linescans with the air-launched system along lines 1 to 5 are shown on Figure 5.37. Locations of the prepared debonding are also included in the figure and the approximate asphalt interfaces of the different layers are included as well for reference (see Figure 5.37a). These

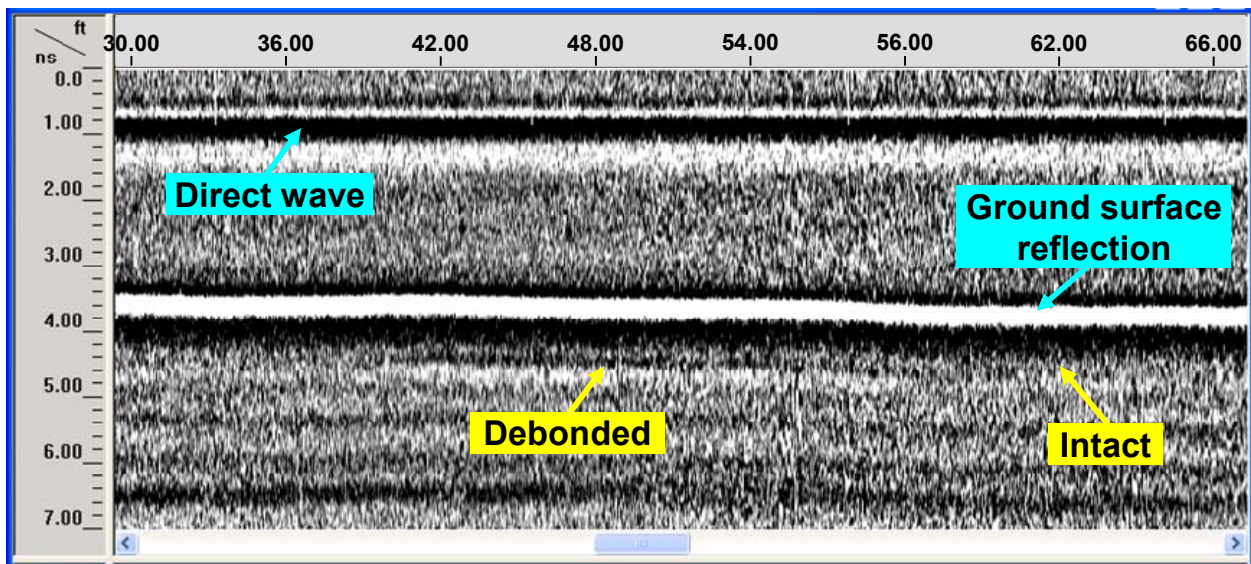


Figure 5.35 – Raw Linescan around the Severe Debonded Area with Air-launched GPR

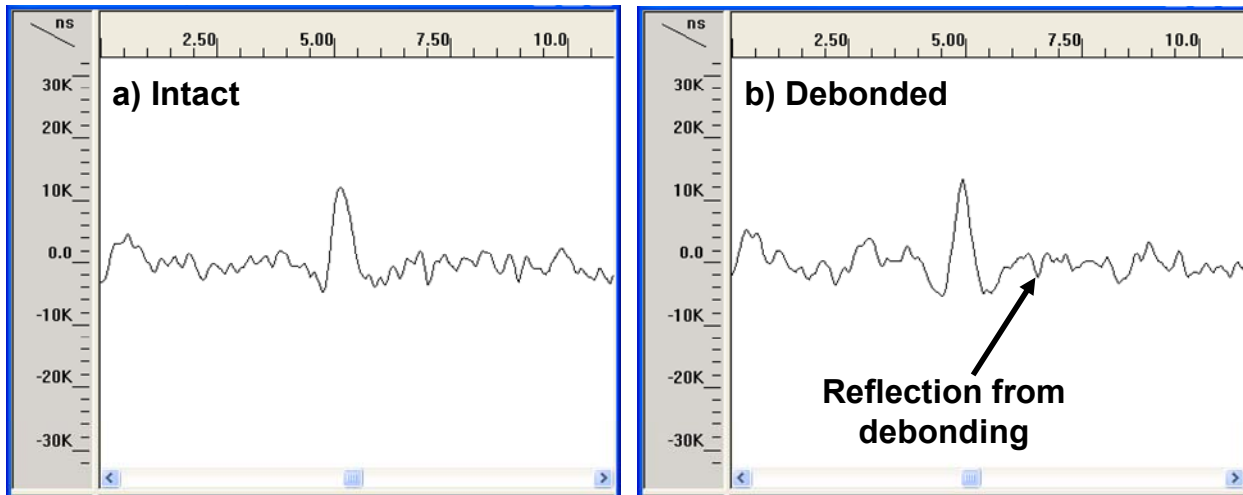


Figure 5.36 – O-scopes for Intact and Severe Debanded Locations with Air-launched GPR linescans were processed with the GSSI RADAN 6.5 software to remove the direct wave, set the time-zero at the pavement surface and eliminate unwanted signals from the data.

Figure 5.37b shows the linescan for Line 2 at 4 ft from the west edge. Some of the debonded areas of 2 ft by 2ft (0.6 m by 0.6 m) were identified at depths of 2.5 in. (63 mm). Some indications of debonding are evident along the 4 ft by 9 ft (1.2 m by 2.7 m) areas in Figures 5.37c to 5.37e, but their manifestation is erratic. The debonded areas detected were primarily in the areas where the talcum powder and clay were used as debonding agents. The significant contrasts in the dielectric constants of these agents and HMA might have been the reason for detecting these areas.

The ground-coupled GPR system used consisted of a GSSI two-channel data acquisition unit controlled by a laptop computer, a 1.5 GHz ground-coupled antenna (GSSI Model 5103), and a survey wheel attached to the antenna. Similar to the air-launched GPR, Lines 1 through 5 were investigated. On average 10 minutes were necessary to complete a line. A typical scan of the severely-debonded area is shown in Figure 5.38. The O-scopes for intact and severely

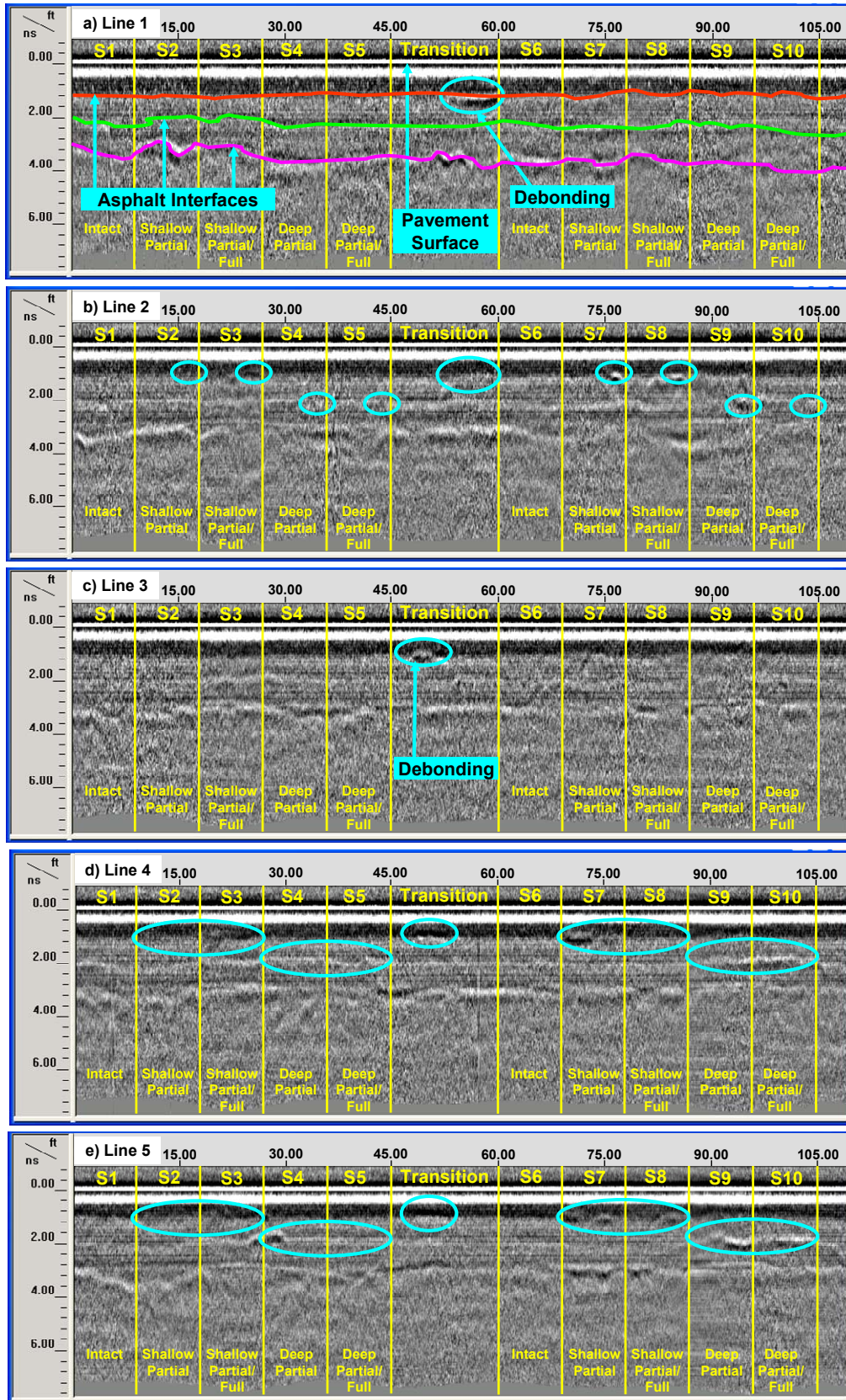


Figure 5.37 – Processed Linescans with Air-launched GPR on Controlled Study

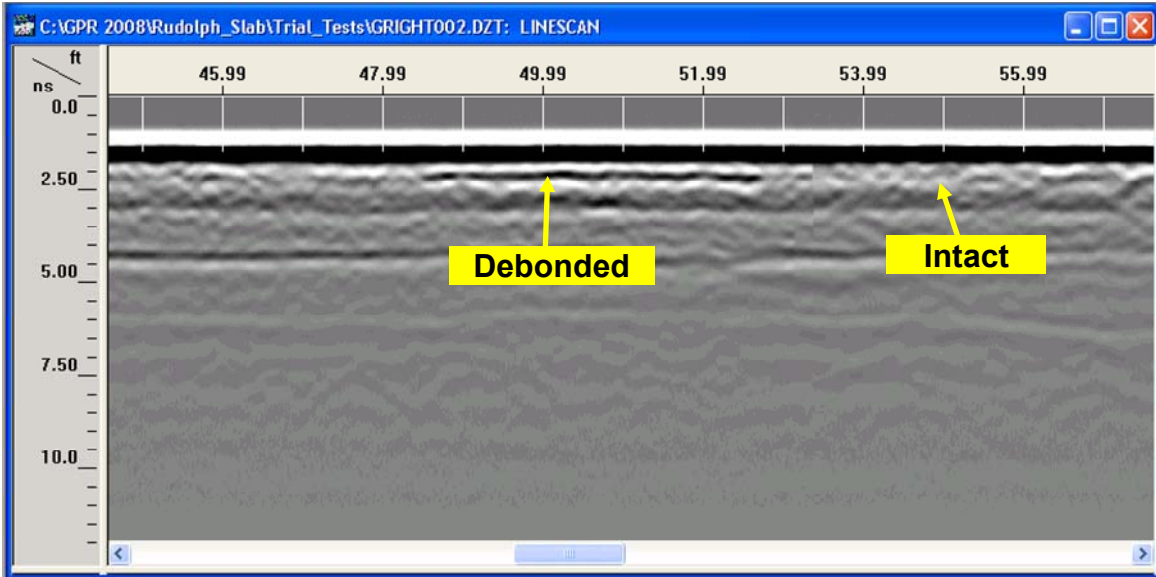


Figure 5.38 – Linescan around the Severe Debonded Area with Ground-coupled GPR

debonded locations are shown in Figure 5.39. The reflections from the severely debonded area can be more easily observed in this case because of the higher amplitude apparent on the O-scan. Complete post-processed linescans for all 5 lines are shown on Figure 5.40. The approximate asphalt interfaces of different layers are shown in Figure 5.40a. The following three analyses were performed to obtain these linescans:

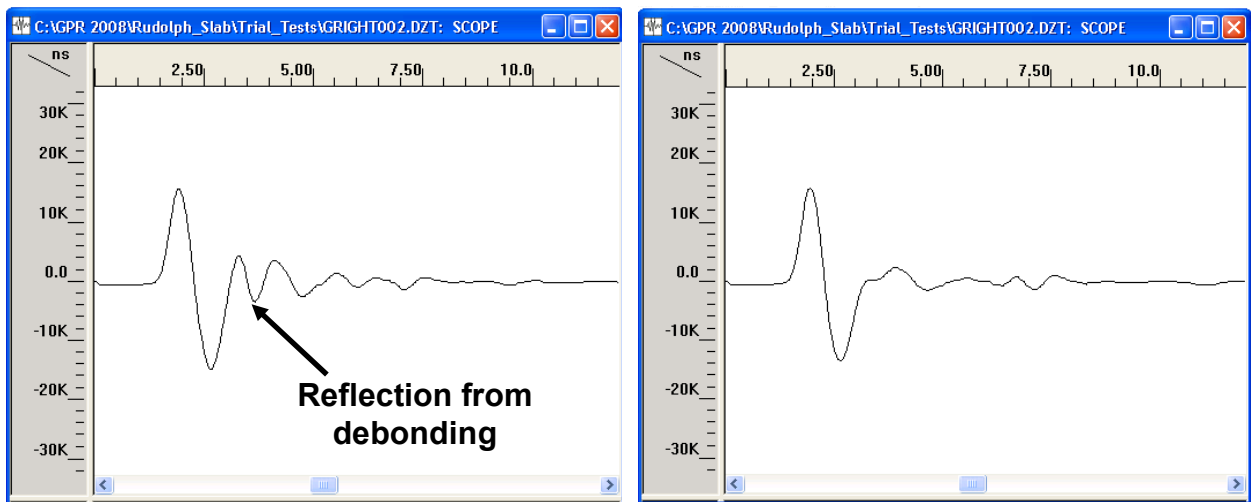


Figure 5.39 – O-scopes for Intact and Severe Debonded Locations with Ground-coupled

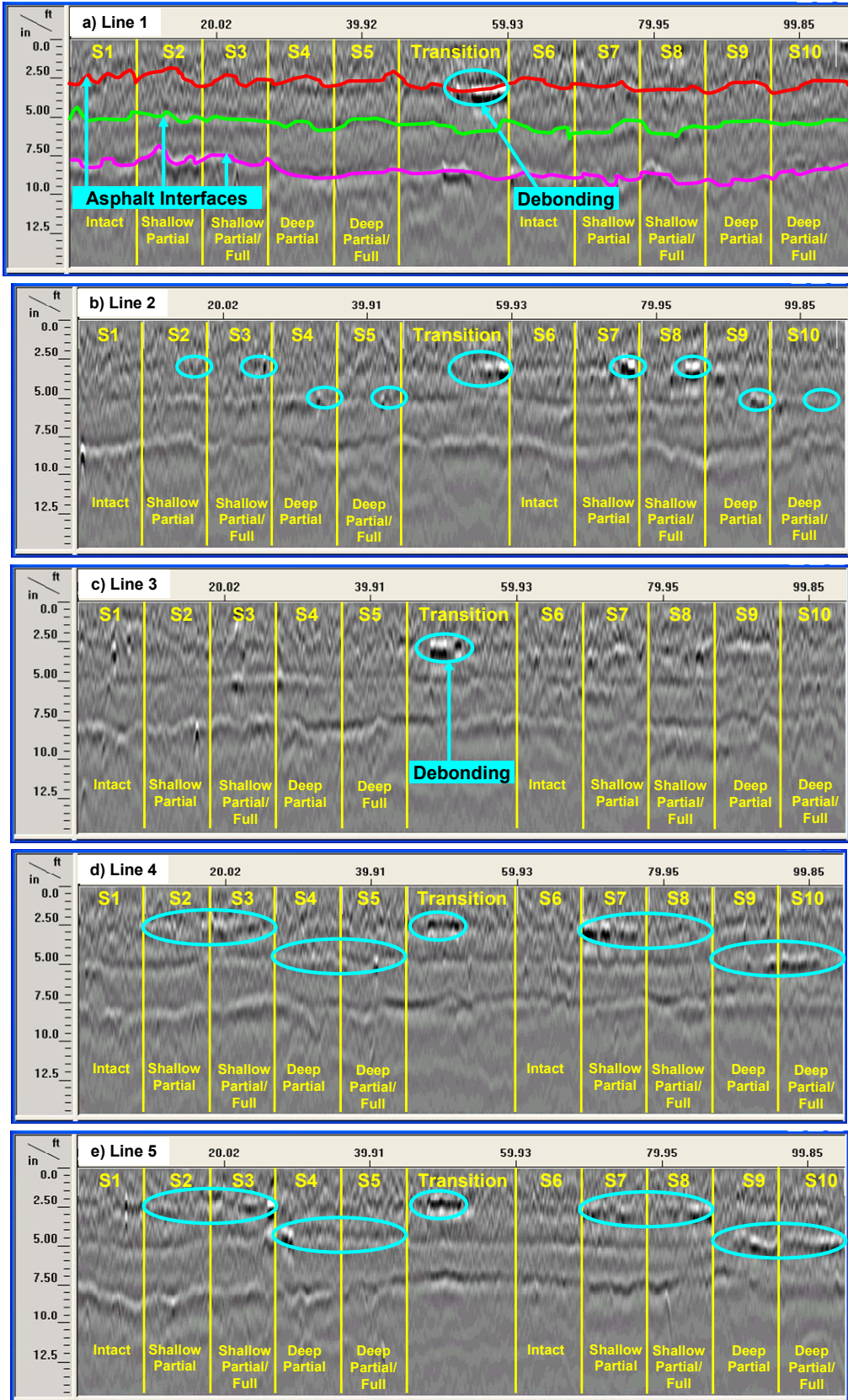


Figure 5.40 – Linescans with Ground-coupled GPR on Controlled Study

- Set Time-Zero (Position): shift the vertical scale so time zero is aligned with the surface reflection in each scan.
- Background Removal: a filter useful for removing horizontal banding.
- Stacking of signals from every 10 scans to accommodate the entire section in a single figure.

Similar to the air-launched GPR, the ground-coupled GPR detected the severely debonded area within the transition zone and some debonded areas primarily constructed on talcum powder or clay (see Figure 5.40).

Simulation of 3D Ground Penetrating Radar

GSSI RADAN 6.5 software is also equipped with a module for creating and analyzing three dimensional (3D) displays of GPR data. The transition zone that contained the severely debonded area and Sections 3 and 5 were investigated with a 3D GPR arrangement. To obtain a 3D representation of an area, a number of closely-spaced survey lines were obtained. GPR data were collected at 6 in. (150 mm) intervals in both longitudinal and transverse directions for the transition area and every 4 in. (100 mm) for Sections 3 and 5. The total time required to collect data at each section was about 1.5 hours. However, with commercially-available 3D GPR antennae, this time will be substantially less.

The images for approximate depths of 0 in. (surface), 2.5 in. (63 mm) and 5 in. (125 mm) extracted from the 3D image reconstruction in the transition area are represented in Figure 5.41a. The debonding agents placed at a depth of 2.5 in. (63 mm) were easy to identify (shown in white), while essentially no defects can be observed at a depth of 5 in. (125 mm). The intensity of the defect detected on the clay slurry is much higher than the thick cardboard. This may

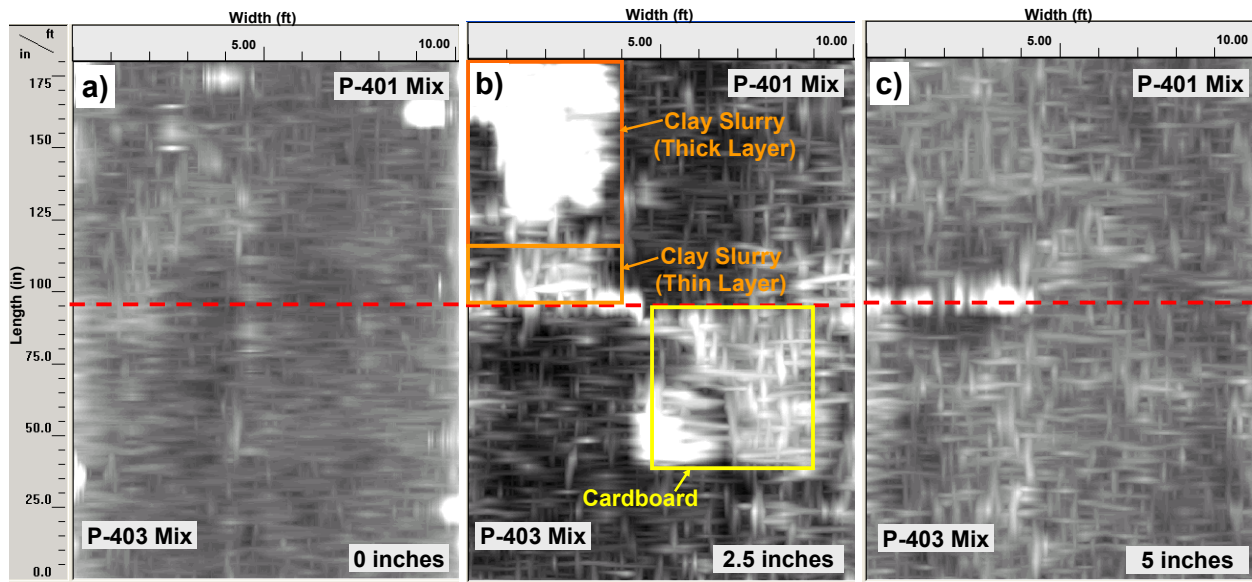


Figure 5.41 – 3D Displays of Transition Section at Different Depths

indicate that the significant differences in the dielectric constants of the clay and HMA might have attributed to its detection.

In actual debonded areas this agent will not exist. The results from testing of Section 3 (shallow debonding) are provided in Figure 5.42 and for Section 5 (deep debonding) in Figure 5.43 for the same depths of 0 in., 2.5 in.(63 mm) and 5 in. (125 mm). The debonding on the talcum powder (partial debonding) area in Section 3 is identified (see Figure 5.42b) but the debonding is not as clear on the paper with oil (fully- debonded). Also the debonded area of 1 ft by 1ft (0.3 m by 0.3 m) is evident, but the 2 by 2 ft (0.6 m by 0.6 m) and 0.5 by 0.5 ft (0.15 m by 0.15 m) are not apparent on the scan. For Section 5 with deep debonding, some indications of delamination appear on the 2 ft by 2 ft (0.6 m by 0.6 m) area but none on the larger area of 4 ft by 9 ft (1.2 m by 2.7 m, see Figure 5.43c).

Based on this study, GPR technology, especially the air-launched GPR, provides limited information about debonding despite its attractiveness as a continuous and rapid survey tool.

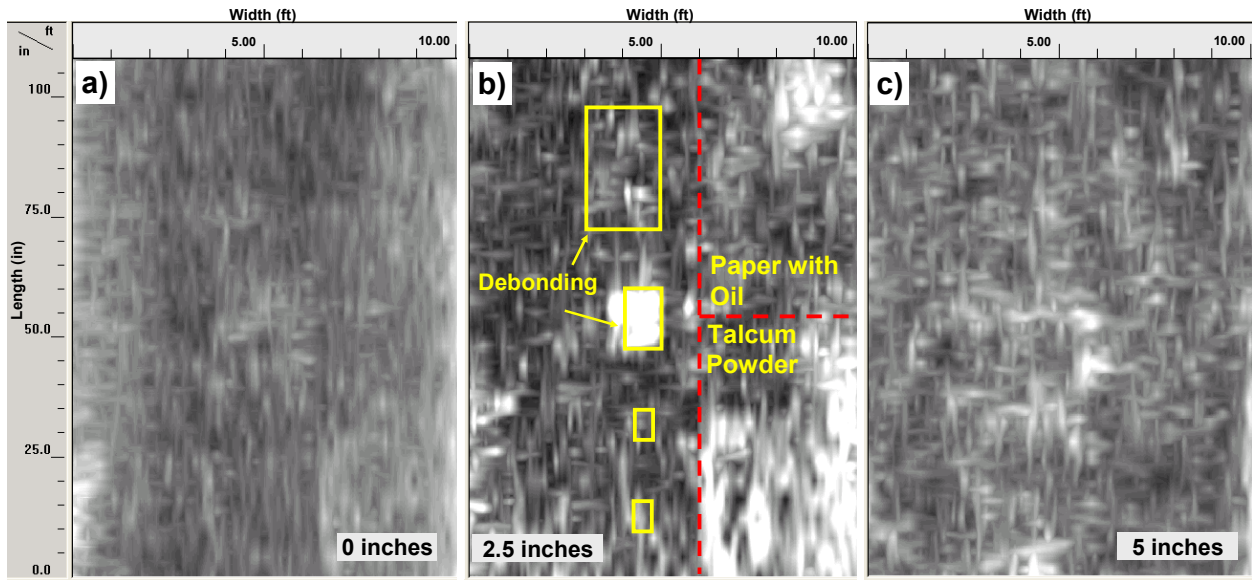


Figure 5.42 – 3D Displays of Section 3 at Different Depths

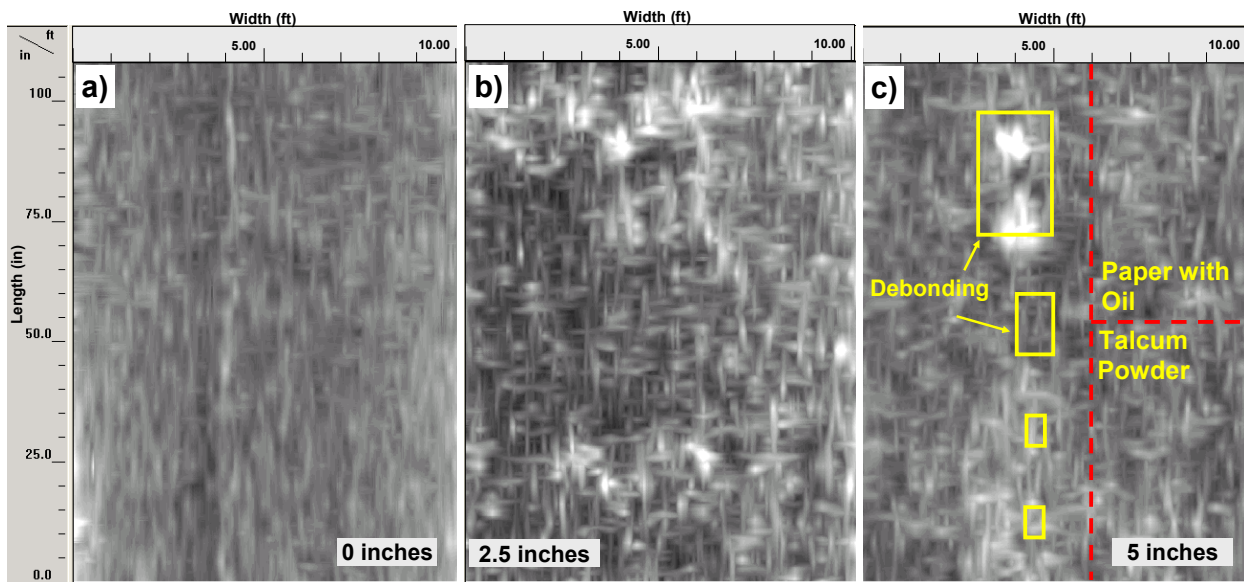


Figure 5.43 – 3D Displays of Section 5 at Different Depths

Coring Results

The goal of the coring operation was to estimate how well the full and partial debonding has been implemented in the filed. As reflected in Figure 5.1, two cores were extracted from each section. These cores were located about at 2.5 ft (0.75 m) from the right edge and at 2 ft (0.6 m) and 7 ft (2.1 m) from the start of each section, respectively. A diamond core system

(Figure 5.44a) was used to extract nominally 4 in. (100 mm) diameter cores (Figure 5.44b). As much as it was practical, the use of water was minimized during coring.

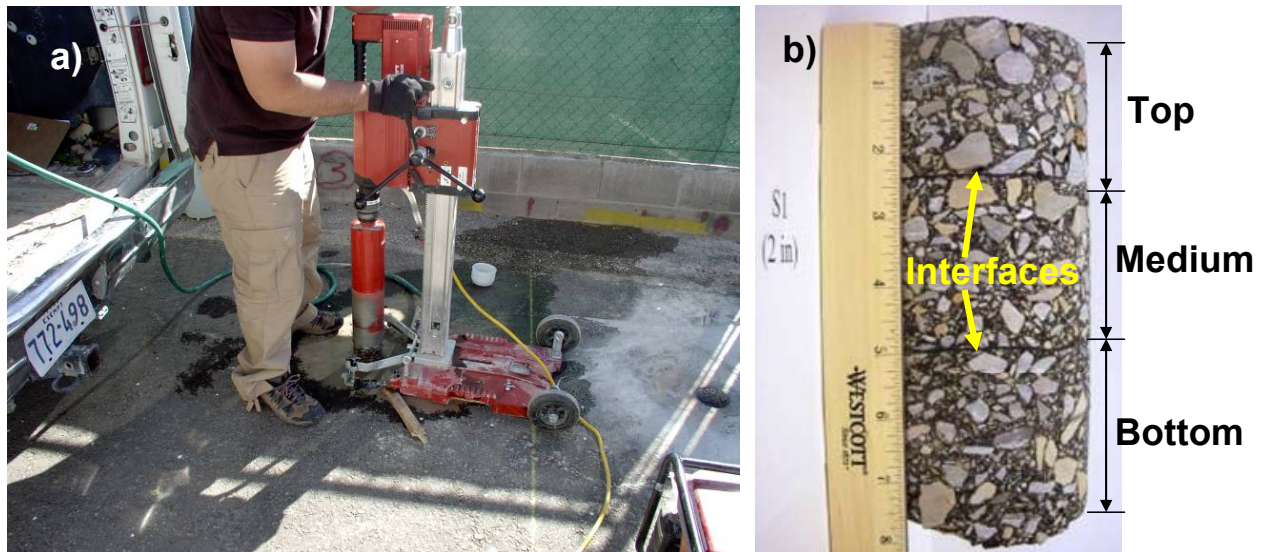


Figure 5.44 – Coring Operations on Controlled Study

Similar to prepared specimens in the lab, direct shear tests were performed to assess the bond strength on the cores. Average shear strengths measured at different layer interfaces are presented on Table 5.4. Detailed results for each core are included in Appendix D. Similar to the laboratory prepared specimens, the highest bond strengths were associated with the tack coat as the bonding agent. The average bond strength for the four specimens with grease as bonding agent was about 40% of the tack coat. However the other specimens, except one with clay slurry, separated after coring operations and were not suitable for testing. In most cases it was difficult to determine whether the coring operation washed the bonding agent or the cores were actually debonded. The bond strengths measured on retrieved intact cores were about twice as much as strengths from the prepared lab specimens (as detailed in Table 4.1). This can be attributed to different compaction methods and the possible negative impact of coring.

Table 5.4 – Summary of Shear Strength Results (psi) for Cores Retrieved

Parameter	Interface at 2.5 inches deep					Interface at 5 inches deep				
	Tack Coat	Grease	Clay Slurry	Talcum Powder	Paper Soaked in Oil	Tack Coat	Grease	Clay Slurry	Talcum Powder	Paper Soaked in Oil
Average	82	41	30	N/A ^a	N/A ^a	84	23	N/A ^a	N/A ^a	N/A ^a
COV, %	17	32	--	--	--	9	14	--	--	--

^a Specimens not feasible for shear testing

CHAPTER 6 – VERIFICATION TESTS OF SELECTED NDT METHODS ON CONTROLLED STUDY

Based on the preliminary results presented in Chapter 5, several of the NDT methods were selected for further study. The list of selected NDT methods is presented on Table 6.1. The more extensive study consisted of testing the sections more densely under different environmental conditions. In addition, some of the operational issues were considered. One such issue consisted of the impact of temperature variation on the results. To fulfill this objective, tests were carried out in cool weather when the average surface temperature of HMA ranged from 60°F to 85°F (16°C to 29°C) and in hot weather when the average HMA surface temperature ranged from 75°F to 120°F (24°C to 49°C). Even though it would have been desirable to carry out these tests in even colder weather, the climatic condition of El Paso in the previous year did not allow for that.

Table 6.1 – List of NDT Technologies Used on Extended Tests on Controlled Study

Electromagnetic	Impulse		Seismic/Sonic	Thermal
Ground Coupled GPR	FWD	Impulse Response	USW	Thermal Imaging

The other major issue that had to be addressed is the fact that in actual field evaluations, one may not be able to identify an area that is considered intact (like Sections 1 and 6 in our experiments). As such, the entire data set were considered when attempting to delineate the debonded areas.

Location of Test Points

As shown in Figure 6.1, 100 points were evaluated on every section, except for the transition section (between Sections 5 and 6) where 150 points were used. Due to the size of the FWD, every other point along five lines (a total of 25 points) was tested.

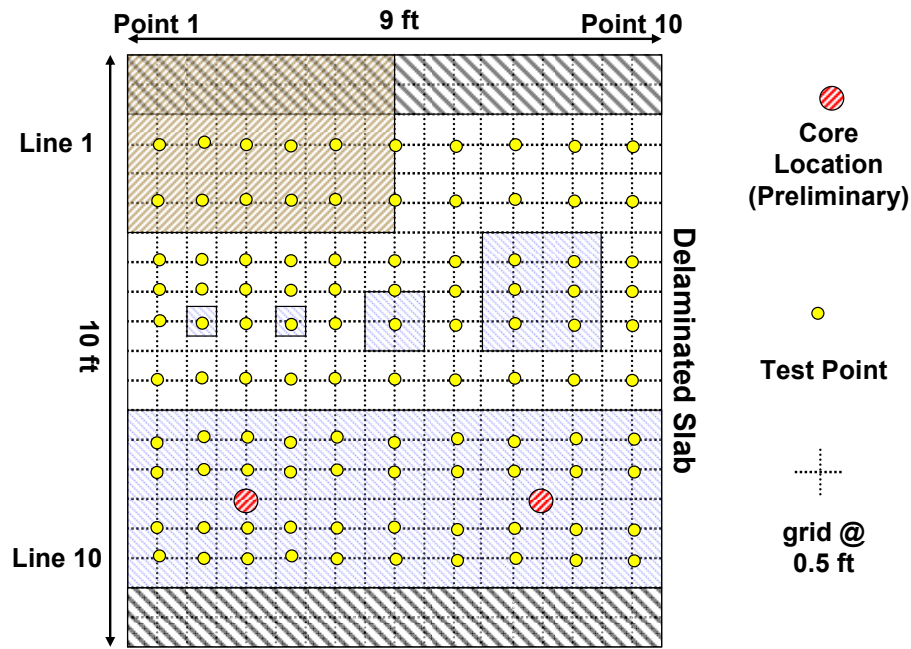
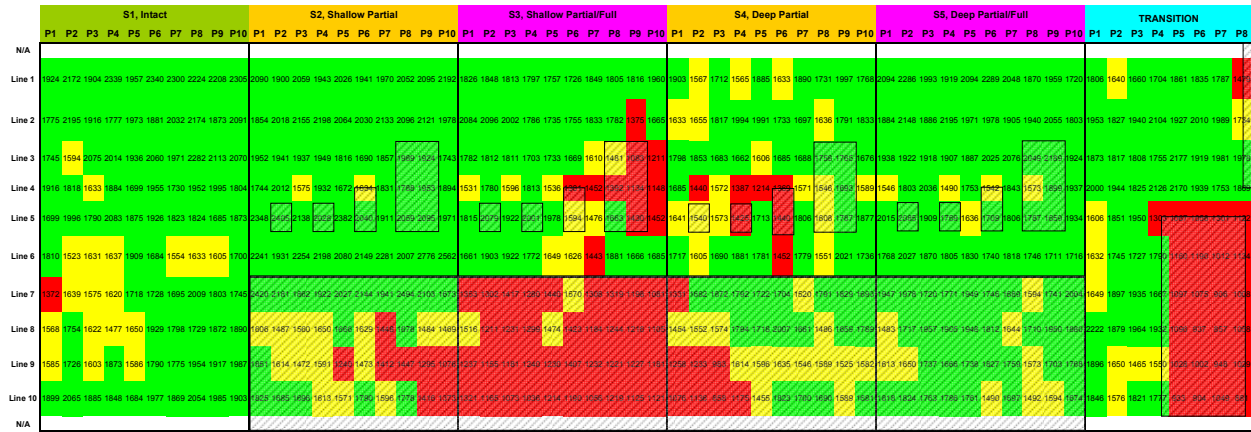


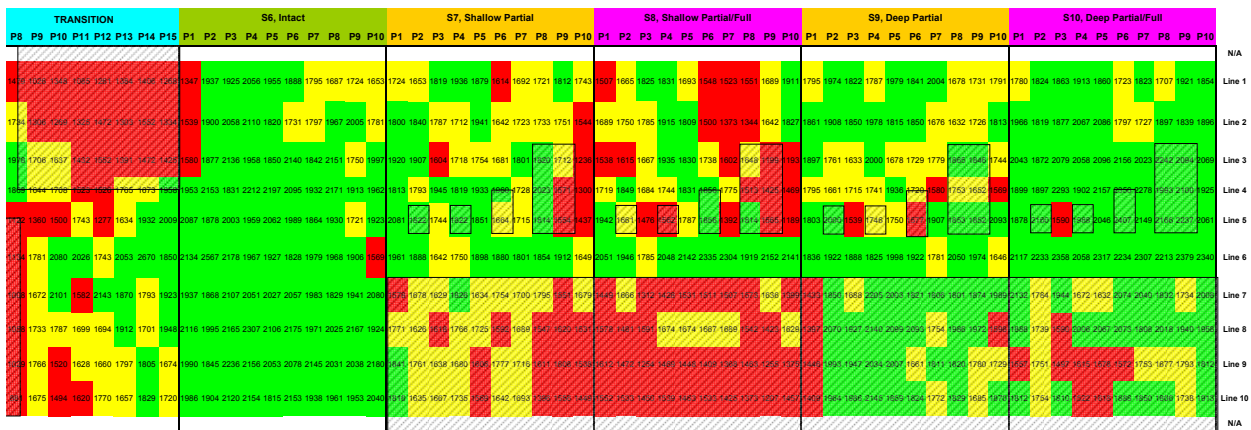
Figure 6.1 – Location of Test Points for a Given Section

Ultrasonic Surface Wave (USW) Method

PSPA was used to conduct USW tests in March (cool weather) and in June (hot weather). The variations in the average moduli for the three HMA lifts along the ten sections are shown in Figure 6.2 for the cool weather tests following the protocol described in Chapter 5. Sections 2 and 3 (shallow partial and low full debonding for the coarse surface mix) generally exhibited lower moduli as anticipated (see Figure 6.2a). Some parts of Section 4 (deep partial debonding) also presented lower moduli, but majority of Section 5 (deep full debonding), exhibited normal moduli. Similar trends are observed for the fine surface mix sections (Figure 6.2b). Most of the shallow and full debonded areas (Sections 7 and 8) exhibited lower moduli but only some on the deep debonded area (Sections 9 and 10). For the case of the small prepared debonded areas, some of the 2 by 2 ft (0.6 m by 0.6 m) areas were detected on the shallow debonded sections, except for Section 2. Almost none of the small deep debonded defects were detected for both mixes. The moduli of the severely debonded areas in the transition zone were substantially less than average as well.



a) Sections 1 to 5

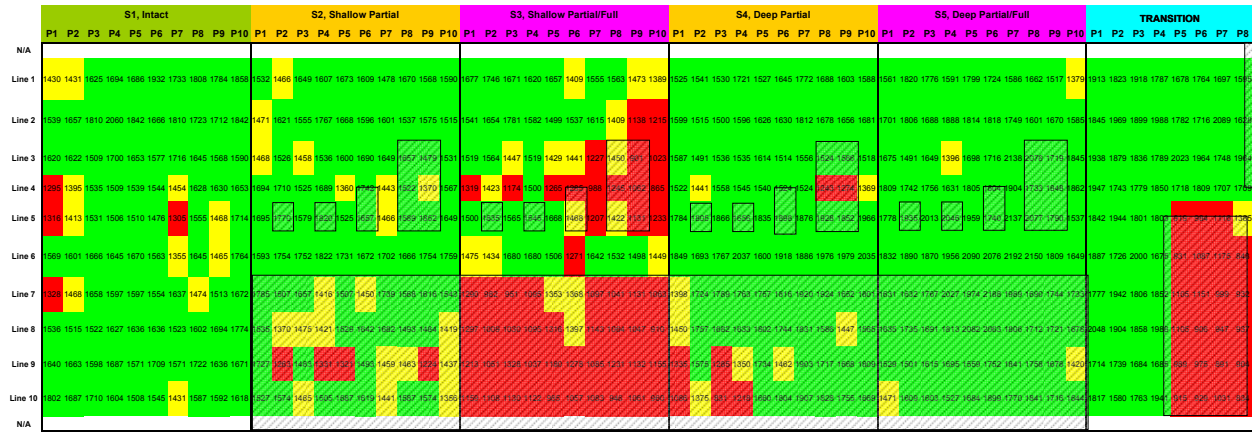


b) Sections 6 to 10

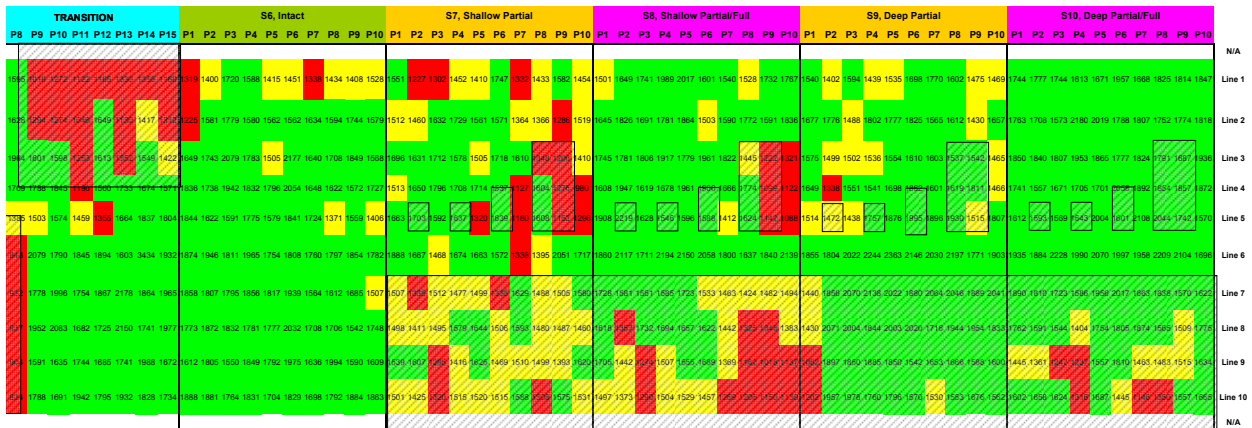
Figure 6.2 – Contour Maps of PSPA Modulus from Extended Tests in Cool Weather

The results from the hot weather tests on the same points as shown in Figure 6.3 are similar to the ones shown in Figure 6.2 for cool weather tests. However, the cool weather tests demonstrated slightly higher resolving power in terms of detecting the debonded areas. This occurs because perhaps during hot temperatures, the bonding agents may provide some additional bonding.

Due to the density of testing, tests started in early morning and continued until late afternoon for several days. To evaluate the impact of the daily temperature fluctuations of 25°F to 45°F (13°C to 25°C) on the seismic moduli of the different mixes, several points were tested repeatedly at different times corresponding to different temperatures. The variations in



a) Sections 1 to 5



b) Sections 6 to 10

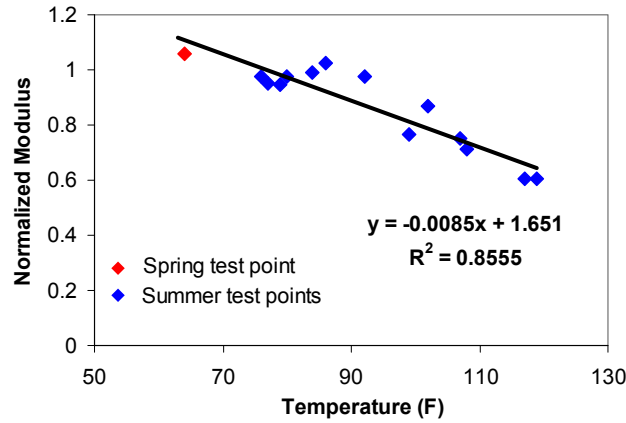
Figure 6.3 – Contour Maps of PSPA Modulus from Extended Tests in Hot Weather

normalized modulus at 77°F (25°C) with temperature for Sections 1 and 6 are presented in Figure 6.4. Linear relationships between normalized modulus and temperature were obtained for both sections with reasonably high R^2 values. The general equations to adjust seismic modulus for temperature were:

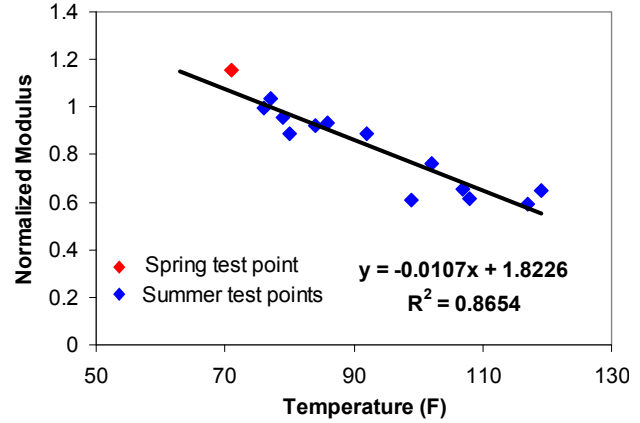
$$E_{77^\circ F} = \frac{E_{T^\circ F}}{-0.0085 \cdot T + 1.651}, \text{ for surface coarse mixes} \quad (6.1)$$

$$E_{77^\circ F} = \frac{E_{T^\circ F}}{-0.0107 \cdot T + 1.823}, \text{ for surface fine mixes} \quad (6.2)$$

where T is the surface temperature (in °F) at the time of PSPA tests. These relationships provided slightly greater adjustment to the moduli than Equation 4.1.



a) Coarse Surface Mix



b) Fine Surface Mix

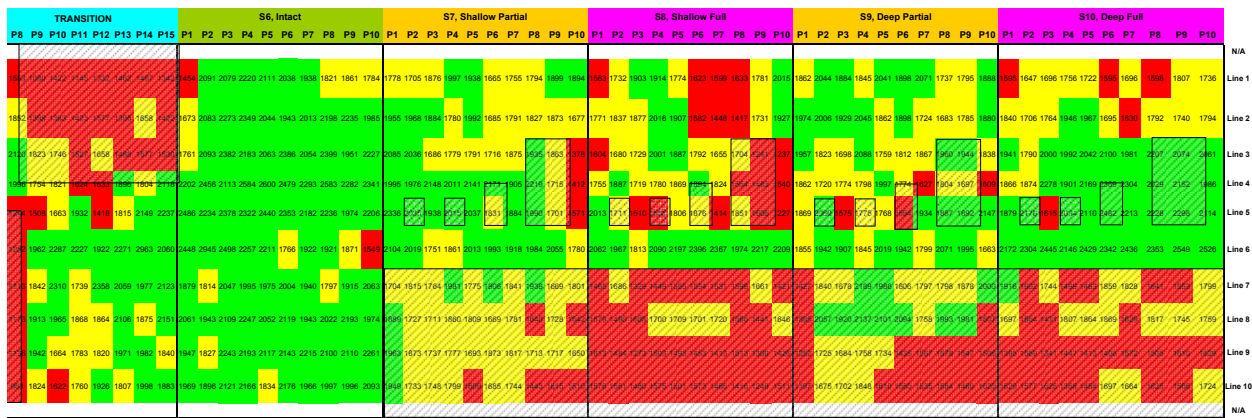
Figure 6.4 – Temperature Influence of PSPA Modulus

The results after temperature adjustments with Equations 6.1 and 6.2 are shown in Figures 6.5 and 6.6. The outcomes are in general similar to those in Figures 6.2 and 6.3. For the cool weather data (Figure 6.5), the resolving power for the fine mixes improved for Sections 9 and 10 (corresponding to the deep debonding). On the other hand, the manifestations of the shallow partial debonding are not obvious for Section 7 after temperature adjustment in hot weather testing (Figure 6.6). This activity indicates that the default temperature adjustment in Equation 4.1 is adequate and that the lack of detection of debonding on some of the sections is related to the shortcomings of the method. Also, the development of a temperature-modulus adjustment relationship as part of the protocol for PSPA tests may be desirable.

So far, the evaluation of debonding was based on the average and standard deviation of the control sections (Sections 1 and 6). In the actual field studies, finding control sections may not be practical. To account for this, a revised protocol was considered to account for the variability and uncertainties that may be encountered in actual field sections. The average and standard deviation were again used to delineate the bonded and debonded sections. However, due to significant differences between the properties of the bonded and debonded areas, the level



a) Sections 1 to 5



b) Sections 6 to 10

Figure 6.5 – Temperature-Adjusted Contour Maps of PSPA Modulus in Cool Weather

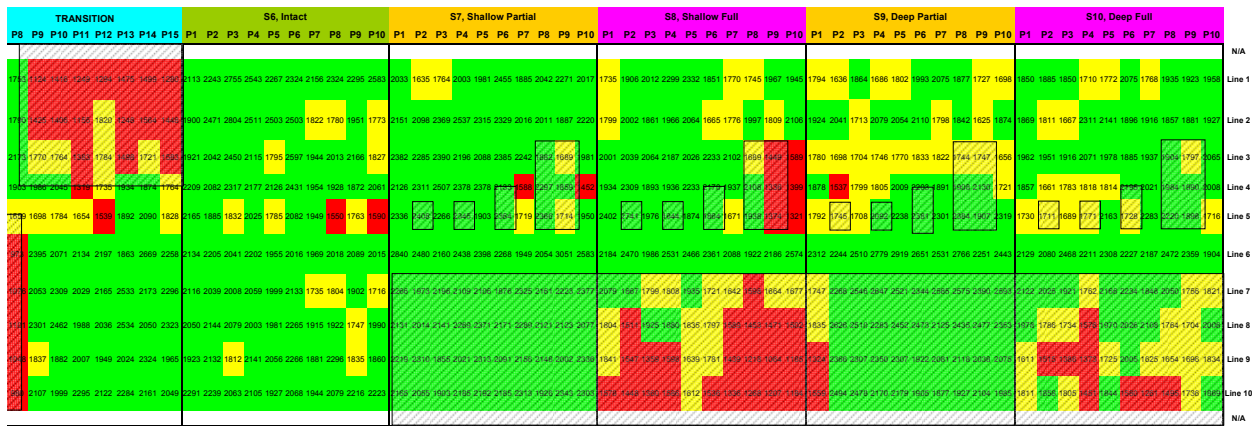
of uncertainty was increased as reflected in Table 6.2. In the revised protocol, one-half and one standard deviation (instead of one and two standard deviations in Table 5.1) were used to evaluate the results.

Based on the revised criteria, color-coded moduli are presented in Figure 6.7 and 6.8. These results are comparable to those in Figures 6.5 and 6.6. From this point forward, the revised criteria will be applied for presenting the results.

The contour plot of average moduli of the top lift (top 2.5 in., 63 mm) for the ten sections tested in cool weather is shown in Figure 6.9. Reduced moduli were observed particularly for Sections 3 and 8 (shallow and partial debonding). Sections with shallow and partial debonding also



a) Sections 1 to 5



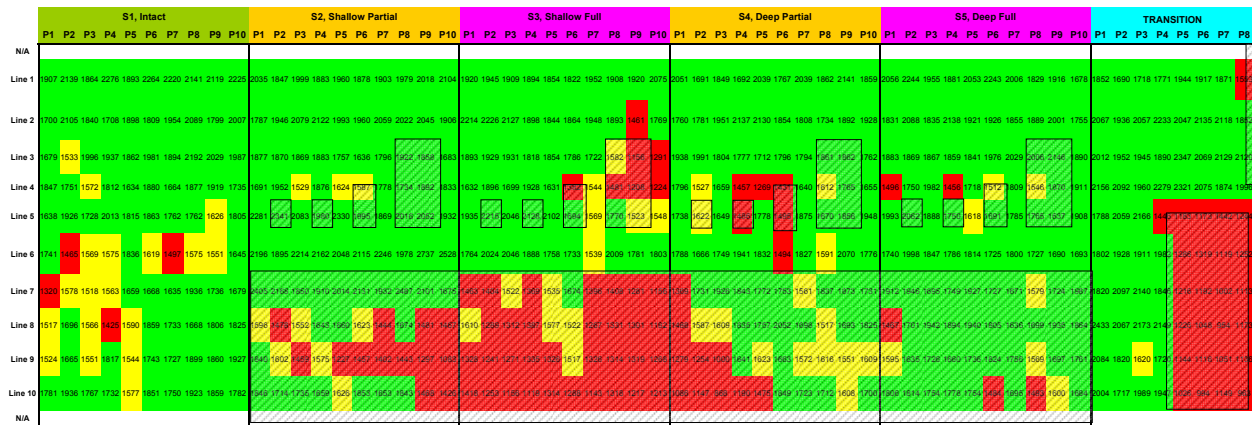
b) Sections 6 to 10

Figure 6.6 – Temperature-Adjusted Contour Maps of PSPA Modulus in Hot Weather

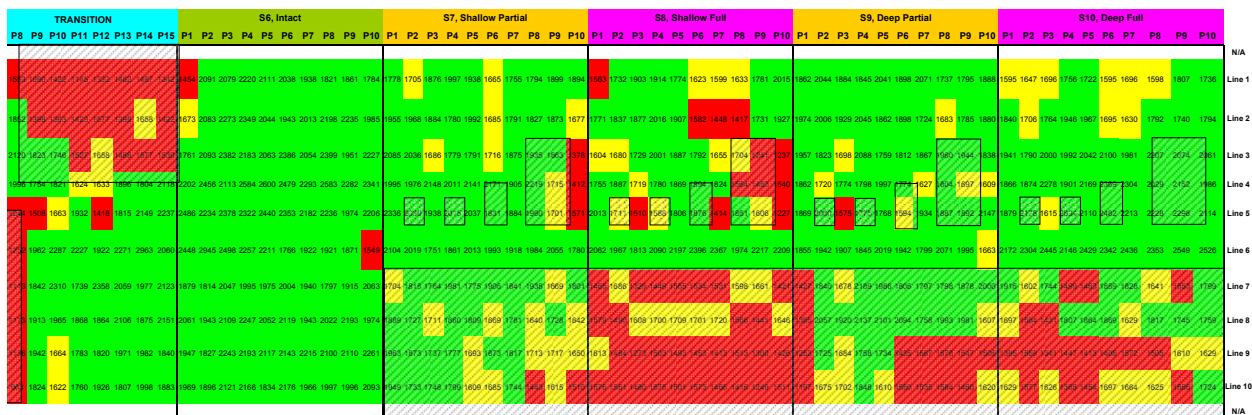
showed some reduction in moduli. This pattern indicates that the quality of the HMA layer (in terms of stiffness) may be compromised when the two adjacent layers are not bonded.

Table 6.2 – Revised Criteria Used to Analyze Moduli

Color Code	Modulus Value	Interpretation
Green	$E > E_{\text{control}} - \frac{1}{2} \sigma_{\text{control}}$	Measured modulus is similar or higher than modulus from control section
Yellow	$E_{\text{control}} - \frac{1}{2} \sigma_{\text{control}} > E > E_{\text{control}} - \sigma_{\text{control}}$	Measured modulus is somewhat less than control modulus
Red	$E < E_{\text{control}} - \sigma_{\text{control}}$	Measured modulus is substantially less than control modulus



a) Sections 1 to 5



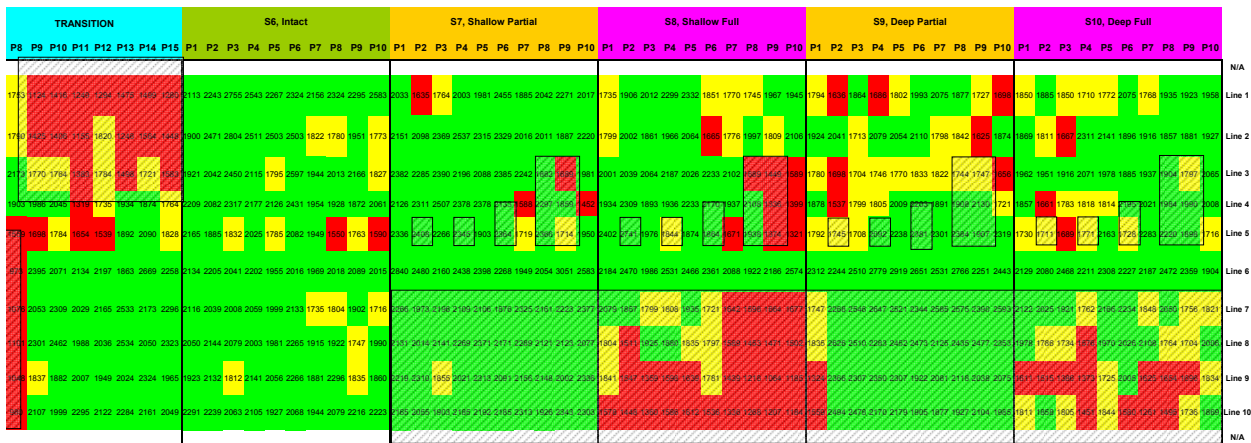
b) Sections 6 to 10

Figure 6.7 – Temperature-Adjusted Contour Maps of PSPA Modulus in Cool Weather based on Revised Statistical Criteria

Contour plots of the dispersion curves (analogous to the variation in modulus with depth) are included in Figure 6.10 for the ten lines tested along all sections during the cool weather. The depths and the extent of the debonding areas are also depicted in the figures, where solid lines correspond to full debonding and the dashed lines to partial debonding. Please note that not all cross-sections contained debonded areas. A reduction in modulus can be observed in most debonded sections at or below the depth of defects, confirming the usefulness of the USW method in identifying at least the fully debonded areas. One complicating (but perhaps beneficial) aspect of the dispersion curve is that a low-quality but bonded lift may exhibit the same patterns in a dispersion curve than a partially debonded interface. Once again, similar conclusions can be drawn from data collected during the hot weather as detailed in Appendix E.



a) Sections 1 to 5



b) Sections 6 to 10

Figure 6.8 – Temperature-Adjusted Contour Maps of PSPA Modulus in hot Weather based on Revised Statistical Criteria

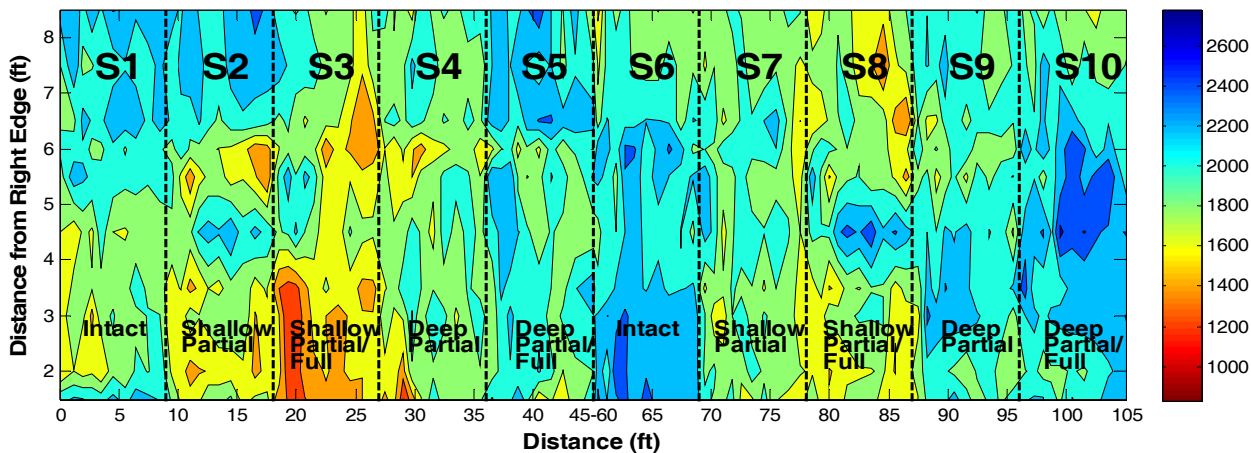


Figure 6.9 – Modulus Contour Plot of Top 2.5 in. from Cool Weather Tests

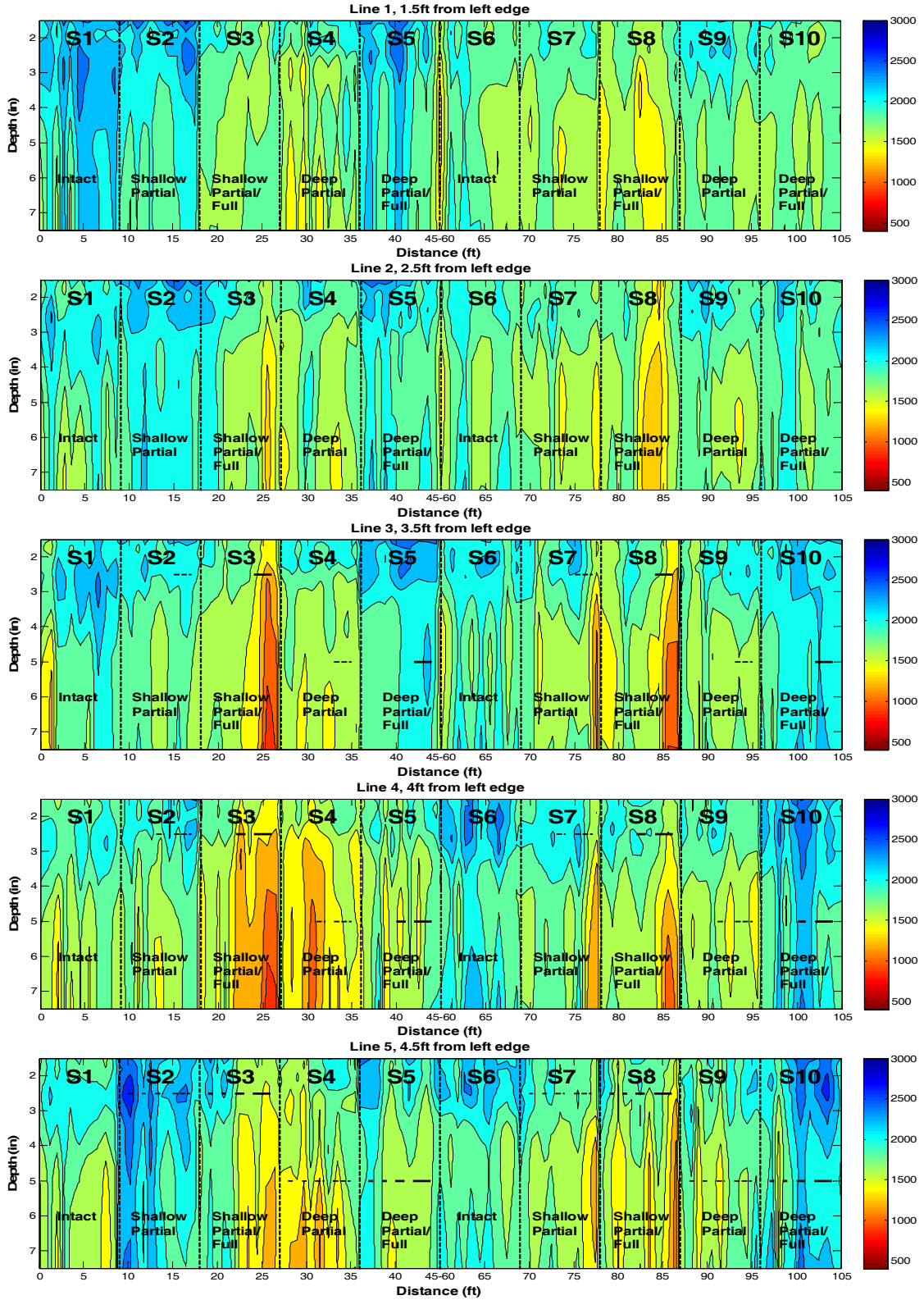


Figure 6.10 – Dispersion Curve Contour Plots for Cool Weather

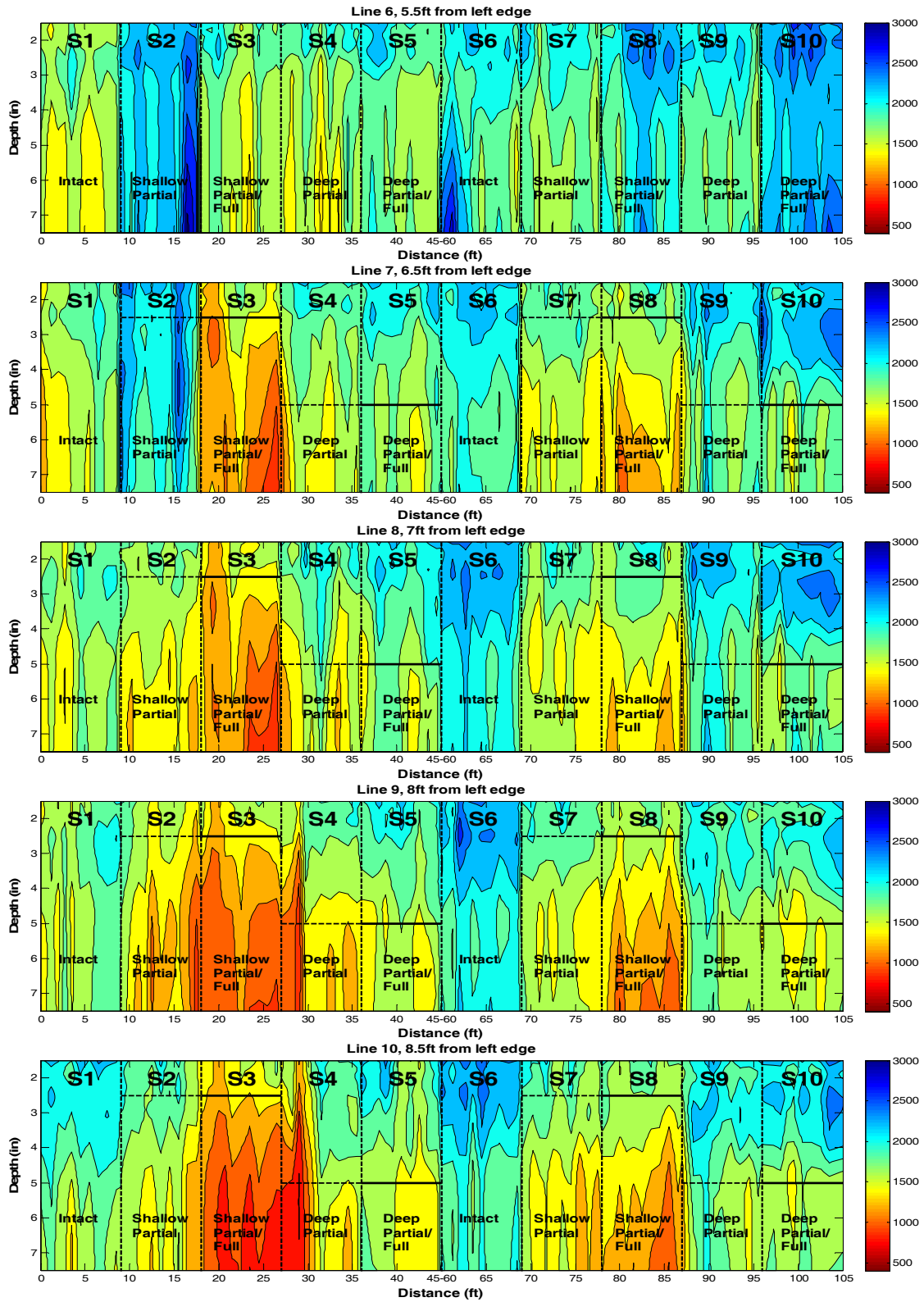
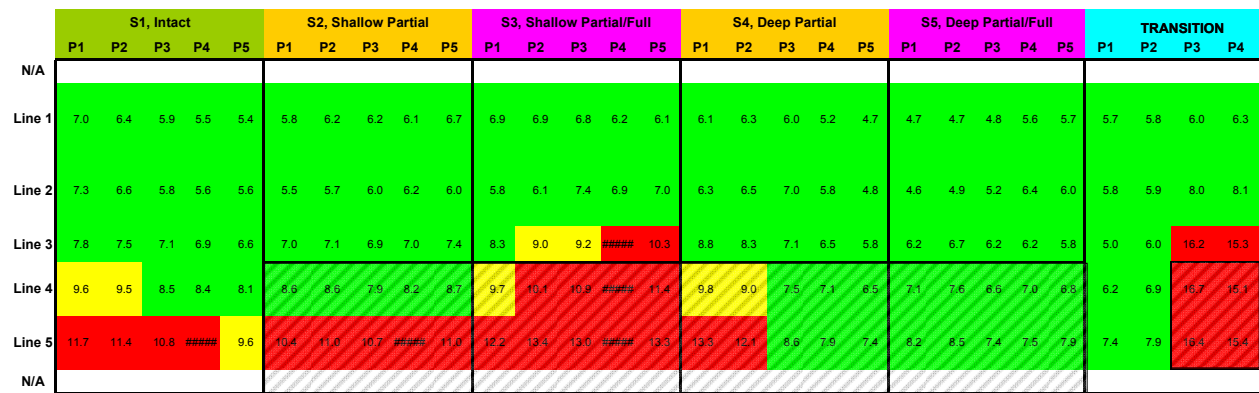


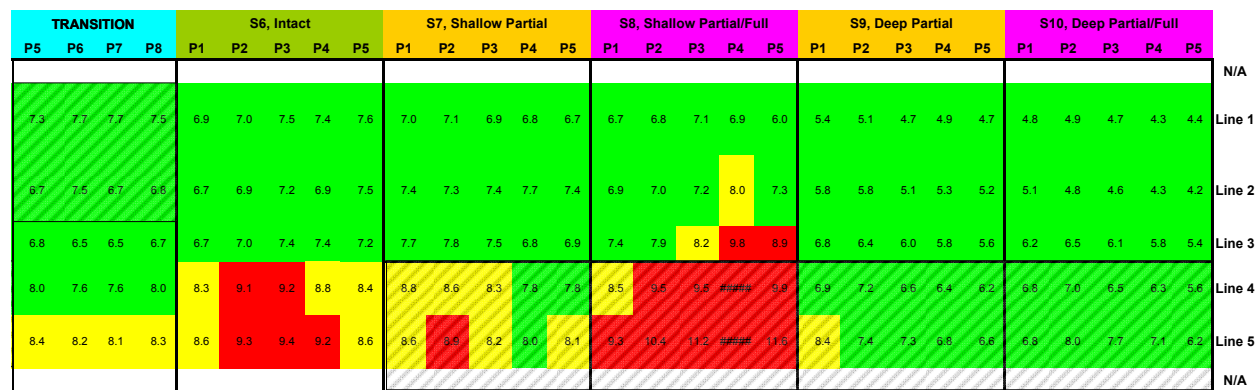
Figure 6.10 Contd. – Dispersion Curve Contour Plots for Cool Weather

Falling Weight Deflectometer (FWD)

The FWD tests were carried out on 25 points on each section (40 on the transition) again in the cool and hot temperatures. The variation in the deflections along the ten sections is shown in Figure 6.11 for the cool weather testing. As a reminder, the criteria presented in Table 6.2 were used to color code the graphs. Almost all of the shallow fully-debonded locations are detected as they exhibited higher than average deflections. Most shallow partially-debonded locations are also detected. However, almost all deep debonded areas exhibit similar deflections to the intact areas. One of the concerns with these results is that some areas in the intact sections are categorized as debonded, and the severely debonded area in the transition is not detected.



a) Sections 1 to 5



a) Sections 6 to 10

Figure 6.11 – Contour Maps of FWD Deflection in Cool Weather based on Revised

Statistical Criteria

The outcomes from the hot weather testing (Figure 6.12) are rather different. The resolving power of the method in detecting debonding is diminished for most debonded sections, while the debonding in Sections 9 and 10 is now apparent. The false positive results (exhibiting the sign of debonding on an intact point) in the intact sections are less severe, but they now show up in Sections 2, 3, 7 and 8.

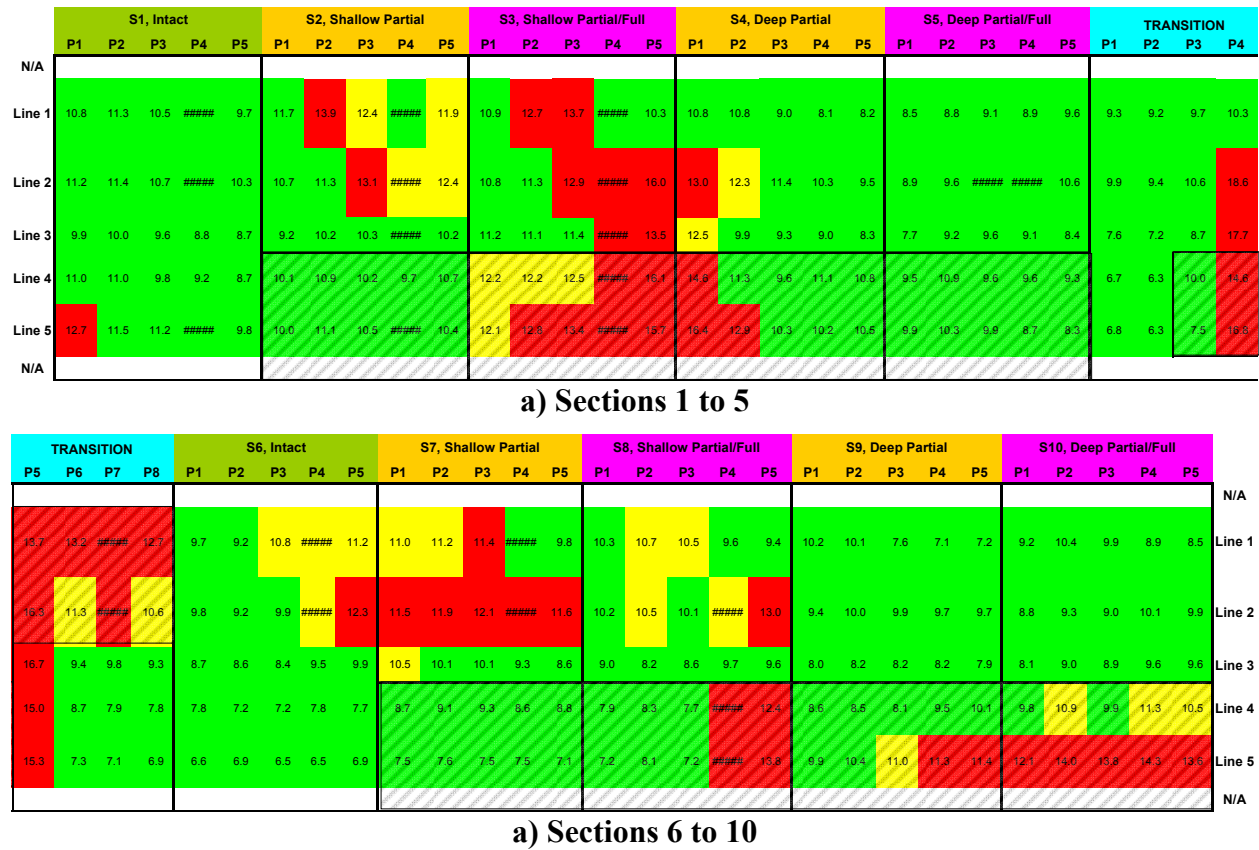


Figure 6.12 – Contour Maps of FWD Deflection in Hot Weather based on Revised Statistical Criteria

One possible explanation for the trends observed with the FWD deflections can be the lack of temperature adjustment. Similar to the USW tests, several points were tested repeatedly at different times corresponding to different temperatures. The variations in normalized deflections at 77°F (25°C) with temperature for Sections 1 and 6 are presented in Figure 6.13 and the general equations to adjust deflections are presented in the following equations:

$$D_{77°F} = \frac{D_{T°F}}{0.0062 \cdot T + 0.5018}, \text{ for surface coarse mixes} \quad (6.3)$$

$$D_{77°F} = \frac{D_{T°F}}{0.0073 \cdot T + 0.4127}, \text{ for surface fine mixes} \quad (6.4)$$

where D denotes deflection and T is the temperature (in °F) at the time of FWD tests. The slopes of the lines are rather flat indicating that the change in deflection with temperature is small. This pattern is anticipated since the majority of the deflection measured with the FWD comes from the deformation of the subgrade.

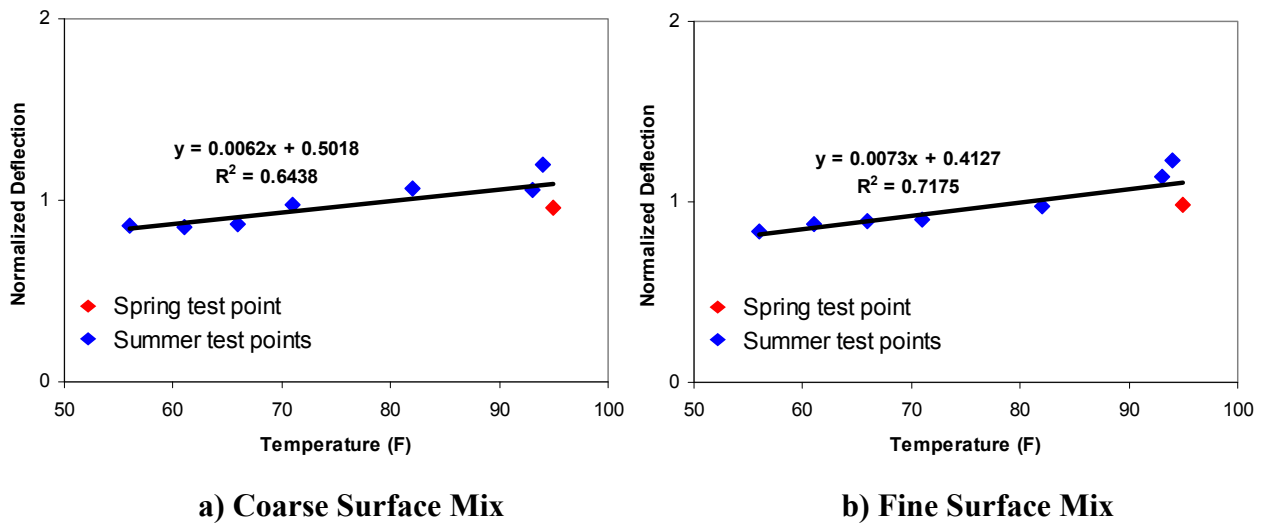
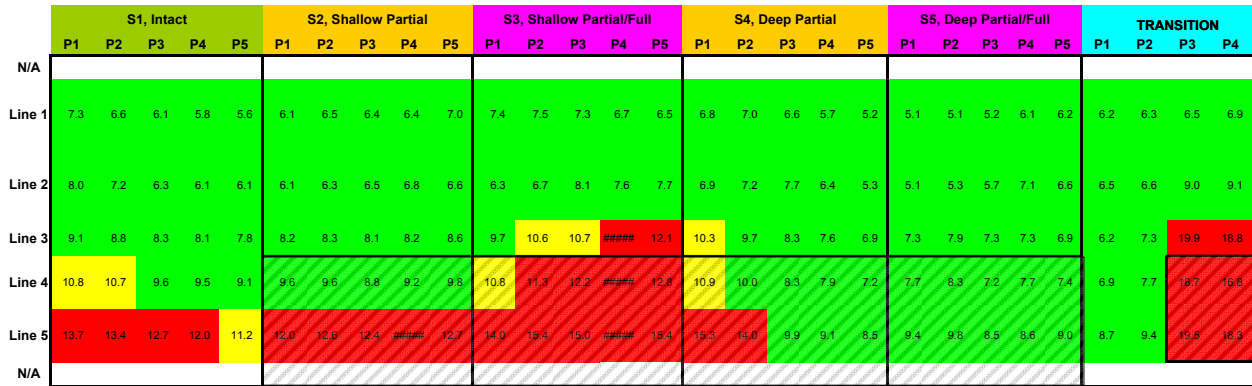


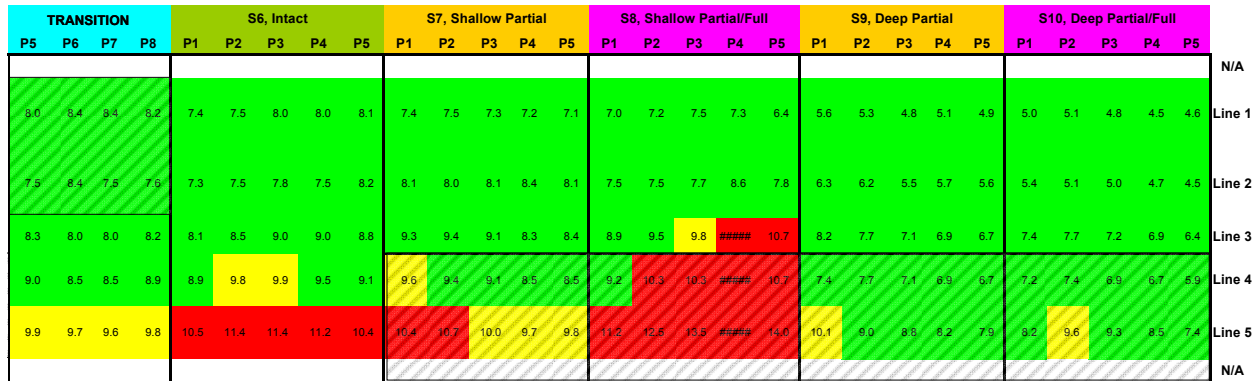
Figure 6.13 – Temperature Influence on FWD Deflection

The results after temperature adjustments with Equations 6.3 and 6.4 are shown in Figures 6.14 and 6.15 for the cool and hot weather tests. The patterns in the variations in deflections in these figures are quite similar to the corresponding ones before temperature adjustments (Figures 6.11 and 6.12).

Since the FWD deflections are strongly influenced by the modulus of the subgrade, the next step was to test the variation in the HMA modulus as a means of detecting debonded areas. HMA moduli were backcalculated using MODULUS 6.0 software (Liu and Scullion, 2001). To



a) Sections 1 to 5

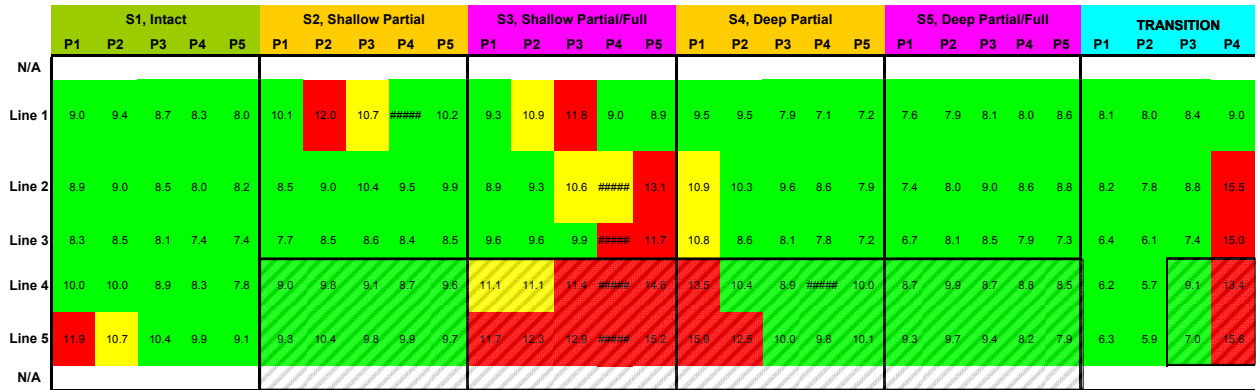


a) Sections 6 to 10

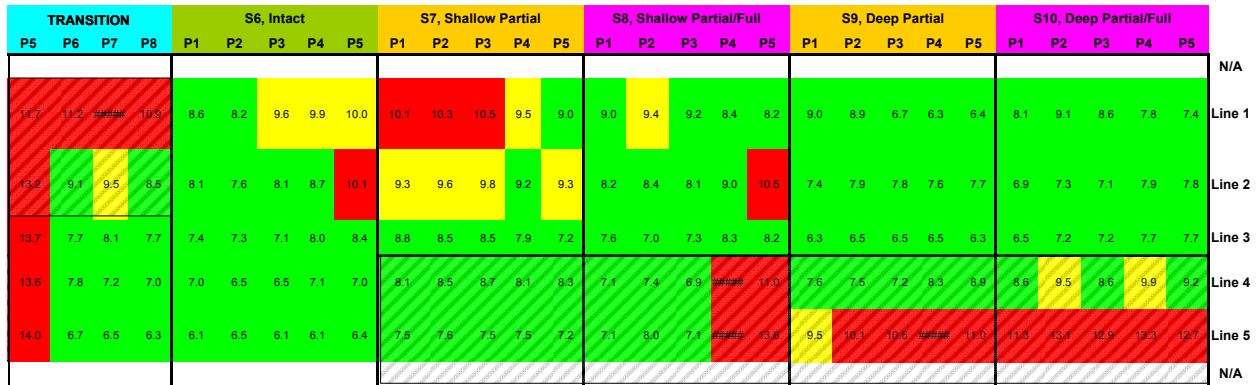
Figure 6.14 – Temperature-Adjusted Contour Maps of FWD Deflection in Cool Weather based on Revised Statistical Criteria

minimize the uncertainty in the backcalculation process, a 2-layer analysis that considered the entire HMA thickness (8 in., 200 mm) as one layer over a subgrade was used. Asphalt moduli before temperature adjustments are shown in Figures 6.16 and Figure 6.17 for the cool and hot weather testing, respectively. For the cool weather testing (Figure 6.16), the two intact sections (Sections 1 and 6) now exhibit normal moduli, and the resolving power of the method for detecting the debonded areas is somewhat improved. These improvements are not evident for the hot weather testing as reflected in Figure 6.17.

The variations in normalized modulus at 77°F (25°C) with temperature for Sections 1 and 6 are presented in Figure 6.18. The general equations to adjust moduli are:



a) Sections 1 to 5



a) Sections 6 to 10

Figure 6.15 – Temperature-Adjusted Contour Maps of FWD Deflection in Hot Weather

based on Revised Statistical Criteria

$$E_{77^{\circ}F} = \frac{E_{T^{\circ}F}}{-1.8144 \cdot \ln(T) + 8.8812}, \text{ for surface coarse mixes} \quad (6.5)$$

$$E_{77^{\circ}F} = \frac{E_{T^{\circ}F}}{-1.8218 \cdot \ln(T) + 8.9098}, \text{ for surface fine mixes} \quad (6.6)$$

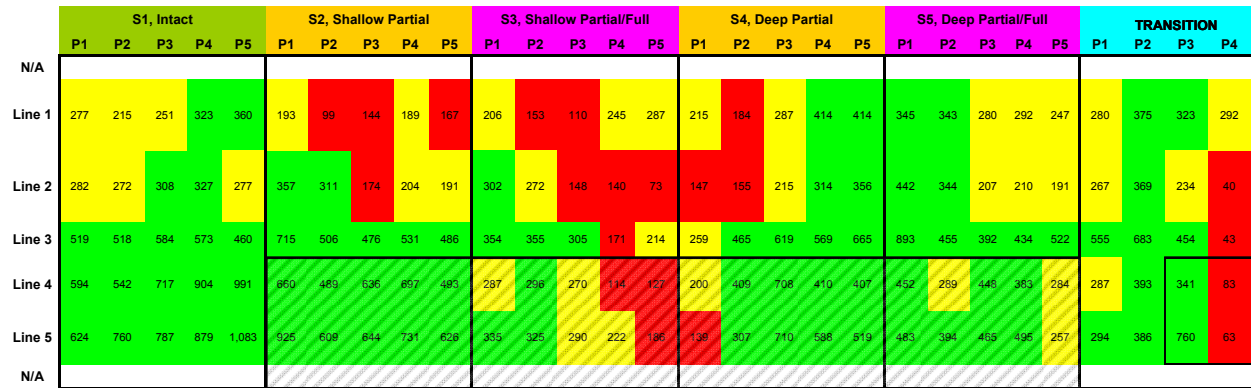
	S1, Intact					S2, Shallow Partial					S3, Shallow Partial/Full					S4, Deep Partial					S5, Deep Partial/Full					TRANSITION			
	P1	P2	P3	P4	P5	P1	P2	P3	P4	P5	P1	P2	P3	P4	P5	P1	P2	P3	P4	P5	P1	P2	P3	P4	P5	P1	P2	P3	P4
N/A																													
Line 1	1,769	1,847	2,644	2,492	3,000	2,786	2,007	2,235	2,597	2,211	1,872	1,798	1,836	2,072	2,494	2,089	2,032	2,098	1,547	3,000	1,395	1,871	3,000	2,214	2,585	2,358	2,714	2,168	1,952
Line 2	1,967	2,445	2,062	2,319	2,491	2,469	2,828	1,628	880	2,303	2,981	2,893	356	1,259	586	2,465	2,096	1,301	671	1,332	1,474	1,390	3,013	420	1,184	2,818	2,626	1,122	904
Line 3	2,170	2,212	2,059	2,283	2,401	2,420	1,892	2,018	2,610	2,273	1,365	1,140	1,070	752	178	1,325	1,515	2,235	2,532	2,921	1,886	927	1,683	795	3,586	988	2,518	89	58
Line 4	1,579	1,579	1,495	1,486	2,063	2,171	1,623	1,642	2,098	1,830	1,307	833	730	577	863	957	1,137	1,801	1,905	2,387	1,542	713	1,766	1,458	586	2,159	2,086	79	58
Line 5	1,383	1,397	1,495	1,337	2,083	1,519	1,211	1,327	1,288	1,065	894	545	640	602	552	512	556	1,526	1,627	1,794	1,165	545	1,446	1,730	1,415	2,213	1,642	113	100
N/A																													

a) Sections 1 to 5

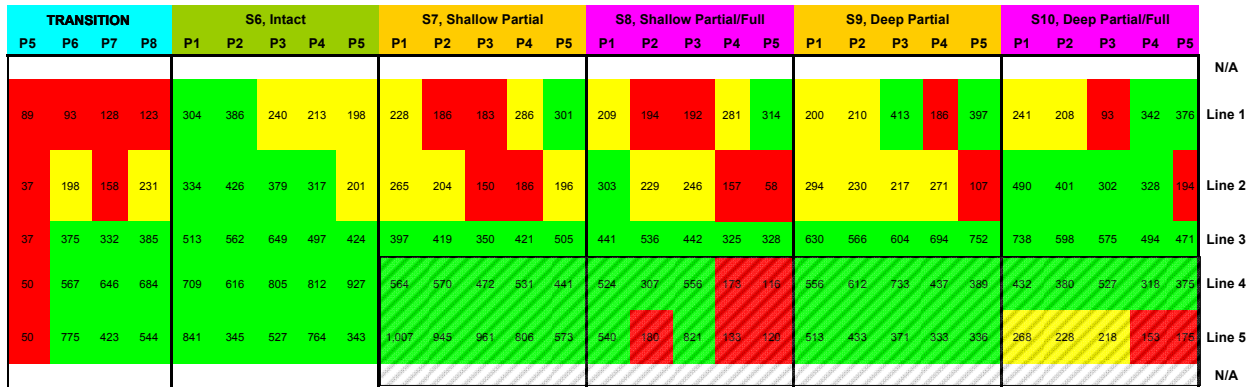
	TRANSITION				S6, Intact					S7, Shallow Partial					S8, Shallow Partial/Full					S9, Deep Partial					S10, Deep Partial/Full				
	P5	P6	P7	P8	P1	P2	P3	P4	P5	P1	P2	P3	P4	P5	P1	P2	P3	P4	P5	P1	P2	P3	P4	P5	P1	P2	P3	P4	P5
N/A																													
Line 1	1,292	1,133	1,184	1,250	2,013	1,931	1,684	1,542	1,400	1,655	1,460	1,623	1,596	1,801	1,826	1,730	1,329	1,380	1,839	2,141	2,291	2,066	1,655	2,277	2,037	1,240	839	1,383	####
Line 2	1,676	656	1,844	1,951	2,174	2,210	1,945	1,596	1,590	1,555	1,513	1,496	1,245	1,423	1,744	1,778	1,467	751	1,130	1,790	1,603	2,178	829	1,065	1,031	811	850	3,000	####
Line 3	1,840	2,145	2,234	2,266	2,435	2,113	2,019	1,909	1,618	1,895	1,523	1,563	2,179	2,100	1,559	1,353	1,124	535	517	1,581	1,748	2,126	2,086	2,068	1,413	913	953	603	910
Line 4	1,313	1,607	1,746	1,601	1,427	1,221	1,155	1,273	1,337	1,103	1,140	1,284	1,472	1,286	935	751	705	306	494	1,267	1,230	1,518	1,595	1,429	938	979	991	497	732
Line 5	1,372	1,503	1,610	1,550	1,468	1,173	1,203	1,232	1,382	1,332	1,184	1,850	1,655	1,400	907	705	466	368	228	930	1,199	1,007	1,229	1,862	1,336	833	868	318	488
N/A																													

a) Sections 6 to 10

Figure 6.16 – Contour Maps of FWD Moduli in Cool Weather based on Revised Statistical Criteria



a) Sections 1 to 5



a) Sections 6 to 10

Figure 6.17 – Contour Maps of FWD Moduli in Hot Weather based on Revised Statistical Criteria

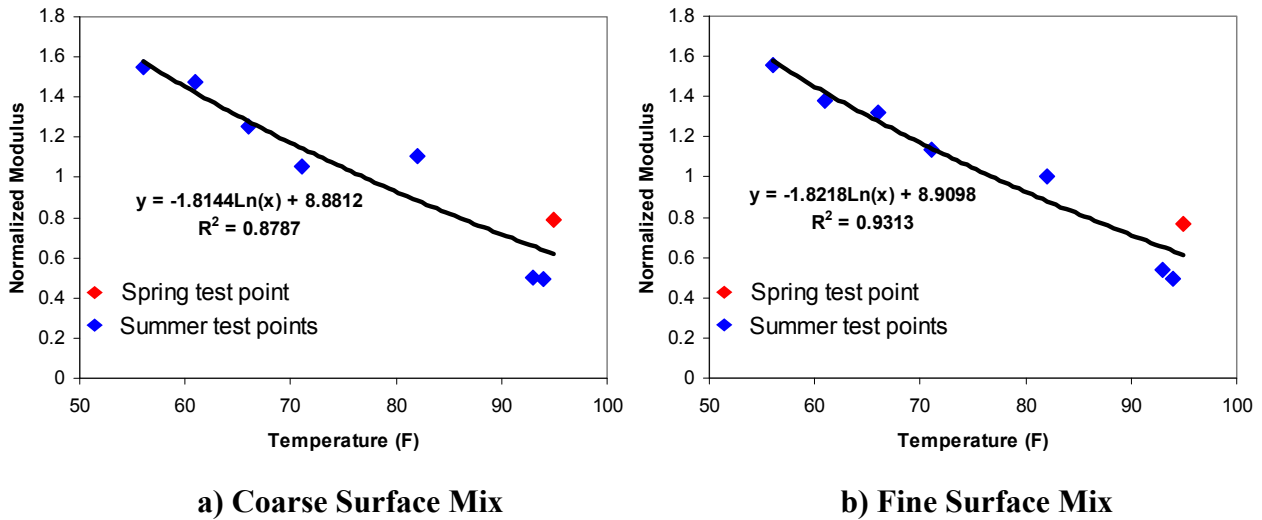


Figure 6.18 – Temperature Influence of FWD Modulus on Controlled Study

The temperature adjusted modulus contour maps are shown in Figures 6.19 and 6.20. Slight improvements in delineating debonded area are observed due to temperature adjustment. However, the number of false positive readings increased, especially for the hot weather tests.

Based on this study, the FWD may be used for detecting the shallow fully-debonded area, and with less certainty partially-debonded area. Similar to the USW method, the FWD is more effective in the cool weather testing than the hot weather testing. One concern with the FWD is the number of false positive readings (estimating low modulus for intact point) especially during the hot temperature testing. This pattern was not observed in the initial testing reported in Chapter 5.

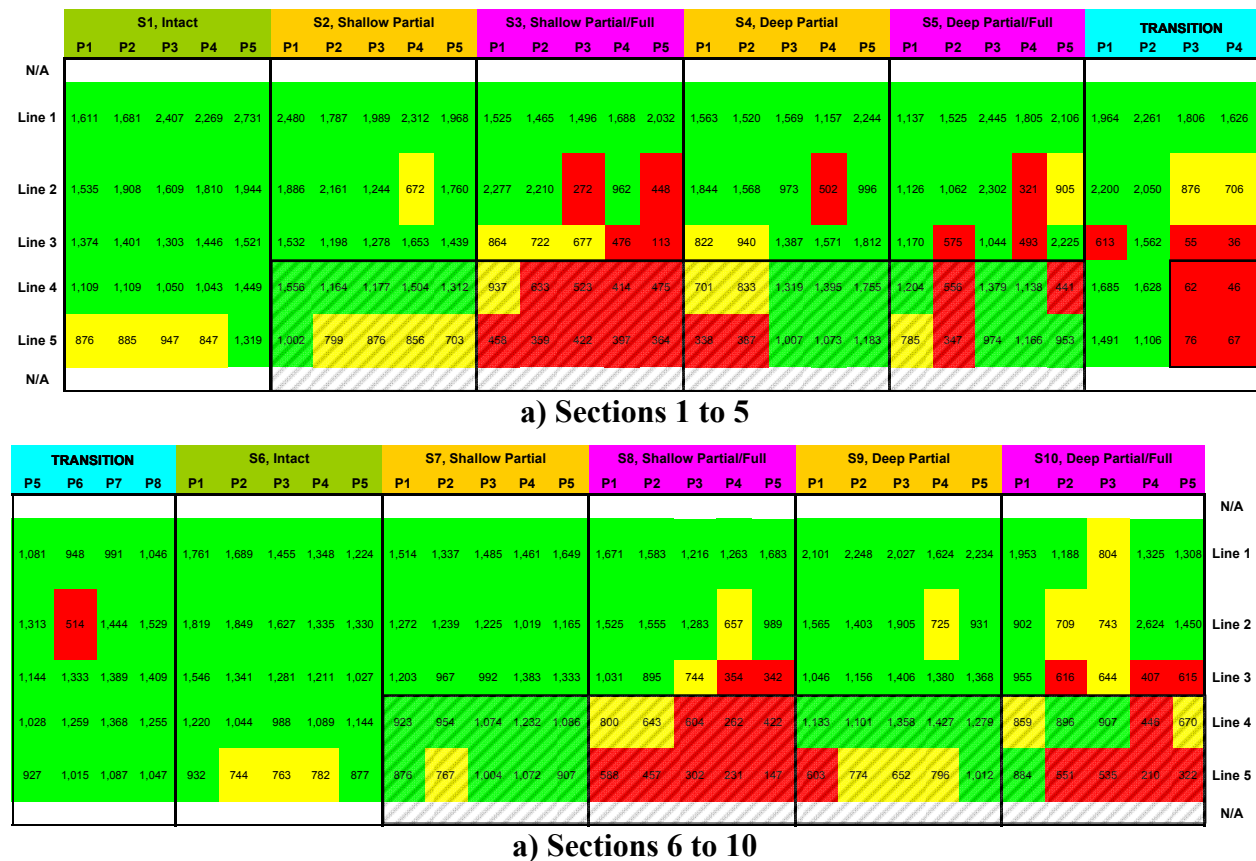
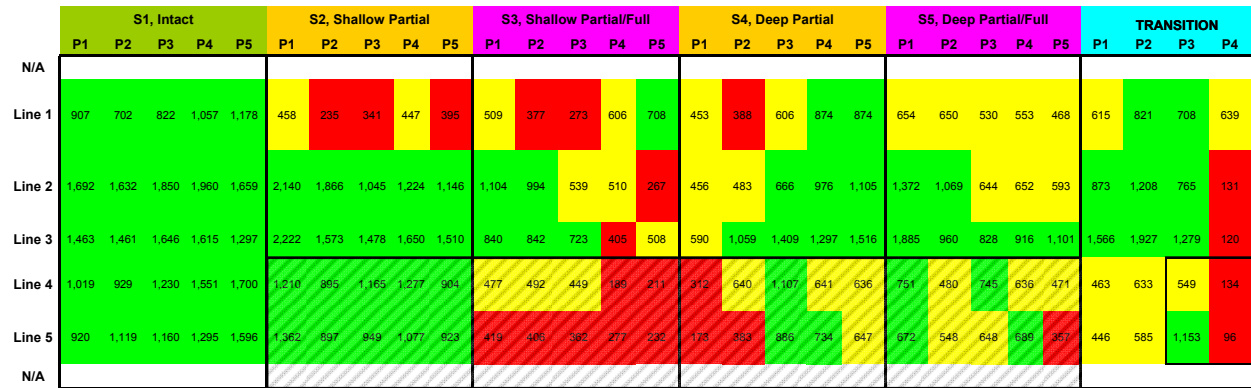
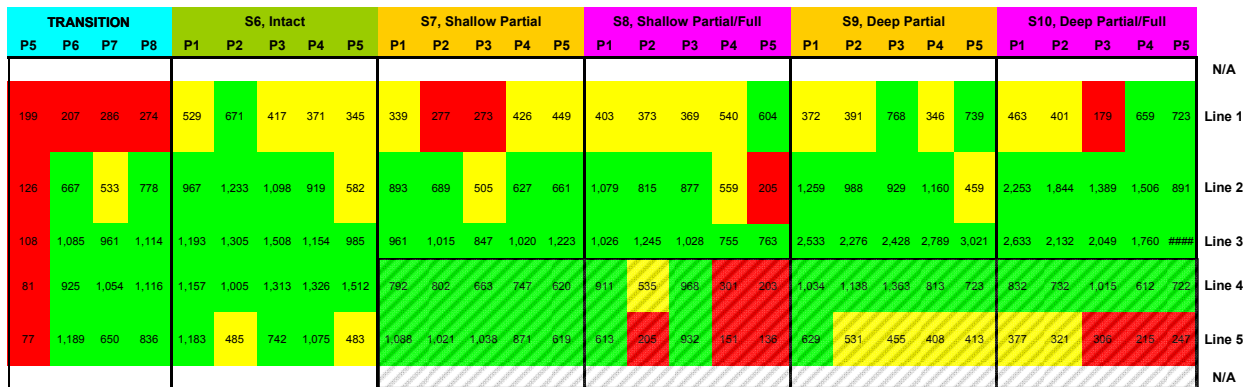


Figure 6.19 – Temperature-Adjusted Contour Maps of FWD Moduli in Cool Weather based on Revised Statistical Criteria



a) Sections 1 to 5



a) Sections 6 to 10

Figure 6.20 – Temperature-Adjusted Contour Maps of FWD Moduli in Hot Weather based on Revised Statistical Criteria

Impulse Response

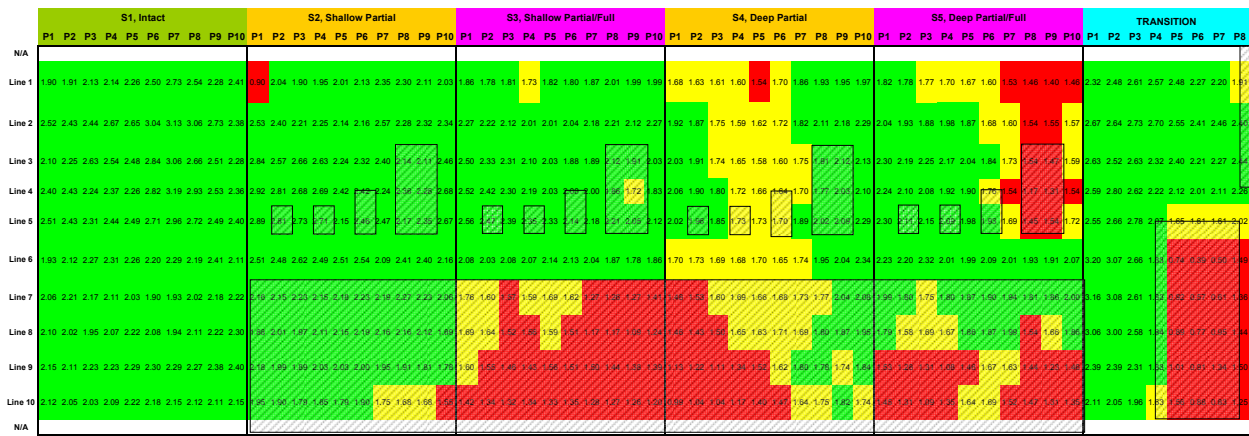
The results from the IR tests for the cool weather testing are summarized in Figure 6.21. Most of the shallow fully-debonded areas on Sections 3 and 8 were identified, but not all of the deep fully-debonded points are picked up. Interestingly, the shallow partially-debonded areas exhibit normal values, whereas the majority of the deep partially-debonded points are either marginally or significantly less stiff. Also, even though all the points in the control Section 1 are categorized as intact, a majority of test points on control Section 6 exhibit false positive results.

For hot weather tests, as shown in Figure 6.22, most defects are identified except those in Sections 5 and 7. Similar to FWD, a number of false positive points are apparent (i.e., a number intact points exhibited flexibility that are higher than average).

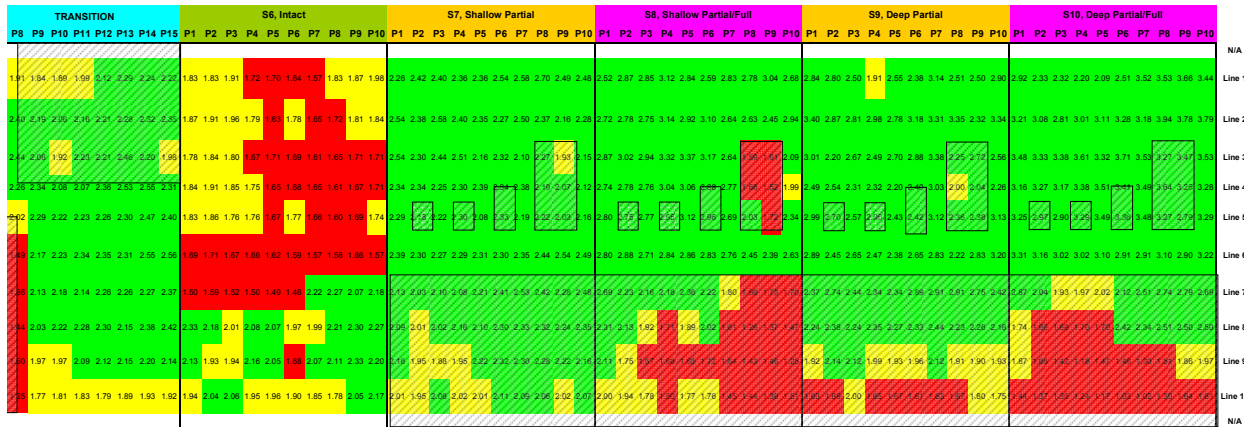
Hoping that considering the impact of temperature may assist in improving the interpretation of the results, the temperature adjustments shown in Figure 6.23 were developed similar to the other methods. The general equations for this purpose are the following:

$$FFT_{77^{\circ}F} = \frac{FFT_{T^{\circ}F}}{-0.009 \cdot T + 1.6958}, \text{ for surface coarse mixes} \quad (6.7)$$

$$FFT_{77^{\circ}F} = \frac{FFT_{T^{\circ}F}}{-0.009 \cdot T + 1.6876}, \text{ for surface fine mixes} \quad (6.8)$$

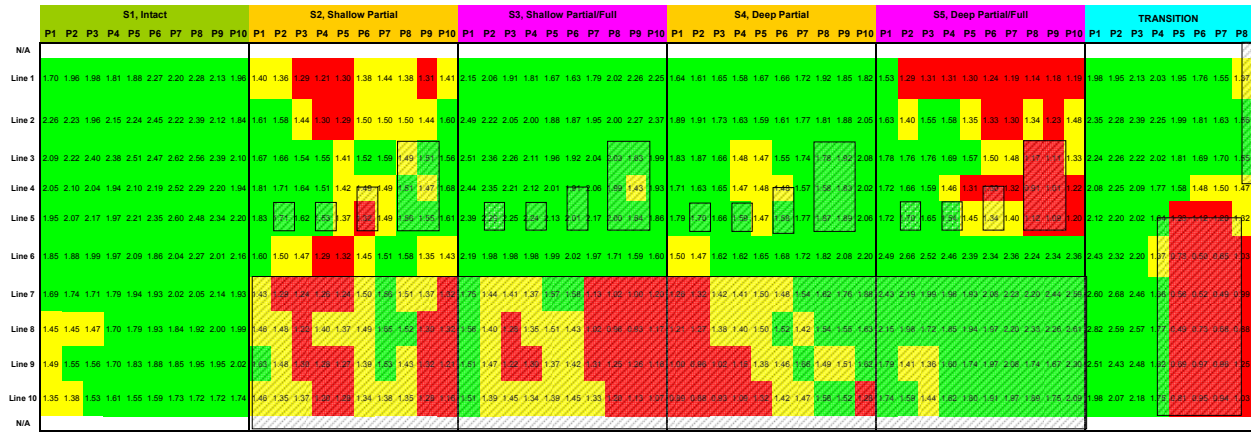


a) Sections 1 to 5

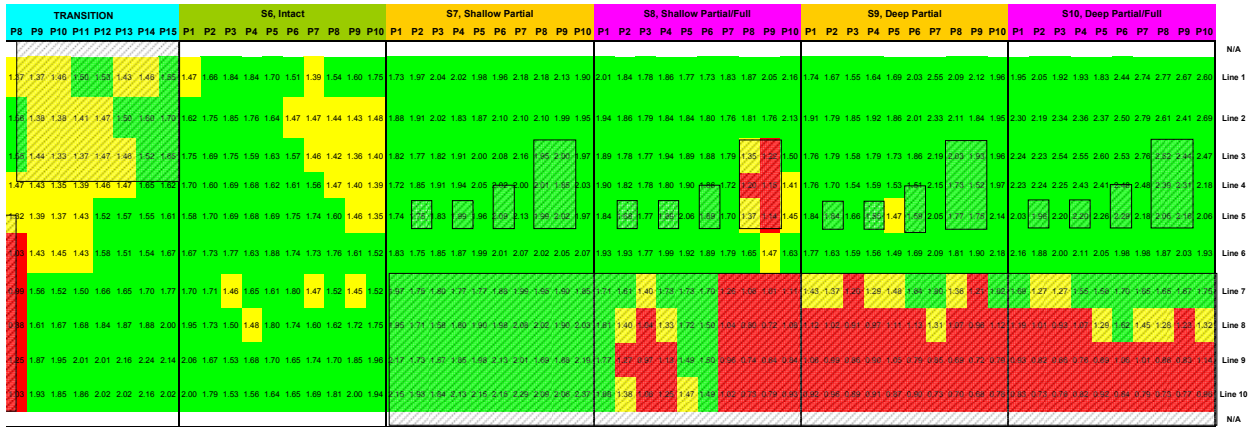


a) Sections 6 to 10

Figure 6.21 – Contour Maps of IR Flexibility in Cool Weather based on Revised Statistical Criteria



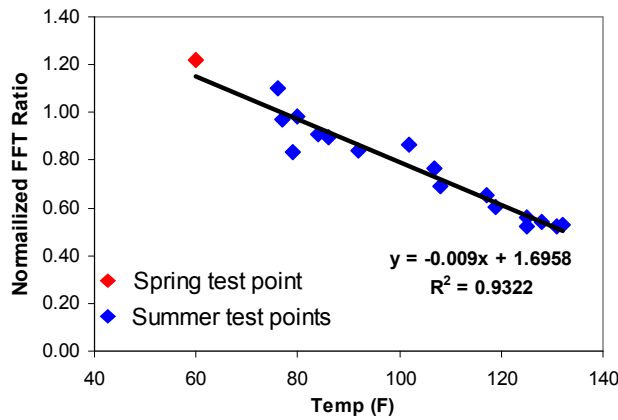
a) Sections 1 to 5



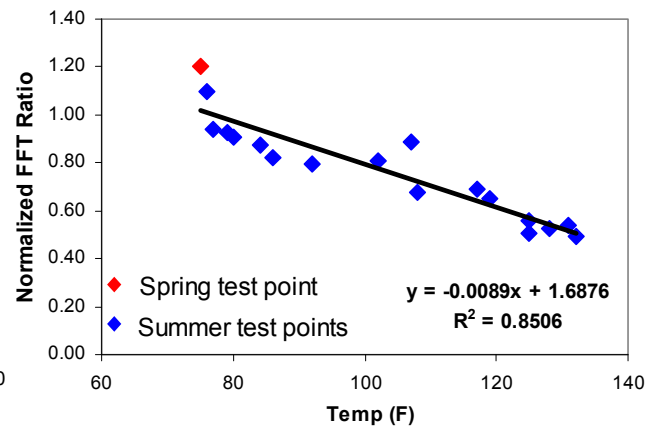
a) Sections 6 to 10

Figure 6.22 – Contour Maps of IR Flexibility in Hot Weather based on Revised Statistical

Criteria



a) Coarse Surface Mix



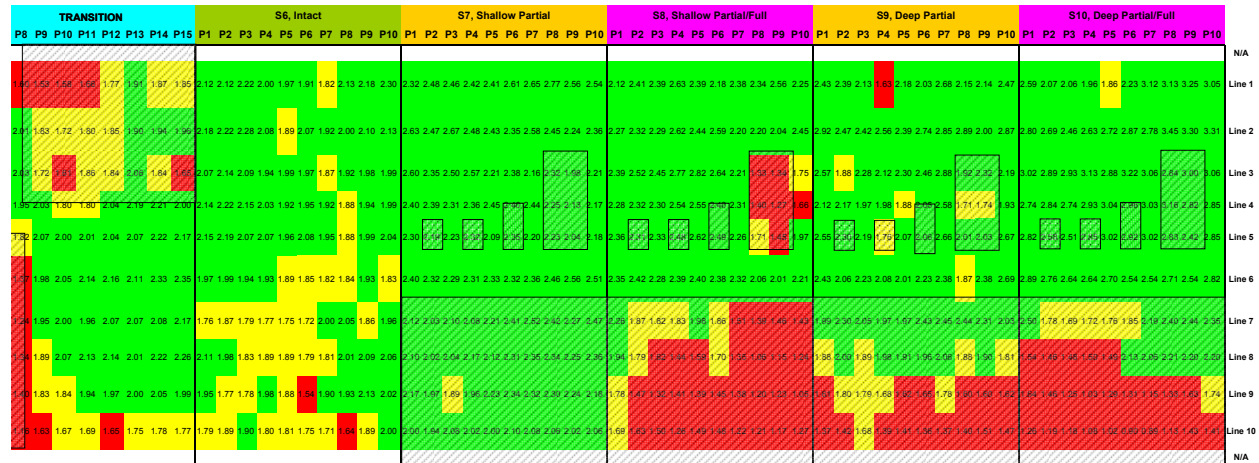
b) Fine Surface Mix

Figure 6.23 – Influence of Temperature on IR Flexibility

As reflected in Figure 6.24, the temperature adjustment of the results for cool weather tests marginally improved the predictive power of the method and significantly reduced the number of false positive points. Similar conclusions can be drawn for the hot weather tests (Figure 6.25).

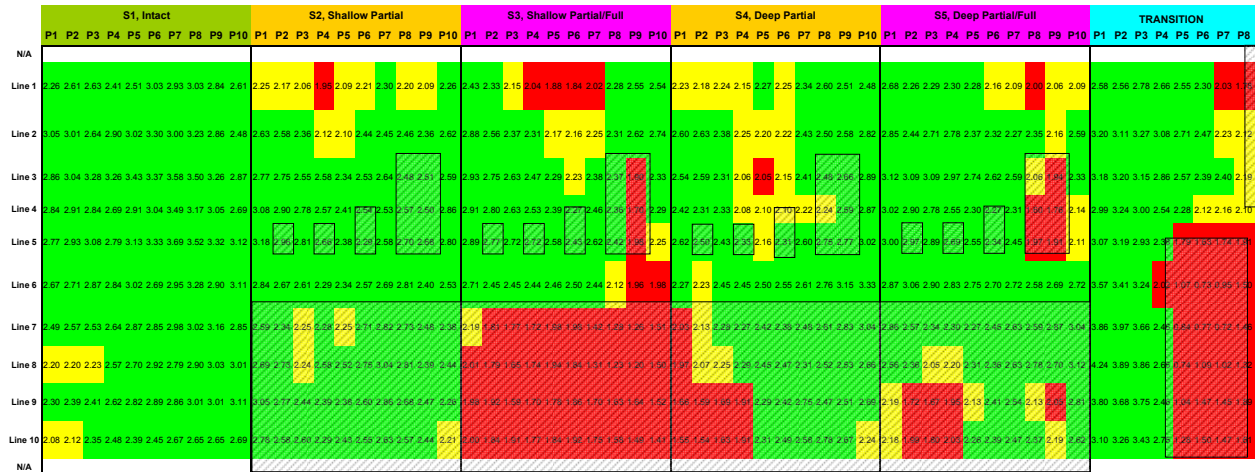


a) Sections 1 to 5

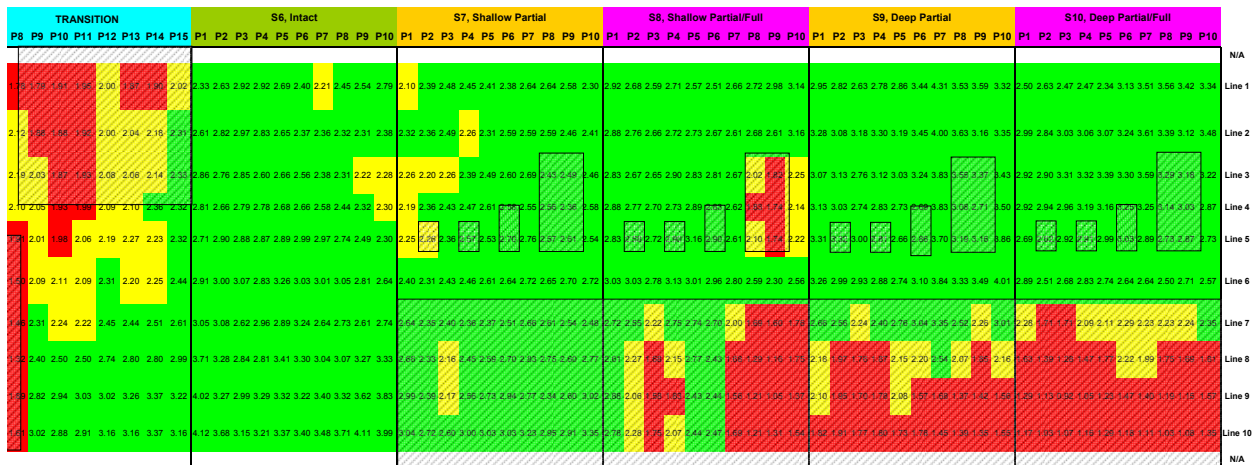


a) Sections 6 to 10

Figure 6.24 – Temperature-Adjusted Contour Maps of IR Flexibility in Cool Weather based on Revised Statistical Criteria



a) Sections 1 to 5



a) Sections 6 to 10

Figure 6.25 – Temperature-Adjusted Contour Maps of IR Flexibility in Cool Weather based on Revised Statistical Criteria

Thermal Methods

The thermal imaging was not deemed successful in Chapter 5. One concern with the earlier survey was the resolution of the camera. A more sensitive camera (a ToughCam Pro from Infrared Cameras Inc.) was acquired and used to reevaluate the thermal method as shown in Figure 6.26. A study was conducted on the transition section to evaluate the feasibility of the more sensitive camera. A total of 120 pictures were obtained, each one covering an area of 1 by 1 ft approximately. The combination of all the pictures is presented in Figure 6.27. Areas of



Figure 6.26 – Infrared Camera on Controlled Study

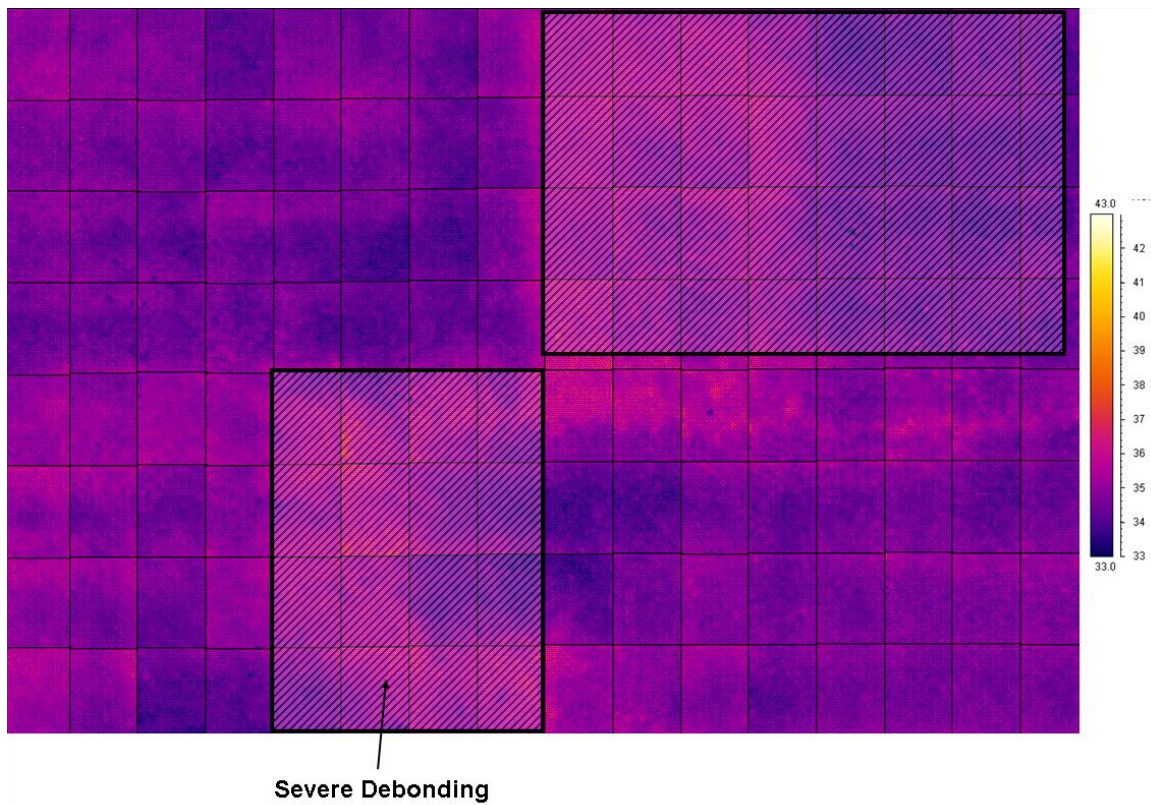


Figure 6.27 – Infrared Camera Results on Transition Area

severe debonding showed marginal change in temperature and other defects could not be detected. As such, the thermographical imaging considered as not a practical method in this

study. Maybe with further advancements in camera or active heating of pavement this method can be of greater utility.

Ground Coupled GPR

The processed linescans obtained with the ground-coupled GPR system along Lines 1 to 10 are shown in Figure 6.28. Locations of the prepared debonding are also included in the figure. The results from this experiment essentially confirmed the results from the preliminary study in Chapter 5. The ground-coupled GPR can clearly detect the severely-debonded areas in the transition zone, but the fully- and partially debonded areas could be sometimes detected, especially when the debonding agents were clay or talcum powder.

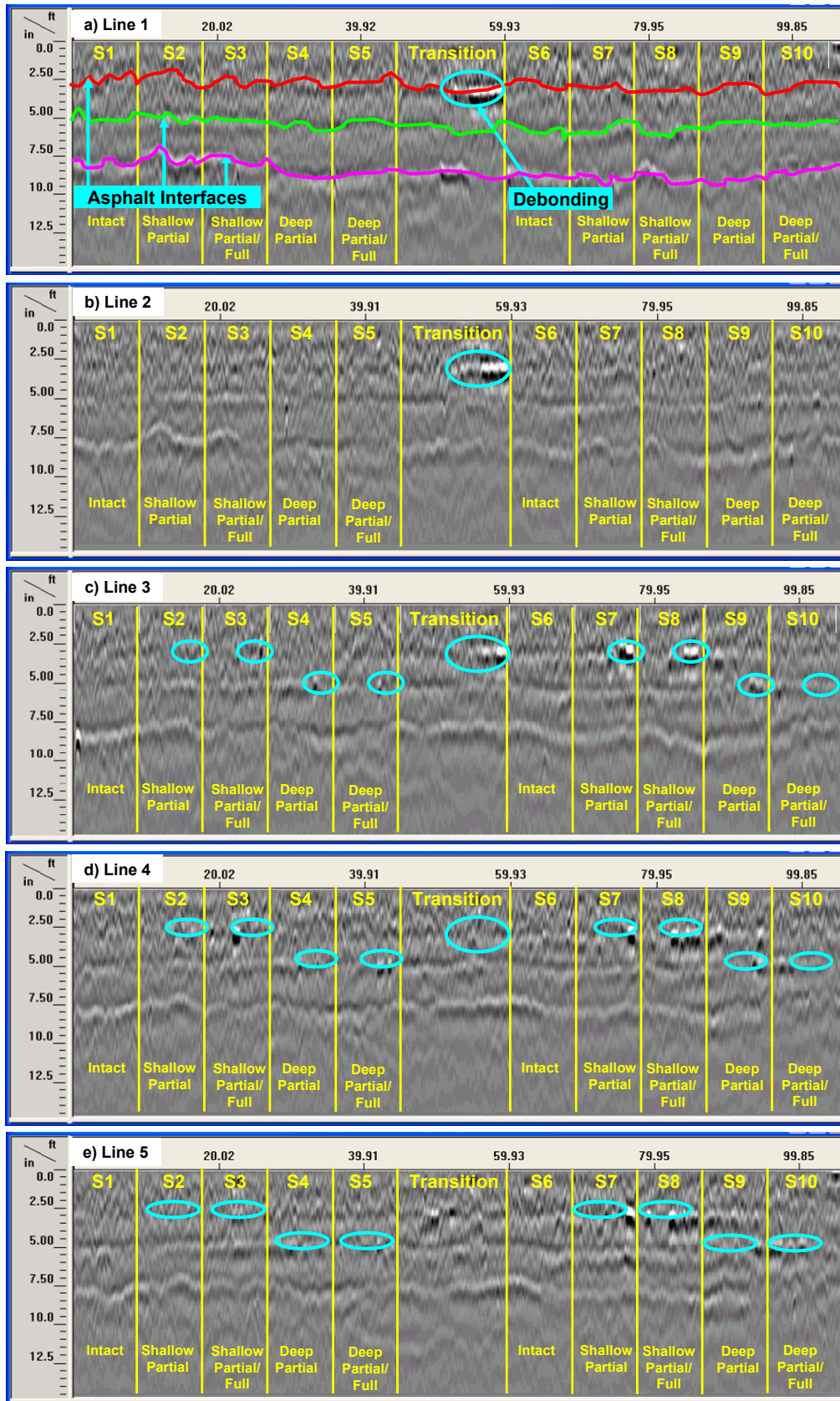


Figure 6.28 – Processed Linecasts with Ground-Coupled GPR from Extended Tests

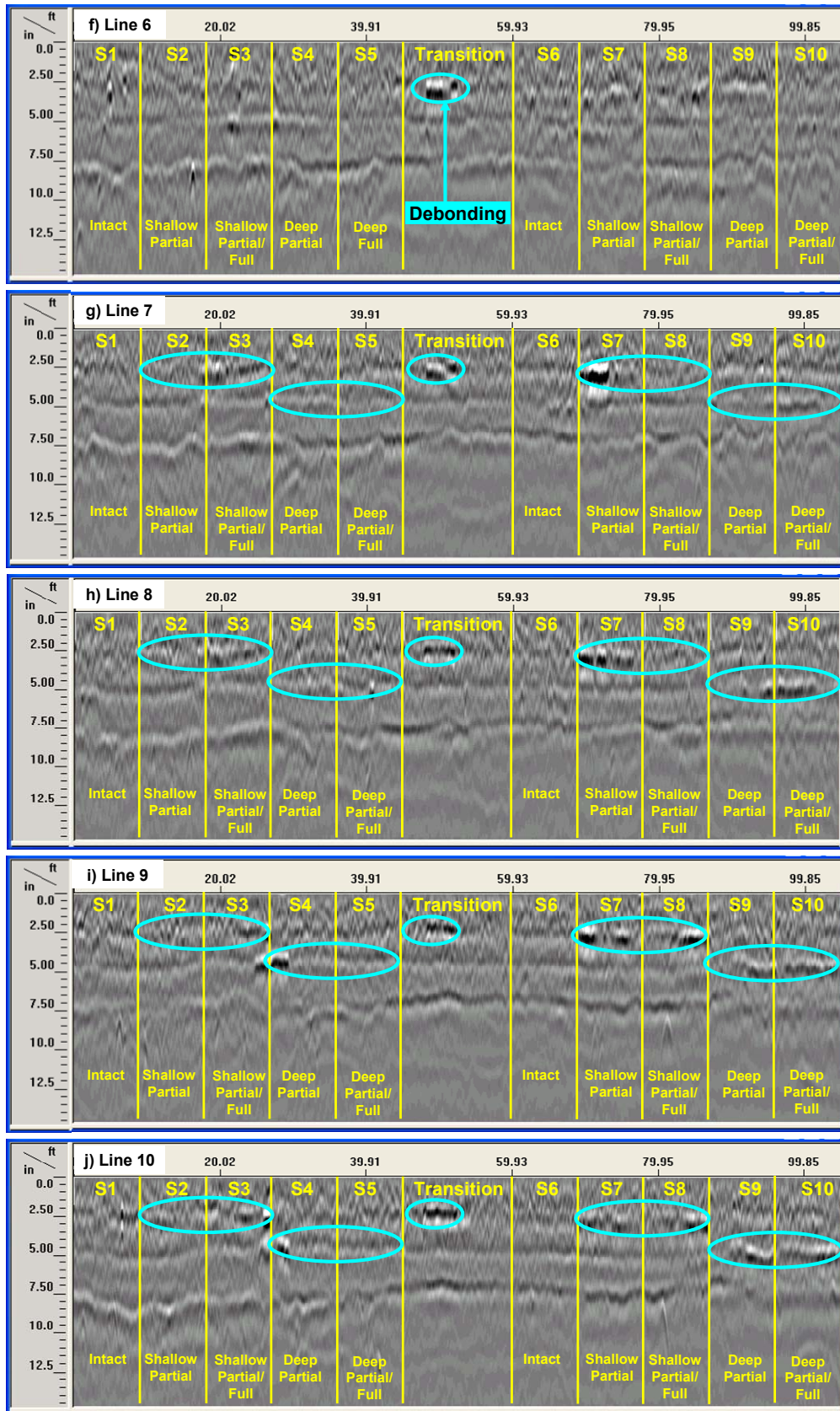


Figure 6.28 Contd. – Processed Linescans with Ground-Coupled GPR from Extended Tests

CHAPTER 7 – FIELD INVESTIGATION OF SELECTED NDT METHODS

Selected NDT methods and test protocols were evaluated on several features of Portland International Airport (PDX) and Boston Logan International Airport (BOS). The primary goal of the field study was to ensure that the methods are reasonable under actual field conditions. Results obtained at PDX and BOS are presented next.

Portland International Airport Site

Several areas of PDX presented low to medium severity longitudinal cracking. The cracking pattern appeared to indicate that the upper lift of the pavement might be debonded. Several areas of PDX that presented these problems or were suspect of being debonded were selected in consultation with PDX staff as shown in Figure 7.1.

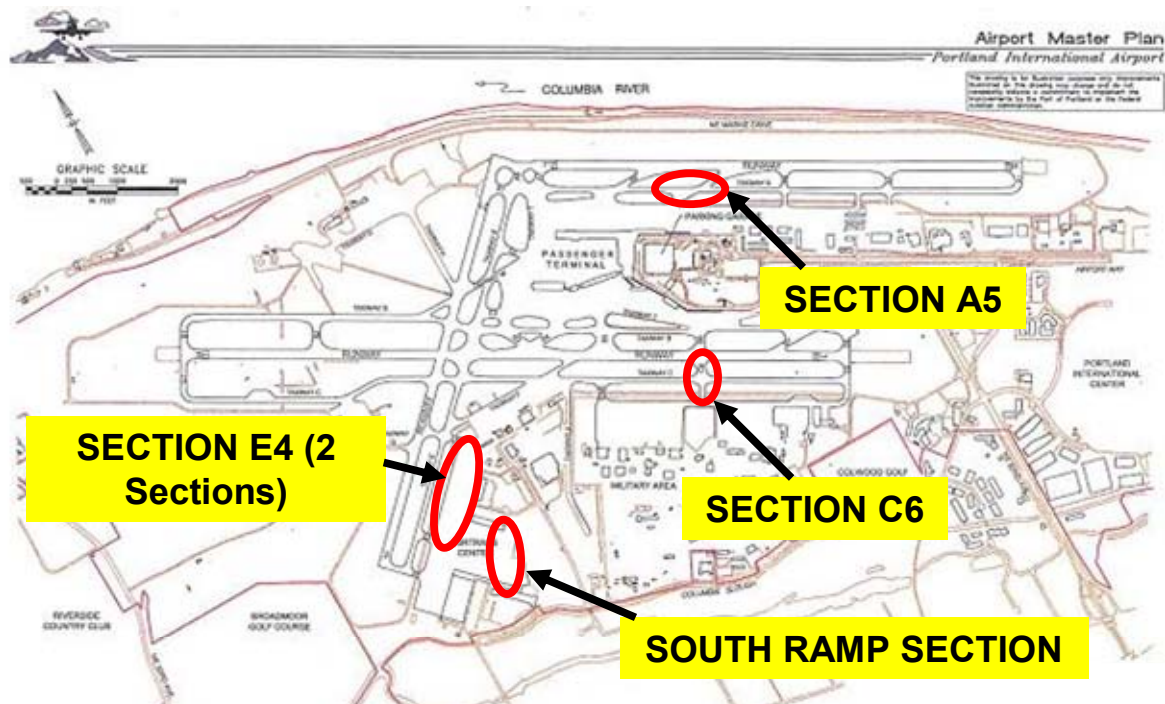


Figure 7.1 – Schematic of PDX and Location of Test Sections

The suspect areas corresponded to sections of Taxiways A, C and E, and the South Ramp. Section A5 was located on Taxiway A, parallel to Runway 10L/28R near Taxiway A5 (Figure 7.2). Taxiway A showed longitudinal cracking. Based on cores extracted by PDX staff, cracking was mostly confined to the top asphalt overlay. According to PDX staff, the overlay in some instances was not tightly bonded to the underlying asphalt lifts, and there was some indication of striping.

Section C6 was located on Taxiway C6 as shown in Figure 7.3. Similar to Taxiway A, there were some indications that the upper lift of pavement was not bonded. However, these problematic areas were already repaired. A section adjacent to the repaired area was tested.

The location of the South Ramp Section is shown in Figure 7.4. Some areas of this section presented advanced stages of longitudinal and transverse cracking that developed into alligator cracking and some areas did not exhibited surface distress (Figure 7.5a), while other areas did not exhibited surface distress (Figure 7.5b).

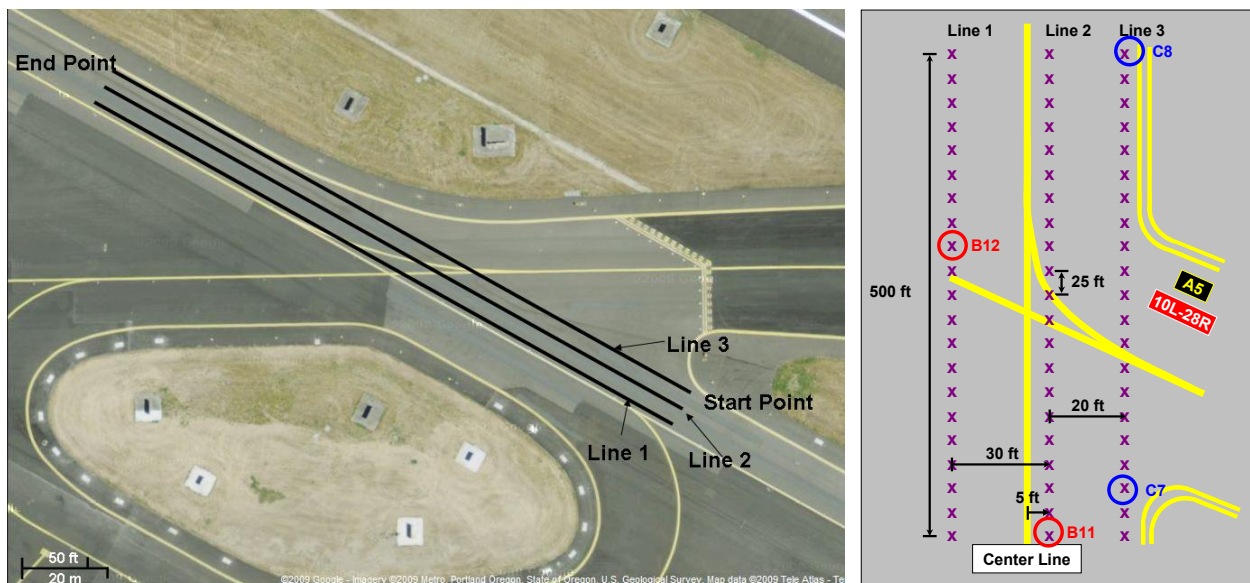


Figure 7.2 – Location of Section A5 and Test Layout

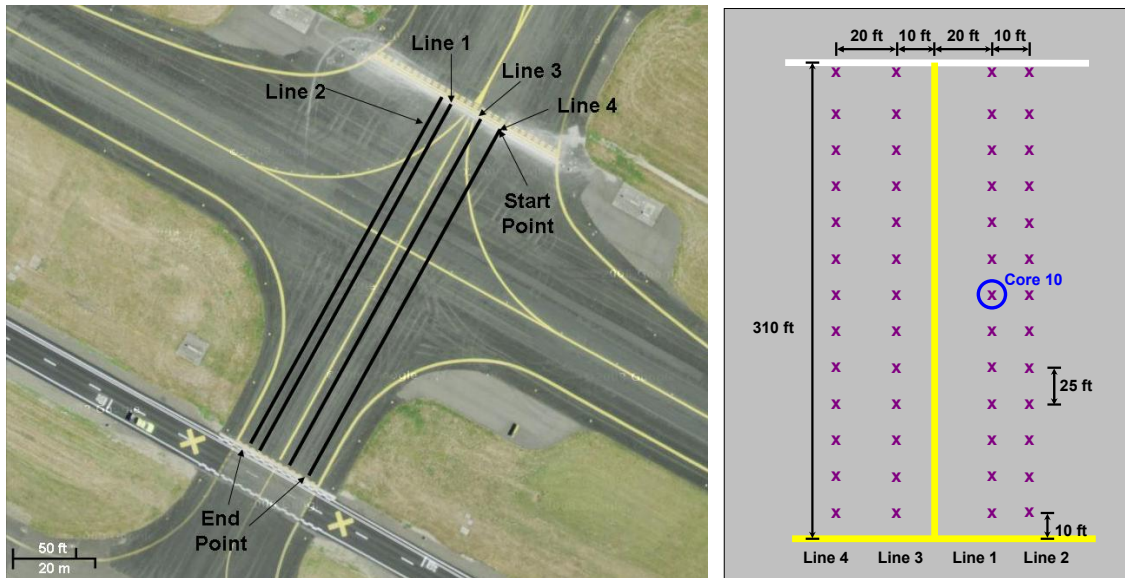


Figure 7.3 – Location of Section C6 and Test Layout

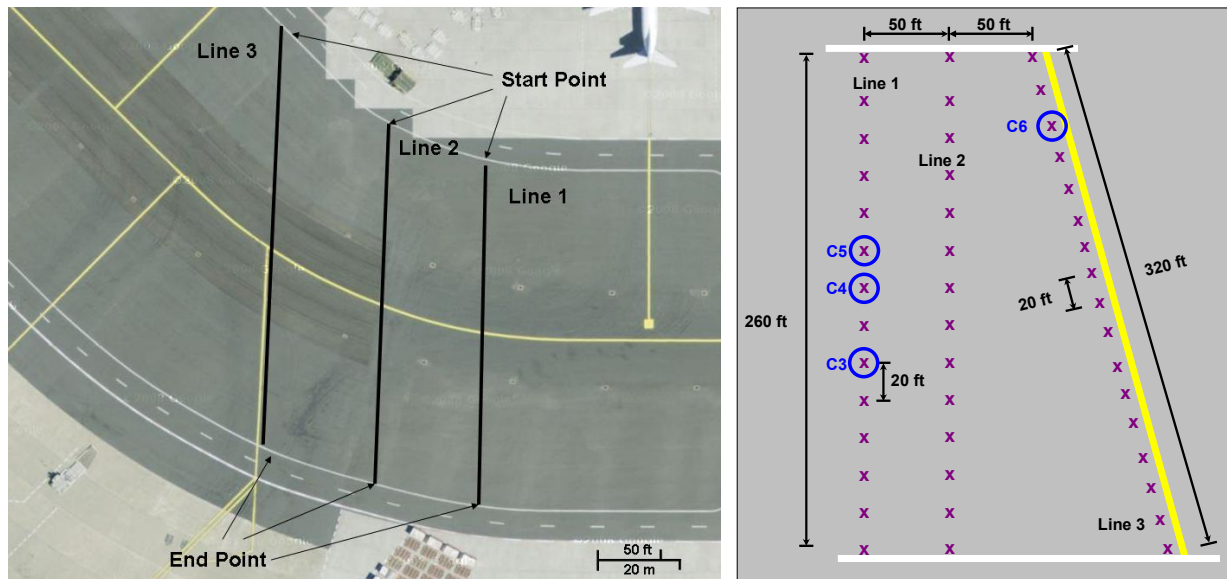


Figure 7.4 – Location of South Ramp Section and Test Layout

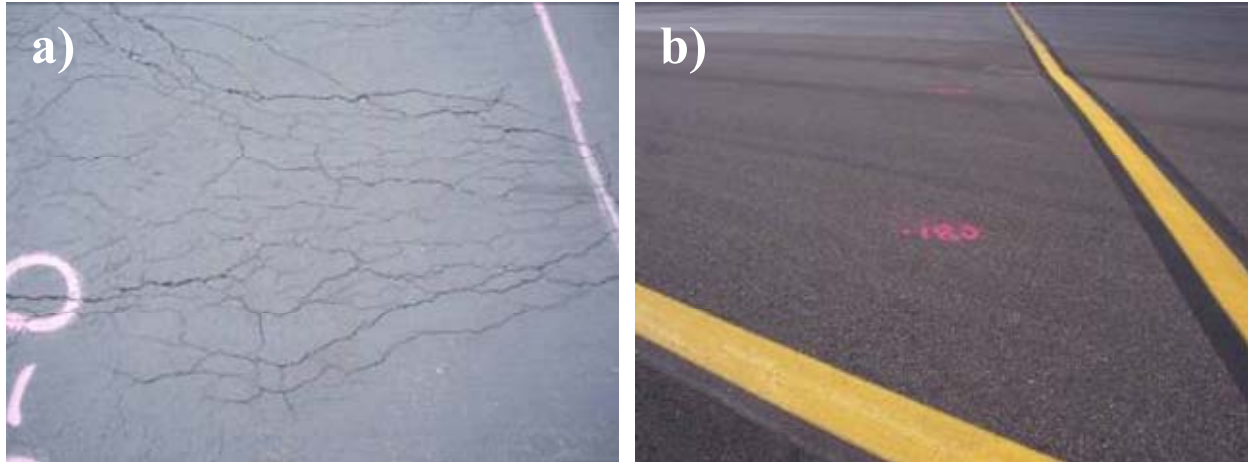


Figure 7.5 – Damaged and Intact Areas on South Ramp Section

Two adjacent sections were investigated next to Taxiway E4 as shown in Figure 7.6. No visual distress was observed throughout the entire section. Section 1 was recently repaired while Section 2 had not been repaired except for the first 30 ft.

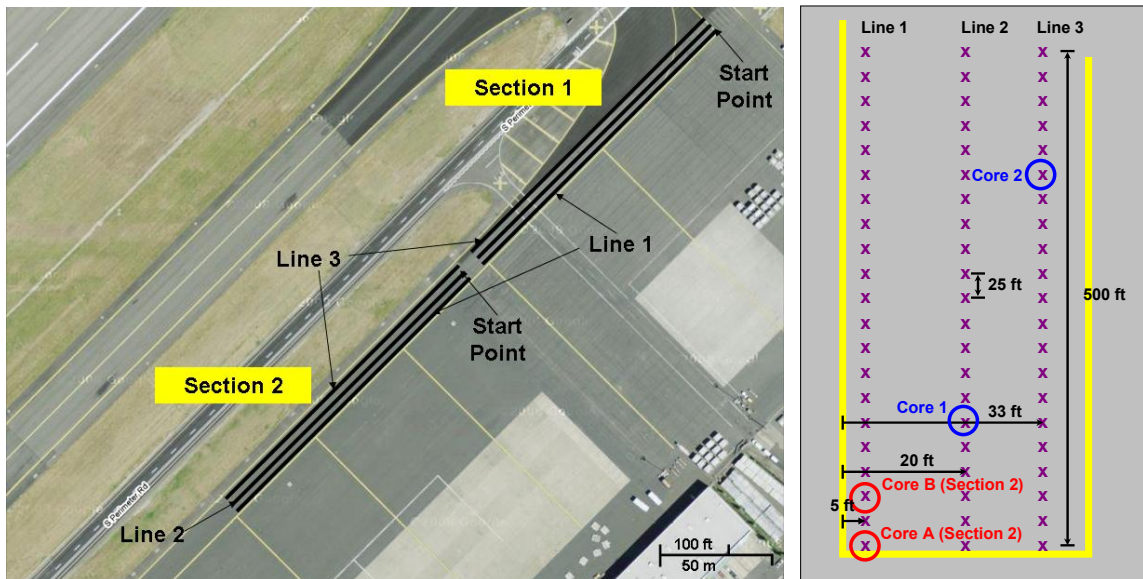


Figure 7.6 – Location of Sections 1 and 2 of E4 and Test Layout

Ultrasonic surface waves, impulse response, ground-coupled GPR and FWD were used to test these sections. The test schemes for each section are also shown in Figures 7.2 through 7.6. Three or four 200- to 500-ft long lines were selected at each site. The GPR tests were carried out along these lines. The other tests were carried out at discrete points between 20 ft to 50 ft apart.

Test Results

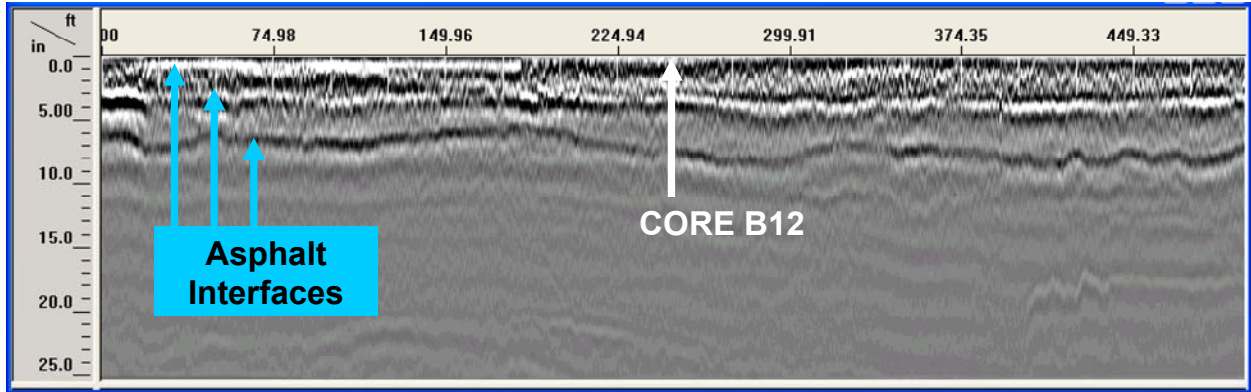
Section A5

Post-processed GPR linescans along the three lines at this section are shown on Figure 7.7. Several HMA layer interfaces are marked. Some of these interfaces showed stronger reflections that might indicate the presence of trapped moisture or the existence of stripping or debonding, particularly for the first 200 ft of Line 3. The results from the other methods are illustrated in Figure 7.8. The data were processed and presented in the same format as Chapter 6 for consistency. All methods and analyses point to problems along Line 3.

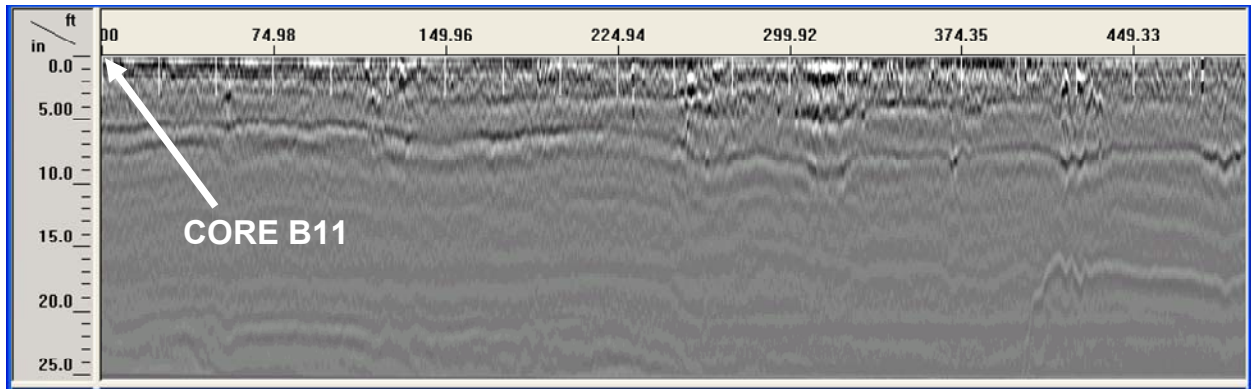
Table 7.1 contains the results of the four confirmatory cores extracted from this section. The results from the three mechanical tests are similar for cores B11 and B12 and point to intact sections. Even though the mechanical tests for the other two cores indicate damaged cores, the cores were reasonably intact but the quality of HMA was in question.

Table 7.1 – Comparison of Core Condition with NDT Results on Section A5

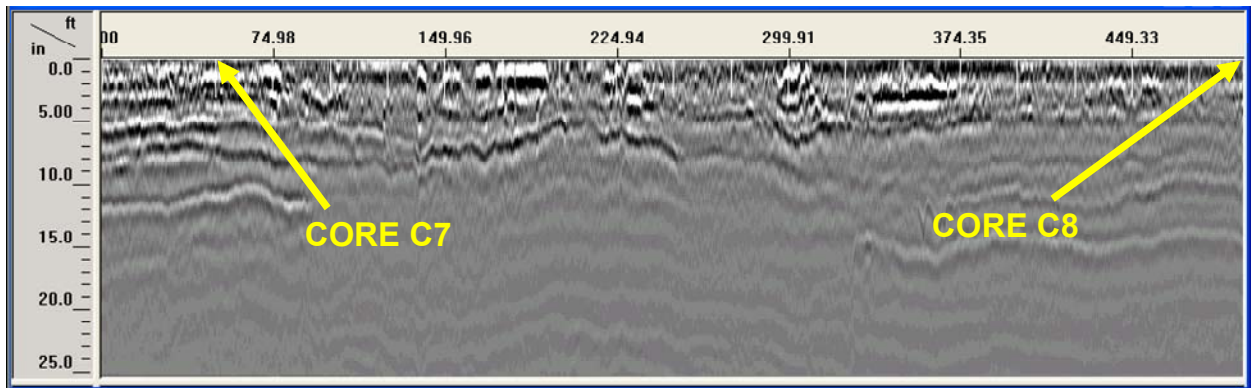
Core #	Location	GPR	PSPA	IR	FWD	Condition/Comments
B11	Line 2 @0 ft	Intact	Intact	Intact	Intact	Intact
B12	Line 1 @250 ft	Suspect	Intact	Intact	Intact	Intact
C7	Line 3 @0 ft	Suspect	Damaged	Damaged	Damaged	Low quality HMA, Core broken at 9.5 in.
C8	Line 3 @500 ft	Intact	Damaged	Damaged	Damaged	Low quality HMA, Intact



a) Line 1



b) Line 2



c) Line 3

Figure 7.7 – Post-processed GPR Linescans on Section A5

		Distance from Start Point (ft)																					
		0	25	50	75	100	125	150	175	200	225	250	275	300	325	350	375	400	425	450	475	481	500
Line 1		1905	1715	2017	1678	1785	1669	2082	1567	1984	1868	2116	1748	1857	1864	1804	1755	1766	1819	2014	1984	N/A	2026
Line 2		2432	2105	1879	2028	2143	2483	1891	1748	2112	2032	2171	1876	2034	1350	2330	1651	2372	1350	2330	2086	2211	1318
Line 3		1120	1220	1150	1383	1960	1730	1210	1319	1439	1049	1558	1665	1772	1314	1688	1879	1765	2063	1714	1627	N/A	1259

a) PSPA Modulus (ksi)

		Distance from Start Point (ft)																					
		0	25	50	75	100	125	150	175	200	225	250	275	300	325	350	375	400	425	450	475	481	500
Line 1		6.8	12.3	11.0	10.0	7.6	9.5	10.9	11.1	9.8	6.9	9.1	5.7	9.3	10.7	6.4	6.6	4.6	5.5	5.5	5.5	N/A	6.1
Line 2		9.8	8.7	9.0	11.6	6.7	11.4	12.5	8.1	7.5	7.7	9.0	5.9	11.0	12.1	13.9	6.3	7.7	3.9	6.5	7.4	6.8	8.4
Line 3		2.6	2.0	2.0	2.2	7.4	9.7	8.4	4.1	5.3	6.0	3.5	8.4	6.0	9.9	5.0	4.1	4.2	4.2	3.5	3.4	N/A	4.0

b) IR Results (FFT Ratios)

		Distance from Start (ft)										
		0	50	100	150	200	250	300	350	400	450	500
Line 1		10.2	9.4	9.5	9.5	8.8	8.9	9.2	9.9	9.6	13.6	14.4
Line 2		11.3	10.3	8.9	8.6	8.7	9.7	8.8	7.2	9.7	13.2	12.7
Line 3		20.9	29.0	9.9	10.4	9.7	8.4	9.5	15.5	16.3	16.1	15.9

c) FWD Deflections (mils)

		Distance from Start (ft)										
		0	50	100	150	200	250	300	350	400	450	500
Line 1		172	187	185	186	199	198	189	177	181	129	122
Line 2		156	170	198	203	199	181	199	245	181	132	139
Line 3		83	60	176	169	181	211	183	112	107	108	110

d) FWD Modulus (ksi)

Figure 7.8 – NDT Results on Section A5

Section C6

Linescan for Line 1 of this section is shown in Figure 7.9 and for all lines in Appendix F. Strong reflections are detected at depths of about 2 and 5 in. along the first 150 ft of the section.

PSPA, IR and FWD results along Section C6 are included in Figure 7.10. Dispersion curves from USW are presented in Appendix F for all lines. Most data points seem to indicate an intact section. The only confirmatory core (Core 10) obtained at this section was on Line 1 as shown in Figure 7.11. As summarized in Table 7.2, the core location was designated as damaged with PSPA and IR, and intact with GPR and FWD. Core C10 was stripped at 5 in. depth as shown in Figure 7.11.

Table 7.2 – Comparison of Core Condition with NDT Results on Section C6

Core #	Location	GPR	PSPA	IR	FWD Deflection	Condition/Comments
C10	L1 @160 ft from start	Intact	Damaged	Damaged	Intact	Stripping between top and middle layer

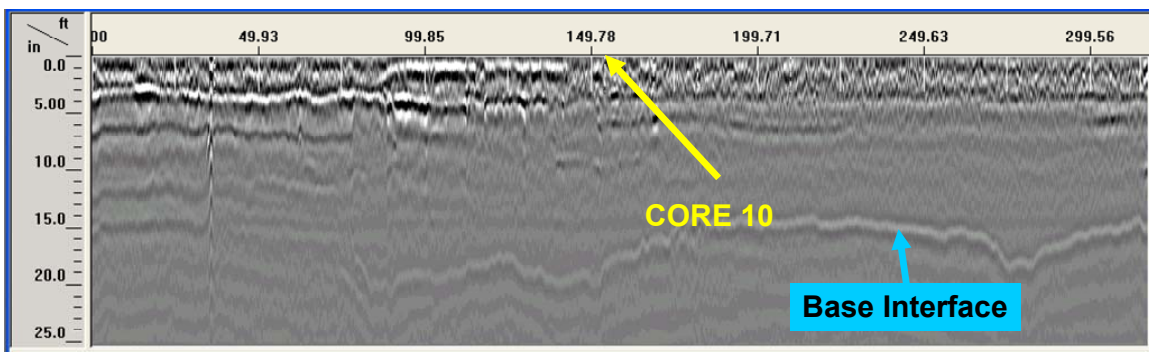


Figure 7.9 – Post-processed GPR Linescans of Line 1 on Section C6

		Distance from Start Point (ft)												
		10	35	60	85	110	135	160	185	210	235	260	285	310
Line 4		2097	2013	1719	1925	1115	1527	1290	1789	1545	1413	1458	1439	1951
Line 3		2225	1376	1849	1830	1390	1513	1705	1710	1409	1635	1761	1516	1905
Line 1		2022	1626	1839	1655	1633	1413	1372	1646	1127	1971	1753	1478	1420
Line 2		2009	1646	1856	1883	1757	1541	1909	1454	1368	1525	1692	1596	1501

a) PSPA Modulus (ksi)

		Distance from Start (ft)												
		10	35	60	85	110	135	160	185	210	235	260	285	310
Line 4		7.5	5.1	6.1	9.1	8.6	7.9	6.2	7.3	7.7	7.8	7.2	7.3	7.7
Line 3		5.5	5.9	5.8	12.2	9.8	9.0	9.4	6.9	8.2	8.1	5.9	6.6	6.4
Line 1		7.4	5.2	5.7	10.9	6.9	7.6	3.7	6.6	4.6	5.2	8.0	6.3	4.4
Line 2		5.8	7.0	7.4	7.8	6.8	9.9	6.9	5.9	5.3	7.2	8.7	8.3	8.1

b) IR Results (stiffness)

		Distance from Start (ft)												
		10	35	60	85	110	135	160	185	210	235	260	285	310
Line 4		20.1	25.0	20.7	14.9	17.5	18.1	19.7	21.9	22.2	23.5	23.0	21.8	20.7
Line 3		28.1	25.0	25.5	14.7	16.4	18.0	20.0	21.8	23.0	23.5	25.2	23.3	21.8
Line 1		23.5	28.9	22.6	14.6	18.3	18.1	18.9	24.0	27.0	24.5	21.7	19.1	22.0
Line 2		19.2	21.4	18.4	16.0	17.1	16.6	18.8	24.0	26.8	21.3	19.9	17.5	20.8

c) FWD Deflections (mils)

		Distance from Start (ft)												
		10	35	60	85	110	135	160	185	210	235	260	285	310
Line 4		86	69	84	118	100	96	89	80	79	74	76	80	84
Line 3		62	70	68	119	106	96	87	80	75	74	69	75	80
Line 1		74	60	77	119	95	96	92	72	64	71	81	91	79
Line 2		91	81	94	109	101	104	93	72	65	82	88	100	84

d) FWD Modulus (ksi)

Figure 7.10 – NDT Results on Section C6

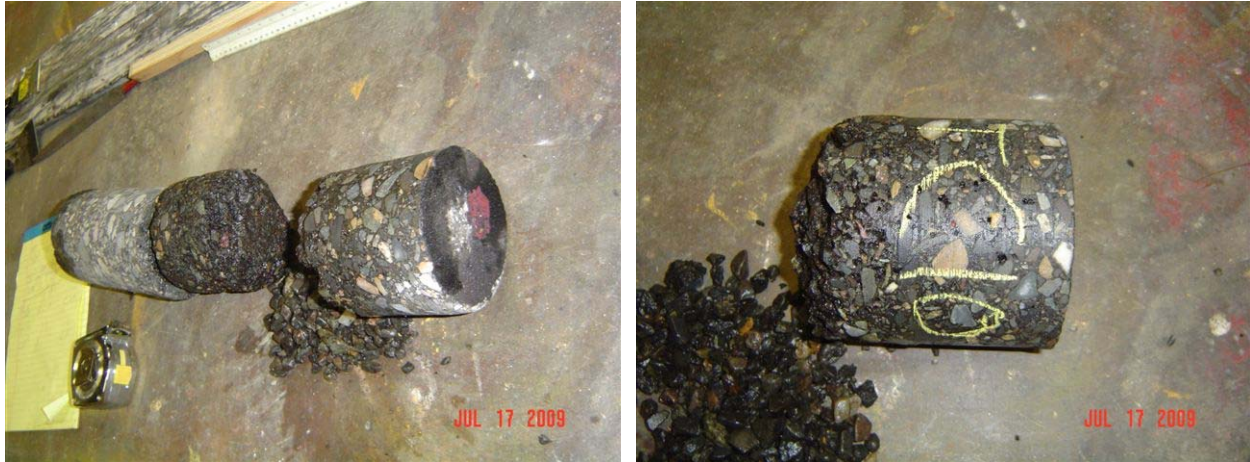


Figure 7.11 – Core C10 Stripped at 5 inches from Section C6

South Ramp Section

The results from all methods at this section are shown in Figures 7.12 and 7.13, and in Appendix F. The PSPA indicates less of a problem at this section than the IR and FWD, especially along Line 1. For that reason, three of the four validation cores were obtained along Line 1 as shown in Figure 7.14. The conditions of these cores with the interpretations of the NDT devices are summarized in Table 7.3. PSPA and FWD detected Core 3 as intact, where IR showed marginal condition. Cores 4 and 5 were categorized as damaged with both IR and FWD and PSPA showed intact condition. For the case of GPR, a strong reflection close to the surface was evident for Core 6.

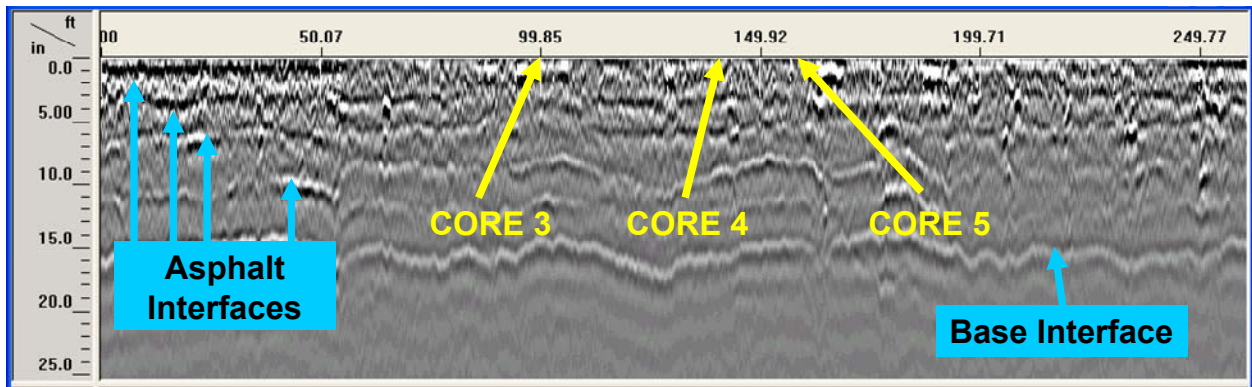


Figure 7.12 – Post-processed GPR Linescans of Line 1 on South Ramp Section

		Distance from Start (ft)																
		-60	-40	-20	0	20	40	60	80	100	120	140	160	180	200	220	240	260
Line 1					2180	2073	2146	1967	1919	1917	1906	2128	2361	1928	1913	1925	1906	1803
Line 2					1981	2122	2112	1469	1966	1868	2135	2138	1530	1516	1954	1983	2053	1380
Line 3		1957	1569	2145	2475	2004	1996	1949	2150	1703	1534	1912	1721	2147	1063	552	2177	1782

a) PSPA Modulus (ksi)

		Distance from Start (ft)																
		-60	-40	-20	0	20	40	60	80	100	120	140	160	180	200	220	240	260
Line 1					7.7	6.6	5.1	4.1	4.0	4.7	4.6	3.1	3.6	3.2	5.8	4.7	7.2	7.2
Line 2					9.7	7.0	8.7	3.2	8.4	6.7	6.1	6.6	3.9	4.2	2.9	5.1	6.7	3.9
Line 3		7.2	6.1	9.6	8.6	8.1	6.0	9.0	8.4	6.0	6.5	8.8	4.9	7.3	3.8	2.8	6.8	9.1

b) IR Results (FFT Ratios)

		Distance from Start (ft)																
		-60	-40	-20	0	20	40	60	80	100	120	140	160	180	200	220	240	260
Line 1					N/A	20.3	20.3	23.0	18.8	23.6	19.9	26.4	31.5	30.7	28.6	22.4	20.7	17.6
Line 2					N/A	18.4	18.2	29.5	18.1	22.0	22.9	22.6	29.0	30.2	38.3	25.7	22.5	28.7
Line 3		N/A	26.2	17.5	18.1	18.4	19.4	17.9	21.3	20.1	20.7	18.9	28.2	24.4	31.7	34.5	29.3	21.0

c) FWD Deflections (mils)

		Distance from Start (ft)																
		-60	-40	-20	0	20	40	60	80	100	120	140	160	180	200	220	240	260
Line 1					N/A	86	86	76	93	74	87	66	55	56	61	78	84	99
Line 2					N/A	95	96	59	97	79	76	77	59	57	45	67	77	60
Line 3		N/A	66	100	96	96	90	98	81	87	84	92	61	71	55	50	59	83

d) FWD Modulus (ksi)

Figure 7.13 – NDT Results on South Ramp Section

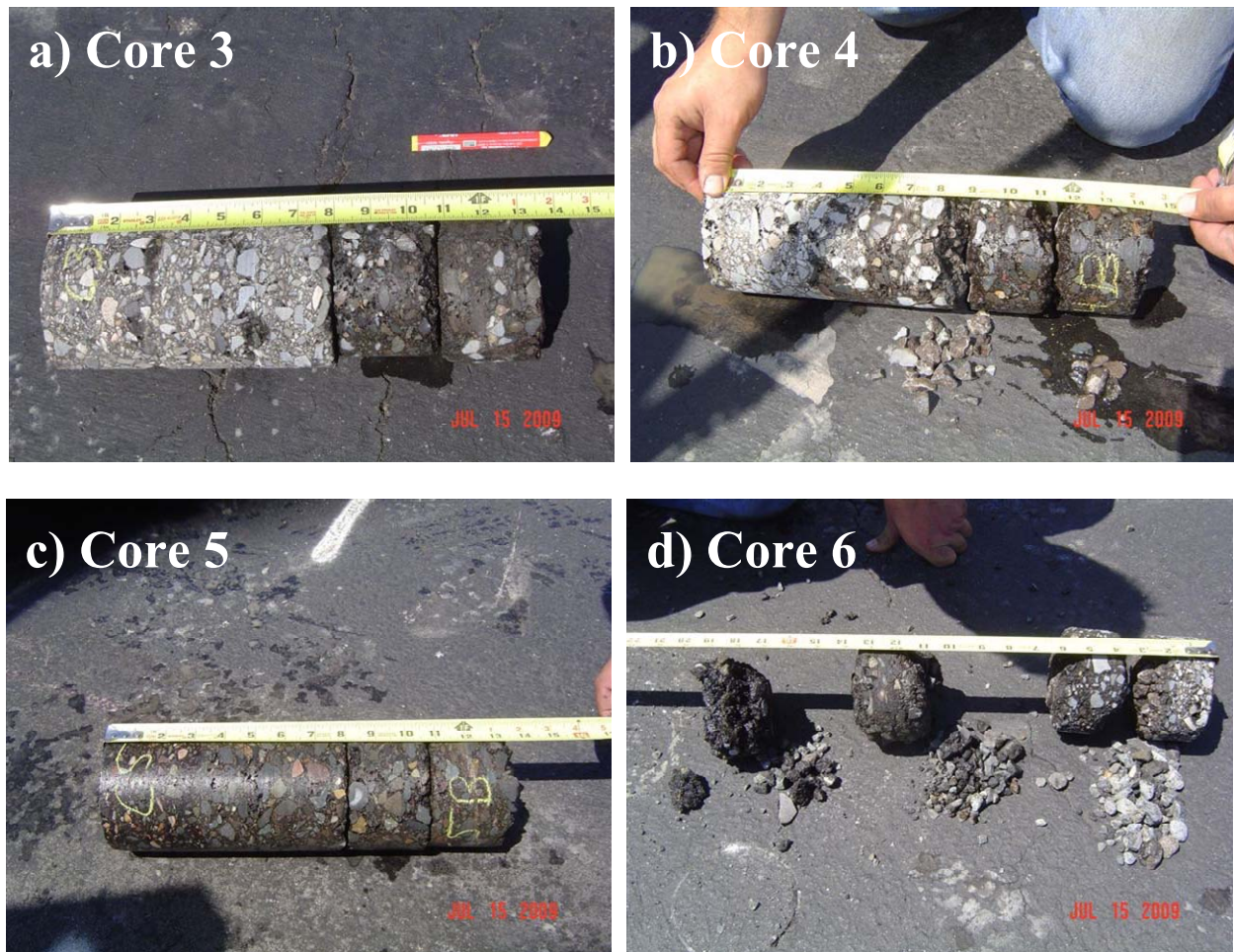


Figure 7.14 – Cores Retrieved from South Ramp Section

Table 7.3 – Comparison of Core Condition with NDT Results on South Ramp Section

Core #	Location	GPR	PSPA	IR	FWD Deflection	Condition/Comments
C3	L1 @100 ft from start	Intact	Intact	Marginal	Intact	Intact.
C4	L1 @140 ft from start	Intact	Intact	Damaged	Damaged	Some stripping at 9 in.
C5	L1 @160 ft from start	Intact	Intact	Damaged	Damaged	Intact
C6	L3 @280 ft from start	Damaged	Damaged	Damaged	Damaged	Severe stripping between each lift

Sections E4

The results from the four tests along the two sections are shown in Figures 7.15 through 7.19 and Appendix F. For Section 1, Line 3 of GPR exhibited two distinctive interfaces at 4 in. and 10 in., while for Section 2, four different interfaces were identified on all lines. However, the strong reflections obtained along the first 75 ft of Section 2 indicate the presence of moisture or possible existence of stripping or debonding.

There are some similarities and differences in the damaged areas identified by different methods. PSPA dispersion curves showed stronger reduction in modulus for points along Lines 2 and 3 from Section 1 and less significant reduction for points of Section 2 (see Appendix F).

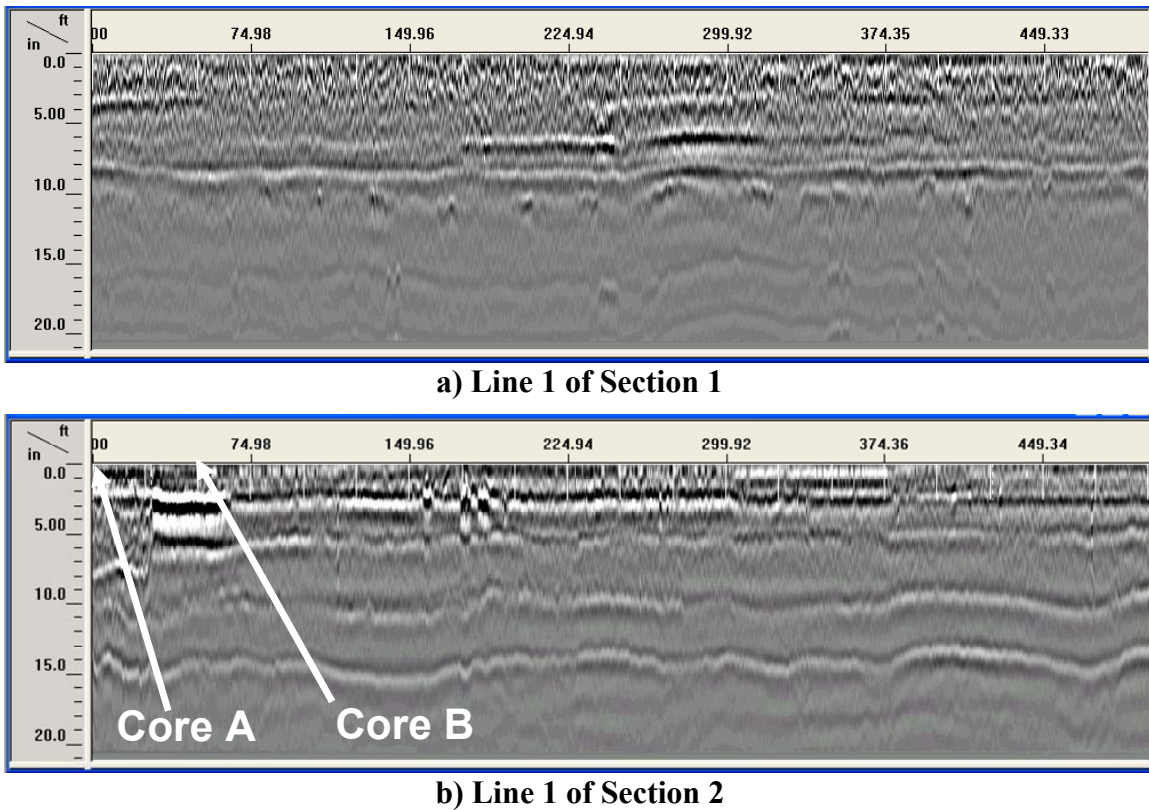


Figure 7.15 – Post-processed GPR Linescans on Line 1 of Sections 1 and 2 of E4

Distance from Start Point (ft)																					
	0	25	50	75	100	125	150	175	200	225	250	275	300	325	350	375	400	425	450	475	500
Line 1	1805	1927	1627	1816	1819	1823	1579	2026	2107	2055	2237	2235	2330	2251	2066	2469	2423	2236	1913	2152	1653
Line 2	1718	2439	1382	1868	1641	2038	1305	1527	1723	1515	2022	1604	1689	1848	1831	2107	1561	1456	1641	1933	1990
Line 3	1880	1613	1868	1766	1740	1694	1499	2031	2367	1564	1785	1653	1507	1775	1608	1544	1775	1831	2074	1985	1640

a) Section 1

Distance from Start Point (ft)																					
	0	25	50	75	100	125	150	175	200	225	250	275	300	325	350	375	400	425	450	475	500
Line 1	1777	1727	2045	2124	2164	2411	2010	2062	1756	2212	1289	1999	2158	2067	1992	2091	2039	2219	2156	2790	2189
Line 2	1657	2017	2140	1973	2188	1806	2051	2126	2237	2212	2212	2172	2319	1923	2193	2383	1872	2049	2365	2320	2148
Line 3	2192	2037	2081	2249	2211	2128	2000	1889	2113	1745	1960	1894	2320	2250	2254	2096	2153	2096	2496	2057	1986

b) Section 2

Figure 7.16 – PSPA Modulus (ksi) on Sections 1 and 2 of E4

Distance from Start Point (ft)																					
	0	25	50	75	100	125	150	175	200	225	250	275	300	325	350	375	400	425	450	475	500
Line 1	13.0	10.7	12.5	13.1	9.3	13.1	9.4	9.4	10.3	9.8	8.6	9.3	10.7	13.2	12.8	9.6	9.1	15.7	11.3	11.0	10.9
Line 2	10.6	11.4	11.5	10.5	9.6	11.0	9.5	10.2	12.1	10.3	11.6	9.0	11.5	11.1	11.4	10.1	10.8	13.1	15.1	9.0	10.5
Line 3	13.5	11.3	11.5	17.1	15.6	9.4	11.3	11.5	10.1	12.2	8.9	9.2	10.6	13.7	11.0	8.1	7.4	10.1	11.9	11.4	10.8

a) Section 1

Distance from Start Point (ft)																					
	0	25	50	75	100	125	150	175	200	225	250	275	300	325	350	375	400	425	450	475	500
Line 1	4.4	6.7	6.9	8.3	8.0	7.2	8.5	6.4	6.9	6.9	7.3	8.4	7.6	8.2	7.8	7.3	6.4	6.3	7.1	7.0	6.7
Line 2	4.5	6.8	6.9	7.5	8.7	7.8	7.1	7.7	9.5	7.8	7.6	6.7	7.2	8.1	7.8	7.0	7.1	6.6	6.8	7.2	6.8
Line 3	4.4	6.0	6.9	6.9	7.4	8.0	7.2	6.7	7.8	6.8	6.8	6.5	6.5	6.3	6.6	7.7	7.3	6.7	6.7	6.8	6.7

b) Section 2

Figure 7.17 – IR Results (FFT Ratios) on Sections 1 and 2 of E4

Distance from Start Point (ft)																					
	0	25	50	75	100	125	150	175	200	225	250	275	300	325	350	375	400	425	450	475	500
Line 1	11.5	11.4	11.9	11.1	12.5	11.5	11.4	11.4	11.0	10.2	11.0	11.4	11.5	10.9	10.9	11.6	11.6	12.2	11.9	12.3	12.5
Line 2	11.2	11.1	11.8	12.2	12.0	12.2	11.7	11.7	11.5	11.3	11.4	11.5	11.4	11.0	11.2	11.3	11.3	11.6	11.9	12.7	12.6
Line 3	11.2	10.5	11.6	11.8	12.6	11.9	12.0	12.2	13.0	13.9	13.1	12.2	13.2	12.0	12.1	12.7	12.6	12.6	12.4	12.6	13.0

a) Section 1

Distance from Start Point (ft)																					
	0	25	50	75	100	125	150	175	200	225	250	275	300	325	350	375	400	425	450	475	500
Line 1	20.3	17.1	16.8	15.6	15.3	14.4	14.5	15.1	15.6	15.6	16.1	15.1	15.6	15.0	15.3	15.3	16.9	16.9	15.9	15.1	17.0
Line 2	18.4	20.8	16.5	17.0	16.4	16.3	15.6	15.4	15.3	15.9	16.4	17.5	16.5	15.7	17.5	16.5	17.7	18.0	17.5	16.4	18.0
Line 3	19.8	19.7	16.3	16.1	15.9	14.9	15.6	15.3	15.6	16.6	17.1	16.0	15.5	16.2	16.7	15.4	14.9	15.2	15.6	14.9	16.4

b) Section 2

Figure 7.18 – FWD Deflection Results (mils) on Sections 1 and 2 of E4

Distance from Start Point (ft)																					
	0	25	50	75	100	125	150	175	200	225	250	275	300	325	350	375	400	425	450	475	500
Line 1	152	154	147	158	139	152	155	153	159	171	160	154	152	161	161	151	151	143	147	142	140
Line 2	156	158	148	144	146	143	149	149	152	155	154	152	153	159	155	155	155	150	147	137	138
Line 3	156	167	150	149	139	147	146	143	134	126	134	143	132	146	145	138	139	139	142	139	134

a) Section 1

Distance from Start Point (ft)																					
	0	25	50	75	100	125	150	175	200	225	250	275	300	325	350	375	400	425	450	475	500
Line 1	85	102	104	112	115	122	121	115	112	112	109	117	112	118	115	115	104	104	110	117	103
Line 2	95	84	106	103	107	108	112	114	115	110	107	100	106	112	100	106	99	97	101	107	98
Line 3	88	88	108	109	111	118	112	115	113	105	102	110	113	108	104	114	118	115	112	118	108

b) Section 2

Figure 7.19 – FWD Modulus Results (ksi) on Sections 1 and 2 of E4

Two cores were extracted from Section 1 and two from Section 2 as summarized in Table 7.4. Cores 1 and 2 were separated at a depth of about 10 in. as shown in Figure 7.20. Core 1 was interpreted as marginal or damaged by the IR and PSPA and intact by the others. Core 2 was identified as damaged with all NDT methods. Aside from the lower quality HMA at depths of about 4 in. to 7 in., the reason for this discrepancy is unknown. For cores from Section 2, Core A was categorized as damaged and Core B as intact by all NDT methods (except GPR). It seems that all mechanical tests have a difficulty delineating between low-quality HMA and debonding.

Table 7.4 – Comparison of Core Condition with NDT Results on Sections 1 and 2 of E4

Core #	Location	GPR	PSPA	IR	FWD Deflection	Condition/Comments
Core 1	L2 @ 150 ft from start of Section 1	Intact	Damaged	Marginal	Intact	Intact
Core 2	L3 @ 375 ft from start of Section 1	Damaged	Damaged	Damaged	Damaged	Intact/Low quality HMA
Core A	L1 @0 ft from start of Section 2	Damaged	Damaged	Damaged	Damaged	Intact/Low quality HMA
Core B	L1 @50 ft from start of Section 2	Damaged	Intact	Intact	Intact	Intact Core. Sample length 14½"

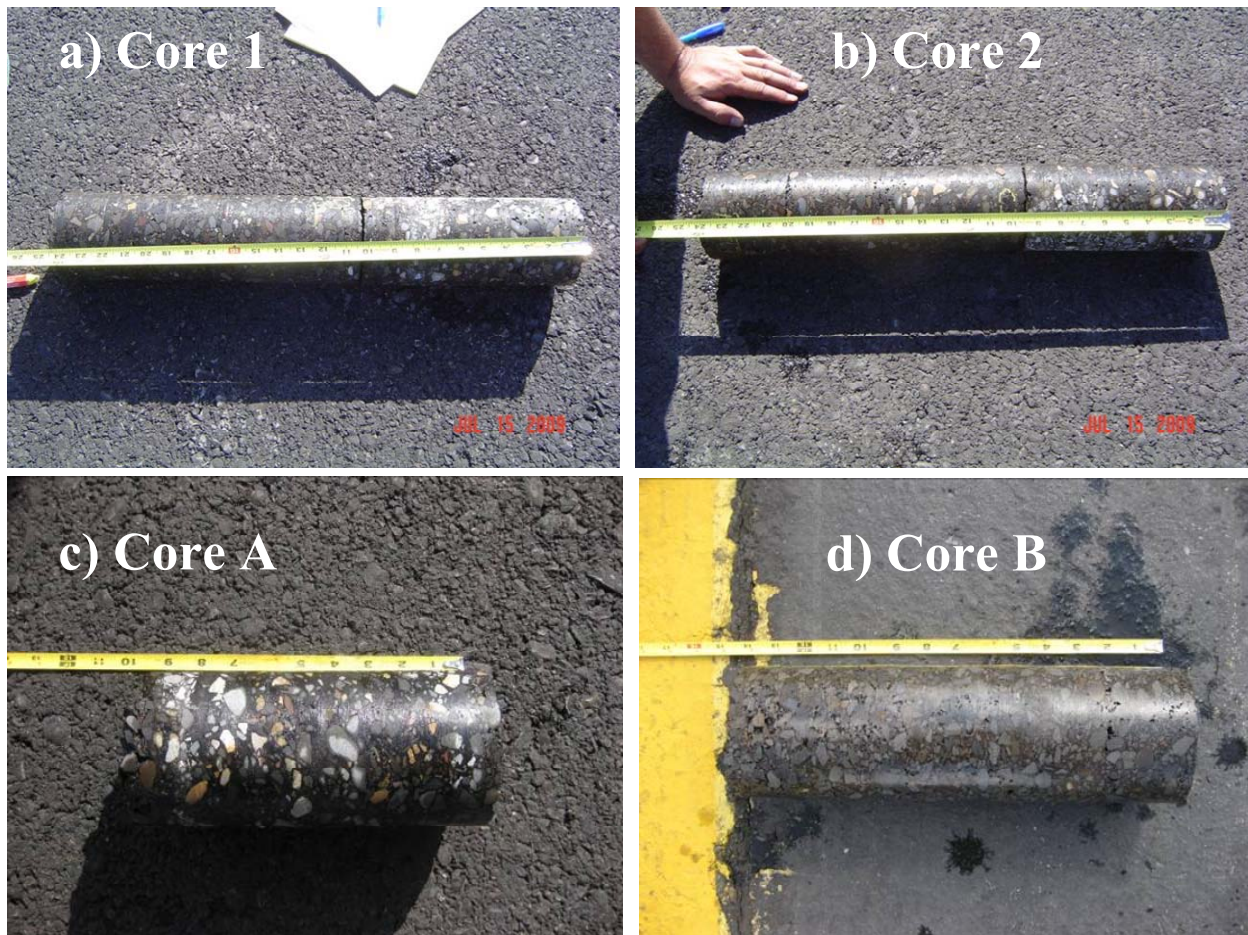


Figure 7.20 – Cores Retrieved from Sections 1 and 2 of E4

Boston Logan International Airport Site

A stretch of Runway 9-27 was tested with several NDT methods concurrent with its rehabilitation in July 2009. Based on previous studies conducted on Runway 9-27 in January 2009, several areas exhibited debonding of the top lift, and in occasions, areas of extreme stripping. Two sections were selected for field testing. Section 1 was located between Taxiways E and C and Section 2 between Runway 15/33 and Taxiway D as illustrated on Figure 7.21.

The test scheme on Section 1 is shown in Figure 7.22a. Seven 700-ft long lines, one located along the centerline and the others 25 ft, 37.5 ft and 50 ft from the centerline on each side, were considered. A total of 29 stations, with a spacing of 25 ft, were investigated on each line. In addition, five core locations previously retrieved were evaluated with some of the NDT methods.



Figure 7.21 – Schematic of BOS and Location of Test Sections

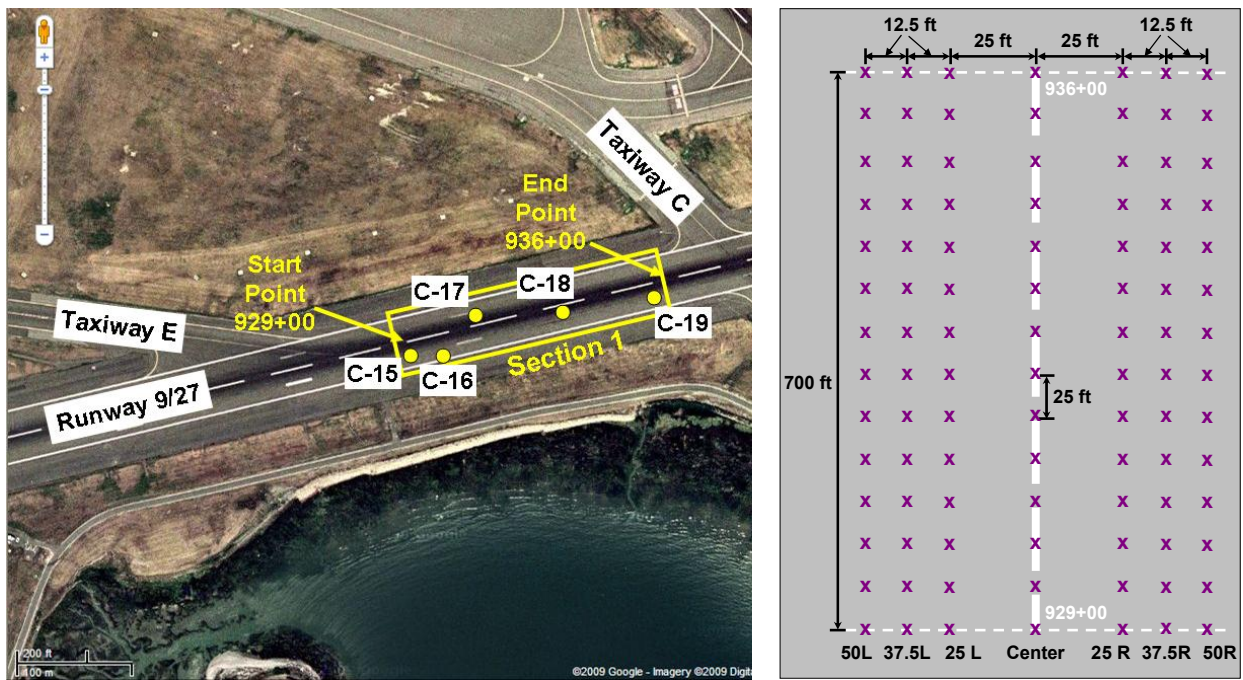


Figure 7.22 – Location of Section 1 and Test Layout

The approximate locations of these cores are also included in Figure 7.22. Some areas of this section exhibited cracking (Figure 7.23a). In addition, the middle 70 ft of the runway had been rehabilitated a few years before showing different asphalt characteristics on the surface mat (see Figure 7.23b).

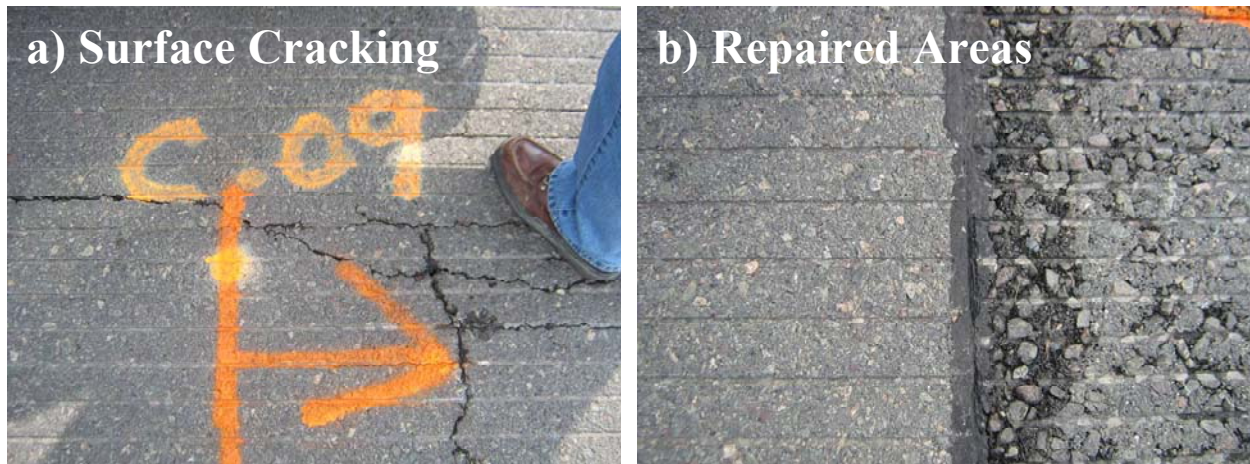


Figure 7.23 – Surface Cracking and Areas with Different Surface Pavement on Section 1

Because of time constraint during field testing and weather condition, only fifteen core locations in Section 2 were evaluated with selected NDT methods. Their approximate locations of the cores are included in Figure 7.24.

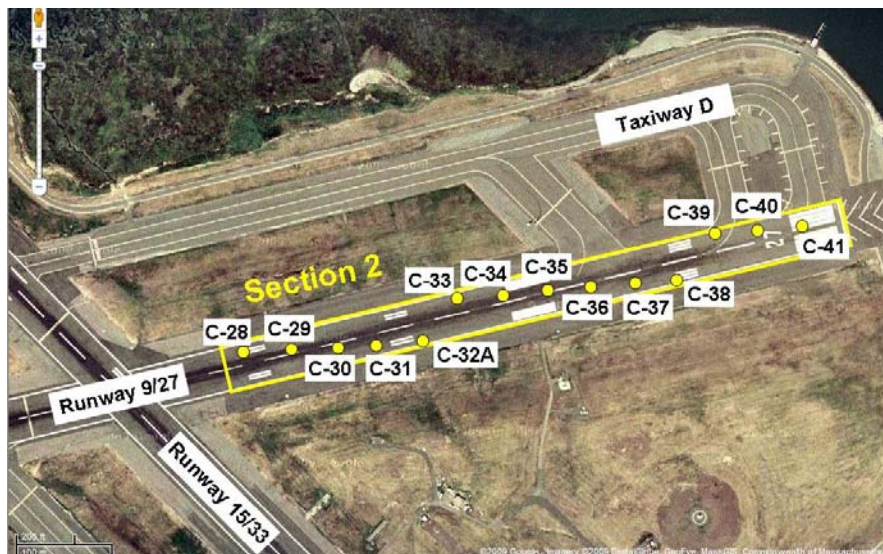


Figure 7.24 – Location of Section 2

Test Results

The selected NDT methods used in BOS were the PSPA and Impulse Response for Sections 1 and 2 and also GPR for Section 1. Results are presented next for the two sections.

Section 1

View from the west end of the section is illustrated on Figure 7.25. The ground-coupled GPR system (1.5 GHz antenna) was used on the seven test lines of Section 1. Post-processed linescans are shown in Figure 7.26. Several horizontal lines associated with the HMA interfaces are marked. Three HMA lifts are observed on all lines at depths of about 2 in., 4 in. and 6 in. Some of these interfaces show strong reflections that might indicate the presence of trapped moisture, stripping or debonding particularly for Lines 37.5'L and 50'R. In addition, two irregularities are found. The first one appeared on all lines at a distance of approximately 600 ft from the start and the other at about 450 ft and on Lines 25'L, Center and 25'R. The GPR traces at the five core locations are depicted in Appendix F.



Figure 7.25 – Field Picture of Section 1

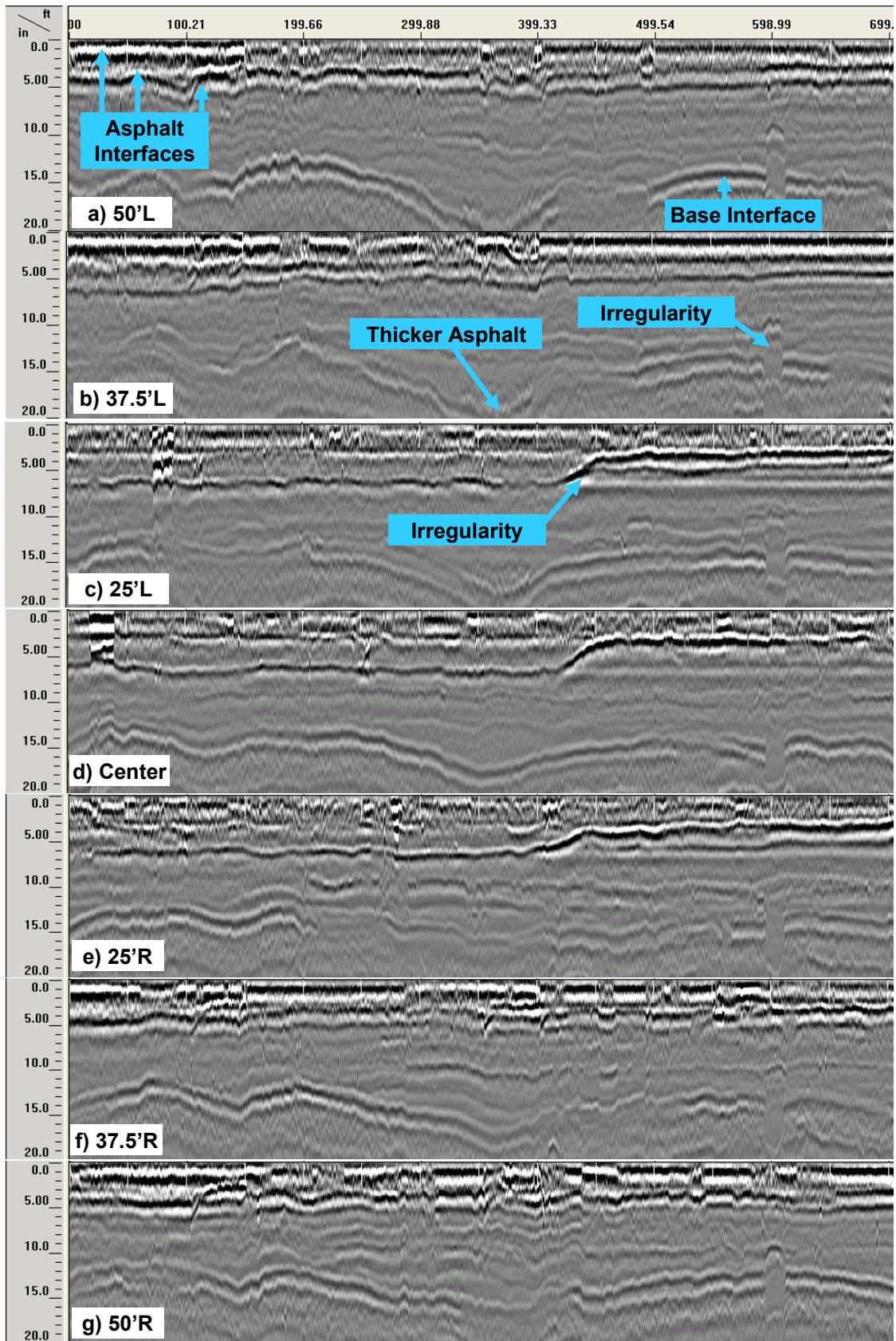


Figure 7.26 – Post-processed GPR Linescans on Section 1

The PSPA and IR results are illustrated in Figures 7.27 and 7.28 for the seven lines of Section 1. Based on both methods, the worst conditions are observed mostly about the centerline. Most of the points on these lines were identified as marginal or damaged. Dispersion curves showed stronger reduction in modulus for points about the centerline of the runway (see Appendix F).

		Test Location																												
		92900	92925	92950	92975	93000	93025	93050	93075	93100	93125	93150	93175	93200	93225	93250	93275	93300	93325	93350	93375	93400	93425	93450	93475	93500	93525	93550	93575	93600
L50		807	1,021	930	1,072	790	1,798	1,383	1,607	787	1,614	1,384	1,792	1,712	1,873	1,815	1,655	1,059	1,838	1,751	1,664	1,896	1,908	1,942	1,850	816	2,287	2,213	1,941	1,998
L37.5		799	1,188	556	1,082	823	635	1,150	997	1,601	1,110	1,998	897	814	931	601	554	548	2,036	2,129	2,129	1,536	2,187	2,226	1,991	2,109	2,179	2,321	2,036	1,937
L25		963	790	823	1,407	1,007	926	963	1,059	867	1,016	847	921	1,003	839	1,141	891	911	771	832	882	902	659	971	1,219	1,129	1,030	1,080	991	1,055
0		402	780	329	385	642	393	298	436	338	549	597	402	680	613	289	565	683	596	247	887	1,259	974	414	358	277	398	277	256	305
R25		690	975	259	594	549	716	581	489	553	654	737	655	682	1,178	609	573	524	425	488	272	542	359	553	569	554	418	375	368	337
R37.5		1,815	1,334	1,539	1,497	1,456	376	2,423	2,024	1,269	1,018	2,007	1,934	1,726	352	701	1,402	415	1,084	1,564	930	1,634	1,778	1,634	1,426	2,075	1,964	1,557	1,425	1,181
R50		1,464	1,360	1,256	1,194	1,659	1,738	1,615	1,677	1,811	1,331	1,180	1,319	1,319	2,089	1,416	1,978	1,402	2,088	1,130	2,432	1,735	2,235	2,012	2,012	1,554	2,099	1,669	2,124	1,931

Figure 7.27 – PSPA Modulus (ksi) on Section 1

		Test Location																												
		92900	92925	92950	92975	93000	93025	93050	93075	93100	93125	93150	93175	93200	93225	93250	93275	93300	93325	93350	93375	93400	93425	93450	93475	93500	93525	93550	93575	93600
L50		6.21	3.79	1.96	2.49	2.70	3.65	4.82	5.71	5.68	7.49	7.37	4.58	6.76	4.87	5.77	5.46	7.44	5.42	4.66	6.23	8.38	6.44	4.91	7.20	6.26	5.26	7.50	6.62	4.33
L37.5		4.66	5.15	4.36	3.28	6.04	3.46	6.57	6.80	9.56	9.08	6.10	4.42	3.51	5.21	4.10	3.28	1.97	5.79	5.19	5.70	6.08	6.53	6.24	4.97	5.52	4.50	6.09	6.17	6.89
L25		1.13	2.77	2.89	1.32	1.87	1.75	2.81	1.83	2.20	1.54	2.54	3.24	3.69	4.17	2.84	3.41	3.59	2.76	3.38	3.06	7.14	2.21	4.22	8.27	4.53	6.24	6.75	3.96	4.16
0		0.56	0.91	1.87	1.49	0.96	0.44	0.98	0.51	0.69	0.71	0.59	0.87	0.89	0.20	0.41	0.50	0.84	0.49	0.21	0.47	0.36	0.33	0.37	1.25	0.19	0.40	0.14	0.44	0.42
R25		0.87	0.60	0.71	0.52	0.63	1.03	0.34	1.78	0.55	0.41	1.03	1.57	2.28	1.83	1.01	4.04	0.94	0.36	0.81	0.62	0.60	0.41	1.48	0.74	0.68	0.58	0.42	0.45	1.32
R37.5		5.01	4.36	1.71	1.32	0.72	0.84	2.18	2.26	2.10	3.10	4.72	5.39	1.73	1.46	1.37	2.11	2.64	3.31	2.20	3.94	4.85	4.55	7.54	4.76	4.21	3.85	4.34	6.71	5.48
R50		2.30	3.49	3.17	3.92	0.89	1.93	3.25	6.17	2.48	3.88	2.67	3.44	2.74	5.50	4.26	7.26	2.90	4.80	1.75	4.50	2.51	4.47	4.22	3.92	9.15	2.99	2.65	5.03	6.22

Figure 7.28 – IR Results on Section 1

The conditions of the five cores previously retrieved are compared with the interpretation of the results from NDT devices in Table 7.5. The conditions of Cores C-15 (intact core) and C-18 (debonded core at 3 in.) as shown in Figure 7.29 correlated well with the results with the

PSPA and IR method. Some discrepancy was found on core C-17 (debonded at 6 in. depth), since PSPA showed marginal condition and IR intact condition, respectively.

Table 7.5 – Comparison of Core Conditions with NDT Results on Section 1

Core #	Location	GPR	PSPA	IR	Condition/Comments
C-15	929+50 @40'R	Intact	Intact	Intact	Intact
C-16	931+00 @60'R	Damaged	N/A	N/A	Intact
C-17	932+50 @10'L	Damaged	Marginal	Intact	Debonding at 6 in.
C-18	934+00 @10'R	Damaged	Damaged	Damaged	Debonding at 3 in.
C-19	935+50 @40'R	Damaged	N/A	N/A	Debonding at 7 in.

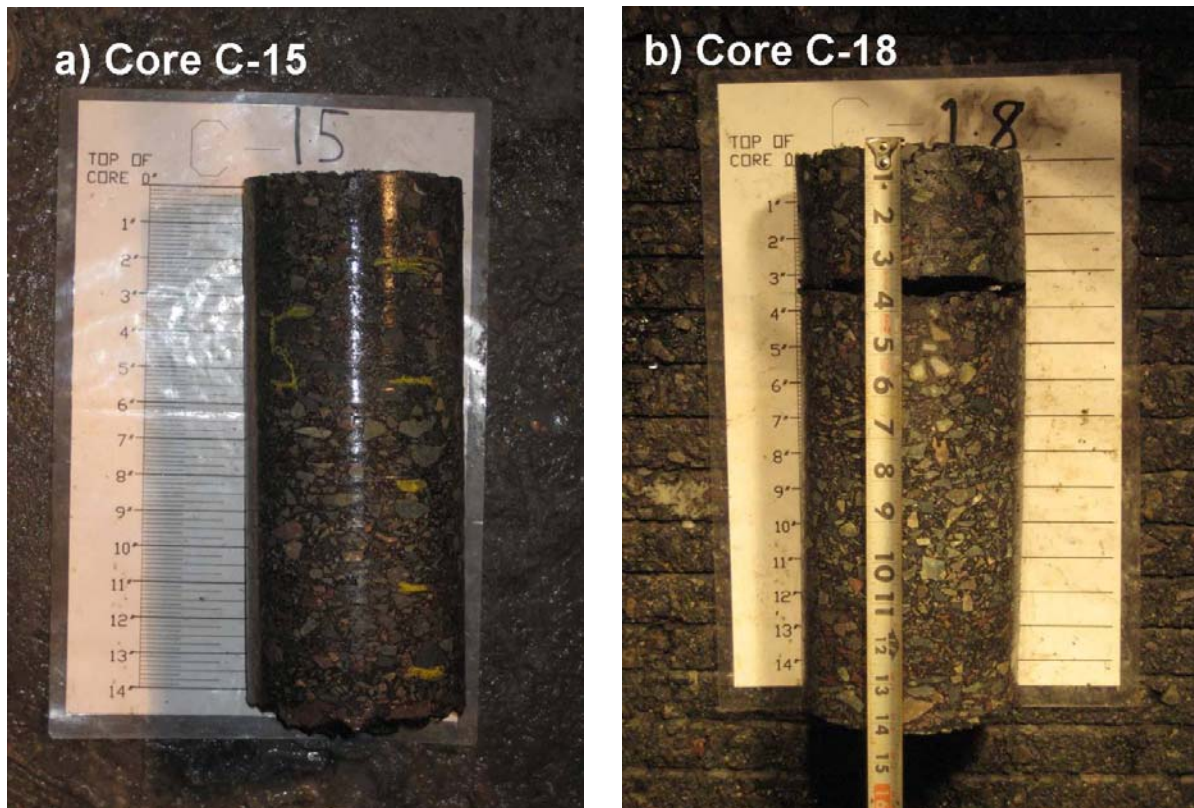


Figure 7.29 – Cores Retrieved from Section 1

Section 2

PSPA and IR results for the 15 core locations investigated are illustrated in Figure 7.30. All tests were carried out within 12 in. of the core locations. The GPR could not be used on this section because of the surface moisture present due to a rainfall.

Table 7.6 contains a comparison of the interpreted conditions from NDT methods and the actual conditions of the cores (see Figure 7.31). Most of the cores were retrieved as intact, with core lengths ranging from 13 in. to 18 in. The majority of the intact cores were classified as intact by the two NDT methods. For cores that presented debonding or stripping, the correlations were for the most part good. In general, the rate of success of the methods in the field was similar to those observed on the controlled section.

Core #	PSPA Modulus, ksi	IR FFT Ratios
C28	812	5.3
C29	1696	2.6
C30	377	2.7
C30A	812	5.8
C31	1613	9.4
C32A	966	8.3
C33	1029	9.6
C34	1197	6.9
C35A	343	4.8
C36	1278	8.2
C37	1542	4.9
C38	1599	3.7
C39	687	3.1
C40	814	2.0
C41	1391	4.8

Figure 7.30 – PSPA and IR Results on Section 2

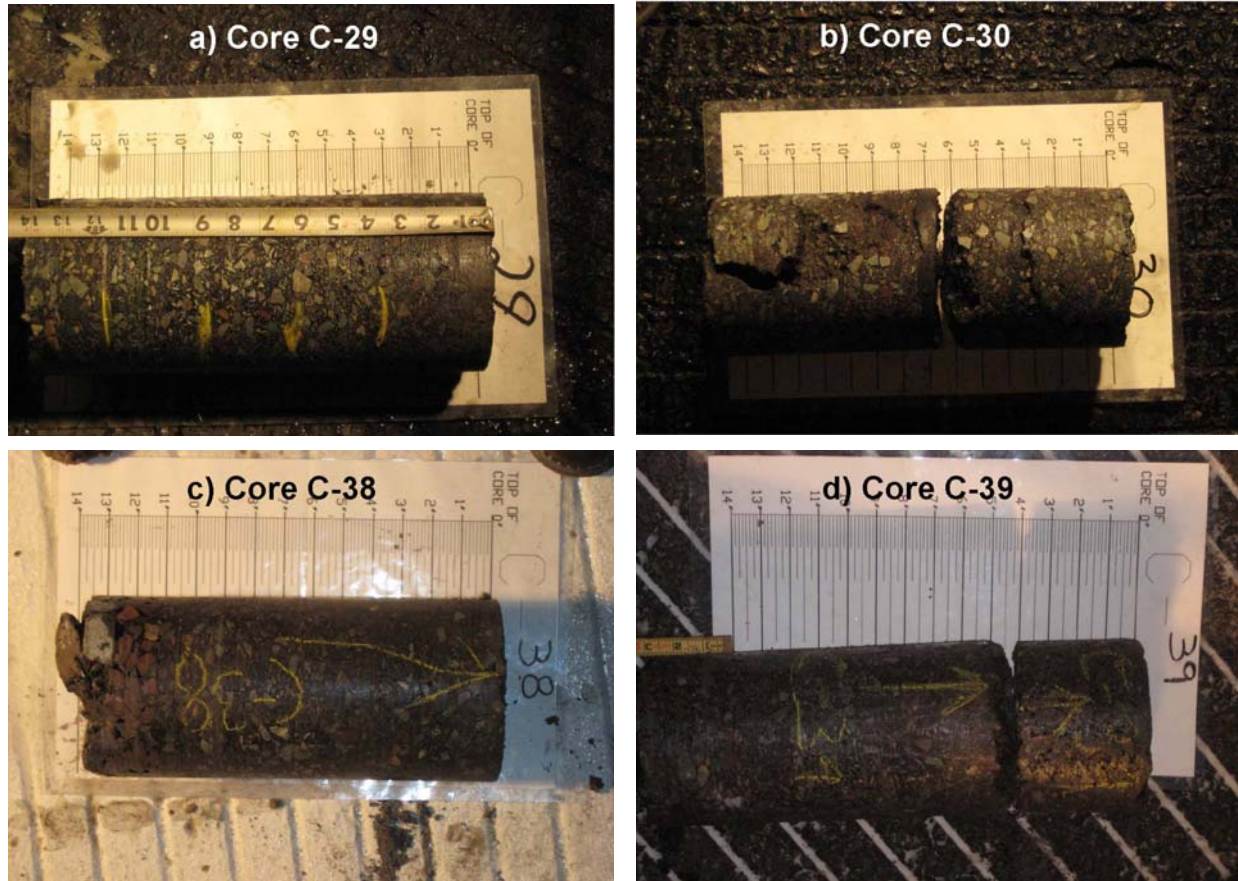


Figure 7.31 – Cores Retrieved from Section 2

These two case studies for the most part confirmed the reasonableness of the conclusions drawn from the controlled study. They also shed some light on some of the complexities of field testing. It seems that all mechanical NDT methods (PSPA, IR and FWD) can detect shallow severely debonded areas with reasonable certainty. The results from the GPR seem to be ambiguous. For complex pavement sections, the effectiveness of the FWD somewhat diminishes. One lesson learned is that the delineation of the low-quality HMA from debonded area is difficult from all mechanical NDT methods. More sophisticated processing of the data should be considered to see whether this problem can be overcome.

Table 7.6 – Comparison of Core Conditions with NDT Results on Section 2

Core #	Location	PSPA	IR	Condition/Comments
C-28	949+00 @40'L	Marginal	Intact	Intact
C-29	950+50 @10'L	Intact	Damaged	Intact
C-30	952+00 @10'R	Damaged	Damaged	Debonding at 6 in.
C-30A	952+05 @10'R	Marginal	Intact	Intact
C-31	953+50 @40'R	Intact	Intact	Intact
C-32A	954+95 @65'R	Intact	Intact	Intact
C-33	956+50 @60'L	Intact	Intact	Intact
C-34	958+00 @40'L	Intact	Intact	Intact
C-35A	959+50 @10'L	Damaged	Intact	Debonding at 7 in.
C-36	961+00 @10'R	Intact	Intact	Intact
C-37	962+50 @40'R	Intact	Intact	Core rig malfunctioned at core had to be stopped at 9 ½".
C-38	964+00 @60'R	Intact	Marginal	Intact
C-39	965+50 @60'L	Marginal	Marginal	Debonding at 4 in.
C-40	967+00 @40'L	Marginal	Damaged	Debonding at 4 in.
C-41	968+50 @10'L	Intact	Intact	Debonding at 4 in.

CHAPTER 8 – EVALUATION OF NDT METHODS FOR DETECTING DELAMINATION OF HMA

The technical and practical parameters that most likely affect the successful detection of delamination with NDT methods include the accuracy, reproducibility, detectability threshold, speed of data collection, speed of data analysis, and the sophistication of data analysis. The approach applied to evaluate each of these parameters is briefly discussed in this chapter. Each of the criteria considered was assigned an individual ranking and a relative weight. The resulting weighted averages were used to rank the potential success of each method.

Accuracy

The accuracy was judged by correlating the response of the NDT methods to the degree of debonding induced in the sections. The accuracy of each method was determined using the criteria summarized in Table 8.1. The success was evaluated in percentage of correct assessment of the three levels of debonding considered. As an example, if the FWD returned an HMA modulus greater than the average minus -0.5 standard deviation (denoted as green in graphs in Chapter 6) for a given point, a value of 1 (or 100% success) was assigned to that point.

Table 8.1 – Criteria Used to Evaluate NDT Accuracy

Condition Measured with Device	Ranking Values								
	Intact			Full-Debonding			Partial-Debonding		
	Green ^a	Yellow ^b	Red ^c	Green ^a	Yellow ^b	Red ^c	Green ^a	Yellow ^b	Red ^c
Intact	1	0	0	--	--	--	--	--	--
Full-Debonding	--	--	--	0	0.5	1	--	--	--
Partial-Debonding	--	--	--	--	--	--	0	1	1

a Parameters above average minus one-half standard deviation

b Parameters between average minus one-half standard deviation and average minus one standard deviation

c Parameters below the average below one standard deviation (substantially less stiff than the control)

However, if the estimated modulus was less than the average minus -0.5 standard deviation (denoted as yellow or red in graphs in Chapter 6), a value of 0 (or a false positive) was assigned to it.

The percentage of success for every method and for every level of bonding was obtained by adding the values from all points in a given debonding category to obtain a score. This score was divided by the total number of points to define the degree of success. As such, for the case of the cool weather FWD deflection testing, the degree of success for detecting partial debonding and full-debonding in cool weather testing were about 65% and 50%, respectively. For the ground-coupled GPR, observed lengths of bonding/debonding on each line corresponding to each bonding level were measured from the linescans and were divided by the actual length corresponding to a level of debonding to obtain the degree of success.

Table 8.2 contains a summary of the degrees of success of the feasible techniques based on the criteria described above. Almost all methods interpret the intact points at a degree of better than 80%. The probability of success of detecting the fully-debonded and partially-debonded sections varied from 26% for GPR to about 70%.

Based on these results, the degree of success of different methods for detecting different defect types were ranked between 0 and 5 using the criteria in Table 8.3. The aggregate ranking of each method for different testing temperature was then obtained by considering the weighted average of the rankings for each bonding category as shown in Table 8.2.

Since detecting the fully-debonded areas are the most critical, a weight factor of 3 was assigned to the ranking for that bonding condition, while a weight of 1 was assigned to the ranking of the intact points and 3 to the ranking of the partially-debonded areas. The major observation from these rankings is that all methods work better in cool weather. Based on the

Table 8.2 – Ranking of Probability of Success of NDT Methods to Detect Delamination

Device/ Analysis Method	Test Period	Degree of Bonding	Probability of Success	Ranking by Degree of Bonding	Ranking by Test Period	Overall Ranking of Technology
PSPA/ USW	Cool	Intact	86%	5	3.1	3
		Full-debonding	60%	3		
		Partial-debonding	55%	3		
	Hot	Intact	82%	5	1.9	
		Full-debonding	60%	3		
		Partial-debonding	37%	1		
FWD/ Deflection	Cool	Intact	89%	5	3.1	3
		Full-debonding	49%	3		
		Partial-debonding	67%	3		
	Hot	Intact	82%	5	1.9	
		Full-debonding	52%	3		
		Partial-debonding	44%	1		
FWD/ Modulus	Cool	Intact	87%	5	1.9	2
		Full-debonding	70%	3		
		Partial-debonding	33%	1		
	Hot	Intact	61%	3	1.2	
		Full-debonding	54%	3		
		Partial-debonding	28%	0		
IR/ Flexibility	Cool	Intact	88%	5	3.8	4
		Full-debonding	72%	5		
		Partial-debonding	51%	3		
	Hot	Intact	89%	5	1.9	
		Full-debonding	67%	3		
		Partial-debonding	47%	1		
GPR/ Ground Coupled	--	Intact	90%	5	0.9	1
		Full-debonding	26%	0		
		Partial-debonding	41%	1		

Table 8.3 – Ranking Criteria for Accuracy of Different Methods

Probability of Detection		Ranking
Minimum	Maximum	
70	100	5
50	70	3
35	50	1
0	35	0

average of the rankings of the cool and hot weather tests, as reflected in Table 8.2, the impulse response method is the most accurate followed by the USW and FWD deflections. Interestingly, the backcalculation of the HMA layer modulus negatively impacted the accuracy of that method.

Most of the 26% to 40% of GPR detected debonded areas correspond to the defects that were constructed with either clay or talcum powder with significantly different dielectric constant than HMA. In practical terms, this indicates that the GPR may be quite successful, if moisture penetrates in the interface of the debonded layers.

Several other methods that were not as successful as anticipated in our initial work plan were not extensively tested and were not considered in the ranking.

Reproducibility

The reproducibility associated with different test procedures was quantified by conducting triplicate tests with each NDT device. Based on the degree of success of the methods, only the reproducibility of the FWD, PSPA and IR were evaluated. The GPR has shown good repeatability in many applications other than detecting debonding.

The results of the reproducibility tests for the three methods and for the cool and hot weather testing are summarized in Table 8.4. The coefficient of variation from the results of the three independent tests at each point was used to describe the reproducibility. However, for the

Table 8.4 – Reproducibility of NDT Methods

NDT Device	Weather		Coarse Surface Mix					Fine Surface Mix					Ranking
			S1	S2	S3	S4	S5	S6	S7	S8	S9	S10	
IR (FFT Ratio)	Cool	COV	4.3%	4.4%	4.6%	4.2%	3.7%	4.2%	6.0%	4.9%	5.3%	4.5%	5
		Avg.	4.2%					5.0%					
	Hot	COV	4.9%	5.9%	4.5%	5.3%	5.5%	4.7%	4.6%	6.5%	6.3%	5.6%	
		Avg.	5.2%					5.5%					
PSPA (Modulus)	Cool	COV	9.8%	9.4%	8.6%	9.6%	8.7%	9.8%	8.9%	8.6%	8.2%	9.0%	3
		Avg.	9.2%					8.9%					
	Hot	COV	6.8%	7.0%	8.6%	8.4%	7.7%	8.6%	10.5%	10.0%	9.1%	8.5%	
		Avg.	7.7%					9.3%					
FWD (Deflections)	Cool	COV	0.6%	0.5%	0.4%	0.5%	0.8%	0.4%	0.4%	0.5%	0.6%	0.8%	5
		Avg.	0.6%					0.6%					
	Hot	COV	1.3%	1.7%	1.5%	1.7%	1.4%	1.5%	1.7%	1.6%	1.2%	1.4%	
		Avg.	1.5%					1.4%					
FWD (Modulus)	Cool	COV	9.6%	6.8%	5.7%	6.1%	12.1%	1.8%	1.7%	1.9%	6.5%	5.6%	5
		Avg.	8.1%					3.5%					
	Hot	COV	4.9%	4.2%	3.8%	3.5%	3.9%	6.0%	4.5%	4.6%	7.2%	4.6%	
		Avg.	4.1%					5.4%					

FWD, because of the logistics, the last three deflections measured without moving the FWD were used. This practice slightly favors the reproducibility of the FWD reported. Rocha et al. (2004) amongst others have shown that the reproducibility of FWD without moving is better than 2% (as is the case here) and better than 5% when the FWD is resituated on a given point. In general, the reproducibility of all methods is better than 10% which is quite reasonable. IR results demonstrated an average COV of about 5%. Based on the average COV values, a ranking is assigned to the reproducibility of each method in Table 8.4.

Detectability Threshold

As reflected in Chapter 4, aside from the 4 ft by 9 ft (1.2 m by 3 m) debonded areas, smaller areas varying from 2 ft by 2 ft (0.6 m by 0.6 m) to 1 ft by 1 ft (0.3 m by 0.3 m) and 0.5 ft by 0.5 ft (0.15 m by 0.15 m) were also introduced in the sections. The outcomes of different technologies on different size defects in terms of detectability were compared to establish the detectability threshold. A comprehensive table that provides the probability of detection as functions of defect size, bonding condition, type of mix and weather condition, is included in Appendix G. Those results are summarized in Figure 8.1. As the defects become smaller and deeper, the predictive power of the selected methods diminishes.

To better quantify the detectability threshold, the percent of defects identified as a function of size, depth and severity were ranked based on the criteria described in Table 8.3. Those results are presented in Table 8.5. A weight factor was assigned to each severity and depth based on how critical they are to the safe operation of an airfield, with 4 being the weight for the shallow fully debonded points and 1 being the weight for the deep partially debonded points. Based on Table 8.5, the degree of success for detecting the 1 ft and 0.5 ft debonded areas are almost nil independent of the technology. The 4 ft by 9 ft debonded areas, especially the shallow fully-debonded ones, can be detected by most technologies with reasonable certainty; while the chance of detecting the 2 ft debonded areas are small. Given the fact that the most feasible technologies are point tests, it can be concluded that the debonded area should be at least 4 ft (1.2 m) in dimensions to be detectable.

Based on the analysis provided in Table 8.5, the Impulse Response and USW methods in relative terms rank somewhat better than FWD for detecting the large debonded areas and

significantly better than FWD for the 2 ft defects. As such, the detectability threshold of the IR and PSPA methods are ranked as 3 and FWD as 1.

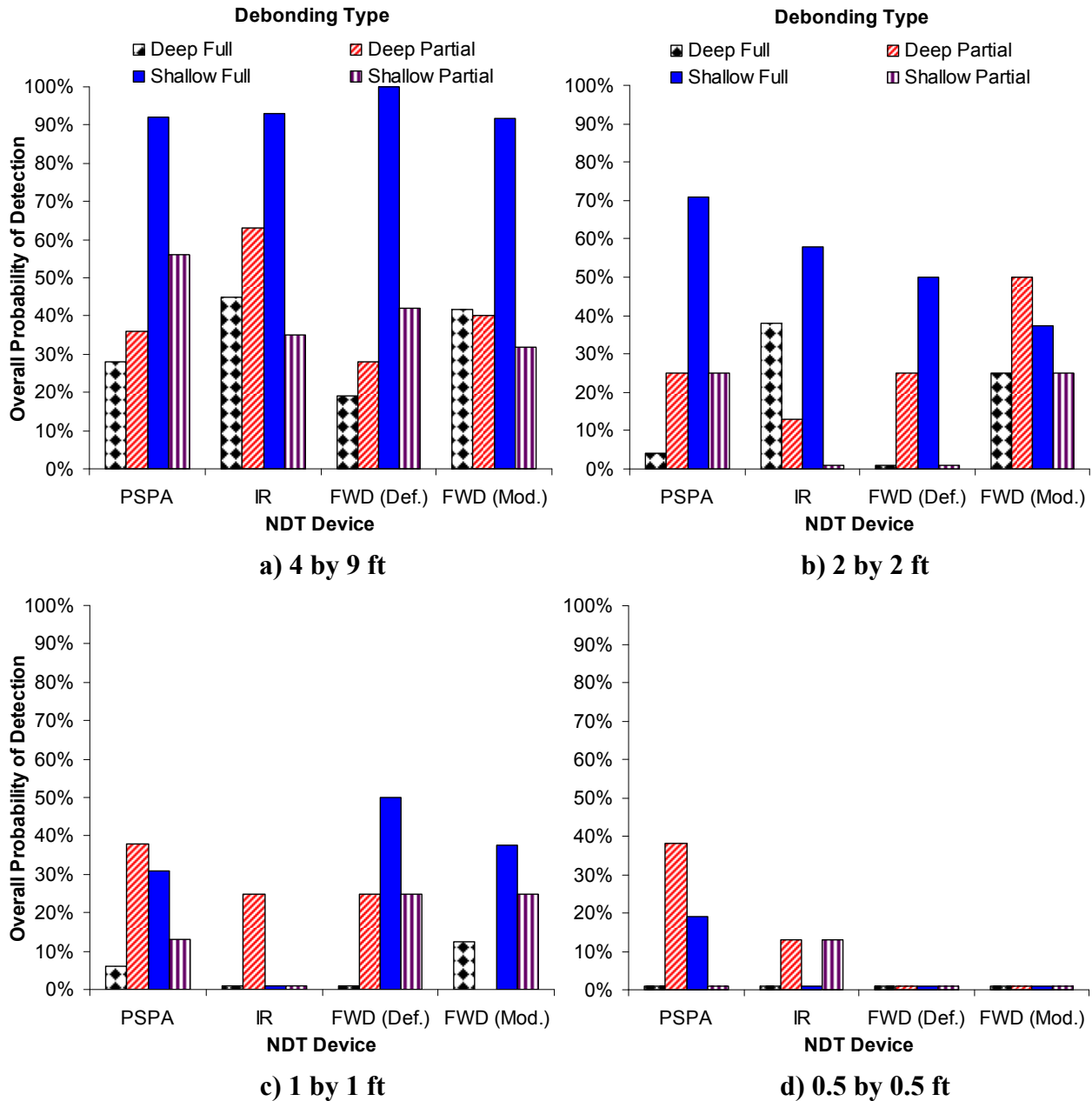


Figure 8.1 – Overall Probability of Detection of NDT Methods

Table 8.5 – Ranking of Detectability Threshold

Defect Size (ft)	Defect Type	Weight Factor	Detection Ranking				Average for all Technologies
			PSPA	IR	FWD (Def.)	FWD (Mod.)	
4 by 9	Deep Full	2	0	1	0	1	0
	Deep Partial	1	1	3	0	1	1
	Shallow Full	4	5	5	5	5	5
	Shallow Partial	3	3	1	1	0	1
	Overall	--	3.0	2.8	2.3	2.3	2.4
2 by 2	Deep Full	2	0	1	0	0	0
	Deep Partial	1	0	0	0	1	0
	Shallow Full	4	5	3	1	1	3
	Shallow Partial	3	0	0	0	0	0
	Overall	--	2.0	1.4	0.4	0.5	1.2
1 by 1	Deep Full	2	0	0	0	0	0
	Deep Partial	1	1	0	0	0	0
	Shallow Full	4	0	0	1	1	0
	Shallow Partial	3	0	0	0	0	0
	Overall	--	0.1	0.0	0.4	0.4	0.0
0.5 by 0.5	Deep Full	2	0	0	0	0	0
	Deep Partial	1	1	0	0	0	0
	Shallow Full	4	0	0	0	0	0
	Shallow Partial	3	0	0	0	0	0
	Overall	--	0.1	0.0	0.0	0.0	0.0

Speed of Data Collection

The speed of data collection for each NDT method is summarized on Table 8.6. For the methods that collect data in a continuous form, the time needed to complete a 100 ft (30 m) longitudinal line is reported. For the methods that collect point by point data, the time required to complete a test is shown. In addition, the time needed to complete the setup of each device before testing is included for reference. Based on this information a ranking of each technology is also included in Table 8.6. Continuous methods were assigned a value of 5 (high) and point by point methods received a value of 3 (medium) since the time needed to collect a point was less than two minutes.

Table 8.6 – Ranking of Speed of Data Collection

NDT Device	Setup Time, minutes	Point Test, seconds	Ranking
PSPA	10	15	3
FWD	20	120	3
IR	15	30	3
Thermal	1	10	5
GPR. Ground Antenna	45	120*	5
GPR. Air Antenna	30	60*	5

* Time needed to collect a longitudinal line on the small scale study (100 ft)

Speed of Data Analysis

The time to complete the analysis of the raw data for each methodology is reported on Table 8.7 as a way of comparison of the speed of analysis for all NDT methods. This parameter also serves as an estimator of the difficulty and experience needed to complete the data analysis. Similar to other parameters, a ranking from 1 to 5 was given to each method. The analysis and interpretation times can be significantly improved when the methods are accepted and automated for the purpose of day to day use. Most of the analysis time for most methods was actually arranging and organizing the results that can be reduce to a minimum if the GPS coordinates of the test points were known and a custom tool were developed to conveniently visualize them.

Table 8.7 – Ranking of Speed of Data Analysis and Interpretation

NDT Device	Analysis Time of Raw Data, sec	Interpretation Time to Assess Debonding, days	Ranking
PSPA	Real Time	2	3
FWD	Real Time	2	3
IR	Real time	2	3
Thermal	Real Time	1	5
GPR. Ground Antenna	1 day	3	1
GPR. Air Antenna	1 day	3	1

Sophistication of Data Analysis

Complexity of data analysis was estimated and summarized in Table 8.8. This was achieved by asking UTEP personnel with different levels of experience to conduct the analysis. The following three levels of experience were considered: 1) an expert, 2) a person that is familiar with the method (intermediate user), and 3) a new user that was just trained. A ranking of 1 (low), 3 (average) or 5 (high) was correspondingly selected. Reduced data from each of the selected personnel was compared and the difficulties associated with each device or reduction software is reported as well.

Table 8.8 – Ranking of Sophistication of Data Analysis Needed and Difficulties Found

NDT Device	Experience Level Needed	Ranking	Difficulties Found
PSPA	Intermediate User	3	Setting parameters can be initially confusing.
FWD	Intermediate User	3	Different parameters on the backcalculation software may lead to considerably different results.
IR	Intermediate User	3	Initial confusion with frequency-domain analysis.
Thermal	New User	5	None.
GPR	Expert	1	Reduction software complicated to use and interpretation not always intuitive.

Overall Ranking of Candidate NDT Methods

The parameters described above were given relative weights to determine an overall ranking for different methods. The relative weights, which are similar to those used in Phase I of this project to conceptually rank the methods, are summarized in Table 8.9. The first three parameters were given higher weights since they are the most important factors in deciding whether a method is appropriate or not. Accuracy was determined as the most important parameter. Time required for data collection was weighted slightly higher than other practical

parameters since the timely collection of information deemed important to the day-to-day operation of an airfield. The data analysis and data presentation is rather important but they were not deemed as important as other practical items.

Table 8.9 – Utility Weights for Selection of NDT Methods

Evaluation Category		Relative Weight
1	Accuracy	0.35
2	Reproducibility	0.20
3	Detectability Threshold	0.20
4	Speed of Data Collection	0.15
5	Speed of Data Analysis	0.05
6	Sophistication of Data Analysis	0.05
Total		1.00

Based on the ranking in Table 8.10, the Impulse Response is ranked the highest, with the PSPA and FWD using the deflection of the first sensor ranking closely with it. The ground penetrating radar and the thermal imaging, which have the potential for rapid data collection, do not seem as feasible as the others.

Table 8.10 – Final Ranking of Feasible NDT Methods

Method \ Parameter	Accuracy	Reproducibility	Detectability Threshold	Speed of Data Collection	Speed of Data Analysis	Sophistication of Data Analysis	Ranking
	Weight Factor						
	0.35	0.2	0.2	0.15	0.05	0.05	
PSPA/ Ultrasonic Surface waves	3	3	3	3	3	3	3
FWD Deflection	3	5	1	3	3	3	3
FWD Modulus	2	3	1	3	3	3	2
Impulse Response	4	5	3	3	3	3	4
GPR Ground Coupled	1	5	1	5	1	1	2

CHAPTER 9 – SUMMARY, CONCLUSIONS AND RECOMMENDATIONS

Summary

A number of NDT methods were evaluated in term of their utility to detected debonding of HMA layers. Based on an extensive information search, the following technologies were considered:

- Falling Weight Deflectometer (FWD)
- Ground Penetrating Radar (GPR)
- High Frequency Sweep (HFS)
- Impact Echo (IE)
- Impulse Response (IR)
- Light Weight Deflectometer (LWD)
- Stiffness Gauge (SG)
- Thermal Imaging (TI)
- Ultrasonic Surface Waves (USW)

A 10 ft by 130 ft (3 m by 40 m) pavement section was constructed with two different mixes specifically to evaluate these methods. The test section contained the following defects:

- Extensively delaminated
- Shallow fully-debonded
- Shallow partially-debonded
- Deep fully-debonded
- Deep partially-debonded

Based on a preliminary study, the methods that were deemed the most promising were the following:

- Falling Weight Deflectometer (FWD)
- Ground-Coupled Ground Penetrating Radar (GPR)
- Impulse Response (IR)
- Ultrasonic Surface Waves (USW)

These methods were extensively studied in cool and hot weather for a number of technical and practical parameters that deem necessary for a tool be considered successful for assessing debonding. These parameters in the order of their perceived significance included the following:

1. Accuracy
2. Reproducibility
3. Detectability Threshold
4. Speed of Data Collection
5. Speed of Data Analysis
6. Sophistication of Data Analysis

Based on this evaluation, the three most promising technologies are the Impulse Response, Ultrasonic Surface Waves and the Falling Weight Deflectometer.

Based on field testing at two airports, the observations made above seem to be quite reasonable in actual field conditions.

Conclusions

Based on this study, the following conclusions can be drawn.

- **Accuracy**
 - No single method could detect all the defects incorporated in the test section.
 - The most critical defects, extensive delamination and shallow fully-debonded areas, could be detected with a degree of success of about 90% by all three methods.
 - The shallow partially debonded areas, which is the most desirable to detect, was detected at a rate of success of 60% by the PSPA and about 30 to 40% by the other two methods.
 - The Impulse Response method performed best for detecting deep fully-debonded areas, however, the detection of the deep partially debonded areas is rather difficult. The rates of success of the three devices to detect deep debonding were 30% to 45%.
 - All methods can detect debonding more readily in the cool weather than the hot weather.
- **Reproducibility**
 - The short term reproducibility of all methods is reasonably good and varies between 5 to 10%.
 - In terms of long term reproducibility (yielding the same conclusions between cool and hot weather tests), the Impulse Response and PSPA performed more favorably than FWD.
- **Detectability Threshold**
 - The practical size of the debonded area that can be detected is about 4 ft (1.2 m).
 - None of the methods could detect defects less than 2 ft in dimensions.
 - PSPA and IR because of their size had higher detectability threshold than the FWD.

- **Speed of Data Collection**

- Data collection can be carried out in less than 2 minutes with all three devices.
- The PSPA and IR device can collect data at twice the rate of an FWD.

- **Speed of Data Analysis and Interpretation**

- All three devices provide the analysis in real time.
- The current data interpretation is rather straight forward for the three methods.

- **Sophistication of Data Analysis**

- The data analysis with the IR and PSPA are the most sophisticated yet the most certain.
- The FWD analysis is rather straightforward, but an experienced analyst is needed to minimize the uncertainty in the backcalculation.

Recommendations

- Based on extensive numerical analyses (not included in this study), it is possible to implement more sophisticated yet practical analyses, at least for the USW and IR methods. This option should be pursued in future studies.
- For the promising techniques, the delineation between low quality HMA and debonded areas is difficult since the detection of debonding is based on relative changes in parameters in the feature tested. The utilization of more sophisticated analyses should address this shortcoming.
- Since the most promising methods are based on spot tests, the feasibility of developing more automated means of performing these tests should be explored. This can range from autonomous scanning devices to rolling sensors.

- Most of the interoperation time for all methods is associated with tedious development of visual tools, such as contour maps. By adding a GPS unit and developing custom-made visualization routines, this matter can be remedied.
- Since the results of the promising methods are temperature dependent, a straightforward temperature adjustment scheme should be developed, especially for the IR method and the FWD.

REFERENCES

Acoustic Control Systems, www.acsys.ru/eng

Al Hakim, B., Al Nageim, H., Pountney, D., and Lesley, L. (1997). “The development of an improved pavement backcalculation.” Proceedings, 1st International Conference on Rehabilitation and Development of Civil Engineering Infrastructure Systems, Lebanon.

Al Hakim, B., Armitage, R., and Thom, N. H. (1998). “Pavement assessment including bonding condition: case studies.” Proceedings, 5th International Conference on Bearing Capacity of Roads and Airfields, University of Trondheim, Trondheim, Norway, 1, 439–448.

Al Hakim, B., Cheung, L. W., and Armitage, R., (2000). “Use of FWD Data for Prediction of Bonding between Pavement Layers.” International Journal of Pavement Engineering, 2000. Vol. 1(1), pp. 49-59.

Ameri-Gaznon, M., and Little, D., “Octahedral Shear Stress Analyses on an ACP Overlay on a Rigid Base,” Proceedings of the Association of Asphalt Paving Technologists, vol. 59, pp. 443-479, 1990.

Armitage, R. J., Kruntcheva, M. R., and Willett, M. R. (2000). “Trials of the Portable Seismic Pavement Analyzer (PSPA).” Report Prepared for Highways Agency, Pavement Engineering Group, Scott Wilson Pavement Engineering, Nottingham, U.K.

Asphalt Institute, “Asphalt in Pavement Maintenance,” Manual Series No. 16 (MS-16), Third Edition.

Bognacki, C. J., Frisvold, A. and Bennert, T. (2007), “Investigation of asphalt pavement slippage failures on Runway 4R-22L, Newark International Airport.” FAA Worldwide Airport Technology Transfer Conference. Atlantic City, New Jersey, USA.

- Bonnaure, F., Gavois, A., and Udron, J., “A New Method for Predicting the Fatigue Life of Bituminous Mixes,” Proceedings of the Association of Asphalt Paving Technologists, vol. 49, pp. 499-529, 1980.
- Carino, N.J., 2001, “The Impact-Echo Method: an Overview.” Proceedings of the 2001 Structures Congress & Exposition, May 21-23, 2001, Washington, D.C., American Society of Civil Engineers, Reston, Virginia (2001), 18 p.
- Carroll, N., M., and Dempsey, B., J. (2007), “Anti-Icing Pavement Coating Study at Chicago O’Hare International Airport. Report No. DOT/FAA/AR-06/58, U.S. DOT, FAA.
- CTL Group. Impulse Response Testing. www.ctlgroup.com
- Delatte, N., Chen, S. E. and Jackson, N. M. “UTW and SASW for General Aviation Airport Pavement Rehabilitation,” 2002 Federal Aviation Administration Technology Transfer Conference, Atlantic City, N.J., May 7, 2002.
- Department of the Air Force. Engineering Technical Letter (ETL) 02-7: Preventing Concrete Deterioration under B-1 and F/A-18 Aircraft, August 7, 2002.
- Eedula ,S., and Tandon, V. (2006), “Tack Coat field acceptance criterion,” Research Report 0-5216-1, Center for Transportation Infrastructure Systems, UTEP, El Paso, TX.
- Ganji, V. (1998). “Preliminary trials of the Portable Seismic Pavement Analyzer (PSPA).” Job No. E298-1, Scott Wilson Pavement Engineering, Nottingham, U.K.
- Garbacz, A. and Garboczi, E. J. “Ultrasonic Evaluation Methods Applicable to Polymer Concrete Composites.” NISTIR 6975; 73 p. April 2003. National Institute of Standards and Technology, Gaithersburg, MD 20899.
- GBG Australia. Non Destructive Techniques for Sub Surface Profiling of Pavement Structures.

- Gomba, S.M. (2004) "Evaluation of interlayer bonding in hot mix asphalt pavements." Master Thesis. Rowan University, Glassboro, New Jersey.
- Hammons, M., I., Von Quintus, H., Maser, K., and Nazarian, S. (2005) "Detection of stripping in hot mix asphalt." Applied Research Associates Project Number 16355, prepared for: Office of Materials and Research, Georgia Department of Transportation.
- Hachiya, Y., and Sato, K., "Effect of Tack Coat on Bonding Characteristics at Interface between Asphalt Concrete Layers," Proceedings of 8th International Conference on Asphalt Pavements, vol. 1, pp. 349-362, 1997.
- Kruntcheva, M. R., Collop, A. C., and Thom, N. H. (2000). "The Portable Seismic Pavement Analyzer: laboratory trials." Project Report PGR 2000-02, University of Nottingham, U.K.
- Kruntcheva, M., R., Collop, A., C. and Thom, N., H. (2004) "Feasibility of assessing bond condition of asphalt concrete layers with dynamic nondestructive testing." Journal of Transportation Engineering, Vol. 130, No. 4.
- Kruntcheva, M. R., Collop, A. C., and Thom, N. H. (2005). "Effect of Bond Condition on Flexible Pavement Performance." Journal of Transportation Engineering, Volume 131, Issue 11, pp. 880-888, November 2005.
- Kruntcheva, M., R., Collop, A., C. and Thom, N., H. (2006) "Properties of asphalt concrete layer interfaces. Journal of Materials in Civil Engineering, Vol. 18, No. 3.
- Kulkarni, M., B. (2004) "Effect of tack and prime coats, and bag-house fines on composite asphalt pavements." Ph.D. Dissertation, North Carolina State University, Raleigh, NC.

- Lepert, P., Poilane, J. P., and Villard-Bats, M. (1992). "Evaluation of various field measurement techniques for the assessment of pavement interface condition." Proceedings, 7th International Conference on Asphalt Pavements, Vol. 3, 224–237.
- Li, Y., and Nazarian, S. (1994), "Evaluation of Aging of Hot-Mix Asphalt Using Wave Propagation Techniques," Engineering Properties of Asphalt Mixtures And the Relationship to Their Performance, ASTM STP 1265, Philadelphia, Pa., pp.166-179.
- Lin, J.M. and Sansalone, M.J., 1996, "Impact-Echo Studies of Interfacial Bond Quality in Concrete: Part I-Effects of Unbonded Fraction of Area," ACI Materials Journal, Vol. 93, No. 3, May-June, pp. 223- 232.
- Liu, W. and Scullion, T. "MODULUS 6.0 for Windows: User's Manual," Research report 0-1869-2. Texas Transportation Institute, College Station, TX, October 2001.
- Maser K. R. (1996), "Condition assessment of transportation infrastructure using ground-penetrating radar", ASCE Journal of Infrastructure Systems, pp. 94-101
- Maser K. R., Holland, T. J., and Roberts, R. (2002) "Nondestructive measurement of layer thickness on newly constructed asphalt pavement." Proceedings of the Pavement Evaluation Conference, Roanoke, VA.
- Medina, R. and Garrido, M. Improving Impact-echo Method by Using Cross-spectral Density. Journal of Sound and Vibration, Volume 304, Issue 3-5, p. 769-778, July 2007.
- Mohammad, L. N., Raqib, M. A., and Huang, B., "Influence of Asphalt Tack Coat Materials on Interface Shear Strength," Transportation Research Record, no 1789, pp. 56-65, 2002.
- Moropoulou, A., Avdelidis, N., P., Kouli, M., and Kakaras, K. (2002) "Flaw detection and evaluation of airport pavements by means of infrared thermography." http://www.flirthermography.com/media/Detection_Evaluation_Airport_Paving.pdf

- Mukhtar, M. T., and Dempsey, B. J., "Interlayer Stress Absorbing Composite (ISAC) for Mitigating Reflection Cracking in Asphalt Concrete Overlays," Final Report Project IHR-533, Illinois Cooperative Highway Research Program, June, 1996.
- Nazarian, S., Baker, M. R., and Crain, K. (1993). "Developing and Testing a Seismic Pavement Analyzer." Technical Report SHRP-H-375, Strategic Highway Research Program, Washington, D.C.
- Nazarian, S., M. Baker, and K. Crain. 1997. "Assessing Quality of Concrete with Wave Propagation Techniques," Materials Journal, ACI, Farmington Hills, MI, Vol. 94 (4) 296-306
- Newman, K., and Shoenberger, J., E. (2002), "Polymer concrete micro-overlay for fuel and abrasion resistant surfacing: laboratory results and field demonstrations." 2002 FAA Airport Technology Transfer Conference.
- Rocha, S., Tandon, V., and Nazarian, S., "Falling Weight Deflectometer Fleet: Repeatability and Reproducibility," International Journal of Road Materials and Pavement Design, Volume 5 – Issue 2/2004, pp. 215-238.
- Sangiorgi, C., Collop, A., C. and Thom, N., H. (2003) "A nondestructive impulse hammer for evaluating the bond between asphalt layers in a road pavement." Non-Destructive Testing in Civil Engineering, International Symposium, Liverpool, UK.
- Sansalone, M. and N. J Carino. 1986. "Impact-Echo: A Method for Flaw Detection in Concrete Using Transient Stress Waves," Report NBSIR 86-3452, Gaithersburg, MD.
- Sebesta S., and Scullion, T. (2002), "Using infrared imaging and ground-penetrating radar to detect segregation in hot-mix overlays", Report No. 4126-1, Texas Transportation Institute.

- Shahin, M. Y., Kirchner, K., Blackmon, E.W., and Tomita, H., “Effect of Layer Slippage on Performance of Asphalt-Concrete Pavements,” *Transportation Research Record*, no. 1095, pp. 79-85, 1986.
- Shahin M.Y. *Pavement management for airports, Roads and Parking Lots*. Springer, 2005.
- Sholar, G. A., Page, G. C., Musselman, J. A., Upshaw, P. B., Moseley, H. L., “Preliminary Investigation of a Test Method to Evaluate Bond Strength of Bituminous Tack Coats,” *Proceedings of the Association of Asphalt Paving Technologists*, Preprints, pp. 107-137, 2004.
- Smith, S., S., Scullion, T. *Development of Ground-Penetrating Radar Equipment for Detecting Pavement Condition for Preventive Maintenance*. SHRP-H-672. Strategic Highway Research Program. National Research Council Washington, DC 1993.
- Stroup-Gardiner M. and Brown E.R. (2000), “Segregation in hot-mix asphalt pavements”, NCHRP Report 441, TRB, National Research Council, Washington, D.C.
- Tschegg, E., Kroer, G., Tan, D., Stanzl-Tschegg, S., and Litzka, J., “Investigation of Bonding between Asphalt Layers on Road Construction,” *Journal of Transportation Engineering*, vol. 121, no. 4, pp. 309-316, 1995.
- Tsubokawa, Y., Mizukami, J., Esaki, T., and Hayano, K. (2007) “Study on infrared thermographic inspection of de-bonded layer of airport flexible pavement.” FAA Worldwide Airport Technology Transfer Conference. Atlantic City, New Jersey.
- Uzan, J., “Influence of the Interface Condition on Stress Distribution in a Layered System,” *Transportation Research Record*, no. 616, pp. 71-73, 1976.

Uzan, J., Livneh, M., and Eshed, Y., "Investigation of Adhesion Properties between Asphaltic-Concrete Layers," Proceedings of the Association of Asphalt Paving Technologists, vol. 47, pp. 495-521, 1978.

West, Randy C; Moore, Jason R; Zhang, Jingna, "Evaluating Tack Coat Applications and the Bond Strength between Pavement Layers," Proceedings of the 2006 Airfield and Highway Pavement Specialty Conference, ASCE, pp, 578-588, 2006.

APPENDIX A – NDT METHODS FOR DELAMINATION DETECTION

Electromagnetic Methods

Ground Penetrating Radar

Ground Penetrating Radar (GPR) is a geophysical nondestructive technique that uses electromagnetic pulses to test, characterize, or detect subsurface materials based on changes in electrical and magnetic properties of the subsurface layers. Its first use can be traced in Austria in 1929. A typical equipment setup for typical GPR surveys is shown in Figure A.1 for air-launched and ground coupled systems. The setup typically includes a GPR Horn (air-launched) or ground antenna together with a survey wheel and a GPS unit for measuring distance and recording the location of test survey lines.



Figure A.1 – Equipment Setup for Air Launched (Left) and Ground Coupled (Right) GPR Units

GPR works using short electromagnetic pulses radiated by an antenna which transmits these pulses and receives reflected returns from the pavement layers, as shown in Figure A.2a. The reflected pulses are received by the antenna and recorded as a waveform, as shown in Figure A.2b. As the equipment travels along the pavement, it generates a sequence of waveforms as shown in Figure A.2c. These waveforms are digitized and interpreted by computing the

amplitude and arrival times from each main reflection. The reflections of these waves at interfaces and objects within the material are analyzed to determine the location or depth of these interfaces and buried objects, and to determine the properties of material. Whenever applicable, GPR can be employed as a rapid nondestructive tool for evaluation of geometrical and material properties of structural components. Unfortunately, claims about the capability of the technology have sometimes been overstated, leading to unrealistic expectations and disappointment in the results (Maser 1996). The main advantage of the GPR is the speed of the operation and almost full-coverage of the airfield. Some of the traditional limitations of GPR have been the cost and complexity of the equipment, the need for interpretive expertise, and the requirement for office data processing. However, recent developments with GPR hardware have yielded systems which are less expensive and easier to operate, and could overcome the equipment complication. On the data processing side, prototype software for automated on-site processing has been developed (Maser et al., 2002) which may overcome some of the processing issues.

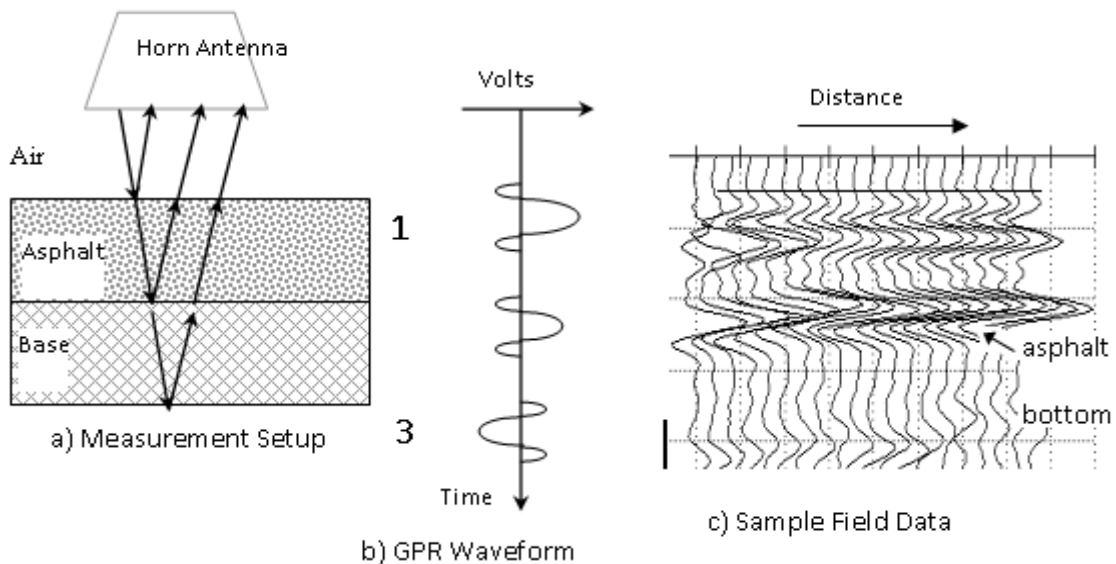


Figure A.2 – Principle of GPR for Pavement Layer Thickness Evaluation

GPR has been extensively used for measuring pavement layer thicknesses (ASTM D4748), locating changes and anomalies in pavement structures, detecting voids under concrete slabs, locating reinforcement and dowels in jointed concrete pavements, and moisture damage (stripping) in asphalt pavements. GPR technology has proven effective in detecting layer thicknesses and identifying areas where non-uniform electromagnetic properties indicate changes in physical properties such as moisture damage, stripping, or other subsurface anomalies (Hammonds et al., 2005). For example, a combination of GPR survey of the roadway followed by seismic tests in selected areas and validation with ground truth data has been successfully used to identify areas with various levels of moisture damage, stripping or other forms of distress.

However, the application of GPR in detection of delamination may require further evaluation. To directly detect the delamination, the reflections from the top and bottom surfaces of the delaminated area should be distinguishable in GPR radagrams. Even at 1 GHz the GPR wavelength in construction material (concrete or HMA) is much too long to resolve the 1-2 mm wide delamination cracks (Maser, 1996). As such, the direct detection of the onset of delamination may be difficult. As the delamination-induced debonding grows, it maybe more likely to be detectable by a GPR. The changes in GPR waveforms as a result of separation (air-filled or water-filled) between HMA layers have been investigated in a multi-phase theoretical, experimental, and field study (Smith and Scullion, 1993). They developed a theoretical model to describe the changes in the input pulse as it travels through the pavement layer system and reflects at each interface. The model incorporated a linear-mixture model, in which the dielectric constant of a mixture was taken as the summation of the dielectric constants of its constituents

weighted by the corresponding volumetric ratios. The dielectric constant of the asphalt mixture (ϵ_{ac}) can be expressed as follows:

$$\epsilon_{ac} = \epsilon_s V_s + \epsilon_{as} V_{as} + \epsilon_a V_a \quad (\text{A.1})$$

where ϵ_{ac} is the dielectric constant of the asphalt mixture, ϵ_s , ϵ_{as} , ϵ_a are the dielectric constants of the aggregate, asphalt, and air, respectively, and V_s , V_{as} , V_a denote the volumetric ratios of aggregate, asphalt, and air, respectively. Assuming layer thicknesses, dielectric constants, and mix characteristics, the radar traces were modeled to simulate the radar response to the pavement distresses of interest. Changes in the dielectric constants were shown to affect both the amplitude and the travel time of the reflected signals. For example, the simulated reflections as a result of an air gap in asphalt are depicted in Figure A.3 as the gap thickness was increased from 0.1 to 2.0 cm. As the gap grows thicker, both shape and amplitude of the reflected waves change. Similar results were obtained when the gap was assumed to be filled with water, but the changes in the signal were more significant due to the high dielectric constant of water. The reflection coefficient versus the gap thickness for the air and water filled gaps are shown in Figure A.4. The simulated results were compared to real-world data and a good agreement was reported.

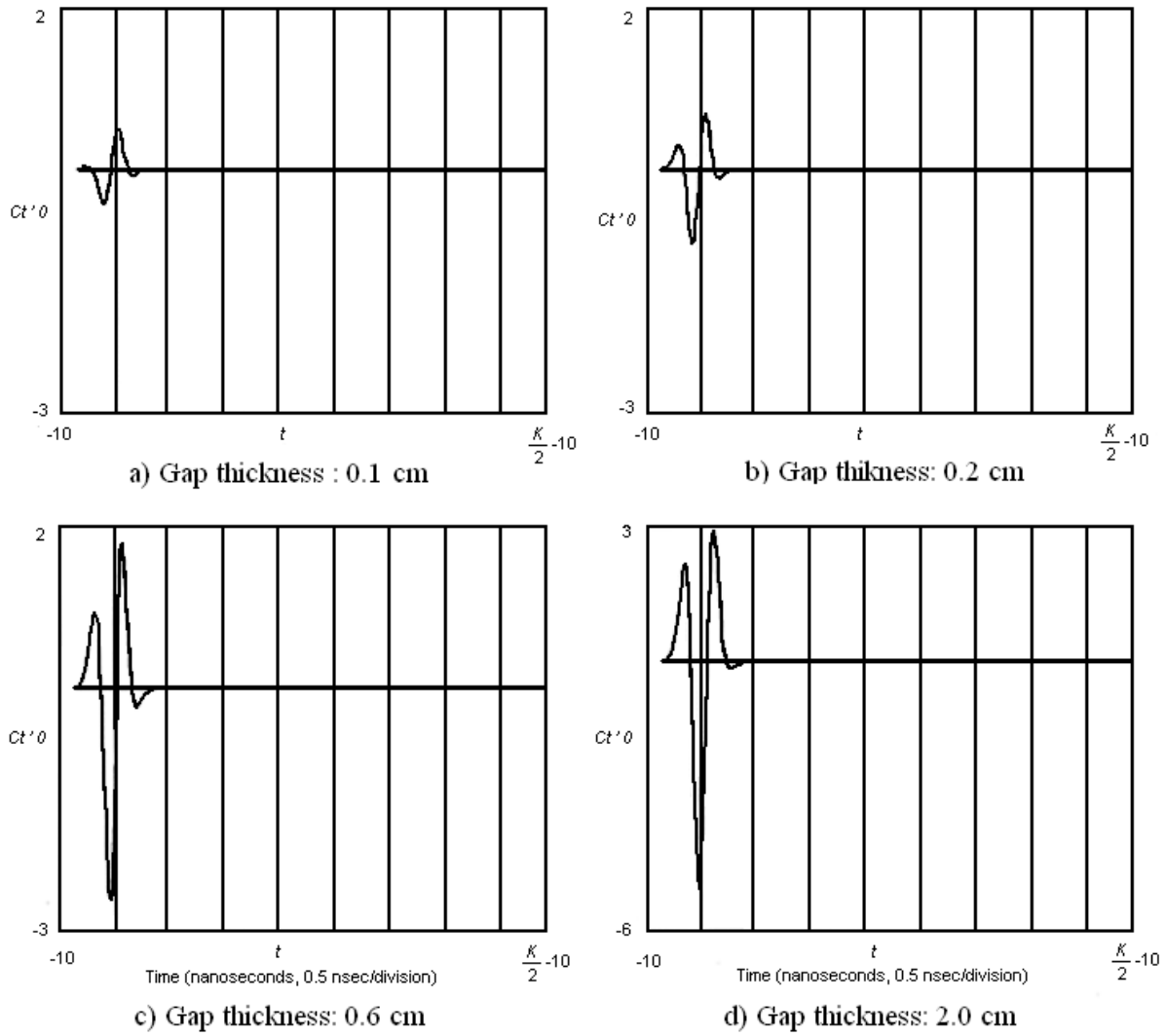


Figure A.3 – Reflections Due to Air-filled Delamination in Asphalt (Smith and Scullion, 1993)

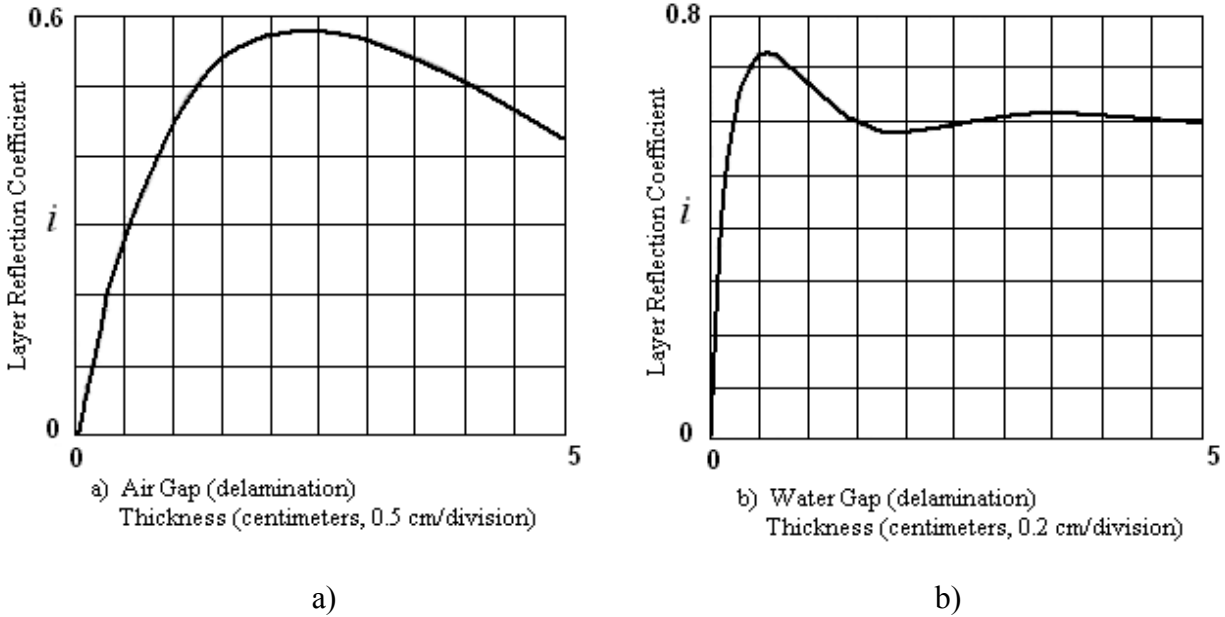


Figure A.4 – Reflection Coefficient Due to Air-filled and Water-filled Delamination (from Smith and Scullion, 1993)

Based on the results of that study, air-filled delamination of 0.5 cm (0.2 in.) or larger at a minimum depth of 5 cm (2 in.) and water-filled delamination of 0.25 cm (0.1 in.) or larger at a minimum depth of 5 cm (2 in.) may be detected by a 2.5-GHz horn antenna. The above tentative guidelines are valid when a dual 1 and 2.5-GHz antenna system is used provided that the maximum data acquisition speed does not exceed 10 mph.

As a part of that study, several field test sections were evaluated using the GPR. The laboratory and field tests did produce promising results. GPR proved to be useful for estimating the layer thicknesses, the moisture content of flexible base course, and the presence of moisture-filled voids. However, in that field testing, the potential of GPR to detect air-filled voids, overlay delamination and stripping in the asphalt could not be fully evaluated and it was recommended that more testing was necessary (Smith and Scullion, 1993).

Other field investigations have reported that GPR survey can provide useful information which may indicate delamination between asphalt layers. For example, the much larger

amplitudes in GPR radargram shown in Figure A.5 mark the location of delaminated zones. This observation was confirmed by the core taken at the perceived location of delamination (GBG Australia).

Based on the available literature, detection of delamination between HMA lifts, especially at its early stage of development, is highly challenging and demands further systematic investigation. More likely, the successful results may be achieved indirectly by using the technology to measure the condition that is associated with the presence or development of delamination in HMA. For example, given the high sensitivity of GPR signals to the changes in moisture, the penetration of moisture within the delaminated region may be detected and assist in identifying delamination. However, the identification of emulsion-rich interfaces from the wet interfaces may be also difficult (Maser, 1996). A combination of GPR with other NDT technique(s) which provide a direct method of detection of delamination may yield the best outcome.

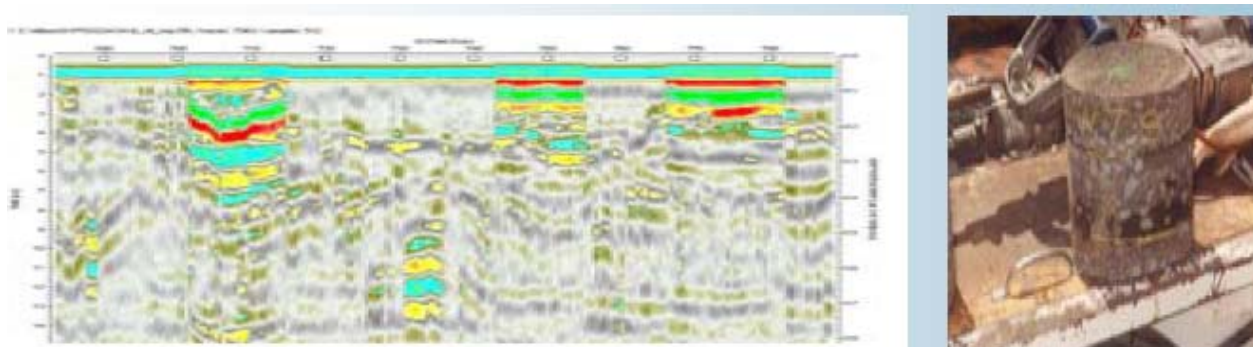


Figure A.5 – Radar Profile and Core Retrieved Showing Asphalt Delamination (GBG Australia)

Impulse Methods

The impulse methods work on the principle of measuring the pavement response (deflection) to a known load. Theoretically, if delamination occurs within an HMA layer, the

deflection of the pavement system should increase. As such, the impulse methods may be utilized in relative terms to detect the delamination. The Falling Weight Deflectometer (FWD), the Light-Weight Deflectometer (LWD) and the Impulse Response method are examples of impulse methods. The potential application of these techniques in detection of interlayer delamination is described below.

Falling Weight Deflectometer (FWD)

The FWD device consists of an impact loading mechanism and a set of sensors to measure vertical surface displacements at the load location and at specified offsets from the load. The loading component delivers a transient load to the pavement surface and the sensors measure the surface deflection at the specified locations. The entire system is typically trailer mounted as shown in Figure A.6. The loading device consists of a load plate that can apply an impulse load of different magnitudes ranging from 1500 to 27000 lb. The load can be applied from standard drop heights resulting in a load pulse of 25 to 60 msec. The load plate is circular and has a standard diameter of 6 in.



Figure A.6 – Trailer Mounted FWD

The pavement response to the applied load in terms of a deflection basin is measured at several radial locations, as shown in Figure A.7. Estimating the best set of pavement properties to fit the measured deflections is then carried out in a process known as backcalculation. The FWD backcalculation results are in-situ effective stiffness of the bituminous layers at the site temperature. Higher deflections are expected if poor bond exists, since the layers will act independently in the absence of shear continuity at the interfaces. In such cases, lower stiffness is usually obtained from FWD test results. Therefore, the FWD backcalculated stiffness may provide some indications of poor bonding between HMA layers.

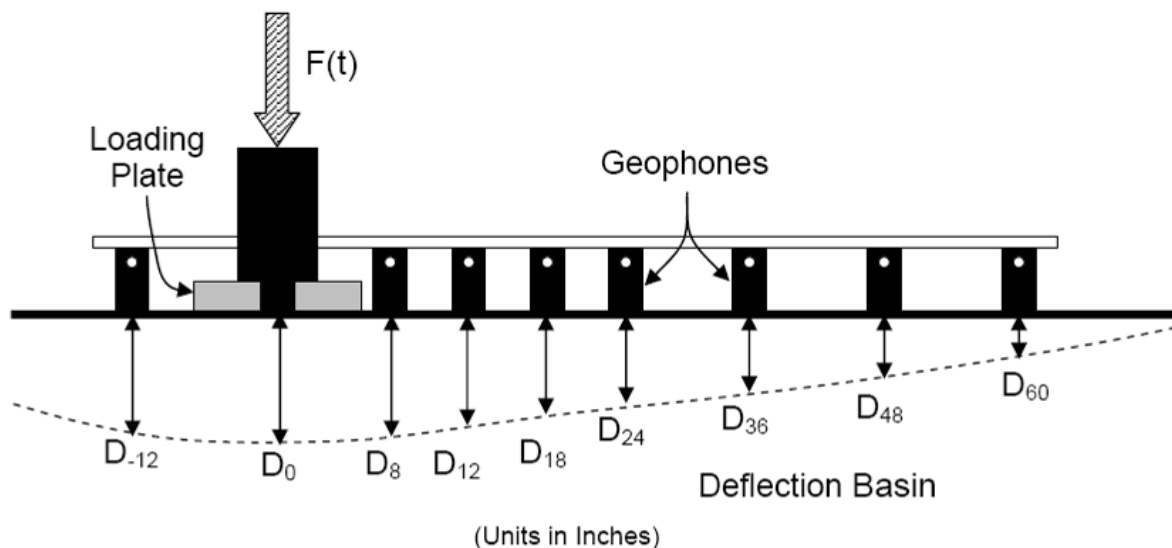


Figure A.7 – Typical Deflection Basin Measured From FWD

Earlier studies concluded that deflection measurements devices such as deflect graph and FWD were not found promising for assessing interface debonding condition (Lepert et al., 1992). A new backcalculation process for assessing the bond condition between the HMA layers using FWD deflections has shown some promise (Al Hakim et al., 1997, 1998, 2000). This new algorithm involves the calculation of an additional parameter called “shear reaction modulus” or K_s from the deflection basin that provides an indication of the bond condition over a relatively

large area. To calculate K_s , the interface between two pavement layers is assumed as a thin layer with a shear modulus G and a thickness t . The shear stress τ at the interface can be expressed as:

$$\tau = (G/t) \cdot \gamma = K_s \cdot \Delta u \quad (A.2)$$

where γ is the shear strain of the thin interface material, Δu is the relative horizontal displacement between the two sides of the interface and K_s is the shear bonding stiffness or shear reaction modulus at the interface.

Al Hakim et al. (2000) performed a sensitivity analysis to investigate the theoretical influence of bonding stiffness on surface deflections and backcalculated layer stiffness in multilayer pavement systems. During the backcalculation process, the interface bond stiffness was considered as a variable and was backcalculated similar to a layer stiffness. First, a constant bond stiffness of 1000 MN/m^3 between layers was assumed and then, the HMA layer stiffness was slightly adjusted. Finally, the bond stiffness between layers (K_s) varied from complete debonding (10 MN/m^3) to full adhesion (10^5 MN/m^3) to find the optimum fit for the deflection basin. To calibrate and verify the proposed theoretical method, FWD was used on several newly-constructed pavements to estimate bonding stiffness. Tests were conducted before sections were opened to traffic and repeated after six months. It was found that a combination of traffic loading and higher temperature during testing improved the bonding between layers. However, sections with very poor bond did not improve with traffic or time. The backcalculated interface stiffness from FWD deflection basis was found not to be successful for assessment of bond condition between thin layers of asphalt (Al Hakim et al., 1997; Kruntcheva et al., 2005).

FWD measurements have also been used to detect debonding between lifts of airport pavements (Gomba, 2004). Data obtained from the Federal Aviation Administration's (FAA) National Airport Pavement Test Facility in Atlantic City, New Jersey, was used to measure

interlayer bonding for pavement sections that had encountered a loss of bond between lifts of the surface HMA. It was found that the calculated stiffness moduli for surface layers could be used as a parameter to determine the quality of interlayer bonding. A parameter called “Tack Coat Failure Ratio” (TFR) was defined and it was attributed to the slippage susceptibility at the interface. TFR was defined as the ratio of the moduli of the HMA layers above and below the debonded interface as backcalculated from FWD results. Therefore, TFR is 1 for a bonded interface, and is 0 when the interface is debonded. Another parameter called ‘Effect of Slip’ in the pavement which was defined as the ratio of the difference in radial stress (between points just above and below the interface) to the maximum difference in radial stress at the interface at full slip. It was found that TFR is well correlated to the Effective Slip (see Figure A.8). It was concluded that surface layer moduli calculated from FWD data can be used to identify a lack of interlayer bonding in pavements and that the effect of slip between two asphalt layers of similar properties will be reflected by the moduli of the top layer being lower than the moduli of the bottom layer (Gomba, 2004).

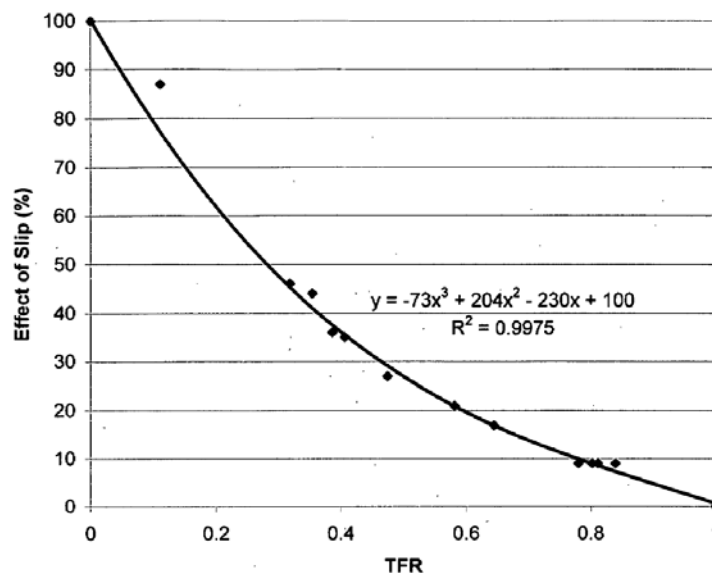


Figure A.8 – Effect of Slip/TFR Correlation (Gomba, 2004)

A forward calculation technique was utilized to calculate the bond stiffness from the FWD deflection basin using closed-form solutions (Hammonds et al., 2005). This technique assumes that the bond modulus is primarily a function of the near-load deflections as described by the radius of curvature of the deflection basin. Because the resulting surface course stiffness is independent of the moduli of other layers within the pavement system, a unique solution is obtained. However, because the surface course stiffness is calculated independently of the other layers in the pavement structure, the values obtained may or may not be reasonable with respect to the total center deflection.

Some approaches have been carried out based on the “AREA” concept (a deflection basin curvature index), that calculates the overall composite modulus of the entire pavement structure (Hammonds et al., 2005). Using the logic of the AREA concept, the stiffness of the bound HMA layer can be given by:

$$E_{AC} = \frac{E_0 \cdot AF_{AC} \cdot k_3^{\sqrt[3]{AF_{AC}}}}{k_3^2} \quad (A.3)$$

where E_{AC} = stiffness or modulus of the upper HMA layer(s), k_3 = thickness ratio of upper layer thickness / load plate diameter = $h_1 / (2a)$, E_0 = composite modulus of the entire pavement system beneath the load plate, and AF_{AC} = AREA factor.

Equation A.3 has been calibrated using a large number of trial elastic layer theory calculations, and it works well for typical materials and modular ratios. Nevertheless, this approach is not totally rigorous or scientific, but rather is empirical in nature. The approach can therefore be used effectively to approximate the relative stiffness of the uppermost layer(s) in a pavement cross section for comparative purposes.

Light Weight Deflectometer (LWD)

The LWD operates in a similar fashion to the FWD with one to three sensors (as opposed to at least seven for FWD); however such a device is generally small and light enough to be carried and operated by one person, as shown in Figure A.9 and is mainly used on unbound materials, where lighter loads are required. The analysis methods described for FWD are also applicable to LWD. After an extensive review of the literature, no study could be found where the application of LWD for detection of delamination between HMA layers was evaluated.

Impulse Response Method

The basic operating principle of the impulse response hammer is to apply an impulsive loading to the pavement surface with the hammer and measure the vertical dynamic response using an accelerometer (Sangiorgi et al., 2003). If structural distresses are present in the form of loss of adhesion between pavement layers, this is reflected in the dynamic response of the pavement structure. The equipment necessary to complete the test is shown in Figure A.10.



Figure A.9 – Light Weight Deflectometer

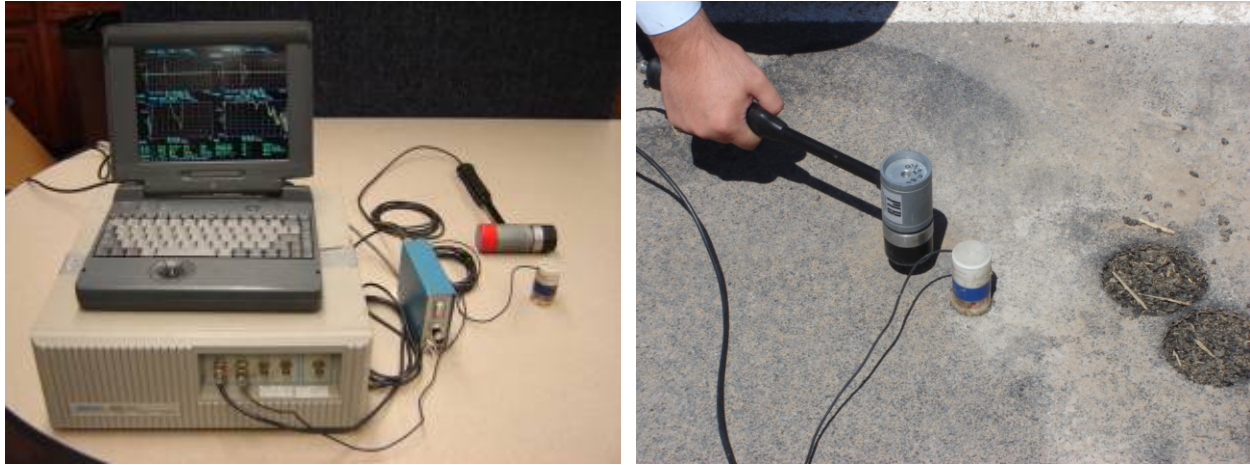


Figure A.10 – Impulse Hammer Test Setup

This method uses a low-strain impact to initiate stress wave propagation through the material under investigation. The response to the impact is measured and analyzed to assess the in-situ condition. The impactor is usually a 2 to 10 lb instrumented hammer. The response is normally measured by a velocity transducer (e.g. geophones) or accelerometer. Both the hammer and the receiver are linked to a portable field computer for data acquisition and storage. The data analysis can be completed in the field and typically includes the calculation of transfer function or mobility by dividing the frequency spectrum of response by that of the input force. The characteristics of the time history of the response as well as the shape of the graph of mobility plotted against frequency contain information about the condition and the integrity of the material under test. An example of two mobility plots obtained on a sound and delaminated slab is shown in Figure A.11. More quantitative assessment is possible by comparing the mobility plots through different calculated parameters such as (CTL, www.ctlgroup.com):

- Dynamic Stiffness
- Mobility and Damping
- Peak/Mean Mobility Ratio

The Impulse Response test has several advantages over most other nondestructive testing methods including the robust nature of the apparatus, the speed of data collection and analysis, the repeatability of test results, and its applicability on relatively rough surfaces (CTL, www.ctlgroup.com).

Kruntcheva et al. (2004) studied the feasibility of using IR method for quantifying bond condition within HMA layers under controlled laboratory condition. Different surfacing thicknesses were considered and the following interface conditions were compared: bonded; debonded; and partially bonded. Results showed that the vibration differences between bonded and debonded surfacing are force-amplitude dependent. To investigate the repeatability of the results, five input-output time histories were recorded at each particular position of the receivers.

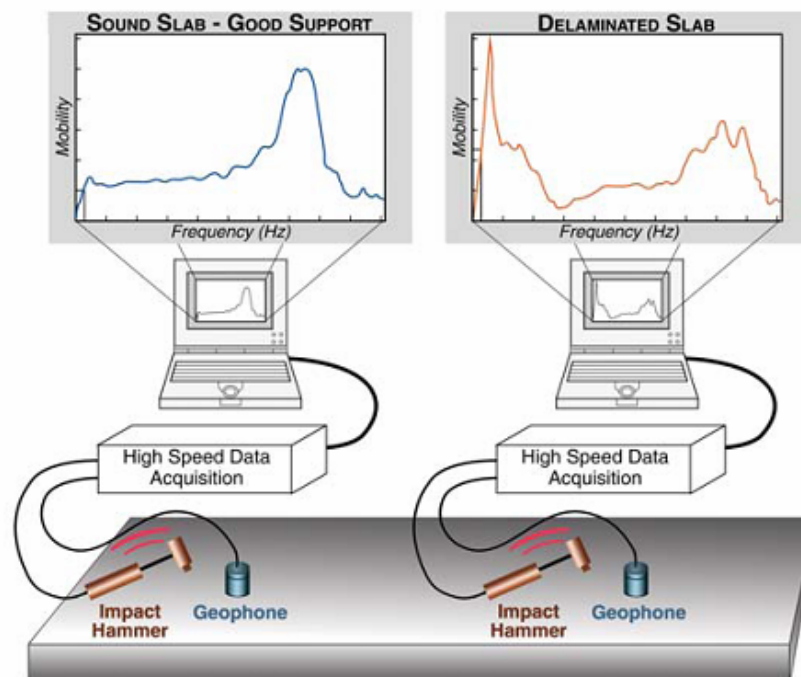


Figure A.11 – Example of IRH Signals for Intact and Delaminated Slabs (CTL, www.ctlgroup.com)

The differences in dynamic responses of the debonded and bonded interfaces are shown in Figure A.12. The bonded system reacts to impulse applied by transmitting displacement wave components of low frequency, whereas the debonded surfacing starts vibrating. This effect can also be recognized by the oscillatory components of the response, which were out of phase with respect to the excitation. Furthermore, the after-impact behavior of the debonded surfacing is clearly oscillatory, indicating a predominant forced damped vibrations with much longer decay time in comparison with the “wave” response of the bonded case. Therefore, the visual inspection the time histories provides a qualitative indicator of bond condition between HMA layers.

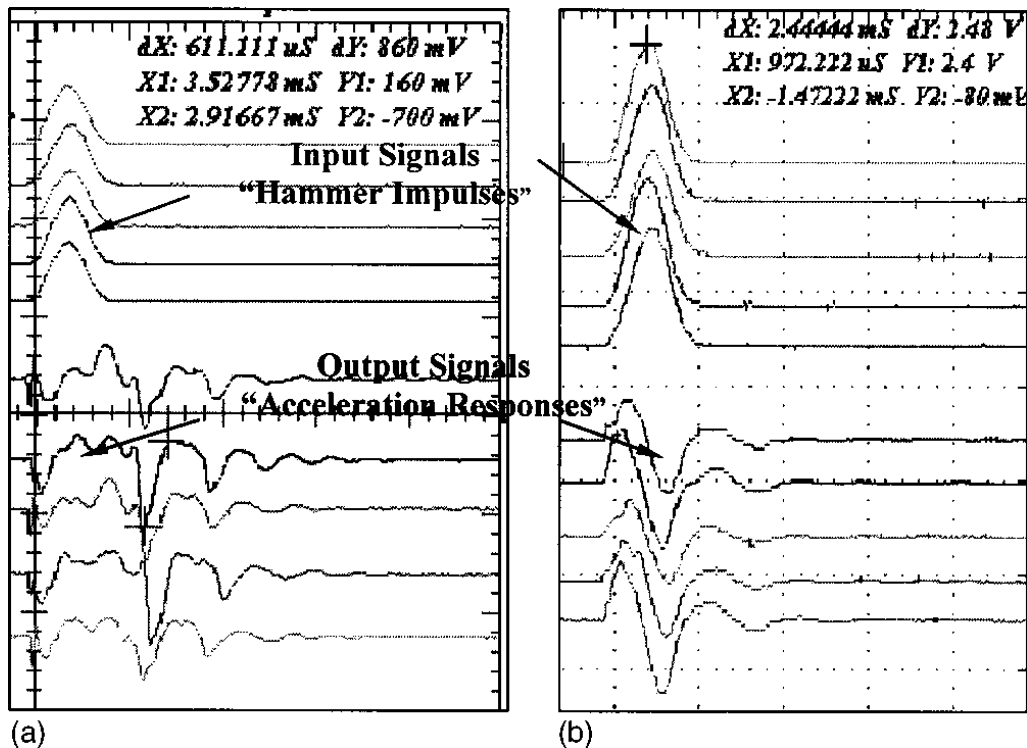


Figure A.12 – Time Histories of Input and Output Signals for Debonded (a) and Bonded (b) Surfacing (Kruncheva et al., 2004)

For a more quantitative assessment, the input-output transfer function estimate (TFE) was obtained from the spectral analysis. The equations that relate the spectral density of the excitation and the response of a system undergoing random vibration are:

$$H(\omega) = \sqrt{\frac{S_{xx}(\omega)}{S_{yy}(\omega)}} \quad (\text{A.4})$$

where $H(\omega)$ is the transfer function estimate (TFE) linking the quantities $S_{xx}(\omega)$ and $S_{yy}(\omega)$ which are the autospectra of the excitation and the response signals, respectively.

The magnitudes of the TFE's for the bonded and debonded cases for a shallow interface are compared in Figure A.13. The maximum amplitudes in both cases occur at a frequency between 1 and 2 kHz but the TFE magnitude for the debonded interface is 10 times larger than the bonded one. The enhanced dynamic response of debonded or partially bonded surfacing to hammer impulse is due to vibrations of the upper pavement layer rather than wave reflection. Therefore, a large increase in this parameter, more than five times relative to the TFE magnitude for bonded surfacing, indicates partial to very poor bond at the interface provided that the other surfacing parameters such as material and thickness remain unchanged. For shallow interfaces 20 to 50 mm a normalized maximum TFE magnitude over 15 was noted as very poor bond or no bond at the uppermost interface.

Similar results were obtained for deeper cases of delamination, but with a shift in the frequency at which the maximum value of TFE occurred. The deeper the surfacing, the higher was the frequency associated with the maximum TFE. For debonding at depth of about 1 in., the maximum TFE occurred around 3.5 kHz and for debonding at a depth of about 2 in., this value

was close to 5 kHz. This observation may be used as an approximate indicator for the surfacing thickness, but more extensive research is needed to confirm this finding

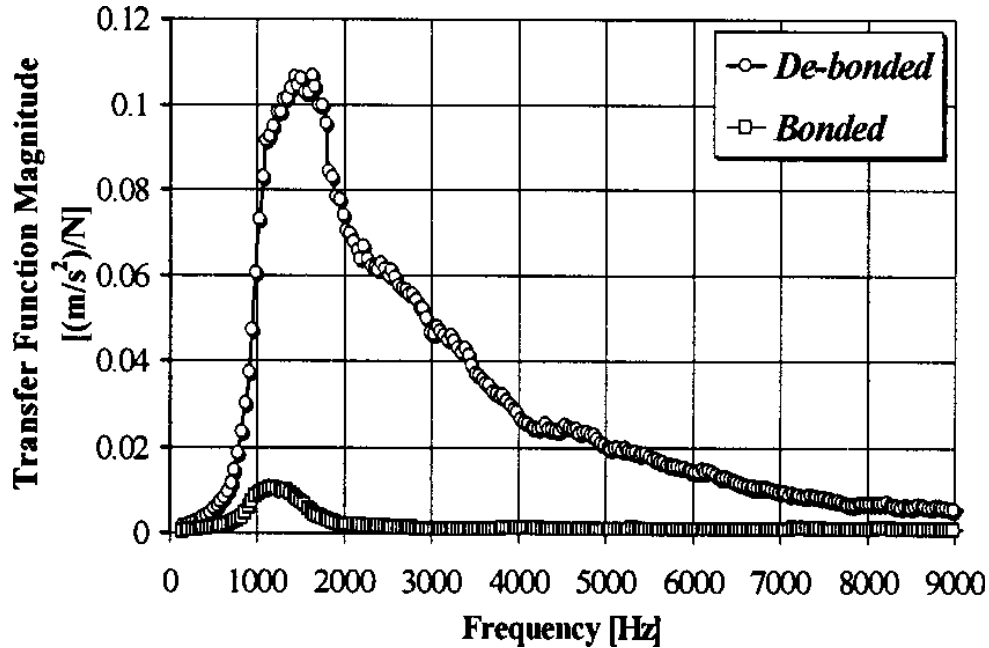
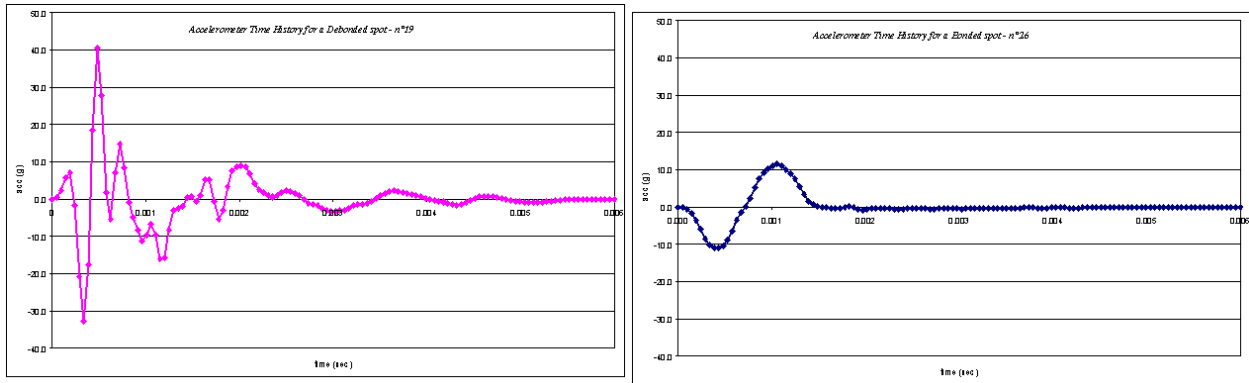


Figure A.13 – Magnitude of TFE versus Frequency for Bonded and Debonded Surfacing
(Kruncheva et al., 2004)

The IR method was used for the in-situ assessment of bond condition between surface and base courses for different types of surface course in another study (Sangiorgi et al., 2003). Two sections with different materials and thicknesses were tested in December and May. One section was overlaid with an about 1 in.-thick and the other section was overlaid with a 1.25 in. layer. Each section was divided into three sub-sections, each one with a different surface treatment to achieve different levels of bond at the interface. This included application of a normal amount of tack coat, a swept surface with no tack coat, and clay slurry applied to the base layer. Typical time histories for two case of intact and debonded interfaces obtained from this study are shown in Figure A.14. Visual inspection of the records yielded similar conclusions to those reported by Kruncheva et al. (2004). The response of the debonded system contains

vibrations of higher frequencies (greater than 1 kHz) and the acceleration does not decay to zero until approximately 6 ms, because of the vibrations induced in the surface layer due to lack of bonding to the layer below. On the contrary, the acceleration history of the bonded system is of lower frequency and is heavily damped and decays to zero after approximately 1.5 ms).

A different data analysis approach based on the fractal theory was used to obtain a quantitative indicator of bond conditions. A fractal is an object with an infinite nesting of sub-structures at different scales. It is possible to apply the fractal theory to "non-mathematically" fractal objects such as time histories and calculate a unique characteristic parameter called fractal dimension (FD) which is a single number between 1 and 2. An elementary technique for determining the F.D. is known as "Box Counting", as shown in Figure A.15. The procedure to determine the F.D. for each measured acceleration time history is as follows. An initial square box dimension (L_{init}) is chosen and the number (N) of boxes required to fully cover the complete signal is determined. In the following step (i) the box dimension is reduced ($L_{(i)}$) and the number of new (smaller) boxes required to fully cover the complete signal is re-calculated. The procedure is repeated for proportionately smaller box dimensions in the next steps. The number of boxes (N) is then plotted against (s), the ratio between the initial box dimension (L_{init}) and the box dimension at each (i) step ($L_{(i)}$) on double logarithmic scales. A straight line is then fitted to the data and the gradient of the line is the F.D. Figures A.15 and A.16 show how the Fractal Dimension is deduced from the $\log(N)$ - $\log(s)$ graph for a classical Koch fractal curve and for a measured accelerometer time history recorded from a well bonded section of the trial pavement. This analysis was applied to the recorded acceleration histories and an average FD at each test point was calculated. The calculated FDs ranged from approximately 1.1 for well bonded areas to about 1.3 for debonded areas. It was also found that the average bond condition improved in



a)

b)

Figure A.14 – Typical Debonded (Left) and Bonded (Right) Time Histories (Sangiorgi et al., 2003)

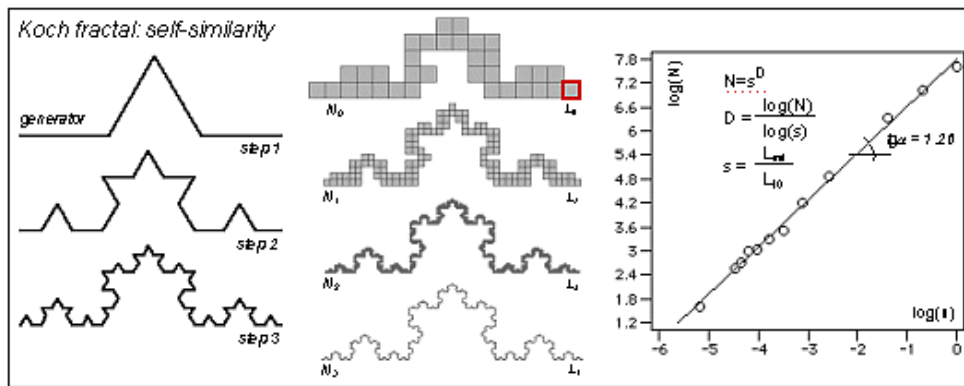


Figure A.15 – Box Counting Fractal Dimension

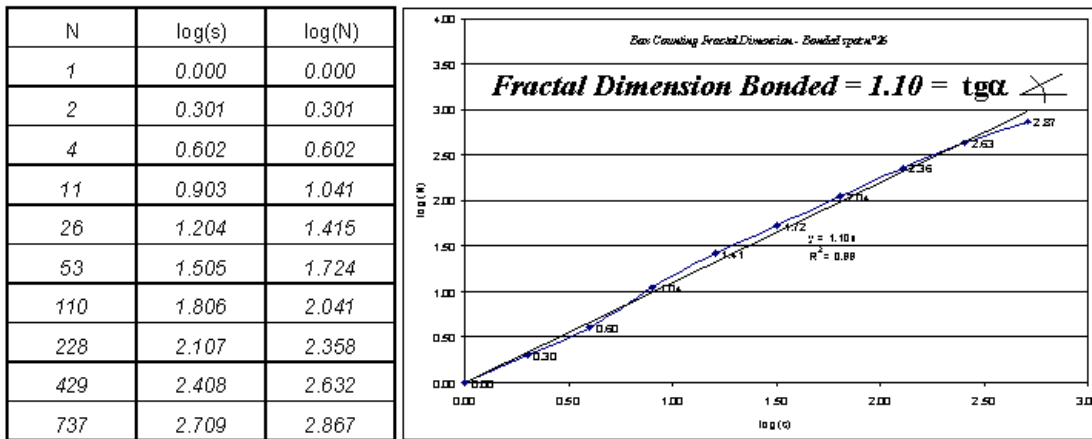


Figure A.16 – Box Counting Fractal Dimension for a Bonded Location

May relative to December, which was attributed to the bitumen healing characteristics at elevated temperatures.

The IR method seems to be a reliable quantitative and qualitative tool to obtain information about the interface bond. The surfacing material and thickness are expected to affect the test results. Therefore, when pavement test sections are of similar material, the results should be always considered relative to the response of an area that is known to be bonded. It should be noted that most of the conclusions cited above are based on the controlled laboratory studies rather than field investigations. More extensive research is needed to verify the applicability of the IR method for assessing the bond condition between HMA lifts.

Vibration Methods

Stiffness Gauge

Soil Stiffness Gauge (SSG) (Figure A.17), which is currently marketed as the Humboldt GeoGauge™, is a recently developed instrument for directly measuring in situ stiffness of soils. The SSG was conceived and developed partially by funding from FHWA in partnership with



Figure A.17 – Soil Stiffness Gauge (SSG) or GeoGauge™

several private firms. The SSG is a 11 inches in diameter and 10 inches in height portable cylinder with a 4.5 in-outer diameter and 3.5 in-inner diameter ring-shaped foot extending from the bottom of the device and it weighs approximately 22 lbs.

In vibratory methods, the pavement is vibrated using controlled input frequencies. The Stiffness Gauge developed for quality control of the granular layers, is an example of such devices. The stiffness gauge vibrates the material in the range of frequencies of 100 Hz to 200 Hz using very small load amplitudes. The variation in stiffness (displacement/load) with frequency (called stiffness spectrum) is used to measure the modulus of the material. For the detection of delamination, the stiffness spectrum can be reinterpreted (similar to impulse-response) to assess the bond quality. Since the stiffness gauge is optimized for low-stiffness geomaterials, neither the force level nor the frequency range seems adequate. The coupling of the ring that imparts load to the pavement to HMA seems problematic too. The lightweight vibrator has proven ineffective when used in a controlled experimental study on a number of special test sections in France to detect different interface conditions (Lepert et al., 1992).

High Frequency Sweep

An alternative vibratory device is a high-frequency, hand-held electromagnetic/piezoelectric shaker developed for military applications by Wilcoxon Research, as shown in Figure A.18, which can be used to impart steady state swept vibration at high-frequencies (several kilohertz) and at high energy (horizontal, vertical or at an angle).

This piezoelectric shaker utilizes piezoelectric ceramic disks, which change thickness proportional to an applied voltage. These disks are sandwiched between a heavy mass and a light fixture, which attaches to the test structure. Although the displacement is very small, the use

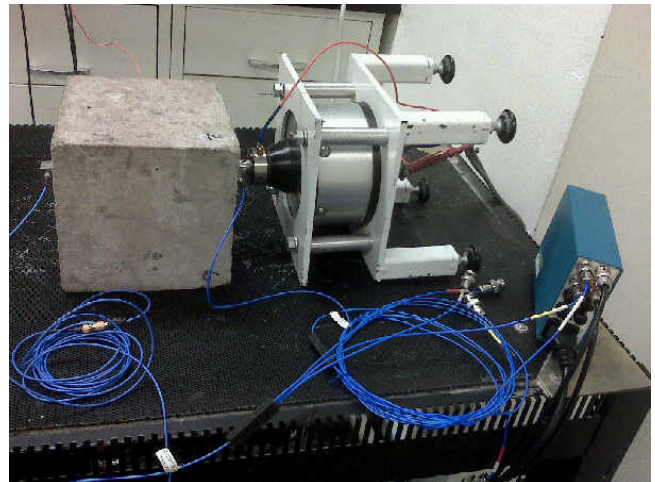
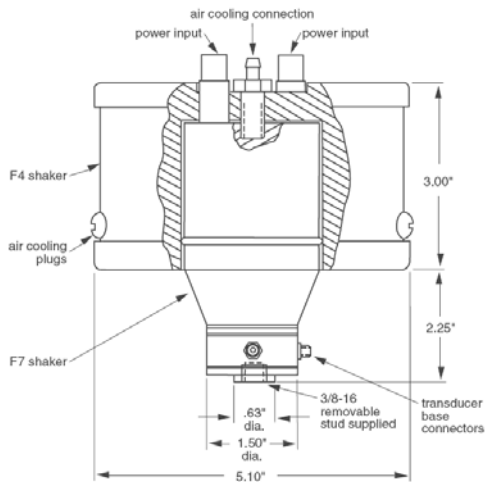


Figure A.18 – Electromagnetic/Piezoelectric Shaker System

of multiple disks and high drive voltages can produce large forces at high frequencies. The high-intensity, high-frequency vibration primarily excites the pavement layer atop the delaminated layer. Such vibrations can be detected by the built-in accelerometer of the shaker, a typical output is shown in Figure A.19. The stiffness spectra from this device can be readily used to detect the delaminated layer similar to the IR method.

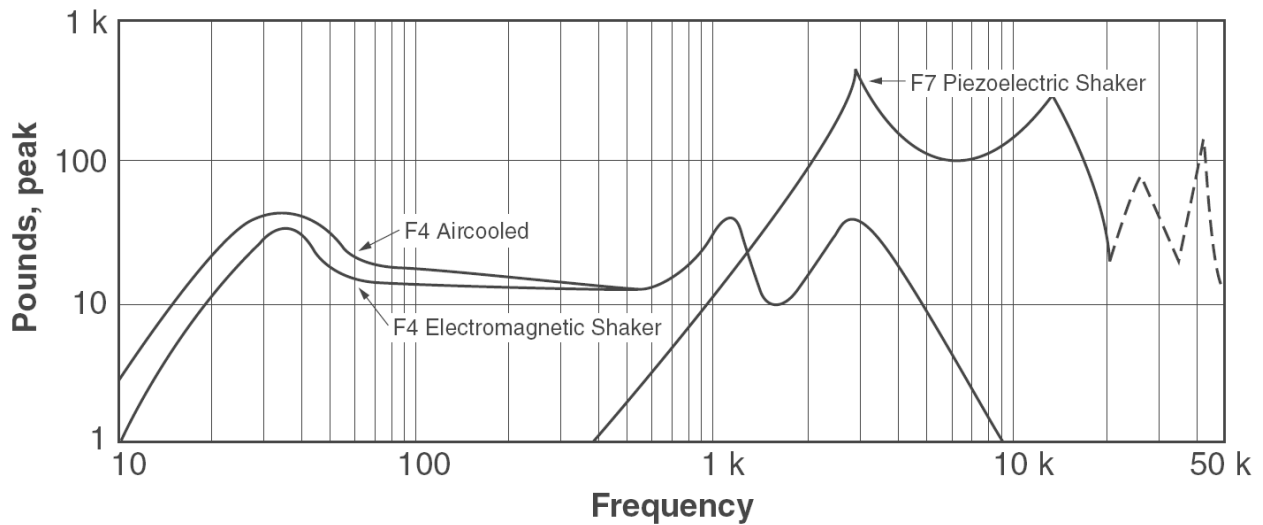


Figure A.19 – Typical Blocked Forced Output

Sonic/Ultrasonic Seismic Methods

Seismic sonic/ultrasonic methods rely on the principles of elastic wave propagation for material characterization and/or defect detection. When the surface of a material is impacted with a point source, several types of elastic waves propagate in that material. These waves can be categorized into two broad groups: body waves and surface waves. Body waves include compression waves (a.k.a. P-waves) or shear waves (a.k.a. S-waves) which propagate along a spherical front within the material. Surface waves (a.k.a. Rayleigh waves, R-waves), on the contrary, propagate along a cylindrical front. Surface waves, which carry about two-thirds of the seismic energy generated within a layer, are of higher amplitudes and attenuate at a lower rate than body waves. A concise but extended description of elastic wave propagation within a material can be found in (Nazarian et al., 1993).

Among seismic methods, the Impact-Echo (IE) and Spectral Analysis of Surface Waves (SASW) or its ultrasonic version, USW, has been successfully used for direct or indirect assessment of the bonding condition between HMA layers. IE test is based on identifying body-wave reflections in the surface response. SASW (or USW) use the changes in surface wave dispersion characteristics or elastic properties as an indication of poor bonding. Ultrasonic testing has been long used for evaluation of concrete. With the recent advances in the testing equipment and data analysis, the application of this technique to defect detection in HMA may become possible. A concise overview of these methods along with their potential applications in detection of delamination in HMA is given below.

Impact Echo

The Impact echo (IE) method involves the application of an impact (of sonic to ultrasonic frequency) and detecting reflections from interfaces of materials with dissimilar elastic

properties (e.g. contrast in impedance). The principal components of an impact echo system are a transducer, a set of spherical impactors, a data acquisition system, and a computer with the appropriate software to analyze the data acquired, a typical IE test system is shown in Figure A.20. The IE method is based on detecting the resonance frequency of the standing wave reflecting from the bottom and the top of the topmost pavement layer, as sketched in Figure A.21.



Figure A.20 – Typical Impact Echo Test System

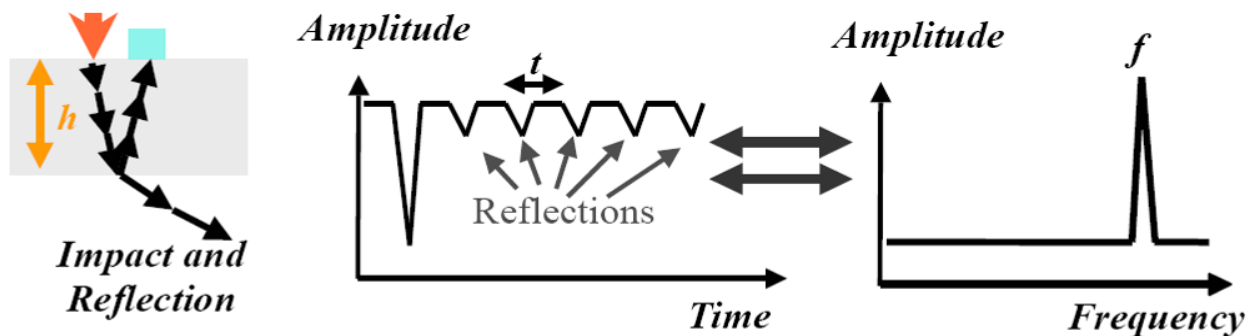


Figure A.21 – Schematic of Impact Echo Method

Upon the application of the impact on the surface of pavement, a part of the source energy is reflected from the topmost interface while some is transmitted into the base and subgrade. If a delamination exists within the top layer, a great portion of the energy is reflected from delamination. The resonance frequencies associated with the reflected waves from various

interfaces within a pavement system can be distinguished in the IE amplitude spectrum, the frequency spectrum of IE record. Knowing the compression wave velocity of the layer (V_p) the depth-to-reflector, h , can be determined from:

$$h = \frac{V_p}{2f} \quad (\text{A.5})$$

where f is the resonant frequency associated with the reflector at a depth h .

The IE method was originally developed to evaluate thickness and locate defects, voids, cracks, and zones of deterioration within concrete structures (Sansalone and Carino, 1986). The method has been used for evaluation of both concrete and asphalt pavements as well as for detection of debonding beneath asphalt overlays (Lin and Sansalone, 1996). While it is not possible to estimate the bond strength, the IE method may determine whether there is extensive porosity at the interface (Carino, 2001). A discontinuity within the top pavement layer due to delamination would reflect all the energy imparted to the pavement resulting in the detection of the depth to interface of the delaminated layer. Available IE devices can be used to detect the delaminated interfaces deeper than 4 in. (Armitage et al., 2000). Shallower delaminated areas can be still identified using IE (from the large amplitude low frequency signals); however, no information regarding the depth to the delamination layer can be drawn. In addition, as detailed in Nazarian et al. (1997), the method is not applicable to very thin layers and situations where the difference in moduli of adjacent materials is small. Other concerns with the method are the viscous behavior of the HMA which may dampen the signal and large surface aggregates that may scatter the signal.

In recent years, focused effort has been directed towards using advanced signal processing techniques to improve the analysis and facilitate the interpretation of IE test results, especially when low-frequency high-amplitude flexural vibrations may mask the resonant

reflections of interest (Medina and Garrido, 2007). In that study, windowing was used to remove the Rayleigh waves, and after that, a multi-cross-spectral density function was defined by applying cross-spectral density to the signals collected at several distances from the impact point. This process eliminated several undesirable peaks contained in the frequency spectrum, thus interpretation of the longitudinal waves becomes much easier. To validate the proposed method, a finite element study was conducted to model composite (asphalt over concrete) thin plates with shallow debonding at the interface of an asphalt overlay placed on a concrete slab. The noise and the undesirable peaks in the frequency domain were reduced after the technique was applied, facilitating the interpretation of results. In another example, a small plate made up of two layers was considered. The radius of the plate was 400 mm, and the top layer (asphalt) and the bottom concrete layer were 20 and 30 mm thick respectively. A shallow delamination in the contact zone between the concrete slab and the asphalt overlay was considered. In the IE spectrum, the resonant frequency of delamination was difficult to detect mainly because the amplitudes of the flexural modes of vibration of the whole plate as well as the thin layer above the delamination were dominating the spectrum. When the low frequency peaks of the flexural modes were removed and the multicross-spectral density function was applied, only the peak corresponding to the delamination depth was evident, demonstrating the usefulness of the proposed method. It should be emphasized that the low frequency flexural peak is very good indication of the debonding at shallow depths. The additional analysis is necessary of the depth of the debonding has to be estimated.

SASW

The SASW method provides the shear wave velocity profile. The ultrasonic surface wave (USW) method is a variation of the SASW where the frequencies are confined to very high

frequencies and therefore the shear wave velocity profile within the topmost layer is resulted (Nazarian et al., 1993). In the SASW/USW, the variation in the phase velocity with wavelength, called a dispersion curve, is generated. At wavelengths less than or equal to the thickness of the uppermost layer, the velocity of propagation of surface waves is more or less independent of wavelength. Assuming that the properties of the uppermost layer are uniform, if one simply generates high-frequency (short-wavelength) waves, the phase velocity of the upper layer can be determined. The wavelength at which the phase velocity is no longer constant is closely related to the thickness of the top layer (Nazarian et al., 1997).

For two layers with similar modulus bonded together, the variation in modulus with depth is more or less constant. However, when the two layers are debonded, the variation in modulus with depth is significantly reduced below the interface of the two layers. This principle can be readily used to not only detect but also identify the approximate depth of the debonded layers. This method has been successfully used in a few forensic studies to detect HMA debonding (Hammons et al., 2005). As an example, typical dispersion curves (the variations in modulus versus depth) obtained through the USW analysis from locations of an intact and a damaged core are shown in Figure A.22. The dispersion curve for the intact core would have been constant if different lifts were of the same material. However, at least four different lifts can be identified in the first 12 in. of the intact core shown in Figure A22a. The top layer (first 4 inches) is significantly stiffer than the rest. From 4 to 6 inches, the material seems to be of lower quality and below 6 inches the modulus increases again. In the case of the damaged core, the top 4 in. seem to be stiffer. A significant drop in modulus is observed at a wavelength of 4 in. where some loss of material was found due to stripping. The modulus increases again at a depth of 6 in.

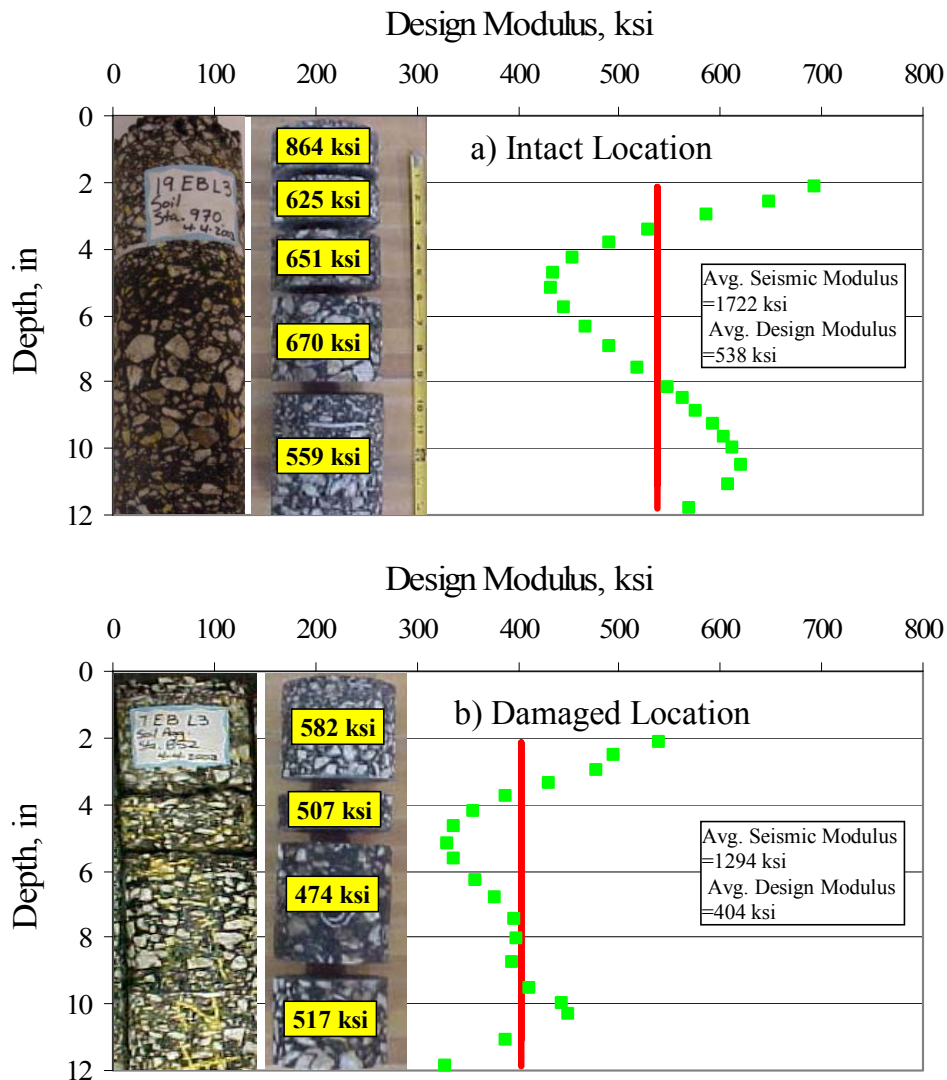


Figure A.22 – Typical Intact and Damaged-Location Dispersion Curves and Variation in Modulus with Depth for Cores after Being Saw cut (a) Intact Location and (b) Damaged Location. (Hammons et al., 2005)

To further investigate the differences observed in dispersion curves, retrieved cores were saw cut into distinct layers, and the seismic modulus of each layer was determined in the laboratory. The core pieces and their corresponding moduli are also shown in Figure A.22. For the intact core, the laboratory measurements demonstrate a similar trend as that delineated by USW. Removal of some material from the interfaces during the saw cut operations, and the

averaging process of moduli of deeper layers inherent in surface wave method may explain the higher values in moduli obtained with the ultrasonic device. For the damaged core, the modulus measured with the USW method compares reasonably well with the modulus from the ultrasonic device for the top 4 in. (depth where the stripping occurred). The USW results below a depth of 4 in. are considerably lower than those from the ultrasonic device because of the significantly lower modulus of the stripped layer (note that the stripped material was lost during coring).

Delatte et al. (2002) recognized the SASW method as an NDT tool for estimating the engineering properties of surface layers. In their study, thin concrete overlays on top of asphalt in airport pavements were investigated with the FWD and SASW techniques to measure stiffness of the top and underlying layers and to detect potential debonding. It was concluded that the SASW method could be used to assess the condition and thickness of pavement layers and could be used to monitor the overlay condition and investigate potential problem areas. A combination of SASW and FWD testing was recommended for better evaluation of airport pavements.

IE-SASW

Nazarian et al. (1993) developed automated testing equipment known as the Seismic Pavement Analyzer (SPA). Later, the same technology was implemented in portable hand-held device called the Portable Seismic Pavement Analyzer (PSPA). PSPA can automatically conduct both IE and SASW tests simultaneously and it is designed so that it would work on rough HMA surfaces. The PSPA measures the average modulus of the exposed surface layers within a few seconds in the field. The operating principle of the PSPA is based on generating and detecting stress waves in a layer. The Ultrasonic Surface Wave (USW) interpretation method (Nazarian et al. 1993) is used to determine the modulus of the material. The PSPA, as shown in Figure A.23, consists of two transducers (accelerometers in this case) and a source

packaged into a hand-portable system, which can perform high-frequency (1 kHz to 50 kHz) seismic tests. The source package is also equipped with a transducer for consistency in triggering. The device is operable from a computer tethered to the hand-carried transducer unit through a cable that carries operational commands to the PSPA and returns the measured signals to the computer.

To collect data with the PSPA, the technician initiates the testing sequence through the computer. All the other data acquisition tasks are handled automatically by the computer. The source, which is a computer-controlled solenoid, is activated four to six times. Pre-recording impacts of the source are used to adjust the amplifiers in a manner that optimizes the dynamic range of the electronics. The outputs of the three transducers from the final three impacts are saved and averaged for more reliability. Typical voltage outputs of the three accelerometers are shown in Figure A.24. In any seismic method, the goal is to determine the velocity of propagation of waves within a material. These records are used to determine the velocity of propagation of waves in the HMA layer.

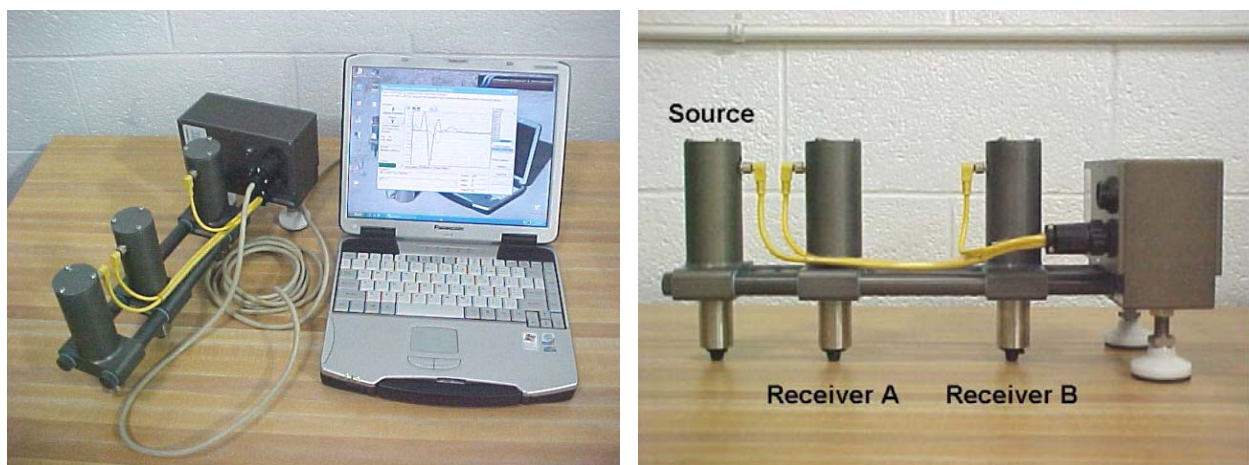


Figure A.23 – Portable Seismic Pavement Analyzer

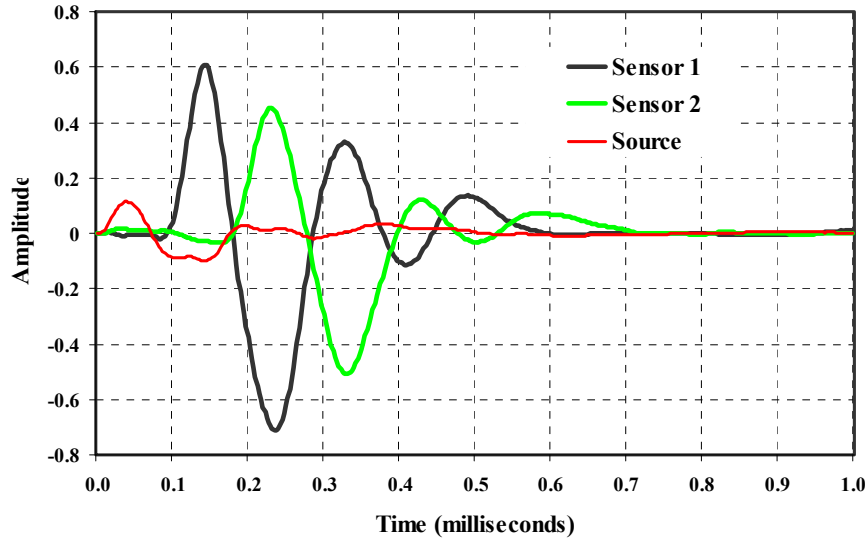


Figure A.24 – Typical Records from PSPA

The SASW method can yield the wave velocity and subsequently the modulus of the uppermost layer. The results of IE test will reveal the locations of defects within the layer. Knowing the velocity from SASW test, one may determine the depth of the reflectors and/or the thickness of the top layer. This process has been automated and incorporated in PSPA. PSPA has been previously used for determining the modulus, and thickness of the upper pavement layer (Ganji, 1998). The old version of the PSPA was proved successful for detection of debonding between bituminous layers with similar properties, provided the interface is deeper than 100 mm from the pavement surface (Armitage et al., 2000; Kruntcheva et al., 2000). The newer version of PSPA is equipped with a higher frequency source that can provide information for shallower depths. PSPA has been recently used to detect stripping and other types of water damage in asphalt pavements (Hammonds et al., 2005). SASW-based moduli provided supplementary information which greatly facilitated the interpretation of IE test results.

Ultrasound

Ultrasonic waves are elastic waves of audible frequency (above 20 kHz). Ultrasonic testing has been used for detection and characterization of internal defects in a material, and measurement of the thickness and mechanical properties of a solid (stresses, toughness, and elasticity constants) by Garbacz and Garboczi (2003).

The ultrasonic-echo method is often used for defect detection. The test procedure involves the generation of a short pulse of ultrasonic frequency and transmitting it through the material by a transducer. After being reflected by the material's heterogeneity (including defects) or by the limiting boundaries, the pulses are recorded by the receiving transducer which can be the transmitter itself as shown in Figure A.25. A portion of the ultrasonic wave which is reflected by the target defect is known as the defect's echo. The portion of the ultrasonic energy that reaches the opposite wall of the tested material, is reflected and returns to the receiver with some delay is known as the back-wall echo. Knowing the ultrasonic wave velocity in the material under investigation, the depth of the defects or other reflecting surfaces can be determined from the measured arrival times of the echoes (Garbacz and Garboczi, 2003).

Ultrasonic testing of multi-phase heterogeneous materials such as HMA is challenging. The challenge lies in the fact that heterogeneities of comparable size (or larger than) the ultrasonic wavelength result in scattering and attenuation of ultrasonic energy. The grain size should be significantly smaller than the target defects; otherwise, any defect echo will be masked by the echoes from the grain boundaries.

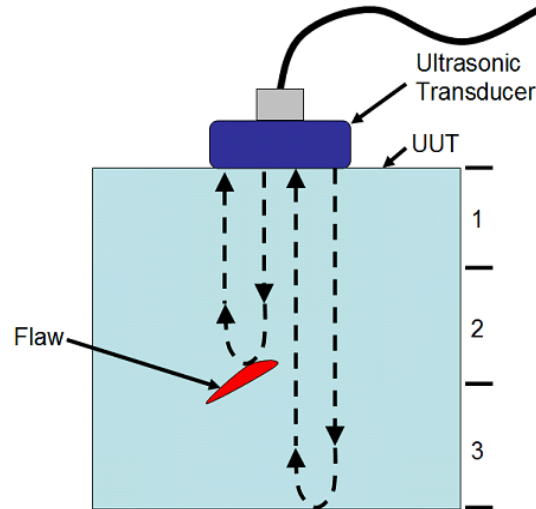


Figure A.25 – Delamination Detection by Ultrasonic Echo Method

Recently a low-cost multi-sensor dry-contact *Ultrasonic Device* (A1040 POLYGON, as shown in Figure A.26) has been developed in Russia (AKC) in cooperation with Germany's Federal Institute for Materials Research and Testing (BAM). The equipment includes 8 to 16 spring-mounted ultrasonic transducers of a nominal frequency of 50 KHz (20-100 KHz). Using real-time tomographic imaging principles, this system provides a detailed image of the interior of the material and can resolve cracks, flaws, and other heterogeneities, as shown in Figure A.27. This equipment has been developed specifically for testing of concrete and has not been used in imaging of HMA (Acoustic Control Systems, www.acsys.ru/eng/).



Figure A.26 – A1040 POLYGON Ultrasonic Device

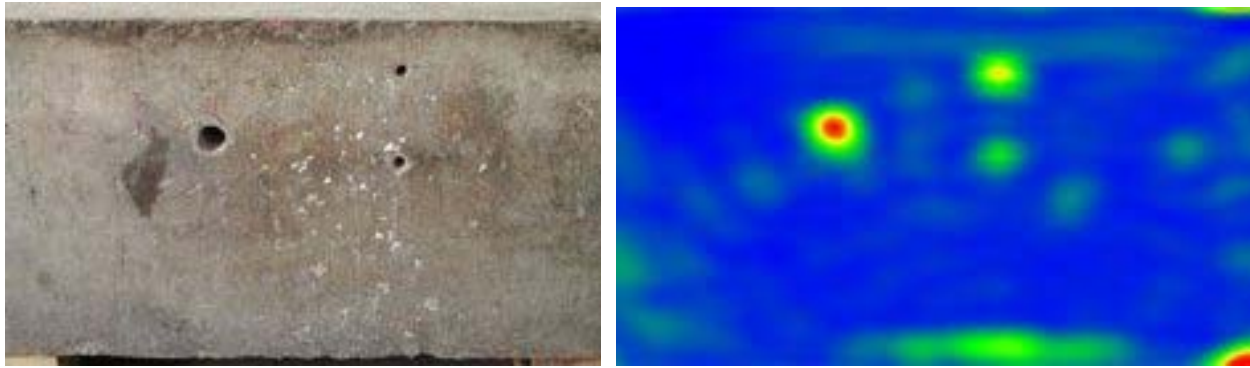


Figure A.27 – Real Time Tomographic Imaging of an Internal Structure of a Concrete Specimen

Thermal Methods

Infrared Thermography

Infrared (IR) thermography provides a nondestructive means of temperature measurement by detecting the differences in infrared radiations emitted from objects at different temperatures. The presence of shallow subsurface voids results in anomalies (hot or cold spots) in surface temperature distribution maps. Therefore, IR thermography can be used to indirectly locate near-surface flaws and voids

The technique involves the use of IR cameras for non-contact surface temperature measurement, as shown in Figure A.28. In some applications, the object to be tested is artificially heated to produce the desired temperature differentials (active method). In other applications, the heat source is either the solar radiation or the natural temperature of the material or structure being tested. In either case the infrared sensor detects the infrared radiation emitted from the object, and converts the radiation measurement into a temperature measurement using the Stefan-Boltzmann Law:

$$Q = \sigma E(T^4 - T_0^4) \quad (A.6)$$

where Q is the radiation emitted from an object, σ is the Stefan-Boltzman constant, E is the emissivity of the object, T is the absolute temperature of the object, and T_0 is the absolute temperature of the surroundings.



Figure A.28 – Infrared Survey Vehicle

IR thermography has found some applications in pavement construction and maintenance. The technology has been used at the time of placement of HMA to investigate the relationships between the rate of cooling of newly placed HMA overlays and the variations in the measured post-construction volumetric and engineering properties of field cores (Sebesta and Scullion, 2002). Stroup-Gardiner and Brown (2000) showed that temperature differentials measured by IR were significantly related to changes in the properties of the finished mat such as air void content and gradation. On existing pavements, the IR technology can be used to relate local temperature gradients to the presence of shallow subsurface flaws in HMA. It is believed that the trapped air in a delamination or cracked zone acts as an insulator blocking the heat transfer between the HMA lifts above and below the delaminated interface. Consequently, the

surface of the pavement over the delaminated exhibits a temperature gradient (negative at night and positive during the day) with respect to its surrounding fully bonded area.

An example of temperature distribution during daytime condition using finite element analysis for an asphalt layer with some delamination is shown in Figure A.29 (Tsubokawa et al., 2007). In one study, the asphalt pavement was actively heated to detect defects (Maser, 2003).

The IR technology has been previously used for detection of shallow delamination in HMA airfield pavements in Japan and Greece (Tsubokawa et al., 2007, Moropoulou et al., 2002). For example, two thermographic images taken from a runway in the International Airport of Athens are shown in Figure A.30. Surveys were carried out through daytime, at times of rapid heat transfer (approximately 3 hours after sunrise), between January and March. The surface temperature of the pavement, as well as the environmental conditions, such as air temperature and relative humidity, were taken into consideration. The defects were identified where a temperature difference of at least 0.5° between the defected areas and intact pavement exists (ASTM standard D4788-88) and marked on the thermographs as shown in Figure A.30. These defects were attributed to the aging of the HMA airfield pavement. They concluded that to achieve the best results, tests should be executed on sunny days and during daytime to allow more rapid and effective energy transfer to the pavement. Since moisture could affect the surface temperature and the defect detection, tests should be completed at times where the pavements are dried out (Moropoulou et al., 2002).

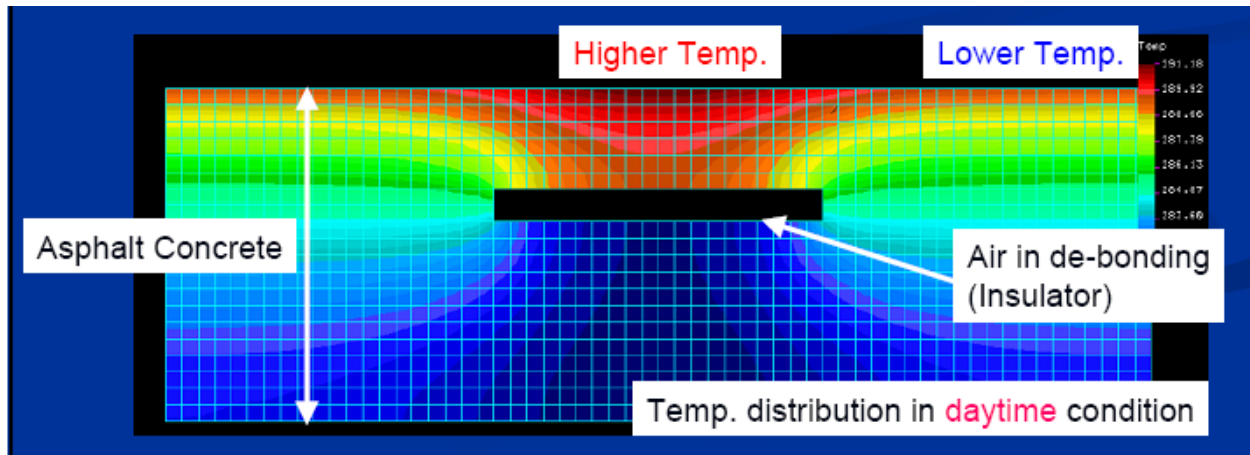


Figure A.29 – Example Image of Thermal Analysis (Daytime Condition) (from Tsubokawa et al., 2007)

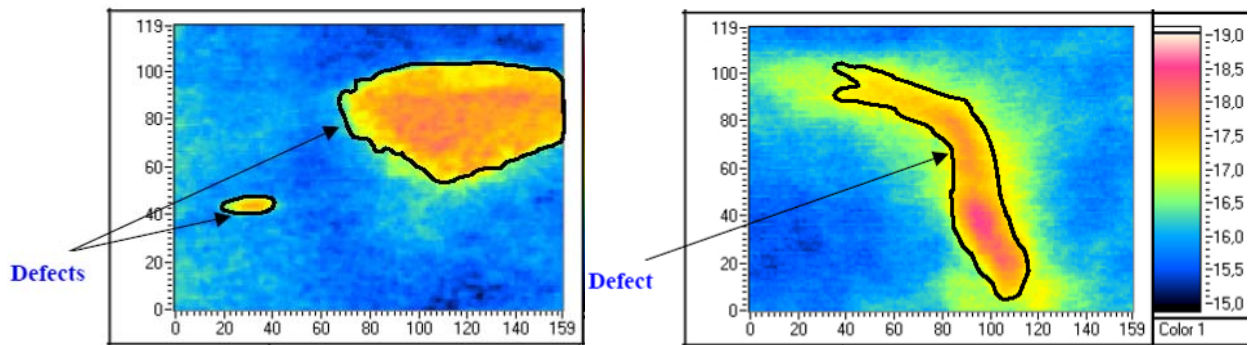


Figure A.30 – Thermographs Showing Defects on Asphalt Runway (Moropoulou et al., 2002)

Infrared thermography and Impact Echo were used side-by-side to detect delamination in airport flexible pavements in Japan (Tsubokawa et al., 2007). A trial section on a runway-taxiway intersection of 10 m by 10 m was used. As shown in Figure A.31a, the inspection area was divided into small squares of 50 cm by 50 cm, each area was tested using IE, and the debonded zones were identified and marked. Later, the infrared images of the same area were taken every 30 min from 0:30 a.m. to 5:30 a.m. (Figure A.31b). Air temperature and intensity of

solar radiation during the tests were recorded. In Figure A.31b, darker areas represent lower temperature than the white areas. The low-temperature areas (cold spots) generally matched the debonded areas found by the IE method. A number of cores were retrieved from the seven low temperature areas marked in Figure A.31b. Shallow debonding (40 to 70 mm below the surface) at all seven locations was confirmed (Tsubokawa et al., 2007).

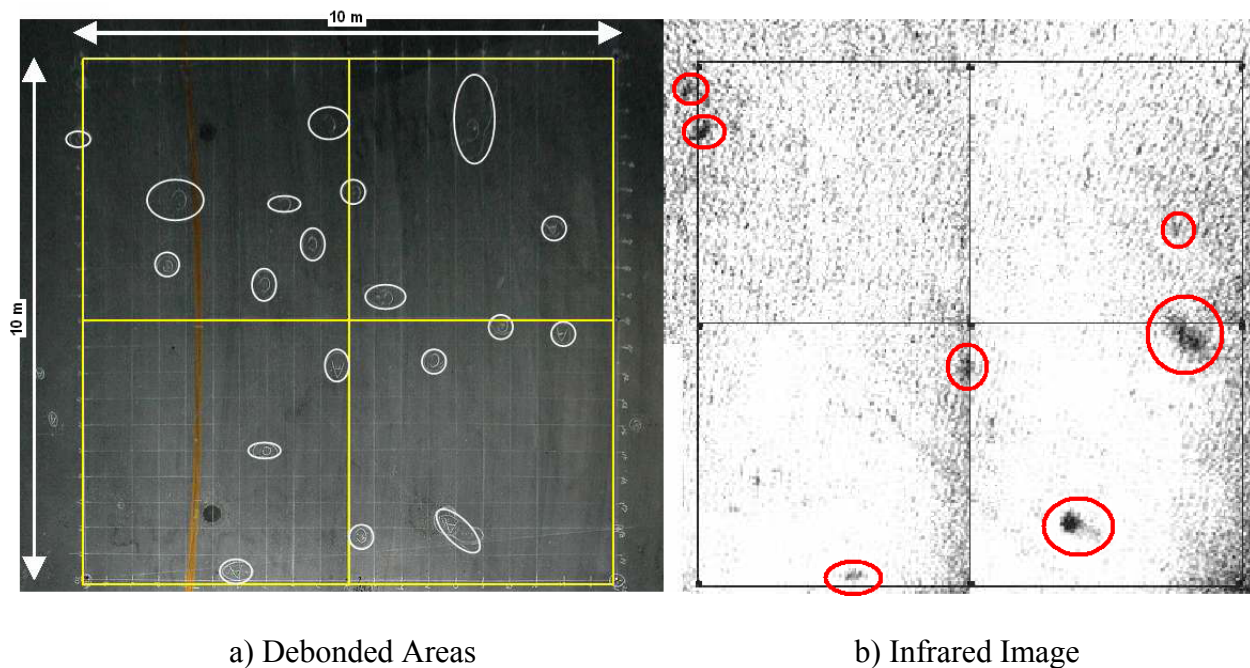


Figure A.31 – Low-temperature Areas Generally Match the Debonded Areas Found by IE.
(Tsubokawa et al., 2007)

In sum, both studies concluded the effective use of the IR for large areal inspection but also reported a number of limitations associated with the application of this technology. The IR technology provides a rapid means of inspection of the large airfield pavements and gives areal images. However, it cannot provide the exact dimensions or the depth of the localized defects. Moreover, the reliability of the results is compromised by its high sensitivity to ambient environmental and surface conditions such as solar radiations, air temperature, wind speeds, surface texture, pavement grooves, the external debris, shadow zones, etc. Some of the

environmental effects can be minimized if the evaluation is based on temperature gradients (relative temperatures) rather than absolute temperature values for the effect of ambient condition will be the same and therefore, will be neutralized in individual thermal shots. The presence of external debris such as rubber on the surface of the runways introduces further difficulties in interpretation of thermal images (Tsubokawa et al., 2007). Furthermore, given the dependency of temperature differentials on air void content, a coarsely segregated spot may be misinterpreted as a delaminated zone.

APPENDIX B – JOB MIX FORMULAE

MATERIAL DATA SHEET

ASPHALTIC CONCRETE MIX DESIGN

February 8, 2008

SOURCE: JOBE MATERIALS, L.P.
MATERIAL: PMBP ITEM P 403 – BASE COURSE
PROJECT: EPIA – RECONSTRUCTION OF TAXIWAY J & M
CLIENT: C F JORDAN INFRASTRUCTURES

SIEVE SIZE	MASTER GRADING	JMF	ACTION LIMIT
1”	100	100	100
3/4 “	76 – 98	96	90 - 100
1/2 “	66 – 86	82	76 – 88
3/8	57 – 77	71	65 - 77
No.4	40 – 60	50	44 - 56
No. 8	26 – 46	35	-----
No.16	17 – 37	26	21 - 31
No.30	11 – 27	19	-----
No.50	7 – 19	13	10 – 16
No.100	6 – 16	7	-----
No. 200	3 – 6	4.7	2.7 – 6.7
Asphalt Content	4.5 – 7.0	4.9	4.45 – 5.35
Percent Air Voids:	4.0%		Design : 2 – 5
Marshal Stability : 2780			Design : 1800 Min.
Flow : 12			Design : 8 – 16
Voids in Mineral Agg (V _{ma}): 15			Minimum: 14
Voids filled with Asphalt: 73 %			Range: 65 -78
TSR : 90 .1%			Minimum: 75 TSR
Dust / Asphalt Ratio : 0.96			Range: 0.8 to 1.4
Asphalt film thickness: 9.7 microns			Minimum: 8 microns

Recommend Mixing / discharge Temp: 320 F, Laboratory molding Temp: 295 F
Design based on 75 blow Marshall method, per Asphalt Institute MS-2 6 th Ed. and ASTM D 6926 & 6927. Asphalt cement is Western refining PG 64-22. Liquid anti-strip Azko Nobel Wet -fix 312, added at a rate of 0.5%. Mix was recently used for Reconstruction of Runway 8R-26L and Taxiway E.

JOBE MATERIALS, LP

RICHARD L. RICE, CET
QUALITY CONTROL

MATERIAL DATA SHEET

ASPHALTIC CONCRETE MIX DESIGN

February 8, 2008

SOURCE: JOBE MATERIALS, L.P.
MATERIAL: PMBP ITEM P 401 – SURFACE COURSE
PROJECT: EPIA – RECONSTRUCTION OF TAXIWAY J & M
CLIENT: C F JORDAN INFRASTRUCTURES

SIEVE SIZE	MASTER GRADING	JMF	ACTION LIMIT
1"	100	100	100
3/4 "	76 – 98	96	90 - 100
1/2 "	66 – 86	82	76 – 88
3/8	57 – 77	71	65 - 77
No.4	40 – 60	50	44 - 56
No. 8	26 – 46	35	-----
No.16	17 – 37	26	21 - 31
No.30	11 – 27	19	-----
No.50	7 – 19	13	10 – 16
No.100	6 – 16	7	-----
No. 200	3 -- 6	4.7	2.7 – 6.7
Asphalt Content	4.5 – 7.0	5.2	4.75 – 5.65

Percent Air Voids: 3.5%
Marshal Stability : 2800
Flow : 13
Voids in Mineral Agg (Vma): 15
Voids filled with Asphalt: 75 %
TSR /Dry Strength @ 5.2 : 92 / 234
Dust / Asphalt Ratio : 0.9
Asphalt film thickness: 10.4 microns

Design : 2.8 – 4.2
Design : 2150 Min.
Design : 10 - 14
Minimum: 14
Range: 65 -78
Minimum: 75 / 200 psi
Range: 0.8 to 1.4
Minimum: 8 microns

Recommend Mixing / discharge Temp: 335 F, Laboratory molding Temp: 305 F
Design based on 75 blow Marshall method, per Asphalt Institute MS-2 6 th Ed. and ASTM D 6926 & 6927. Asphalt cement is Western Refining PG 76-22. Liquid anti-strip Akzo Nobel Wet-fix 312 added at a rate of 0.5%. Mix was recently used for Reconstruction of Runway 8R-26L and Taxiway E.

JOBE MATERIALS, LP

RICHARD L. RICE, CET
QUALITY CONTROL

APPENDIX C – CONSTRUCTION DETAILS OF CONTROLLED STUDY

Schematic of Delamination on Controlled Study

Details on the distribution of the debonding for each of the prepared sections are illustrated on Figure C.1 for the coarse mix sections, Figure C.2 for the fine mix sections and Figure C.3 for the transition area.

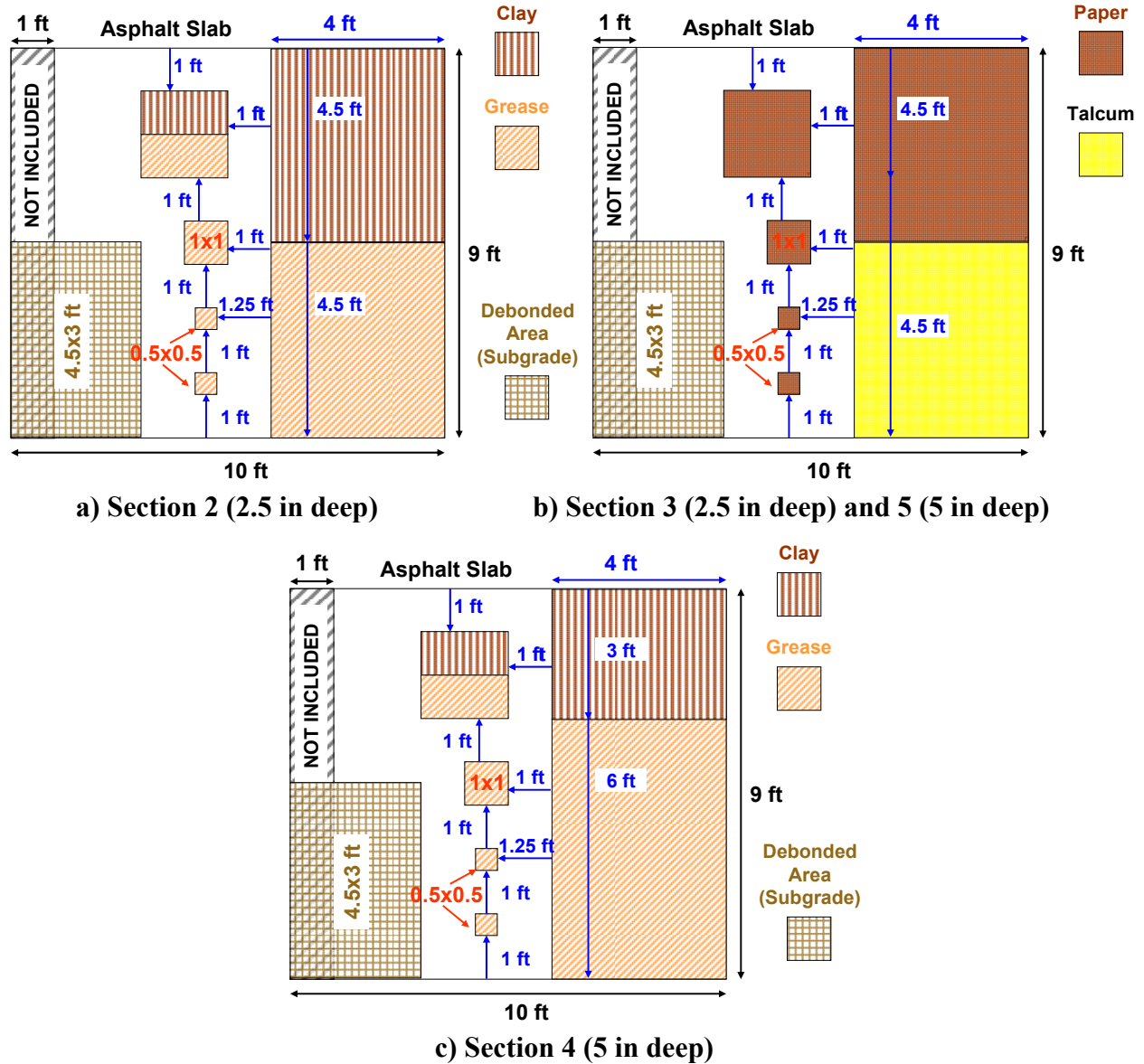
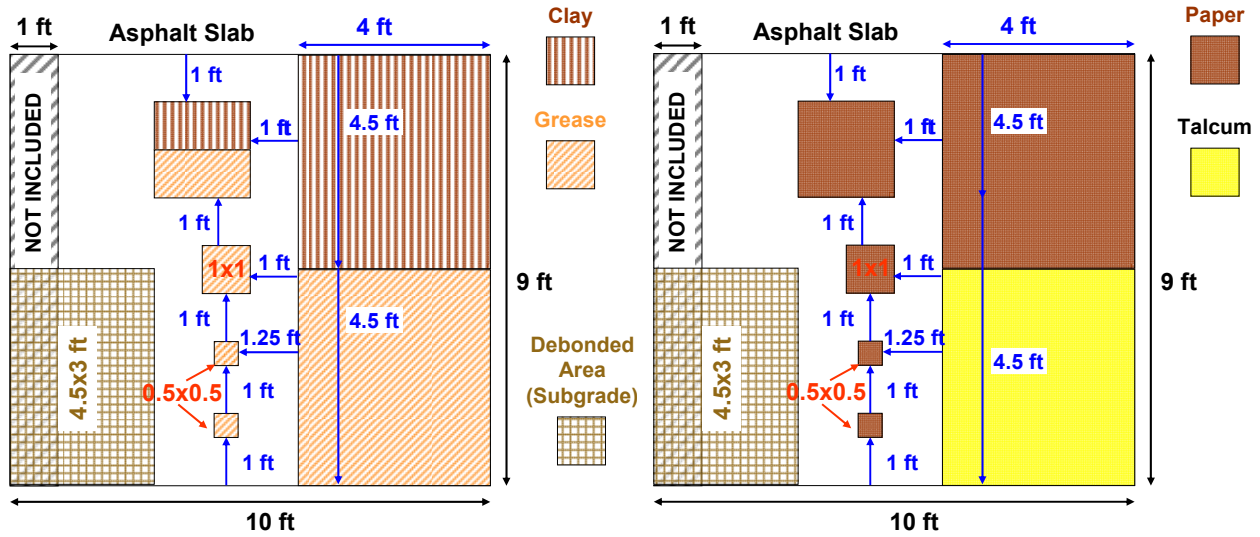


Figure C.1 – Layout of Delamination on Coarse Mix Sections



a) Section 7 (2.5 in deep) and 9 (5 in deep) b) Section 8 (2.5 in deep) and 10 (5 in deep)

Figure C.2 – Layout of Delamination on Fine Mix Sections

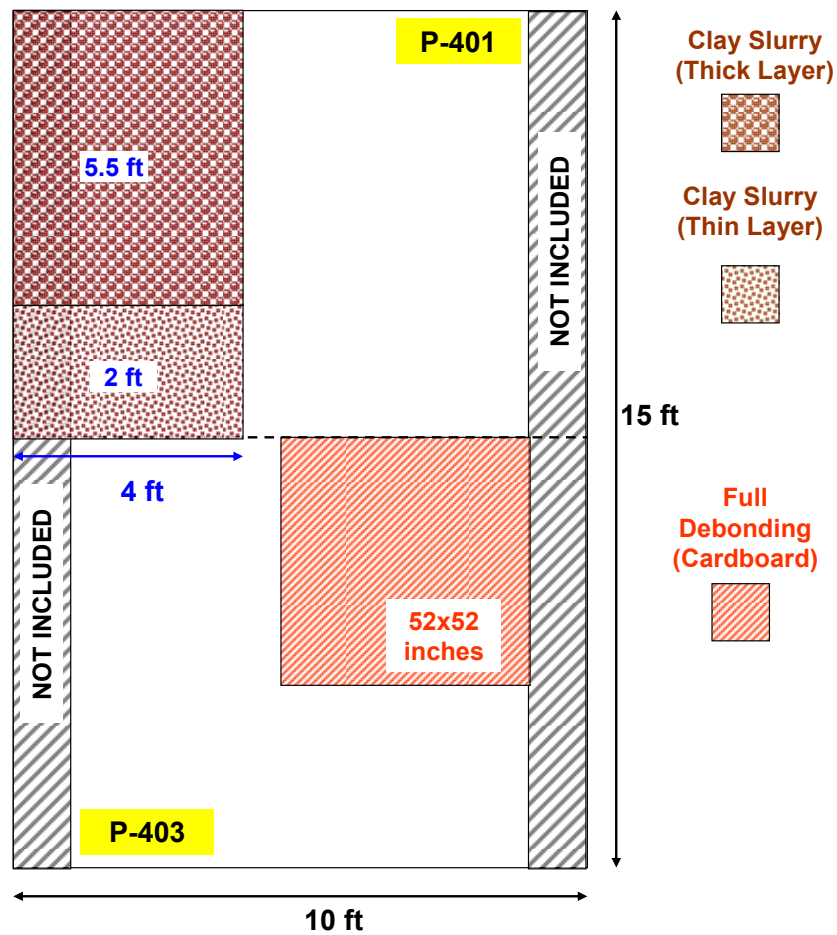


Figure C.3 – Layout of Delamination on Transition Sections

Subgrade Preparation and Construction of Asphalt Base

During the first day of construction, the subgrade was prepared to accommodate the asphalt base. The subgrade was reworked, graded, watered and compacted during the first day of construction (see Figure C.4).



Figure C.4 – Preparation of Subgrade

On the second day, the marking of the sections and the placement of the subgrade debonding material was conducted initially. Sections of 4.5 by 3 ft corrugated cardboard soaked in motor oil were used to simulate debonding between the subgrade and the asphalt base, as detailed in Figure C.5a.

Once the subgrade was prepared, the asphalt base mix (P-403) was shipped to UTEP and placed in the asphalt paver (see Figure C.5b). An asphalt paver distributed the asphalt on a 10 foot wide lane along the length of the section (Figures C.5c and C5.d). After the asphalt base was laid down a static compactor was used to compact the asphalt to the desired compaction level and to match the required thickness of 3 inches (Figures C.5e and C5.f).

After the asphalt base was compacted and the surface was cool enough, the locations of the different debonded areas were marked on Sections 4, 5, 9 and 10. As an example, Figure C.6a shows debonding areas on sections 9 and 10 after they were marked out on the pavement. The



a)



b)



c)



d)



e)



f)

Figure C.5 – Construction of Asphalt Base

spreading of the debonding agents on these sections was next. Figure C.6b illustrates the application of grease, clay slurry and talcum powder on the same sections. After these materials dried out, debonding areas were covered with pieces of corrugated cardboard and plywood to avoid intrusion from emulsion and prevent damage from construction traffic (see Figure C.6c). Then, a standard amount of tack coat was applied on the entire section, as depicted in Figure C.6d.



a)



b)



c)



d)

Figure C.6 – Construction of Debonding Sections on Asphalt Base (Deep Debonding)

As recommended by the technical panel a thermocouple to measure the temperature of the asphalt was installed in Section 1. A small groove was excavated and the thermocouple was inserted and attached to the pavement (see Figure C.7). The temperature sensor is used at the time of field testing to measure temperature profiles within the pavement structure.



Figure C.7 – Installation of Thermocouple on Asphalt Base

Construction of Asphalt Pavement

After the tack coat on the asphalt base was dry, the material used as first layer of asphalt (P-401 mix) was distributed with the paver (see Figures C.8a and C.8b). Some loose material was spread on top of the small debonding areas these areas to avoid any damage from the paver (Figure C.9a). The big debonding areas dig not show any damage from the paver as it was going trough (see Figure C.9b). After the asphalt was placed, the same static compactor was used to achieve the desired height of 2.5 inches (see Figure C.9c). Similarly to the asphalt base, a thermocouple was installed after the asphalt was compacted. In this case, the thermocouple was placed on the transition section (see Figure C.9d).



Figure C.8 – HMA Delivery to the Site

On the third day the construction of the top layer of HMA was accomplished. The same process followed to construct the debonding areas the day before was reproduced on the second layer of HMA (see Figure C.10a) for Sections 2, 3, 7 and 8. After the asphalt was placed with the paver, it was compacted with a static compactor followed by a pneumatic roller to finish the section (see Figure C.10b).

In addition to the predetermined debonded areas, two supplementary areas were located on the transition section. One area of severe debonding was constructed on the coarse mix segment. A cardboard section of 52x52 inches was attached to the bottom layer of HMA (see Figure C.11a). The other area covered a section of 7.5 foot long and 4 foot wide on the fine mix. On the first 2 feet a very thin application of clay slurry was used and on the other 5.5 feet a very thick layer of the same material was employed as shown in Figure C.11b.



a)



b)



c)



d)

Figure C.9 – Construction of Bottom Layer of HMA



a)



b)

Figure C.10 – Construction of Top Layer of HMA



a)



b)

Figure C.11 – Construction of Additional Debonding on Transition Section

Table C.1 – NDG Density Results after Completion of Controlled Study

Location	Section Number and Density (pcf)										
	1	2	3	4	5	T	6	7	8	9	10
LWP	139.2	150.1	141.8	142.9	137.5	141.5	148.5	140.8	141	138.8	148.9
Center	138.8	139.8	136.1	151.1	139.7	142.3	138.8	143.8	140.7	138	140.7
RWP	138.3	137.3	136.9	140.4	159.3	147.7	140.8	146.8	135.5	140	140.1
						145.8					

Table C.2 – Percentage of Marshall Density Obtained with NDG after Completion of Controlled Study

Location	Section Number and % of Marshall Density*										
	1	2	3	4	5	T	6	7	8	9	10
LWP	92.9	100.1	94.6	95.4	92	94.4	99	93.9	94.1	92.6	99.3
Center	92.6	93.2	90.8	100.8	93.2	94.9	92.6	95.9	93.9	92.1	93.9
RWP	92.3	91.6	91.3	93.6	106.2	98.5	93.9	97.9	90.4	93.4	93.4
						97.2					

* 100% of Marshall Density was 149.9 pcf

Table C.3 – PSPA Results after Second Day of Construction (Lifts 1 and 2 Combined)

Location	Point	Seismic Modulus (ksi)		
		LWP	Center	RWP
S10, Deep and Full Debonding	2	1858	1708	1222
	1	1891	1901	1108
S9, Deep and Partial Debonding	2	2004	1703	1312
	1	1651	2065	1503
S8, Shallow and Full Debonding	2	1759	2051	1858
	1	2112	2197	1957
S7, Shallow and Partial Debonding	2	1910	1877	1731
	1	1656	1811	1642
S6, Intact Area	2	1995	2018	1717
	1	1943	2037	1905
TRANSITION	1	1850	1872	1896
S5, Deep and Full Debonding	2	1868	1703	1133
	1	1797	1440	1056
S4, Deep and Partial Debonding	2	1774	1623	1171
	1	1534	1585	1110
S3, Shallow and Full Debonding	2	1670	1614	1548
	1	1599	1726	1651
S2, Shallow and Partial Debonding	2	1614	1689	2004
	1	1585	1670	1642
S1, Intact Area	2	1872	1543	1717
	1	1759	1402	1640

Table C.4 – PSPA Results after Second Day of Construction (Top Lift)

Location	Point	Seismic Modulus (ksi)		
		LWP	Center	RWP
S10, Deep and Full Debonding	2	1825	1769	1563
	1	1938	2216	1470
S9, Deep and Partial Debonding	2	2013	1891	1440
	1	1736	2183	1778
S8, Shallow and Full Debonding	2	1821	2140	1882
	1	2070	2169	1882
S7, Shallow and Partial Debonding	2	2009	1966	1736
	1	1741	1910	1637
S6, Intact Area	2	2131	2206	1835
	1	1976	2145	1999
TRANSITION	1	1995	1924	1818
S5, Deep and Full Debonding	2	1990	1712	1494
	1	1731	1618	1317
S4, Deep and Partial Debonding	2	1821	1604	1442
	1	1505	1585	1352
S3, Shallow and Full Debonding	2	1679	1604	1609
	1	1646	1778	1614
S2, Shallow and Partial Debonding	2	1637	1844	1853
	1	1806	1694	1651
S1, Intact Area	2	1849	1548	1698
	1	1712	1427	1621

Table C.5 – PSPA Results after Completion of Construction (3 Lifts Combined)

Location	Point	Seismic Modulus (ksi)		
		LWP	Center	RWP
S10, Deep and Full Debonding	2	1628	1948	1684
	1	1885	1797	1648
S9, Deep and Partial Debonding	2	1774	1659	1741
	1	1745	2023	1794
S8, Shallow and Full Debonding	2	1938	1888	1321
	1	1717	1872	1197
S7, Shallow and Partial Debonding	2	1936	1679	1511
	1	1587	1590	1806
S6, Intact Area	2	1901	1792	2055
	1	1891	1941	1853
TRANSITION	1	1626	1549	1769
S5, Deep and Full Debonding	2	1979	1524	1229
	1	1853	1969	1559
S4, Deep and Partial Debonding	2	2104	2007	1870
	1	1764	2032	1618
S3, Shallow and Full Debonding	2	1599	1800	1465
	1	2092	1621	1440
S2, Shallow and Partial Debonding	2	1599	1844	1344
	1	2177	2079	1650
S1, Intact Area	2	2506	2042	1874
	1	1835	1943	1882

Table C.6 – PSPA Results after Completion of Construction (Top Lift)

Location	Point	Seismic Modulus (ksi)		
		LWP	Center	RWP
S10, Deep and Full Debonding	2	1929	2434	2051
	1	2079	1905	2070
S9, Deep and Partial Debonding	2	1849	1891	1949
	1	1976	2308	1982
S8, Shallow and Full Debonding	2	2432	2095	1936
	1	1924	2129	1479
S7, Shallow and Partial Debonding	2	2065	1872	1684
	1	1706	1915	2096
S6, Intact Area	2	2023	1929	2324
	1	2366	2136	2124
TRANSITION	2	1946	1643	1896
	1	2010	1978	1752
S5, Deep and Full Debonding	2	1943	2336	2004
	1	2365	2214	2206
S4, Deep and Partial Debonding	2	1679	2148	2244
	1	2070	2007	1951
S3, Shallow and Full Debonding	2	2311	1681	1761
	1	2007	2264	1652
S2, Shallow and Partial Debonding	2	2515	2380	2102
	1	2779	2368	2004
S1, Intact Area	2	2032	2279	1966
	1	2018	2173	1886

Appendix D – COMPLETE NDT RESULTS ON CONTROLLED STUDY

Table D.1 – PSPA Results on Small Scale Study (3 Lifts Combined). Coarse Mix

Section	Point	Seismic Modulus from PSPA (for 8 in), ksi				
		Line 1	Line 2	Line 3	Line 4	Line 5
S5, Deep and Full Debonding	5	1733	1851	1652	1508	1627
	4	1845	1767	1914	1599	1421
	3	1914	1879	1684	1690	1481
	2	1783	1374	1614	1573	1284
	1	1666	1827	1651	1442	1527
S4, Deep and Partial Debonding	5	1645	1712	1984	1837	1437
	4	1724	1502	2025	1653	1511
	3	1668	1612	1676	1696	1726
	2	1955	1729	1815	1817	1548
	1	1808	1715	1666	1453	1044
S3, Shallow and Full Debonding	5	1633	1347	1747	1387	1091
	4	1933	1643	1714	1266	1054
	3	1956	1611	1617	1326	1313
	2	1891	1527	2325	987	1151
	1	1983	1874	1908	1289	1048
S2, Shallow and Partial Debonding	5	1929	1626	1563	1320	1146
	4	2214	1778	1974	1768	1774
	3	1951	1755	1899	1740	1626
	2	2236	1957	1807	1643	1667
	1	2231	1685	1977	1804	1902
S1, Intact	5	1991	1829	1825	1751	1922
	4	1736	1636	1589	1891	1876
	3	1812	1714	1854	1963	1683
	2	1777	1690	1835	1626	1699
	1	1768	1921	1674	1602	1745

Table D.2 – PSPA Results on Small Scale Study (3 Lifts Combined). Fine Mix and Transition

Section	Point	Seismic Modulus from PSPA (for 8 in), ksi				
		Line 1	Line 2	Line 3	Line 4	Line 5
S10, Deep and Full Debonding	5	1875	1925	2340	1958	1812
	4	1802	1993	2213	2018	1677
	3	1760	2356	2234	2073	1572
	2	1990	1902	2058	2006	1615
	1	1873	1899	2117	1888	1557
S9, Deep and Partial Debonding	5	1802	1569	1646	1598	1729
	4	1655	1753	2050	1986	1820
	3	1845	1720	1922	2093	1661
	2	1882	1741	1825	2140	2034
	1	1828	1795	1836	1397	1446
S8, Shallow and Full Debonding	5	1869	1469	2141	1629	1375
	4	1448	1513	1919	1542	1463
	3	1524	1856	2335	1667	1409
	2	1873	1744	2048	1674	1469
	1	1598	1719	2051	1578	1612
S7, Shallow and Partial Debonding	5	1644	1300	1649	1531	1538
	4	1727	2023	1854	1547	1611
	3	1628	1960	1880	1592	1777
	2	1824	1819	1750	1766	1680
	1	1762	1813	1961	1771	1841
S6, Intact	5	1717	1962	1569	1924	2180
	4	1827	2171	1968	2025	2031
	3	1809	2095	1828	2175	2078
	2	2083	2212	1967	2307	2156
	1	1443	1953	2134	2116	1990
TRANSITION	8	2200	1909	2137	2218	2010
	7	1558	1921	1854	1901	2064
	6	1373	1668	2268	1647	1983
	5	1680	2155	2229	2121	1747
	4	2037	2217	1607	1448	1185
	3	1995	1970	1411	1518	1163
	2	2321	2111	2254	2388	1925
	1	1989	1994	2246	1946	2041

Table D.3 – PSPA Results on Small Scale Study (Top Lift). Coarse Mix

Section	Point	Seismic Modulus from PSPA (for 2.5 in), ksi				
		Line 1	Line 2	Line 3	Line 4	Line 5
S5, Deep and Full Debonding	5	2130	2067	1858	1719	1599
	4	1891	1790	1989	1808	1500
	3	2106	1968	1909	1761	1758
	2	1862	1632	1773	1751	1528
	1	1899	1654	1936	1680	1888
S4, Deep and Partial Debonding	5	1771	1963	2179	2112	1736
	4	2086	1981	2118	1830	1768
	3	1705	1903	1862	1920	2178
	2	2225	1915	2104	2138	1963
	1	2043	1892	1973	2007	1487
S3, Shallow and Full Debonding	5	2008	1579	1942	1619	1347
	4	2169	1778	1775	1823	1537
	3	1947	1404	1626	1739	1643
	2	2071	1633	2242	1377	1508
	1	2001	2124	1889	1261	1457
S2, Shallow and Partial Debonding	5	2223	2078	2071	1427	1571
	4	2586	2022	2190	2026	2111
	3	2057	1999	2319	1952	2079
	2	2374	2206	2401	2007	2148
	1	2350	1828	2240	1997	2318
S1, Intact	5	2069	1701	2171	2111	2063
	4	2209	1805	1791	2169	2172
	3	2022	1875	1960	1854	1893
	2	2057	1773	2141	1886	1753
	1	2023	1842	1848	1868	1862

Table D.4 – PSPA Results on Small Scale Study (Top Lift). Fine Mix and Transition

Section	Point	Seismic Modulus from PSPA (for 2.5 in), ksi				
		Line 1	Line 2	Line 3	Line 4	Line 5
S10, Deep and Full Debonding	5	1977	2060	2403	2190	2292
	4	1832	2083	2422	2327	2068
	3	1882	2534	2440	2286	2020
	2	2105	2110	2162	2231	1973
	1	1989	2341	2297	2202	1994
S9, Deep and Partial Debonding	5	2084	1899	1767	1907	1878
	4	1862	1944	2212	2116	2128
	3	2170	2177	2277	2317	1826
	2	2211	1815	2240	2287	2028
	1	2063	2123	2157	1747	1878
S8, Shallow and Full Debonding	5	1929	1776	2279	1729	1717
	4	1522	1882	2226	2038	1832
	3	1657	1981	2377	2034	1780
	2	2003	1981	2366	1861	1669
	1	1754	1932	2054	1653	1779
S7, Shallow and Partial Debonding	5	1890	1630	1799	1694	1812
	4	1933	2198	2117	1825	1868
	3	1842	2094	2103	1815	2147
	2	1971	2148	1945	1998	1957
	1	1842	2003	2291	2025	1955
S6, Intact	5	1877	1954	1944	2293	2355
	4	1986	2443	2070	2365	2315
	3	1903	2034	2140	2359	2371
	2	2084	2434	2213	2455	2424
	1	1653	2309	1911	2215	2331
TRANSITION	8	2244	2344	2035	2234	2098
	7	1731	2066	1992	2045	2183
	6	1458	1713	2379	1806	2066
	5	1808	2489	2432	2465	2281
	4	2125	2162	1877	1888	1361
	3	2432	2413	2015	1988	1685
	2	2340	2484	2676	2561	2034
	1	2386	2431	2326	2364	2407

Table D.5 – FWD Results on Small Scale Study

Section	Point	Geophone S1 Deflection (mils)			Modulus, ksi		
		Line 1	Line 3	Line 5	Line 1	Line 3	Line 5
S10, Deep and Full Debonding	5	5.0	5.1	8.7	990	914	307
	3	5.5	5.1	9.8	741	899	252
	1	5.3	5.1	9.3	835	876	265
S9, Deep and Partial Debonding	5	4.9	5.4	7.3	898	689	409
	3	4.4	4.8	6.7	1085	881	458
	1	5.2	4.8	5.6	759	856	692
S8, Shallow and Full Debonding	5	5.1	6.8	8.2	849	380	228
	3	5.3	5.5	6.4	749	628	357
	1	5.5	5.7	5.6	697	598	495
S7, Shallow and Partial Debonding	5	5.2	6.4	6.0	784	451	489
	3	5.2	6.5	5.7	862	282	619
	1	5.5	5.3	5.7	856	903	685
S6, Intact Area	5	5.6	5.2	5.3	804	946	815
	3	5.7	4.9	5.8	749	1073	619
	1	5.2	5.0	5.2	876	927	869
Transition	5	5.7	5.3	N/A	N/A	N/A	N/A
	4	6.3	5.4	N/A	N/A	N/A	N/A
	3	6.2	7.9	16.7	N/A	N/A	N/A
	2	4.8	12.5	N/A	N/A	N/A	N/A
	1	4.4	4.5	N/A	N/A	N/A	N/A
S5, Deep and Full Debonding	5	4.5	5.2	6.7	1008	786	487
	3	4.1	5.1	7.6	1279	871	346
	1	4.2	4.7	7.4	1273	1081	374
S4, Deep and Partial Debonding	5	3.9	4.7	7.0	1606	1184	527
	3	4.1	5.3	6.3	1375	920	741
	1	5.0	5.9	8.1	912	763	408
S3, Shallow and Full Debonding	5	4.7	6.8	11.6	1091	524	195
	3	5.5	6.3	10.0	783	672	244
	1	5.4	5.6	8.9	918	870	328
S2, Shallow and Partial Debonding	5	5.2	5.7	7.6	916	846	493
	3	5.7	6.0	6.9	757	749	660
	1	5.6	5.6	6.9	812	877	675
S1, Intact	5	4.7	5.1	5.9	1306	1108	1046
	3	4.6	5.0	6.7	1289	1080	769
	1	4.9	5.1	7.0	1093	989	692

Table D.6 – LWD Results on Small Scale Study. Coarse Mix

Section	Point	Geophone Deflection (mils)					Modulus, ksi				
		Line 1	Line 2	Line 3	Line 4	Line 5	Line 1	Line 2	Line 3	Line 4	Line 5
S5, Deep and Full Debonding	5	9.4	7.8	9.1	8.8	9.1	21.4	19.2	19.5	23.8	18.0
	4	8.0	8.9	8.8	7.2	9.5	20.0	15.2	19.9	22.7	16.4
	3	8.6	11.3	8.6	7.6	10.5	20.7	16.7	18.7	19.9	17.4
	2	8.3	10.2	9.2	8.6	9.8	19.5	21.2	21.8	16.4	23.0
	1	8.8	8.1	7.9	10.4	7.4	19.3	18.2	22.0	18.9	19.5
S4, Deep and Partial Debonding	5	7.8	11.5	9.6	8.5	8.9	22.1	14.8	17.3	19.7	17.8
	4	7.7	11.5	9.9	8.7	9.7	22.3	15.7	17.9	19.0	13.1
	3	12.8	10.9	9.6	9.0	13.1	13.4	21.3	16.5	22.7	15.0
	2	7.7	9.1	10.4	7.6	11.4	22.3	18.8	16.7	19.5	18.1
	1	11.7	7.8	10.3	8.8	9.5	14.6	22.0	7.7	17.8	20.1
S3, Shallow and Full Debonding	5	8.2	9.8	9.1	10.5	13.0	21.0	17.5	18.9	16.3	13.1
	4	7.5	10.9	8.5	9.0	9.4	22.8	15.7	20.1	19.0	18.3
	3	7.2	11.4	10.6	9.2	8.5	23.8	15.1	16.2	18.7	20.0
	2	7.3	9.5	10.2	9.3	8.9	23.4	18.0	16.7	18.5	19.2
	1	6.8	10.5	8.6	10.4	7.3	25.1	16.3	19.9	16.5	23.4
S2, Shallow and Partial Debonding	5	6.4	9.3	11.0	7.5	8.8	26.7	18.5	15.6	22.9	19.5
	4	6.5	11.4	10.9	10.5	9.8	26.4	15.0	15.8	16.4	17.5
	3	6.5	11.4	10.1	8.9	8.4	26.5	15.0	16.9	19.2	20.5
	2	6.9	10.7	10.7	7.0	8.4	25.0	16.0	16.1	24.4	20.5
	1	7.6	11.3	9.0	9.5	8.9	22.5	15.2	19.1	18.1	19.2
S1, Intact	5	8.1	9.3	10.4	7.2	7.9	21.2	18.4	16.5	23.6	21.8
	4	7.6	10.4	10.5	7.5	8.9	22.7	16.5	16.4	22.9	19.2
	3	7.9	10.3	8.9	8.5	8.7	21.6	16.7	19.3	20.1	19.6
	2	8.7	11.5	9.2	9.2	7.6	19.6	14.9	18.6	18.7	22.7
	1	8.7	10.5	8.9	9.1	8.5	19.7	16.4	19.3	18.8	20.2

Table D.7 – LWD Results on Small Scale Study. Fine Mix and Transition

Section	Point	Geophone Deflection (mils)					Modulus, ksi				
		Line 1	Line 2	Line 3	Line 4	Line 5	Line 1	Line 2	Line 3	Line 4	Line 5
S10, Deep and Full Debonding	5	7.1	6.9	10.1	9.3	9.0	24.0	24.9	17.0	18.4	19.1
	4	9.5	8.6	10.0	9.9	10.5	18.1	19.9	17.1	17.3	16.4
	3	8.6	8.0	8.6	9.8	11.1	20.0	21.5	20.0	17.4	15.4
	2	11.2	13.5	9.9	9.2	11.3	15.3	12.7	17.3	18.7	15.2
	1	8.5	9.7	10.2	6.3	9.6	20.2	17.7	16.9	27.2	17.8
S9, Deep and Partial Debonding	5	10.2	11.0	14.6	6.6	9.8	16.7	15.6	11.7	25.9	17.5
	4	8.6	10.4	10.1	6.8	11.1	19.7	16.4	17.0	25.1	15.5
	3	9.7	10.2	10.2	5.5	9.7	17.7	16.8	16.8	31.3	17.7
	2	8.4	10.0	9.5	5.9	7.8	20.3	17.1	18.0	28.8	22.0
	1	10.9	10.5	9.0	6.7	9.0	15.7	16.4	19.0	25.7	19.1
S8, Shallow and Full Debonding	5	10.5	10.8	8.7	9.6	14.3	16.4	15.9	19.7	17.9	12.0
	4	9.9	10.6	11.0	8.9	10.7	17.3	16.1	15.5	19.2	16.1
	3	11.0	10.7	9.8	8.9	11.2	15.6	15.9	17.5	19.3	15.3
	2	13.5	13.5	11.1	6.9	9.7	12.6	12.6	15.4	24.9	17.7
	1	12.9	11.5	10.3	8.6	8.5	13.3	14.8	16.6	20.0	20.1
S7, Shallow and Partial Debonding	5	9.6	9.3	9.0	8.1	10.4	17.8	18.5	19.1	21.1	16.5
	4	12.1	9.8	9.0	7.2	8.1	14.2	17.5	19.0	23.8	21.1
	3	10.1	11.7	10.8	7.8	8.6	16.9	14.7	15.9	21.9	19.9
	2	12.0	10.9	8.0	8.0	7.9	14.3	15.8	21.3	21.3	21.8
	1	11.9	10.5	10.4	8.1	9.3	14.4	16.4	16.5	21.2	18.4
S6, Intact	5	8.4	11.1	7.8	7.4	13.2	20.4	15.4	21.9	23.1	12.9
	4	12.4	9.7	9.5	8.2	8.5	13.9	17.6	18.0	20.8	20.2
	3	11.2	9.5	7.7	8.6	8.7	15.3	18.0	22.3	20.0	19.7
	2	10.9	10.2	8.6	7.7	8.8	15.7	16.8	20.0	22.2	19.5
	1	11.2	9.1	9.0	7.2	7.9	15.3	18.8	19.0	23.9	21.6
Transition	8	10.4	9.4	9.3	8.9	10.7	16.4	18.2	18.5	19.2	16.1
	7	10.9	9.6	10.3	7.6	8.7	15.6	17.8	16.7	22.4	19.7
	6	10.2	7.4	8.3	6.9	6.9	16.8	23.0	20.6	24.9	25.0
	5	10.5	9.0	7.6	7.2	7.9	16.4	19.0	22.7	23.6	21.8
	4	9.5	10.0	12.0	15.1	7.4	18.1	17.1	14.3	11.4	23.0
	3	9.5	9.1	9.8	15.2	15.9	18.0	18.9	17.5	11.2	10.8
	2	8.2	10.0	7.6	8.4	8.5	20.8	17.1	22.4	20.3	20.1
1	8.7	9.7	8.7	8.2	9.3	19.7	17.7	19.6	21.0	18.4	

Table D.8 – IR Results (Voltage) on Small Scale Study. Coarse Mix

Section	Point	Hammer Voltage, volts					Geophone Voltage, volts				
		Line 1	Line 2	Line 3	Line 4	Line 5	Line 1	Line 2	Line 3	Line 4	Line 5
S5, Deep and Full Debonding	5	3.16	3.10	2.69	2.98	3.05	0.59	0.72	0.66	0.76	0.81
	4	2.94	3.18	3.11	3.14	2.74	0.65	0.69	0.69	0.80	0.85
	3	3.23	2.46	3.08	2.64	2.99	0.66	0.64	0.71	0.76	0.84
	2	3.31	2.90	3.52	2.64	3.41	0.65	0.61	0.70	0.76	0.88
	1	3.29	3.52	3.44	3.31	3.10	0.64	0.66	0.70	0.75	0.82
S4, Deep and Partial Debonding	5	3.36	2.77	3.32	2.65	2.84	0.61	0.57	0.62	0.65	0.76
	4	3.11	3.20	3.59	2.76	3.16	0.62	0.65	0.68	0.70	0.78
	3	3.04	2.68	3.29	2.85	3.11	0.60	0.63	0.69	0.66	0.69
	2	3.20	2.52	3.07	3.38	3.40	0.62	0.64	0.68	0.72	0.73
	1	2.87	3.25	3.00	3.10	3.54	0.75	0.71	0.71	0.77	0.88
S3, Shallow and Full Debonding	5	3.46	3.10	2.88	3.32	3.43	0.64	0.71	0.72	0.92	0.97
	4	3.34	3.37	3.10	3.26	3.32	0.64	0.76	0.77	0.95	1.00
	3	3.58	3.31	3.18	2.92	3.22	0.67	0.66	0.74	0.80	0.83
	2	3.69	3.56	2.53	3.01	3.52	0.67	0.69	0.70	0.79	0.82
	1	3.39	2.98	2.81	3.44	2.94	0.65	0.60	0.71	0.77	0.77
S2, Shallow and Partial Debonding	5	3.20	2.91	3.13	3.06	3.19	0.62	0.59	0.63	0.68	0.74
	4	2.97	3.03	3.14	3.33	2.90	0.61	0.66	0.65	0.68	0.64
	3	2.87	3.25	3.38	3.57	2.90	0.62	0.60	0.63	0.69	0.67
	2	3.24	3.42	3.31	3.34	3.64	0.63	0.65	0.64	0.70	0.71
	1	2.86	3.27	3.00	3.68	3.16	0.64	0.62	0.62	0.67	0.63
S1, Intact	5	4.10	2.44	2.57	3.29	2.96	0.61	0.52	0.56	0.59	0.61
	4	2.61	2.42	2.89	3.46	3.57	0.48	0.51	0.56	0.64	0.63
	3	2.53	2.31	3.23	2.88	3.57	0.51	0.51	0.60	0.64	0.65
	2	2.42	2.40	3.21	3.25	3.75	0.51	0.51	0.57	0.63	0.66
	1	3.05	2.39	2.80	3.34	3.33	0.54	0.53	0.57	0.62	0.67

Table D.9 – IR Results (Voltage) on Small Scale Study. Fine Mix and Transition

Section	Point	Hammer Voltage, volts					Geophone Voltage, volts				
		Line 1	Line 2	Line 3	Line 4	Line 5	Line 1	Line 2	Line 3	Line 4	Line 5
S10, Deep and Full Debonding	5	3.37	3.65	3.65	3.75	3.17	0.60	0.65	0.71	0.71	0.76
	4	3.22	3.19	2.91	3.41	3.29	0.59	0.64	0.64	0.72	0.71
	3	3.77	4.15	3.85	3.35	3.11	0.62	0.64	0.65	0.69	0.77
	2	3.46	3.80	3.83	3.47	2.88	0.64	0.61	0.66	0.70	0.75
	1	3.30	3.33	3.64	3.24	2.93	0.63	0.61	0.63	0.66	0.69
S9, Deep and Partial Debonding	5	3.62	3.52	3.13	3.25	3.05	0.56	0.59	0.65	0.75	0.72
	4	3.63	3.33	3.06	2.94	3.33	0.53	0.58	0.55	0.70	0.65
	3	3.37	3.83	3.82	3.03	3.29	0.56	0.57	0.62	0.68	0.58
	2	3.55	3.59	3.87	2.89	3.17	0.59	0.60	0.60	0.73	0.63
	1	3.48	3.33	3.55	3.23	3.41	0.56	0.57	0.60	0.60	0.66
S8, Shallow and Full Debonding	5	3.41	2.97	3.60	3.45	2.86	0.58	0.63	0.67	0.75	0.73
	4	3.74	3.05	3.32	4.11	3.14	0.59	0.71	0.69	0.77	0.93
	3	2.86	3.24	2.93	3.50	3.02	0.57	0.61	0.61	0.66	0.67
	2	3.30	2.76	3.56	3.14	2.50	0.63	0.63	0.71	0.64	0.68
	1	3.36	3.23	3.23	4.16	3.69	0.61	0.65	0.72	0.76	0.73
S7, Shallow and Partial Debonding	5	3.47	3.25	2.78	3.20	2.96	0.63	0.64	0.67	0.71	0.65
	4	3.33	4.06	3.34	3.09	2.81	0.60	0.69	0.70	0.65	0.63
	3	2.93	3.46	3.36	3.55	3.76	0.61	0.65	0.65	0.63	0.63
	2	3.21	3.51	2.72	3.31	3.76	0.62	0.64	0.62	0.65	0.63
	1	3.08	3.51	3.58	3.35	3.40	0.62	0.64	0.65	0.63	0.61
S6, Intact	5	3.82	3.72	3.88	3.42	3.72	0.63	0.69	0.65	0.66	0.66
	4	3.36	3.42	3.88	3.07	3.85	0.62	0.63	0.65	0.62	0.65
	3	3.55	3.31	3.07	3.38	3.57	0.62	0.63	0.63	0.63	0.68
	2	3.25	3.43	4.02	3.16	3.49	0.61	0.64	0.67	0.65	0.67
	1	2.80	3.09	2.92	3.64	3.38	0.59	0.64	0.68	0.66	0.67
Transition	8	2.88	3.13	3.03	3.32	3.56	0.58	0.63	0.68	0.65	0.66
	7	3.04	2.99	3.61	2.97	3.58	0.60	0.61	0.65	0.67	0.63
	6	2.97	2.95	3.33	3.48	3.34	0.62	0.64	0.69	0.70	0.64
	5	3.06	3.30	2.86	3.52	3.40	0.62	0.63	0.65	0.66	0.72
	4	3.50	3.54	2.94	2.96	3.03	0.60	0.64	0.93	2.68	1.17
	3	2.91	2.70	3.39	2.74	3.13	0.57	0.61	1.77	2.79	1.36
	2	3.32	3.21	3.05	3.67	3.45	0.58	0.62	0.63	0.59	0.65
1	3.34	3.35	3.48	3.32	3.41	0.59	0.62	0.62	0.62	0.64	

Table D.10 – IR Results (FFT) on Small Scale Study. Coarse Mix

Section	Point	Maximum Amplitude FFT Hammer					Maximum Amplitude FFT Geophone				
		Line 1	Line 2	Line 3	Line 4	Line 5	Line 1	Line 2	Line 3	Line 4	Line 5
S5, Deep and Full Debonding	5	14.5	18.7	15.7	16.6	16.8	6.7	11.1	7.7	9.1	11.2
	4	16.6	15.0	15.9	16.5	14.7	8.9	8.9	8.0	10.5	12.6
	3	17.3	13.9	16.5	14.9	15.9	8.2	8.1	8.3	9.3	10.2
	2	16.7	13.7	17.8	14.9	17.6	8.3	6.8	8.0	9.3	12.4
	1	15.4	18.2	18.3	16.3	16.1	7.2	8.9	8.4	7.9	9.5
S4, Deep and Partial Debonding	5	17.4	13.3	17.3	13.4	15.7	7.0	5.7	6.9	6.2	9.2
	4	15.3	15.4	16.6	15.3	14.8	6.3	7.6	7.0	7.6	8.2
	3	15.0	15.0	17.1	16.4	15.1	6.3	9.4	9.1	8.0	7.0
	2	15.2	14.1	17.7	15.4	17.9	6.6	8.8	9.5	8.2	8.7
	1	13.6	15.9	18.1	16.6	16.6	7.5	8.4	10.2	10.6	11.2
S3, Shallow and Full Debonding	5	18.0	15.1	15.9	16.9	17.9	7.9	9.2	8.9	17.6	17.2
	4	16.8	18.2	16.4	15.7	16.5	6.6	11.3	10.0	18.6	17.0
	3	15.8	14.9	15.3	14.8	15.3	6.6	7.6	10.5	10.7	11.3
	2	17.1	17.5	14.2	15.9	18.1	7.1	8.3	9.7	12.4	12.7
	1	15.2	15.1	15.5	17.3	17.1	7.0	7.1	8.4	10.0	9.1
S2, Shallow and Partial Debonding	5	14.4	12.9	18.0	15.5	15.3	6.4	5.6	8.3	8.2	7.3
	4	13.3	17.6	14.0	15.6	16.5	6.4	11.0	6.8	7.9	7.1
	3	16.2	16.4	16.7	16.2	16.1	8.4	9.1	7.8	7.8	7.6
	2	14.4	15.5	15.7	16.6	15.9	8.3	8.4	8.2	9.1	8.5
	1	13.5	17.7	14.2	17.4	16.4	8.3	9.2	7.4	8.8	7.9
S1, Intact	5	19.9	11.6	11.1	14.7	13.5	7.6	6.1	6.4	6.8	5.7
	4	11.6	11.9	13.7	15.2	16.7	5.5	5.6	6.3	6.6	7.4
	3	11.3	10.3	15.3	15.0	15.7	5.8	5.2	6.9	8.4	7.5
	2	11.5	11.4	13.7	14.7	16.8	6.1	5.7	6.1	5.8	5.9
	1	12.9	11.0	14.6	14.1	17.2	5.2	5.7	6.3	5.3	7.1

Table D.11 – IR Results (FFT) on Small Scale Study. Fine Mix and Transition

Section	Point	Maximum Amplitude FFT Hammer					Maximum Amplitude FFT Geophone				
		Line 1	Line 2	Line 3	Line 4	Line 5	Line 1	Line 2	Line 3	Line 4	Line 5
S10, Deep and Full Debonding	5	14.0	17.9	16.9	17.2	14.2	5.9	8.3	8.1	9.6	12.1
	4	15.6	14.9	13.4	15.2	15.5	6.8	8.2	7.5	9.0	10.4
	3	16.9	16.8	16.5	14.8	14.0	7.7	7.3	7.4	11.1	10.7
	2	15.7	17.3	16.1	15.5	16.6	8.8	8.0	7.1	9.9	14.6
	1	14.4	14.2	16.1	14.1	14.5	7.9	6.9	7.1	9.0	11.1
S9, Deep and Partial Debonding	5	15.1	16.4	14.9	14.2	15.8	5.7	7.2	8.2	10.6	12.2
	4	15.0	14.4	14.3	14.4	13.9	5.4	6.4	6.5	9.1	8.5
	3	16.1	15.7	19.4	14.3	14.7	8.0	6.0	8.1	8.0	6.9
	2	14.7	17.6	15.7	14.0	15.4	7.4	8.4	7.5	8.4	8.1
	1	14.3	16.3	16.4	16.4	15.4	6.5	6.9	7.8	7.9	8.4
S8, Shallow and Full Debonding	5	15.8	14.1	18.4	17.2	12.7	6.1	8.9	11.0	11.7	10.0
	4	17.5	14.4	18.1	17.3	15.2	6.8	10.3	12.1	12.0	16.8
	3	14.3	14.0	15.1	16.0	16.2	5.7	5.9	7.2	9.6	11.3
	2	14.4	13.8	14.8	14.1	16.1	5.8	7.5	9.3	8.0	14.0
	1	15.0	15.8	16.3	18.4	16.1	5.9	6.3	9.6	10.6	10.1
S7, Shallow and Partial Debonding	5	16.9	18.0	14.5	15.0	15.5	6.8	6.4	7.7	9.1	8.7
	4	15.9	18.5	14.8	16.6	14.2	5.9	6.3	6.4	9.3	8.2
	3	16.1	17.2	16.3	17.0	16.6	7.2	6.4	7.1	7.0	6.7
	2	17.4	15.0	14.6	14.0	16.6	7.2	5.6	7.2	6.4	6.7
	1	14.2	16.8	17.7	17.8	16.3	6.4	6.1	8.2	9.1	8.1
S6, Intact	5	15.9	18.7	18.0	15.2	16.9	5.3	7.2	8.3	7.1	7.8
	4	15.7	14.5	18.0	14.1	16.2	5.4	6.5	8.3	6.6	6.5
	3	15.9	15.2	13.9	18.3	15.2	5.6	6.7	6.9	8.1	6.7
	2	13.7	15.6	18.1	14.7	17.1	5.3	6.3	8.1	6.5	7.4
	1	12.6	13.7	14.4	16.3	15.4	4.7	5.3	7.6	7.4	7.4
Transition	8	16.1	13.4	16.0	13.9	17.1	6.3	5.4	8.4	6.5	7.5
	7	12.6	16.8	16.7	14.0	17.5	4.8	6.6	6.6	7.7	7.3
	6	15.0	14.7	17.0	15.0	15.8	6.6	6.3	6.8	6.7	6.6
	5	13.1	16.3	13.4	17.5	16.9	5.5	7.0	7.9	6.8	7.4
	4	13.9	16.7	12.6	14.6	18.3	5.9	6.9	30.3	163.6	42.9
	3	15.5	12.5	16.1	16.0	15.2	6.8	6.1	61.4	173.8	41.3
	2	14.6	14.4	15.2	16.2	16.9	6.0	6.0	7.1	5.5	7.5
1	14.4	18.8	18.8	16.8	14.8	6.0	7.4	7.2	7.2	7.2	

Table D.12 – Geogauge Results on Small Scale Study. Coarse Mix

Section	Point	Modulus, ksi					Signal to Noise Ratio, ksi				
		Line 1	Line 2	Line 3	Line 4	Line 5	Line 1	Line 2	Line 3	Line 4	Line 5
S5, Deep and Full Debonding	5	27.6	54.9	55.9	54.6	41.2	39.6	39.8	44.0	41.4	45.6
	4	72.2	65.2	63.1	69.7	38.8	40.7	42.4	39.5	36.7	40.7
	3	32.4	71.8	28.4	65.3	47.7	42.2	41.4	40.9	33.2	41.5
	2	64.5	32.3	48.8	44.5	57.7	36.6	44.4	39.4	40.1	40.7
	1	35.4	65.6	53.2	65.4	64.7	45.5	40.3	48.2	36.6	47.0
S4, Deep and Partial Debonding	5	60.0	31.7	38.3	51.4	48.4	31.9	45.9	39.9	42.4	43.6
	4	43.2	47.5	42.7	32.4	54.0	41.4	44.0	39.3	40.9	18.8
	3	53.5	37.6	56.8	44.9	39.1	32.4	46.8	41.7	40.2	43.6
	2	46.5	63.3	51.1	47.0	46.0	36.9	37.4	36.4	42.8	33.8
	1	69.3	65.8	35.1	49.1	38.8	38.3	40.3	45.0	43.3	47.2
S3, Shallow and Full Debonding	5	57.5	59.1	33.6	48.6	36.2	35.6	40.9	43.5	42.2	45.6
	4	69.2	77.4	54.4	40.5	46.2	37.2	36.7	42.2	42.4	42.6
	3	67.6	43.1	57.7	39.2	26.6	39.5	39.5	40.1	39.3	49.9
	2	45.5	47.1	42.7	51.2	38.9	40.9	45.0	44.4	41.8	46.2
	1	65.2	40.8	54.3	31.1	37.8	35.3	41.9	38.1	46.8	47.0
S2, Shallow and Partial Debonding	5	60.4	43.3	44.2	65.5	52.6	39.9	42.8	44.0	39.9	41.7
	4	24.7	51.6	51.4	50.4	74.6	46.1	37.8	38.3	41.8	35.0
	3	54.5	35.6	48.8	61.4	47.1	36.6	43.7	42.5	36.5	41.3
	2	32.1	33.7	30.4	71.6	45.4	41.7	44.7	50.5	35.7	43.3
	1	70.0	35.1	46.8	72.6	50.2	40.3	39.5	40.3	39.1	37.5
S1, Intact	5	63.6	43.8	30.8	60.1	44.6	39.2	40.6	34.3	38.6	39.1
	4	64.9	63.6	52.6	51.6	56.8	36.6	40.0	41.4	44.2	41.3
	3	55.8	56.2	48.0	44.0	51.6	38.6	42.0	41.6	43.7	40.8
	2	78.2	50.0	54.6	61.9	48.9	38.3	42.8	37.9	38.6	41.3
	1	58.4	49.6	57.8	80.0	75.9	41.1	38.8	40.4	38.3	47.5

Table D.13 – Geogauge Results on Small Scale Study. Fine Mix and Transition

Section	Point	Modulus, ksi					Signal to Noise Ratio, ksi				
		Line 1	Line 2	Line 3	Line 4	Line 5	Line 1	Line 2	Line 3	Line 4	Line 5
S10, Deep and Full Debonding	5	64.6	63.6	63.0	51.6	59.9	41.0	39.8	37.1	31.0	39.8
	4	47.4	39.1	43.4	62.5	90.1	44.9	39.6	36.0	37.0	39.7
	3	52.6	26.8	61.8	59.9	54.8	41.2	35.7	26.6	44.0	35.7
	2	38.6	65.9	55.1	48.4	45.8	40.2	39.9	31.7	36.4	39.9
	1	47.5	44.7	52.7	26.1	59.2	39.0	35.7	39.9	41.8	34.7
S9, Deep and Partial Debonding	5	65.6	58.8	51.8	40.8	40.2	41.8	45.9	37.0	15.6	43.1
	4	65.7	45.1	50.2	55.9	44.2	41.3	40.8	43.3	41.1	41.3
	3	47.1	61.8	57.2	39.0	60.3	45.0	49.4	42.6	42.5	41.7
	2	64.5	42.6	66.8	44.7	31.6	37.9	40.0	35.2	43.6	39.0
	1	34.6	60.9	39.9	49.1	43.3	40.1	39.8	42.3	38.9	48.8
S8, Shallow and Full Debonding	5	43.1	62.7	46.3	44.6	49.3	38.4	39.1	38.6	47.2	42.2
	4	50.6	54.4	57.9	46.1	36.1	43.1	40.9	39.5	40.7	41.3
	3	59.4	49.0	42.8	39.5	46.0	42.1	43.1	39.3	41.4	43.3
	2	38.1	51.6	46.6	56.5	62.5	45.9	39.3	42.5	41.3	39.0
	1	45.5	49.0	50.8	46.3	50.5	43.6	44.4	49.2	45.1	43.6
S7, Shallow and Partial Debonding	5	45.5	51.0	36.2	58.4	47.4	38.5	42.3	38.6	44.5	40.3
	4	63.7	42.3	44.0	61.7	41.7	32.5	36.7	33.2	42.0	37.9
	3	38.3	49.2	56.5	68.1	57.5	44.6	48.2	40.4	43.5	45.6
	2	39.5	69.6	33.8	57.2	51.6	13.5	34.6	41.9	41.6	40.1
	1	41.6	49.4	38.3	93.7	58.5	41.9	17.1	41.5	35.7	43.5
S6, Intact	5	39.4	72.2	37.3	46.0	72.0	41.2	38.2	42.9	36.8	37.9
	4	52.3	53.6	75.7	76.7	56.8	40.1	37.2	37.6	37.4	32.9
	3	44.0	67.8	66.0	64.1	41.5	42.2	42.9	37.2	34.5	41.6
	2	63.0	62.8	41.3	64.1	73.7	35.3	35.6	38.8	37.5	36.1
	1	42.1	82.9	45.5	56.1	56.4	44.6	35.9	39.7	24.9	42.8
Transition	8	46.3	58.3	55.1	62.0	63.7	29.1	40.7	37.6	43.2	33.2
	7	55.4	51.0	35.0	35.0	35.6	44.1	35.6	40.7	42.1	45.4
	6	41.9	55.7	25.0	64.1	61.9	36.5	43.2	21.7	42.6	36.5
	5	41.3	33.2	50.0	35.7	43.3	44.8	40.5	44.4	41.3	38.8
	4	41.9	70.5	34.7	22.1	23.0	40.2	39.0	39.5	38.9	47.0
	3	73.4	58.7	33.7	35.1	29.2	39.0	37.1	46.6	39.0	39.9
	2	26.6	72.4	51.0	37.0	50.7	43.9	40.5	44.4	38.0	39.8
1	42.7	49.4	59.8	72.2	58.8	44.9	50.7	39.8	37.8	42.7	

Table D.14 – Shear Strength Results (psi) for Cores Retrieved at 2 ft from Start from Small Scale Study

Section #	Interface at 2.5 inches deep			Interface at 5 inches deep		
	Tack Coat	Grease	Talcum Powder	Tack Coat	Grease	Talcum Powder
1	42 ^a			86 ^a		
2		32 ^a		88 ^a		
3			0 ^{a,c}	94 ^a		
4	82 ^a				25 ^a	
5	71 ^a					0 ^{a,c}
6	84 ^b			90 ^a		
7		50 ^b		63 ^a		
8			0 ^{b,c}	96 ^a		
9	95 ^b				21 ^a	
10	91 ^b					0 ^{a,c}
Average	78	41	0	86	23	0
COV, %	24.8	32.3	--	13.9	14.1	--

^a P403/P401 Interface

^b P401/P401 Interface

^c Specimen not feasible for shear testing

Table D.15 – Shear Strength Results (psi) for Cores Retrieved at 7 ft from Start from Small Scale Study

Section #	Interface at 2.5 inches deep			Interface at 5 inches deep		
	Tack Coat	Clay Slurry	Paper Soaked in Oil	Tack Coat	Clay Slurry	Paper Soaked in Oil
1	74 ^a			78 ^a		
2		0 ^{a,c}		86 ^a		
3			0 ^{a,c}	76 ^a		
4	88 ^a				0 ^{a,c}	
5	75 ^a					0 ^{a,c}
6	97 ^b			93 ^a		
7		30 ^a		78 ^a		
8			0 ^{b,c}	84 ^a		
9	88 ^b				0 ^{b,c}	
10	97 ^b					0 ^{b,c}
Average	87	30	0	83	0	0
COV, %	11.7	141.4	--	7.8	--	--

^a P403/P401 Interface

^b P401/P401 Interface

^c Specimen not feasible for shear testing

**APPENDIX E – COMPLETE NDT RESULTS OF EXTENDED TESTS ON SMALL
SCALE STUDY**

**Table E.1 – PSPA Results on Small Scale Study (3 Lifts Combined). Fine Mix and
Transition (Cool Weather)**

Section	Point	Seismic Modulus from PSPA (for 8 in), ksi									
		Line 1	Line 2	Line 3	Line 4	Line 5	Line 6	Line 7	Line 8	Line 9	Line 10
S10, Deep and Full Debonding	10	1736	1794	2061	1986	2114	2526	1799	1759	1629	1724
	9	1807	1740	2074	2152	2298	2549	1553	1745	1610	1566
	8	1598	1792	2207	2029	2228	2353	1641	1817	1505	1625
	7	1696	1630	1981	2304	2213	2436	1828	1629	1572	1664
	6	1595	1695	2100	2369	2482	2342	1859	1869	1408	1697
	5	1722	1967	2042	2169	2110	2429	1463	1864	1413	1454
	4	1756	1946	1992	1901	2034	2146	1499	1807	1447	1368
	3	1696	1764	2000	2278	1615	2445	1744	1431	1341	1626
	2	1647	1706	1790	1874	2178	2304	1602	1564	1569	1577
	1	1595	1840	1941	1866	1879	2172	1916	1697	1395	1629
S9, Deep and Partial Debonding	10	1888	1880	1838	1609	2147	1663	2000	1607	1506	1620
	9	1795	1785	1944	1697	1892	1995	1878	1981	1547	1460
	8	1737	1683	1960	1804	1887	2071	1798	1993	1578	1584
	7	2071	1724	1867	1627	1934	1799	1797	1758	1567	1535
	6	1898	1898	1812	1774	1594	1942	1806	2094	1435	1580
	5	2041	1862	1759	1997	1768	2019	1986	2101	1734	1610
	4	1845	2045	2088	1798	1775	1845	2189	2137	1758	1848
	3	1884	1929	1698	1774	1575	1907	1678	1920	1684	1702
	2	2044	2006	1823	1720	2060	1942	1840	2057	1725	1675
	1	1862	1974	1957	1862	1869	1855	1427	1385	1252	1197
S8, Shallow and Full Debonding	10	2015	1927	1237	1540	1227	2209	1421	1646	1426	1511
	9	1781	1731	1241	1483	1606	2217	1661	1441	1300	1249
	8	1633	1417	1704	1564	1851	1974	1598	1566	1513	1416
	7	1599	1448	1655	1824	1414	2367	1531	1720	1413	1466
	6	1623	1582	1792	1894	1876	2396	1534	1701	1453	1573
	5	1774	1907	1887	1869	1806	2197	1555	1709	1493	1501
	4	1914	2016	2001	1780	1588	2090	1449	1700	1503	1575
	3	1903	1877	1729	1719	1510	1813	1329	1608	1273	1480
	2	1732	1837	1680	1887	1711	1967	1686	1490	1484	1561
	1	1563	1771	1604	1755	2013	2062	1465	1579	1613	1576
S7, Shallow and Partial Debonding	10	1894	1677	1378	1412	1571	1780	1801	1642	1650	1510
	9	1899	1873	1863	1715	1701	2055	1669	1728	1717	1615
	8	1794	1827	1935	2219	1990	1984	1938	1640	1713	1443
	7	1755	1791	1875	1905	1884	1918	1841	1781	1817	1744
	6	1665	1685	1716	2171	1831	1993	1906	1669	1873	1685
	5	1938	1992	1791	2141	2037	2013	1775	1809	1693	1609
	4	1997	1780	1779	2011	2015	1861	1981	1860	1777	1799
	3	1876	1884	1686	2148	1938	1751	1764	1711	1737	1748
	2	1705	1968	2036	1976	2035	2019	1815	1727	1873	1733
	1	1778	1955	2085	1995	2336	2104	1704	1889	1963	1949

**Table E.1 Contd. – PSPA Results on Small Scale Study (3 Lifts Combined). Fine Mix and
Transition (Cool Weather)**

S6, Intact	10	1784	1985	2227	2341	2206	1549	2063	1974	2261	2093
	9	1861	2235	1951	2282	1974	1871	1915	2193	2110	1996
	8	1821	2198	2399	2583	2236	1921	1797	2022	2100	1997
	7	1938	2013	2054	2293	2182	1922	1940	1943	2215	1966
	6	2038	1943	2386	2479	2353	1766	2004	2119	2143	2176
	5	2111	2044	2063	2600	2440	2211	1975	2052	2117	1834
	4	2220	2349	2183	2584	2322	2257	1995	2247	2193	2166
	3	2079	2273	2382	2113	2378	2498	2047	2109	2243	2121
	2	2091	2083	2093	2456	2234	2945	1814	1943	1827	1896
	1	1454	1673	1761	2202	2486	2448	1879	2061	1947	1969
TRANSITION	15	1342	1422	1530	2118	2237	2060	2123	2151	1840	1883
	14	1487	1658	1577	1804	2149	2963	1977	1875	1982	1998
	13	1462	1395	1488	1896	1815	2271	2059	2106	1971	1807
	12	1332	1577	1658	1633	1418	1922	2358	1864	1820	1926
	11	1145	1423	1527	1624	1932	2227	1739	1868	1783	1760
	10	1422	1363	1746	1821	1663	2287	2310	1965	1664	1622
	9	1080	1398	1823	1754	1508	1962	1842	1913	1942	1824
	8	1553	1852	2120	1996	1244	1252	1113	1173	1136	963
	7	1871	2118	2129	1874	1442	1119	1002	954	1051	1149
	6	1917	2135	2069	2075	1173	1319	1192	1048	1116	994
	5	1944	2047	2347	2321	1183	1286	1216	1226	1144	1026
	4	1771	2233	1890	2279	1446	1982	1846	2149	1720	1947
	3	1718	2057	1945	1960	2166	1911	2140	2173	1620	1989
	2	1690	1936	1952	2092	2059	1928	2097	2067	1820	1717
	1	1852	2067	2012	2156	1788	1802	1820	2433	2084	2004

Table E.2 – PSPA Results on Small Scale Study (3 Lifts Combined). Coarse Mix (Cool Weather)

Section	Point	Seismic Modulus from PSPA (for 8 in), ksi									
		Line 1	Line 2	Line 3	Line 4	Line 5	Line 6	Line 7	Line 8	Line 9	Line 10
S5, Deep and Full Debonding	10	1678	1755	1890	1911	1908	1693	1987	1864	1761	1684
	9	1916	2001	2146	1870	1637	1690	1724	1935	1697	1600
	8	1829	1889	2006	1546	1765	1727	1579	1699	1569	1493
	7	2006	1855	2029	1809	1785	1800	1671	1636	1756	1695
	6	2243	1926	1976	1512	1691	1725	1727	1805	1824	1484
	5	2053	1921	1841	1718	1618	1814	1927	1940	1736	1754
	4	1881	2138	1859	1456	1750	1786	1749	1894	1660	1778
	3	1955	1835	1867	1982	1888	1847	1695	1942	1726	1754
	2	2244	2088	1869	1750	2062	1998	1946	1701	1635	1814
	1	2056	1831	1883	1496	1993	1740	1912	1467	1595	1806
S4, Deep and Partial Debonding	10	1859	1928	1762	1655	1948	1776	1731	1825	1609	1700
	9	2141	1892	1862	1765	1856	2070	1873	1693	1551	1608
	8	1862	1734	1861	1612	1670	1591	1837	1517	1616	1712
	7	2039	1808	1794	1640	1875	1827	1561	1698	1572	1723
	6	1767	1854	1796	1431	1495	1494	1753	2052	1663	1849
	5	2039	2130	1712	1269	1778	1832	1772	1757	1623	1475
	4	1692	2137	1777	1457	1486	1941	1843	1835	1641	1190
	3	1849	1951	1804	1659	1649	1749	1926	1609	1000	868
	2	1691	1781	1991	1527	1622	1666	1731	1587	1254	1147
	1	2051	1760	1938	1796	1738	1788	1369	1488	1279	1086
S3, Shallow and Full Debonding	10	2075	1769	1291	1224	1548	1803	1156	1182	1268	1213
	9	1920	1461	1156	1208	1523	1781	1281	1301	1319	1217
	8	1908	1893	1582	1481	1770	2009	1408	1331	1314	1318
	7	1952	1948	1722	1544	1569	1539	1396	1267	1326	1143
	6	1822	1864	1786	1382	1694	1733	1674	1522	1517	1288
	5	1854	1844	1854	1631	2102	1758	1535	1577	1326	1314
	4	1894	1898	1818	1928	2128	1888	1369	1387	1335	1119
	3	1909	2127	1931	1699	2046	2046	1522	1312	1271	1156
	2	1945	2226	1929	1896	2215	2024	1404	1289	1241	1253
	1	1920	2214	1893	1632	1935	1764	1463	1610	1328	1418
S2, Shallow and Partial Debonding	10	2104	1906	1683	1833	1932	2528	1675	1467	1083	1426
	9	2018	2045	1858	1892	2052	2737	2101	1481	1297	1468
	8	1979	2022	1922	1734	2016	1978	2487	1674	1443	1843
	7	1903	2059	1796	1778	1869	2246	1932	1444	1402	1653
	6	1878	1960	1636	1587	1995	2115	2131	1623	1457	1853
	5	1960	1993	1757	1624	2330	2048	2014	1660	1227	1626
	4	1883	2122	1883	1876	1980	2162	1910	1643	1575	1659
	3	1999	2079	1869	1529	2083	2214	1850	1552	1459	1735
	2	1847	1946	1870	1952	2341	1895	2168	1478	1602	1714
	1	2035	1787	1877	1691	2281	2196	2405	1596	1840	1846
S1, Intact	10	2225	2007	1987	1735	1805	1645	1679	1825	1927	1782
	9	2119	1799	2029	1919	1626	1551	1736	1806	1860	1859
	8	2141	2089	2192	1877	1762	1575	1936	1668	1899	1923
	7	2220	1954	1894	1664	1762	1497	1635	1733	1727	1750
	6	2264	1809	1981	1880	1863	1619	1668	1859	1743	1851
	5	1893	1898	1862	1634	1815	1836	1659	1590	1544	1577
	4	2276	1708	1937	1812	2013	1575	1563	1425	1817	1732
	3	1864	1840	1996	1572	1728	1569	1518	1566	1551	1767
	2	2139	2105	1533	1751	1926	1465	1578	1696	1665	1936
	1	1907	1700	1679	1847	1638	1741	1320	1517	1524	1781

Table E.3 – PSPA Results on Small Scale Study (Top Lift). Fine Mix and Transition (Cool Weather)

Section	Point	Seismic Modulus from PSPA (for 2.5 in), ksi									
		Line 1	Line 2	Line 3	Line 4	Line 5	Line 6	Line 7	Line 8	Line 9	Line 10
S10, Deep and Full Debonding	10	1947	2006	2168	2060	2100	2403	2358	2190	2292	2283
	9	1884	1868	2188	2275	2596	2368	2363	2376	2161	2397
	8	1742	1922	2178	2083	2473	2422	2268	2327	2068	2100
	7	1804	2136	2102	2426	2297	2613	2207	2324	1970	2065
	6	1936	1828	2317	2534	2538	2440	2309	2286	2020	2210
	5	1866	2155	2274	2349	2269	2649	2077	2272	1970	1972
	4	2039	2170	2032	2110	2138	2162	2123	2231	1973	2039
	3	1854	2305	2250	2394	1872	2433	2065	2143	1916	2219
	2	2044	1872	2026	2118	2195	2311	2059	2263	2046	2219
	1	1959	2019	2141	2341	2065	2297	2512	2202	1994	2184
S9, Deep and Partial Debonding	10	2158	2009	2009	1899	2205	1767	2226	1907	1878	2079
	9	1956	1910	2176	1874	2132	2122	2109	2164	1835	1981
	8	1866	1858	2039	1944	1933	2212	2083	2116	2128	2041
	7	2210	2043	2118	1845	2143	2088	2083	2222	2039	1903
	6	2152	2187	1916	2177	1746	2277	2266	2317	1826	2096
	5	2159	1984	2129	2127	2029	2184	2272	2321	1961	2289
	4	2070	2351	2090	1815	1896	2240	2417	2287	2028	2137
	3	2102	2090	1766	2020	1718	2012	2070	2313	2099	2071
	2	2198	2216	1761	1821	2053	2202	2300	2451	2112	2054
	1	2041	2085	2003	2123	1945	2157	1900	1747	1878	1789
S8, Shallow and Full Debonding	10	2002	1856	1404	1776	1533	2279	1861	1729	1717	1763
	9	1878	1769	1547	1665	1765	2428	1726	1613	1586	1758
	8	1693	1351	1914	1882	1929	2226	1983	2038	1832	1653
	7	1758	1664	1900	1969	1827	2547	1997	2017	1787	1937
	6	1635	1678	1904	1981	2012	2377	1785	2034	1780	1846
	5	1884	1904	2148	1992	1957	2462	1858	1939	1710	1889
	4	1964	2042	1992	1981	1861	2366	1668	1861	1669	1690
	3	1875	1850	1813	2051	1592	2049	1575	1960	1580	1621
	2	1755	1862	1730	2174	1937	2012	1856	1711	1758	1738
	1	1657	1851	1689	1932	2326	2054	1743	1653	1779	1952
S7, Shallow and Partial Debonding	10	2014	1766	1599	1630	1691	1799	1786	1694	1812	1707
	9	2061	1858	1946	1843	1891	2038	1830	1907	1892	1756
	8	1900	1965	2260	2198	1917	2117	2004	1825	1868	1804
	7	1892	1855	2202	2114	1878	2010	1763	2045	1953	2067
	6	1851	1832	2023	2094	1828	2103	1995	1815	2147	1773
	5	1971	2163	2009	2113	2129	2147	1920	2194	1846	1741
	4	2127	1816	1896	2148	1922	1945	2037	1998	1957	2102
	3	1947	1965	1749	2091	1921	1719	1838	1709	1880	1920
	2	1823	1991	2154	1950	2035	2142	1951	1674	2044	1975
	1	1922	1762	2153	2003	2330	2291	1754	2025	1955	2046
S6, Intact	10	1787	1966	2213	1954	2221	1944	2222	2293	2355	2342
	9	1929	1947	1873	2263	2150	2205	2188	2340	2315	2363
	8	1884	2087	2178	2443	2191	2070	2135	2365	2315	2275
	7	1795	1925	2205	2256	2301	2100	2297	2335	2347	2330
	6	1884	1921	2213	2034	2087	2140	2179	2359	2371	2502
	5	1881	1972	2128	2431	2337	2289	2300	2287	2308	2257
	4	2105	2063	2128	2434	2385	2213	2244	2455	2424	2452
	3	1925	2138	2105	2074	1933	1999	2247	2323	2578	2369
	2	2149	2109	2205	2248	2113	2186	2015	2405	2070	2195
	1	1560	1746	1904	2309	2256	1911	2061	2215	2331	2437

**Table E.3 Contd. – PSPA Results on Small Scale Study (Top Lift). Fine Mix and Transition
(Cool Weather)**

TRANSITION	15	1412	1519	1577	1799	2283	1992	2041	1835	1716	1716
	14	1441	1730	1528	1568	2172	1750	1941	1911	1809	1912
	13	1376	1375	1383	1537	1779	1630	1849	1857	1843	1822
	12	1404	1424	1560	1419	1384	2016	1656	1845	1756	1898
	11	1271	1381	1432	1440	2342	2356	1653	1712	1458	1919
	10	1305	1341	1799	1929	1811	2248	2222	2155	1578	1837
	9	1107	1437	2023	1818	1594	2050	2080	1919	2130	2016
	8	1517	1869	2182	2011	1696	1586	1455	1530	1409	1349
	7	1692	2048	2069	1888	2019	1490	1249	1375	1369	1369
	6	2028	2108	2036	2015	1636	1777	1747	1507	1747	1595
	5	1929	1876	2238	2178	1730	1883	1653	1671	1482	1461
	4	1831	1963	1916	1851	1499	2057	2078	2291	1810	1794
	3	1812	2069	2262	1885	2078	2058	2142	2053	1638	1829
	2	1783	1866	1953	2274	2035	2083	2206	2168	1797	1683
	1	1871	2147	2125	2068	1872	1873	1923	2484	1950	2087

Table E.4 – PSPA Results on Small Scale Study (Top Lift). Coarse Mix (Cool Weather)

Section	Point	Seismic Modulus from PSPA (for 2.5 in), ksi									
		Line 1	Line 2	Line 3	Line 4	Line 5	Line 6	Line 7	Line 8	Line 9	Line 10
S5, Deep and Full Debonding	10	1829	2020	2303	1997	2231	1868	2319	2192	1998	2066
	9	2295	2176	2302	2060	1808	1830	2188	2171	1940	1936
	8	1989	1914	2289	1858	2102	1942	1915	2047	1790	1656
	7	2175	2218	2421	2097	2215	2018	2005	1871	2079	1816
	6	2556	2090	2410	1744	1912	1924	2062	2164	2222	1653
	5	2387	2189	2307	1981	1793	2028	2039	2198	2041	2042
	4	2150	2342	2067	1732	1932	2208	2082	2144	2002	2374
	3	2163	2182	2186	2084	2345	2334	2139	2232	2191	2151
	2	2348	2338	2342	1986	2285	2228	2244	2135	2024	2107
	1	2224	2205	2313	1763	2398	2110	1901	1829	1909	2229
S4, Deep and Partial Debonding	10	2079	1899	1948	1709	1802	1960	1916	2108	1988	1966
	9	2100	1927	2051	1897	2026	2071	2021	1972	1970	1874
	8	1940	1885	1941	1874	2097	1882	1918	1755	1917	1972
	7	2027	1863	2021	1752	2063	2136	1899	2043	1902	1922
	6	1942	2090	1914	1740	1866	1722	1989	2194	1959	2120
	5	2193	2114	2040	1502	1892	1968	2000	1859	1938	1787
	4	1691	2269	2106	1617	1595	2139	2103	2223	1952	1492
	3	1938	1961	1950	1823	1767	1838	2139	1830	1482	1189
	2	1785	1824	2081	1600	1655	1840	1902	1758	1710	1711
	1	2085	1827	2008	1795	1848	1976	1777	1956	1724	1552
S3, Shallow and Full Debonding	10	2054	1912	1539	1452	1740	1824	1566	1605	1641	1718
	9	1711	1641	1415	1508	1627	1856	1551	1613	1604	1588
	8	1833	1857	1631	1561	1777	2023	1699	1613	1647	1515
	7	1892	1982	1833	1680	1687	1668	1668	1558	1550	1515
	6	1784	1951	1872	1434	1684	1661	1835	1597	1617	1564
	5	1904	2088	1884	1845	2108	1882	1712	1689	1556	1479
	4	2036	2155	1770	1915	2256	1993	1562	1437	1477	1392
	3	1990	2100	1910	1801	2025	2237	1345	1330	1322	1274
	2	2017	2194	2044	1926	2328	2033	1318	1282	1339	1398
	1	2083	2303	1955	1791	2075	1974	1414	1610	1689	1497
S2, Shallow and Partial Debonding	10	2346	2307	2083	1543	1406	2129	1838	1707	1674	1847
	9	2516	2245	2170	1462	1628	2268	1696	1586	1532	1844
	8	2232	2388	2155	1672	1787	2080	1940	1994	1753	1737
	7	2286	2267	2105	1768	1700	2379	1945	1964	1694	2038
	6	2161	2096	1966	1799	1882	2221	1730	1971	1673	1946
	5	2042	2158	2086	1808	1830	2300	1801	1880	1606	1990
	4	2183	2255	2233	1945	1719	2218	1619	1813	1588	1763
	3	2382	2391	2055	1974	1453	1927	1532	1918	1522	1675
	2	2154	2289	2118	2142	1746	1899	1808	1682	1715	1778
	1	2291	2056	2152	1921	2072	1945	1700	1633	1757	1976
S1, Intact	10	2245	2260	2312	2029	2146	1822	1847	2005	2113	2196
	9	2318	2125	2134	2131	2024	1855	1942	2021	1986	2239
	8	2224	2100	2361	2103	2077	1838	2121	1931	2052	2278
	7	2356	2189	2309	1983	2061	1780	1906	1823	1810	2148
	6	2415	2109	2353	2155	2117	1801	1930	2022	1934	2259
	5	2177	2134	2128	1961	2057	2100	1943	1895	1611	2122
	4	2355	1986	2189	1893	2170	1773	1816	1530	1756	2165
	3	2114	1941	2282	2161	2236	1856	1808	1818	1709	2204
	2	2337	2364	1940	2106	2317	1659	1871	1908	1797	2239
	1	2282	1970	1983	2034	1913	1807	1585	1715	1600	2133

Table E.5 – PSPA Results on Small Scale Study (3 Lifts Combined). Fine Mix and Transition (Hot Weather)

Section	Point	Seismic Modulus from PSPA (for 8 in), ksi									
		Line 1	Line 2	Line 3	Line 4	Line 5	Line 6	Line 7	Line 8	Line 9	Line 10
S10, Deep and Full Debonding	10	1958	1927	2065	2008	1716	1904	1821	2006	1834	1869
	9	1923	1881	1797	1990	1898	2359	1756	1704	1696	1736
	8	1935	1857	1904	1984	2220	2472	2050	1764	1654	1495
	7	1768	1916	1937	2021	2283	2187	1848	2108	1625	1261
	6	2075	1896	1885	2195	1728	2227	2234	2026	2005	1580
	5	1772	2141	1978	1814	2163	2308	2166	1970	1725	1844
	4	1710	2311	2071	1818	1771	2211	1762	1576	1373	1451
	3	1850	1667	1916	1783	1689	2468	1921	1734	1386	1805
	2	1885	1811	1951	1661	1711	2080	2025	1786	1515	1858
	1	1850	1869	1962	1857	1730	2129	2122	1978	1611	1811
S9, Deep and Partial Debonding	10	1698	1874	1656	1721	2319	2443	2593	2353	2075	1985
	9	1727	1625	1747	2130	1907	2251	2390	2477	2038	2104
	8	1877	1842	1744	1908	2384	2766	2575	2435	2118	1927
	7	2075	1798	1822	1891	2301	2531	2585	2125	2081	1877
	6	1993	2110	1833	2203	2381	2651	2344	2473	1922	1905
	5	1802	2054	1770	2009	2238	2919	2521	2452	2307	2179
	4	1686	2079	1746	1805	2092	2779	2647	2283	2350	2170
	3	1864	1713	1704	1799	1708	2510	2546	2510	2307	2478
	2	1636	2041	1698	1537	1745	2244	2268	2626	2366	2494
	1	1794	1924	1780	1878	1792	2312	1747	1835	1324	1559
S8, Shallow and Full Debonding	10	1945	2106	1589	1399	1321	2574	1677	1502	1185	1184
	9	1967	1809	1449	1336	1374	2186	1664	1471	1064	1207
	8	1745	1997	1689	2108	1938	1922	1598	1453	1218	1268
	7	1770	1776	2102	1937	1671	2088	1642	1589	1439	1336
	6	1851	1665	2233	2170	1864	2361	1721	1797	1781	1536
	5	2332	2064	2026	2233	1874	2466	1935	1835	1639	1612
	4	2299	1966	2187	1936	1844	2531	1808	1880	1598	1586
	3	2012	1861	2064	1893	1976	1986	1799	1925	1359	1360
	2	1906	2002	2039	2309	2741	2470	1867	1511	1547	1448
	1	1735	1799	2001	1934	2402	2184	2079	1804	1841	1578
S7, Shallow and Partial Debonding	10	2017	2220	1981	1452	1950	2583	2377	2077	2336	2303
	9	2271	1887	1689	1859	1714	3051	2223	2123	2002	2343
	8	2042	2011	1882	2297	2366	2054	2161	2121	2148	1926
	7	1885	2016	2242	1588	1719	1949	2325	2289	2156	2313
	6	2455	2329	2385	2133	2364	2268	1876	2171	2091	2185
	5	1981	2315	2088	2378	1903	2398	2106	2371	2313	2192
	4	2003	2537	2196	2378	2345	2438	2109	2269	2021	2185
	3	1764	2369	2390	2507	2266	2160	2196	2141	1855	1903
	2	1635	2098	2285	2311	2408	2480	1973	2014	2310	2055
	1	2033	2151	2382	2126	2336	2840	2266	2131	2219	2165
S6, Intact	10	2583	1773	1827	2061	1590	2015	1716	1990	1860	2223
	9	2295	1951	2166	1872	1763	2089	1902	1747	1835	2216
	8	2324	1780	2013	1928	1550	2018	1804	1922	2296	2079
	7	2156	1822	1944	1954	1949	1969	1735	1915	1881	1944
	6	2324	2503	2597	2431	2082	2016	2133	2265	2266	2068
	5	2267	2503	1795	2126	1785	1955	1999	1981	2056	1927
	4	2543	2511	2115	2177	2025	2202	2059	2003	2141	2105
	3	2755	2804	2450	2317	1832	2041	2008	2079	1812	2063
	2	2243	2471	2042	2082	1885	2205	2039	2144	2132	2239
	1	2113	1900	1921	2209	2165	2134	2116	2050	1923	2291

Table E.5 Contd. – PSPA Results on Small Scale Study (3 Lifts Combined). Fine Mix and Transition (Hot Weather)

TRANSITION	15	1280	1448	1583	1764	1828	2258	2296	2323	1965	2049
	14	1499	1564	1721	1874	2090	2669	2173	2050	2324	2161
	13	1475	1248	1498	1934	1892	1863	2533	2534	2024	2284
	12	1294	1820	1784	1735	1539	2197	2165	2036	1949	2122
	11	1249	1155	1383	1319	1654	2134	2029	1988	2007	2295
	10	1416	1406	1764	2045	1784	2071	2309	2462	1882	1999
	9	1124	1425	1770	1986	1698	2395	2053	2301	1837	2107
	8	1753	1790	2173	1903	1559	973	1076	1101	1048	980
	7	1854	2292	1935	1905	1252	1343	1151	1110	1037	1208
	6	1916	1878	2177	2023	1101	1239	1324	1059	1140	1086
	5	1822	1951	2243	1921	1028	1061	1272	1292	1156	1069
	4	1943	2184	1984	2074	2021	1910	2134	2324	1972	2272
	3	2087	2092	2035	1999	2023	2284	2083	2172	1973	2066
	2	1986	2176	2082	1962	2189	1974	2243	2226	2041	1854
	1	2086	2045	2148	2197	2079	2160	2055	2394	2015	2136

Table E.6 – PSPA Results on Small Scale Study (3 Lifts Combined). Coarse Mix (Hot Weather)

Section	Point	Seismic Modulus from PSPA (for 2.5 in), ksi									
		Line 1	Line 2	Line 3	Line 4	Line 5	Line 6	Line 7	Line 8	Line 9	Line 10
S5, Deep and Full Debonding	10	1579	1833	2169	2177	1797	1938	2037	2006	1643	1922
	9	1746	1925	2007	2145	2087	2123	2033	2043	1936	1988
	8	1903	1838	2409	1999	2415	2520	1955	2018	2022	2113
	7	1808	2000	2463	2183	2478	2566	2283	2114	2113	2014
	6	1955	2072	1965	1828	2013	2427	2493	2399	2006	2143
	5	2040	2067	1944	2056	2266	2443	2249	2420	1785	1901
	4	1790	2140	1594	1858	2369	2281	2313	2113	1948	1722
	3	1982	1905	1879	2001	2335	2174	2019	1976	1863	1805
	2	2015	2028	1695	1985	2247	2191	1866	2034	1739	1809
	1	1716	1902	1900	2061	2067	2118	1867	1921	1778	1652
S4, Deep and Partial Debonding	10	1670	1785	1624	1470	2074	2148	1907	1645	1915	1760
	9	1691	1755	1670	1364	1959	2082	1739	1521	1754	1841
	8	1779	1774	1619	1328	2045	2074	2014	1665	1794	1907
	7	1866	1910	1647	1623	1994	1975	1998	1921	1976	1978
	6	1730	1714	1597	1619	2023	2004	1880	1828	1508	1861
	5	1605	1710	1703	1635	1956	1672	1818	1888	1789	1713
	4	1805	1678	1622	1644	1761	2137	1834	1713	1399	1261
	3	1601	1577	1627	1661	1979	1861	1869	1765	1338	864
	2	1608	1593	1581	1539	1910	1791	1810	1846	1648	1435
	1	1588	1682	1685	1628	1883	1964	1475	1525	1404	1138
S3, Shallow and Full Debonding	10	1503	1295	1083	913	1288	1514	1107	945	1185	982
	9	1600	1210	953	1122	1182	1565	1176	1086	1160	1085
	8	1696	1494	1532	1318	1486	1600	1081	1102	1261	967
	7	1685	1709	1295	1047	1261	1715	1137	1184	1110	1107
	6	1525	1622	1520	1365	1533	1328	1415	1446	1307	1082
	5	1793	1581	1508	1344	1743	1573	1400	1362	1207	1008
	4	1748	1676	1601	1590	1617	1755	1136	1136	1065	1148
	3	1798	1895	1524	1241	1641	1755	989	1071	1368	1155
	2	1873	1768	1646	1500	1926	1498	1024	1051	1087	1133
	1	1794	1655	1597	1387	1577	1541	1348	1355	1259	1185
S2, Shallow and Partial Debonding	10	1924	1846	1584	1631	1729	1838	1612	1482	1491	1430
	9	1931	1906	1530	1425	1938	1828	1687	1549	1271	1653
	8	2049	1849	1715	1580	1660	1732	1636	1557	1518	1660
	7	1807	1914	1707	1496	1530	1766	1812	1753	1515	1502
	6	1960	1897	1749	1803	1725	1730	1510	1710	1549	1681
	5	2038	1982	1936	1408	1588	1791	1569	1592	1371	1751
	4	1939	2103	1859	1750	1900	1890	1475	1482	1380	1561
	3	1971	1854	1764	1580	1652	1822	1725	1541	1534	1519
	2	1738	1935	1847	1774	1857	1828	1569	1434	1305	1630
	1	1800	1759	1776	1759	1783	1664	1858	1609	1782	1580
S1, Intact	10	2018	2051	1755	1833	1926	2000	1933	1984	1868	1826
	9	1969	1900	1720	1796	1641	1653	1734	1890	1830	1782
	8	1991	1906	1794	1783	1731	1848	1675	1784	1926	1763
	7	1902	1996	1861	1582	1446	1516	1845	1692	1757	1578
	6	2115	1831	1699	1670	1629	1741	1738	1814	1912	1692
	5	1846	2024	1782	1666	1667	1860	1786	1814	1757	1651
	4	1840	2256	1843	1640	1662	1839	1794	1820	1897	1782
	3	1751	1973	1645	1677	1690	1872	1871	1717	1808	1930
	2	1531	1800	1779	1532	1560	1806	1664	1726	1893	1937
	1	1519	1666	1788	1429	1453	1779	1513	1767	1878	2106

Table E.7 – PSPA Results on Small Scale Study (Top Lift). Fine Mix and Transition (Hot Weather)

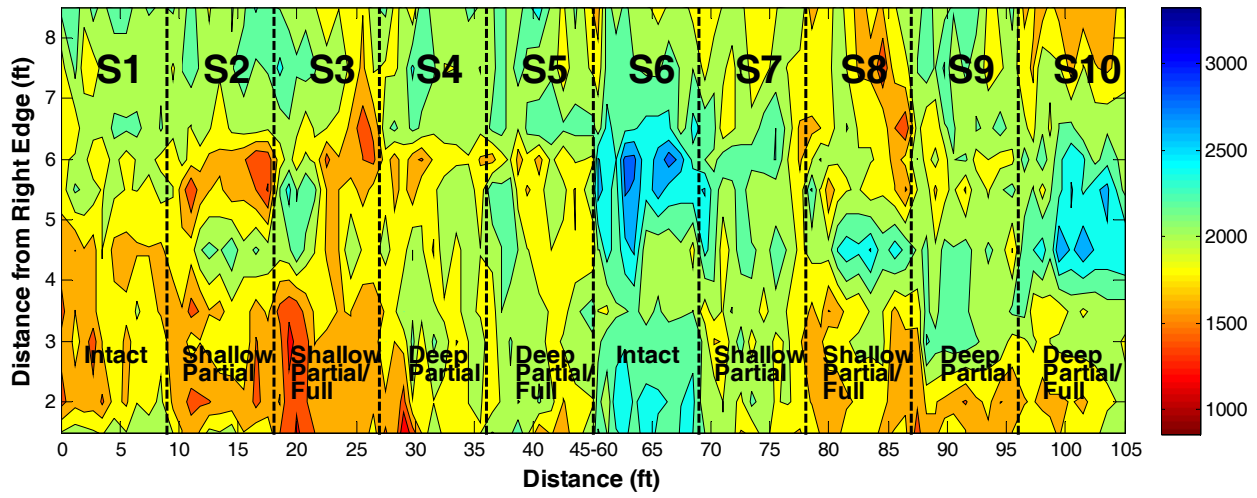
Section	Point	Seismic Modulus from PSPA (for 2.5 in), ksi									
		Line 1	Line 2	Line 3	Line 4	Line 5	Line 6	Line 7	Line 8	Line 9	Line 10
S10, Deep and Full Debonding	10	2106	2033	2260	2031	1812	1797	2023	2021	2085	1964
	9	2216	1832	1926	2150	1964	2178	1857	1728	1899	1688
	8	2048	2041	1974	2106	2209	2508	2387	1753	1842	1872
	7	2117	1946	1876	2305	2183	2047	1728	2131	1724	1680
	6	2059	2183	1957	2213	2034	2279	2056	2268	2294	1460
	5	1957	2344	2128	1826	2105	2066	2228	1898	1749	2164
	4	1953	2286	2074	1903	1930	2205	1959	1501	1552	1541
	3	2019	1744	1931	1911	1655	2221	2151	1855	1697	1894
	2	1872	1916	1997	1903	1983	1953	1795	1941	1758	1864
	1	1909	1993	1960	1955	1772	1954	1964	2190	1641	1966
S9, Deep and Partial Debonding	10	1557	1884	1696	1507	2009	1824	1853	1811	1702	1645
	9	1471	1697	1837	2035	1558	1701	1963	1967	1763	1814
	8	1752	1746	1624	1696	2180	2262	1856	1944	1719	1736
	7	1887	1588	1619	1622	2139	2026	2120	1759	1740	1838
	6	1702	2053	1760	2099	2065	2091	1880	2050	1949	1867
	5	1738	1685	1882	1964	2070	2533	2231	1877	1940	1988
	4	1622	2006	1690	1853	2049	2078	1955	1852	2116	1832
	3	1688	1619	1816	1587	1581	1980	1956	2111	1966	1982
	2	1604	1799	1754	1592	1673	1936	1966	2141	1945	1914
	1	1665	1752	1626	1827	1776	1902	1858	1706	1383	1428
S8, Shallow and Full Debonding	10	1901	1840	1666	1323	1377	2280	1641	1702	1484	1548
	9	1866	1871	1525	1438	1392	1930	2081	1680	1399	1522
	8	1682	1881	1671	1967	1690	1799	1735	1583	1473	1514
	7	1843	1861	1966	2125	1674	1896	1750	1637	1901	1668
	6	1765	1726	2020	2111	1803	2078	1770	1853	1737	1617
	5	2061	2071	1732	2020	1808	2062	1851	1718	1860	1733
	4	2218	1942	2138	1918	1777	2289	1790	1671	1880	1711
	3	1837	1764	2008	1615	1678	1856	1727	1974	1421	1529
	2	1829	1845	1872	2074	2074	2234	1736	1554	1735	1653
	1	1665	1785	1923	1803	2094	2031	2040	1688	1858	1784
S7, Shallow and Partial Debonding	10	1653	1827	1466	1333	1825	1967	1614	1498	1582	1375
	9	1729	1700	1313	1444	1458	2075	1872	1633	1797	1784
	8	1594	1487	1665	1888	1936	1492	1732	1850	1523	1632
	7	1412	1514	1555	1483	1751	1727	1709	1845	1558	1765
	6	1995	1799	1756	1881	2116	1730	1785	1668	1715	1711
	5	1639	1974	1895	2081	1954	1954	1658	1939	1994	1877
	4	1688	1994	1913	2313	1884	1938	1960	1930	1932	1611
	3	1343	1905	2024	2010	2069	1844	1795	1722	1589	1696
	2	1525	1883	1800	1832	2140	1939	1650	1652	1873	1611
	1	1800	1677	2014	1546	1963	2211	1737	1739	1758	1677
S6, Intact	10	1435	1754	1661	1946	1759	1841	1622	2032	1701	2366
	9	1587	1988	1962	1897	1896	1889	1756	1719	1914	2254
	8	1858	1691	1729	1840	1579	1836	1667	1936	2249	2029
	7	1720	1784	1841	1722	1888	1857	1641	2000	1899	1864
	6	1811	1999	2177	2009	1904	1900	2042	2059	1987	2002
	5	1638	1978	1719	1886	1763	1800	2007	1862	1991	1884
	4	1380	2005	1910	1988	1767	2143	1910	1870	1997	1915
	3	2775	2076	2210	2107	1504	1792	1872	1926	1599	1805
	2	2171	1766	1946	1899	1690	1923	1846	1841	1903	1983
	1	1491	2077	1883	1948	1938	2016	1803	1929	1793	2072

**Table E.7 Contd. – PSPA Results on Small Scale Study (Top Lift). Fine Mix and Transition
(Hot Weather)**

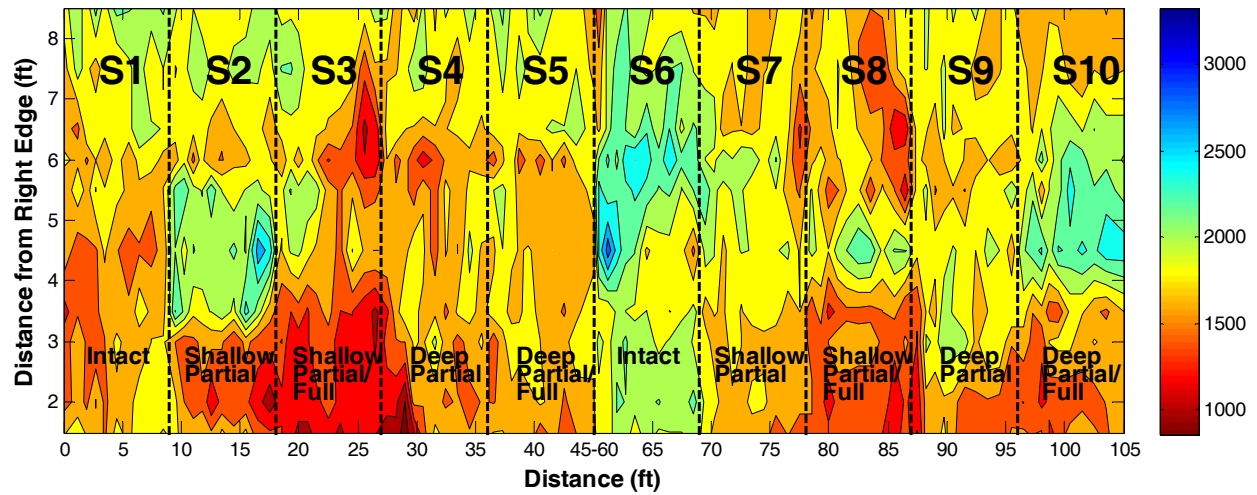
TRANSITION	15	1337	1586	1550	1584	1426	1937	2554	2272	1836	2060
	14	1456	1712	1630	1678	2170	3233	2127	2342	2531	2074
	13	1462	1400	1309	1673	1651	1497	2215	2413	1718	2031
	12	1463	1742	1592	1526	1590	1899	1527	1881	2028	2220
	11	1508	1151	1371	1381	1521	1982	1877	1932	1875	2338
	10	1542	1472	1742	2015	1950	1863	2421	2570	1753	1994
	9	1164	1428	1813	2022	1705	2274	2115	2361	1791	2056
	8	1657	1791	2138	1747	1594	1313	1410	1560	1491	1630
	7	1870	2306	2070	1789	1346	2022	1584	1609	1966	2113
	6	1960	1761	2010	1968	1338	1609	1798	1370	1723	1890
	5	1698	1782	2312	1839	1399	1765	1649	1807	1941	1570
	4	1648	2022	1883	2011	1989	1849	2029	2448	2025	2439
	3	2144	1945	1955	1875	2049	2063	2170	2044	2090	1954
	2	1930	2096	2027	1878	2079	2166	2201	2174	1991	1748
	1	2111	2078	2095	1987	2057	2053	2023	2434	1916	2108

Table E.8 – PSPA Results on Small Scale Study (Top Lift). Coarse Mix (Hot Weather)

Section	Point	Seismic Modulus from PSPA (for 2.5 in), ksi									
		Line 1	Line 2	Line 3	Line 4	Line 5	Line 6	Line 7	Line 8	Line 9	Line 10
S5, Deep and Full Debonding	10	1465	1745	1771	1890	1626	1766	1906	1875	1644	1927
	9	1816	1679	1840	1990	2109	1725	1938	1973	1919	2046
	8	1555	1601	2257	1983	2404	2215	1786	1806	1989	2265
	7	1551	1843	2324	2080	2390	2346	2152	2127	2129	1859
	6	1786	1872	2040	1832	2188	2355	2308	2298	2076	2215
	5	1715	1898	1941	2126	2325	2364	2264	2261	1954	2013
	4	1822	2069	1785	1961	2238	2123	2152	2225	2147	1856
	3	1836	1846	1725	1836	2050	1985	1933	2044	1924	1922
	2	1939	1980	1616	1903	1875	2082	1946	2048	1776	1896
	1	1628	1722	1901	1783	2026	2042	1882	1981	1769	1853
S4, Deep and Partial Debonding	10	2079	1899	1948	1709	1802	1960	1916	2108	1988	1966
	9	2100	1927	2051	1897	2026	2071	2021	1972	1970	1874
	8	1940	1885	1941	1874	2097	1882	1918	1755	1917	1972
	7	2027	1863	2021	1752	2063	2136	1899	2043	1902	1922
	6	1942	2090	1914	1740	1866	1722	1989	2194	1959	2120
	5	2193	2114	2040	1502	1892	1968	2000	1859	1938	1787
	4	1691	2269	2106	1617	1595	2139	2103	2223	1952	1492
	3	1938	1961	1950	1823	1767	1838	2139	1830	1482	1189
	2	1785	1824	2081	1600	1655	1840	1902	1758	1710	1711
	1	2085	1827	2008	1795	1848	1976	1777	1956	1724	1552
S3, Shallow and Full Debonding	10	1515	1574	1599	1383	1642	1600	1510	1541	1824	1483
	9	1682	1350	1223	1523	1403	1706	1554	1594	1596	1624
	8	1776	1569	1740	1447	1615	1778	1504	1551	1579	1379
	7	1669	1864	1617	1378	1585	1937	1577	1574	1721	1368
	6	1552	1707	1723	1402	1543	1464	1571	1638	1444	1444
	5	1791	1784	1811	1528	1933	1888	1631	1668	1559	1400
	4	1729	1664	1835	1676	1625	1929	1412	1259	1394	1671
	3	1776	2068	1732	1411	1680	1857	1176	1337	1508	1541
	2	1782	1956	1806	1608	1923	1536	1163	1208	1236	1581
	1	1836	1645	1753	1538	1695	1759	1528	1460	1586	1570
S2, Shallow and Partial Debonding	10	1742	1713	1831	1758	1741	1956	2175	1729	1459	1769
	9	1563	1751	1735	1659	2152	1900	1911	1797	1429	1811
	8	1630	1799	1831	1679	1748	1842	1836	1689	1638	2076
	7	1563	1596	1809	1893	1546	2004	2036	1878	1631	1630
	6	1792	1758	1957	1835	1882	1916	1604	1792	1702	1836
	5	1767	1744	1927	1612	1724	1975	1939	1724	1481	2026
	4	1666	1815	1440	1908	1998	2082	1863	1727	1644	1758
	3	1629	1632	1430	1882	1868	1700	2021	1759	1694	1785
	2	1561	1722	1572	1892	1912	1825	2115	1757	1500	1734
	1	1471	1596	1688	1806	1918	1759	2081	1684	1841	1712
S1, Intact	10	1956	1962	1603	1709	1706	1852	1589	1856	1783	1723
	9	1797	1767	1614	1727	1645	1592	1603	1784	1731	1613
	8	1863	1782	1773	1765	1692	1697	1624	1572	1748	1732
	7	1858	1772	1908	1659	1492	1507	1755	1617	1580	1545
	6	1940	1754	1726	1743	1603	1752	1614	1772	1778	1711
	5	1799	1917	1782	1678	1628	1846	1766	1832	1649	1624
	4	1710	2222	1700	1636	1556	1895	1710	1865	1870	1613
	3	1734	1876	1600	1635	1754	1758	1776	1745	1726	2004
	2	1502	1760	1793	1625	1535	1697	1591	1698	1783	1786
1	2252	1718	1759	1438	1480	1768	1475	1653	1698	1890	



a) 2.5 inches



b) 8 inches

Figure E.1 – Overall Modulus Results (Top View) on Small Scale Study. Hot Weather Results

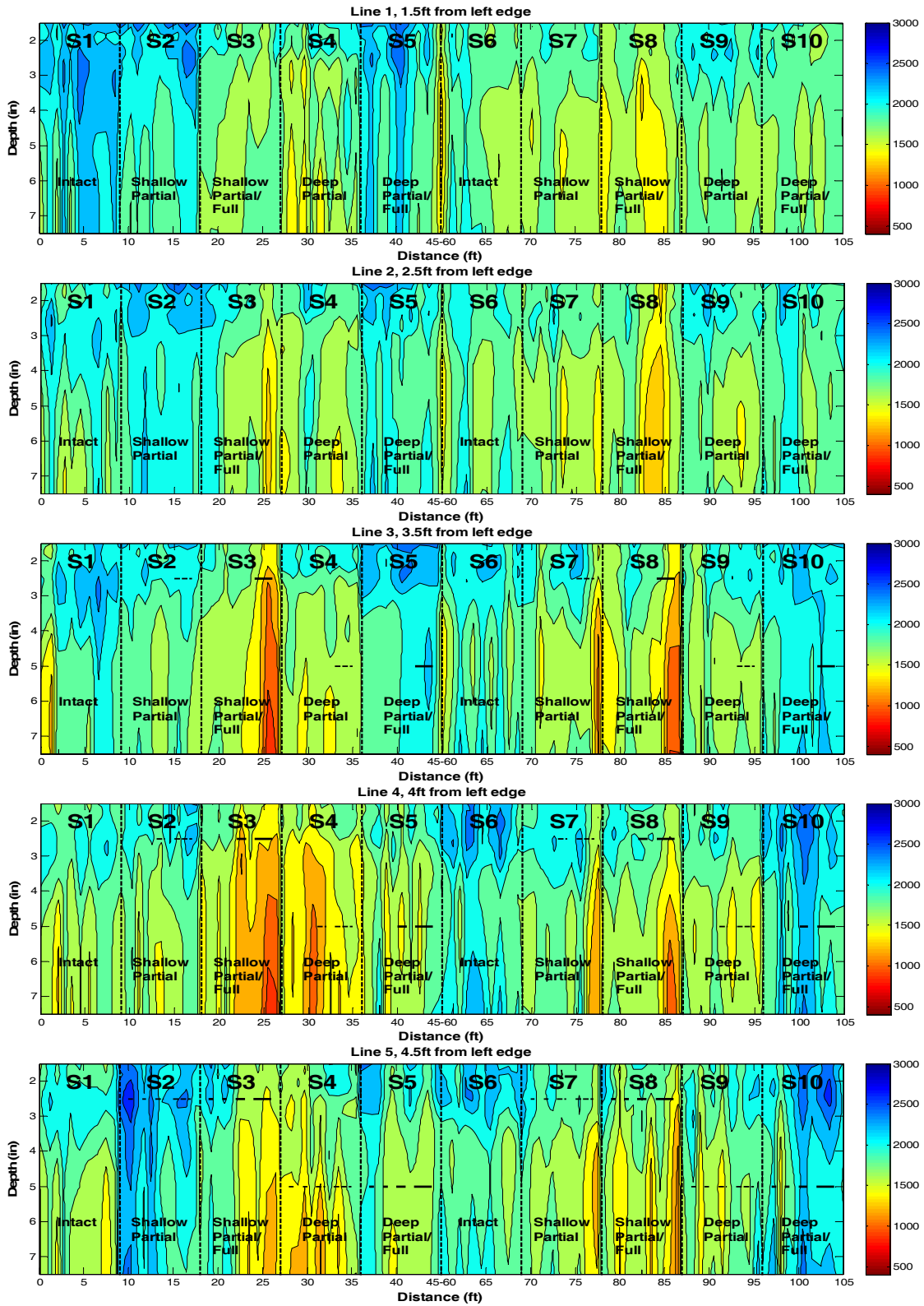


Figure E.2 – Dispersion Curve Results for 10 Lines of Extended Testing (Cross Section and Cool Weather)

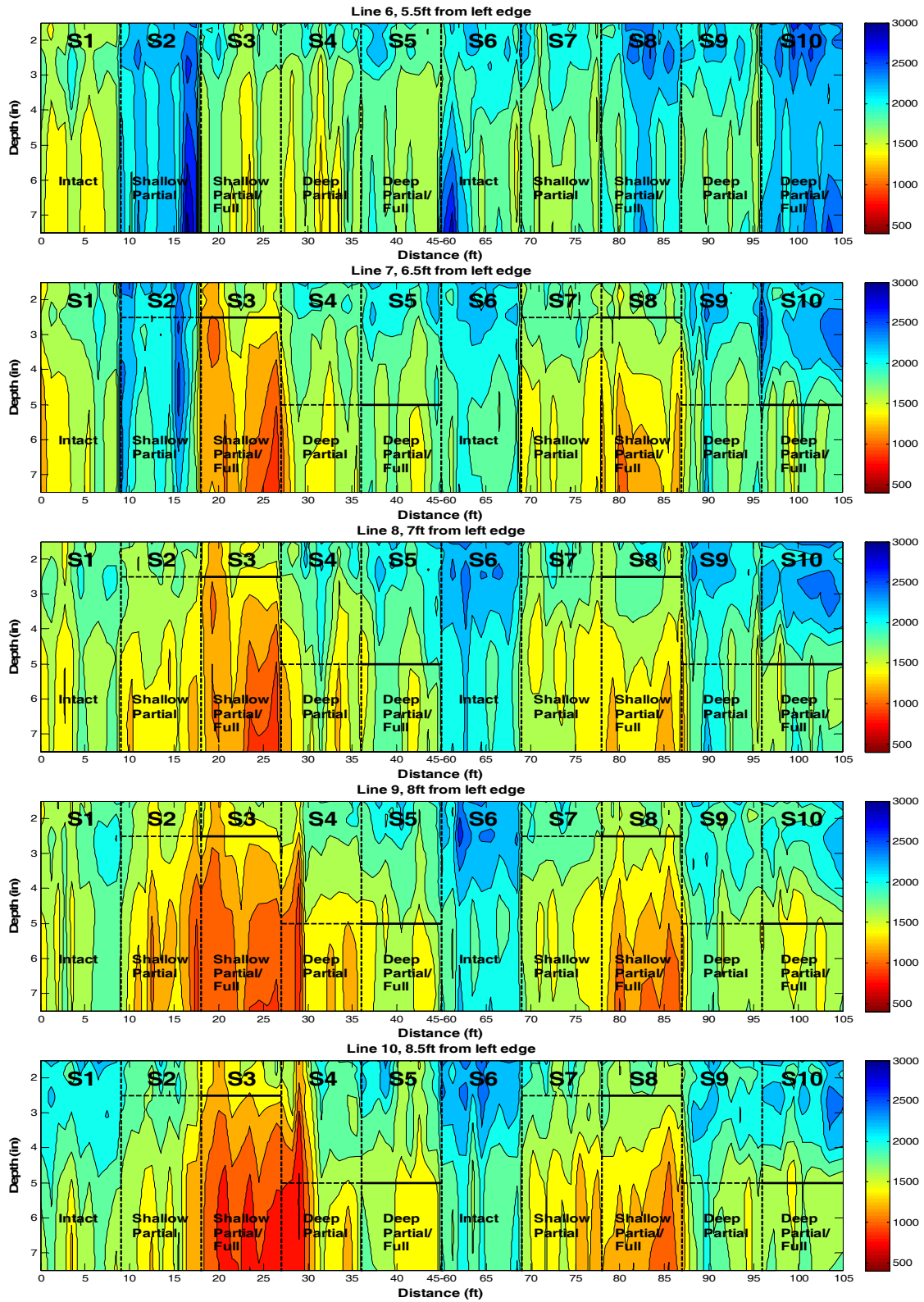


Figure E.2 Contd. – Dispersion Curve Results for 10 Lines of Extended Testing (Cross Section and Cool Weather)

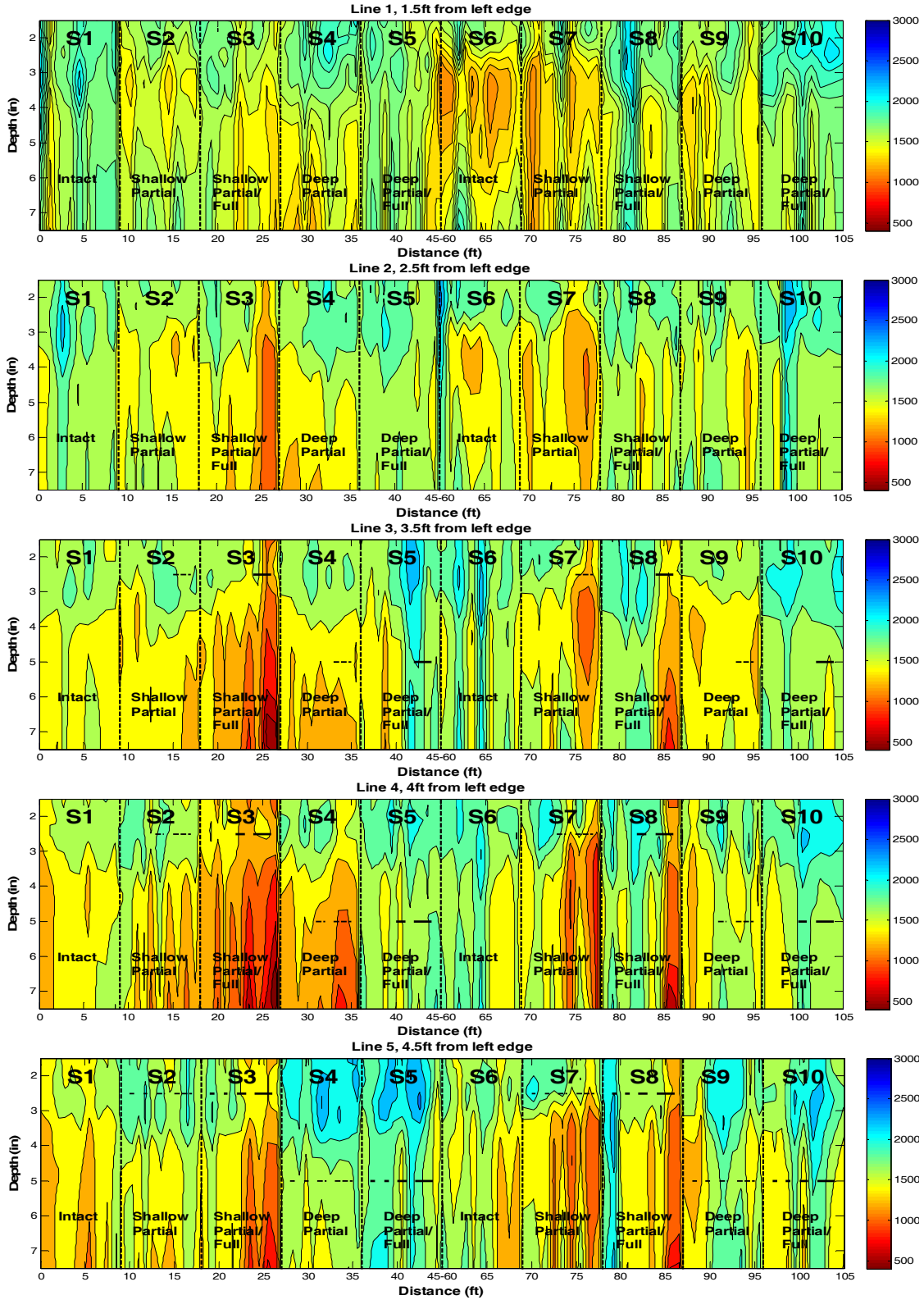


Figure E.3 – Dispersion Curve Results for 10 Lines of Extended Testing (Cross Section and Hot Weather)

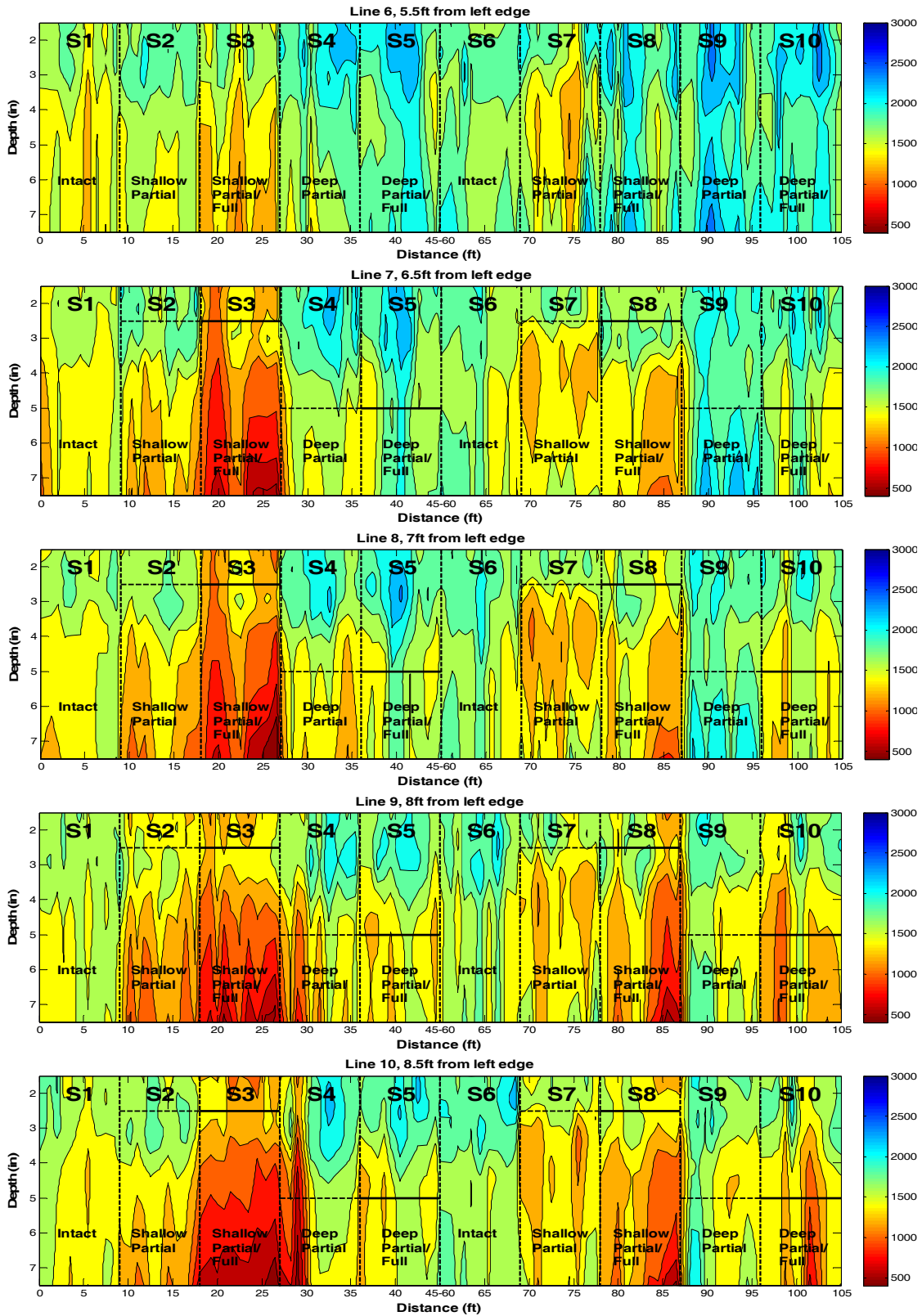


Figure E.3 Contd. – Dispersion Curve Results for 10 Lines of Extended Testing (Cross Section and Hot Weather)

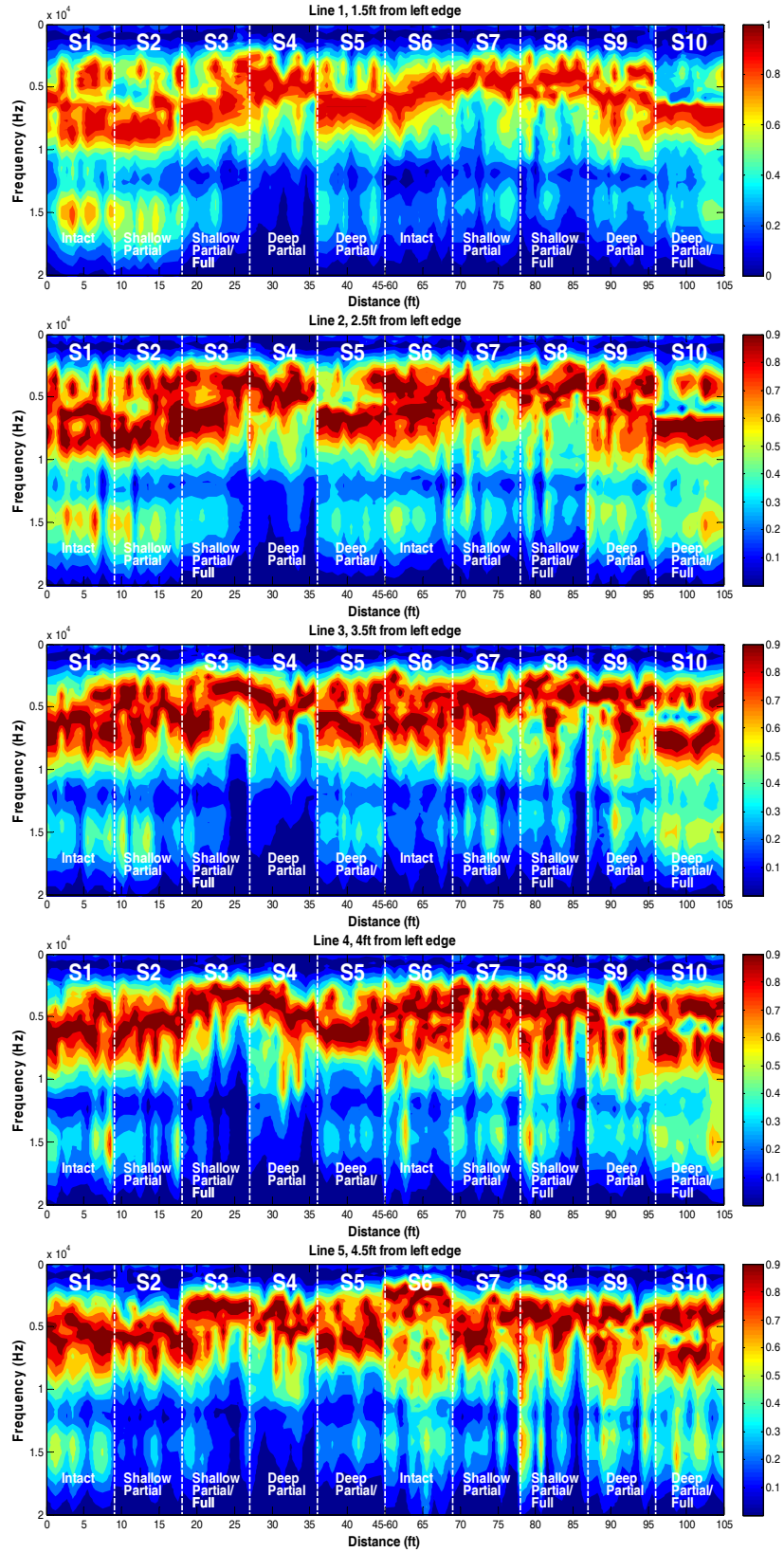


Figure E.4 – IE Results with PSPA on Extended Tests of Small Scale Study (Cool Weather)

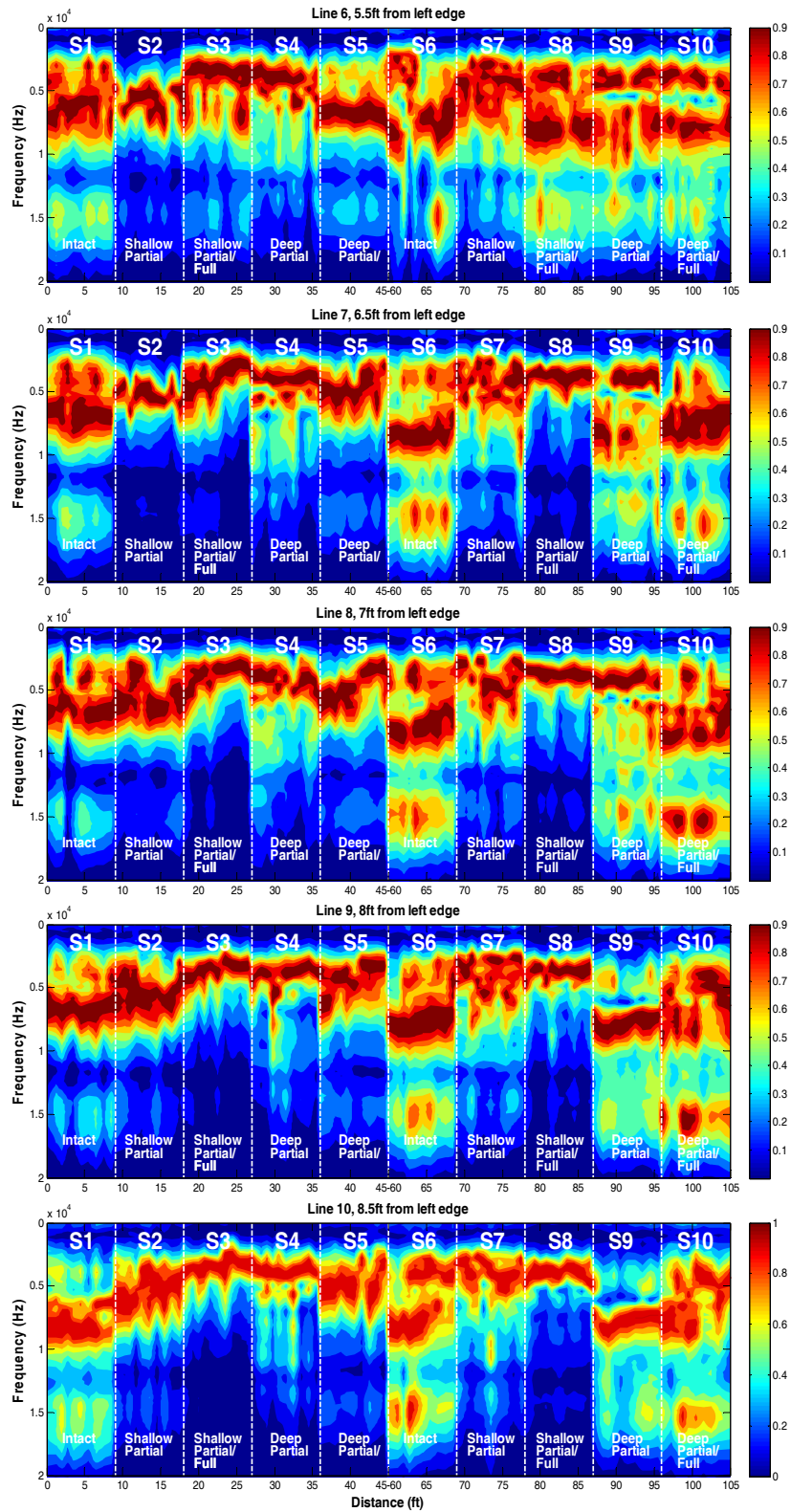


Figure E.4 Contd. – IE Results with PSPA on Extended Tests of Small Scale Study (Cool Weather)

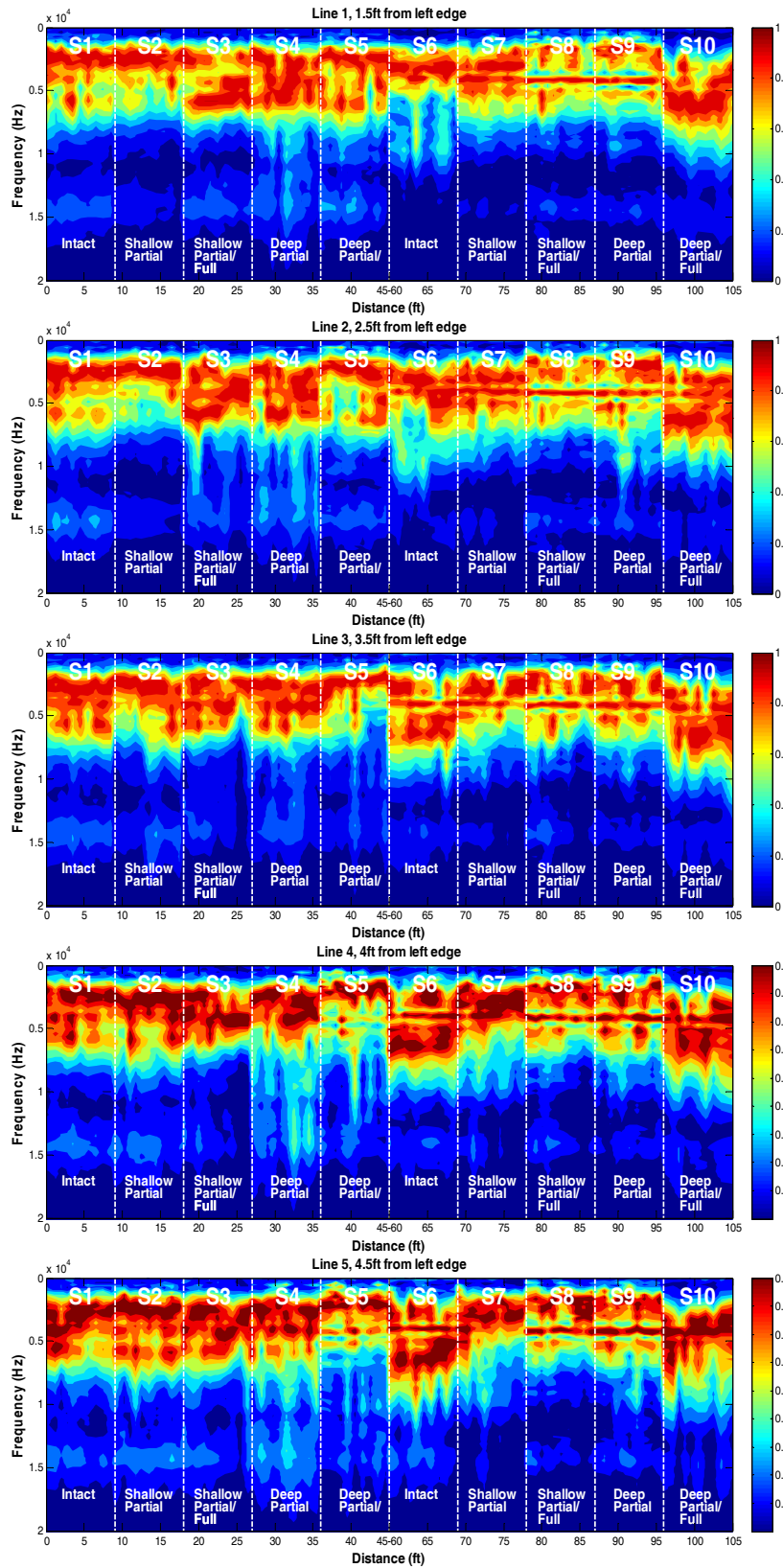


Figure E.5 – IE Results with PSPA on Extended Tests of Small Scale Study (Hot Weather)

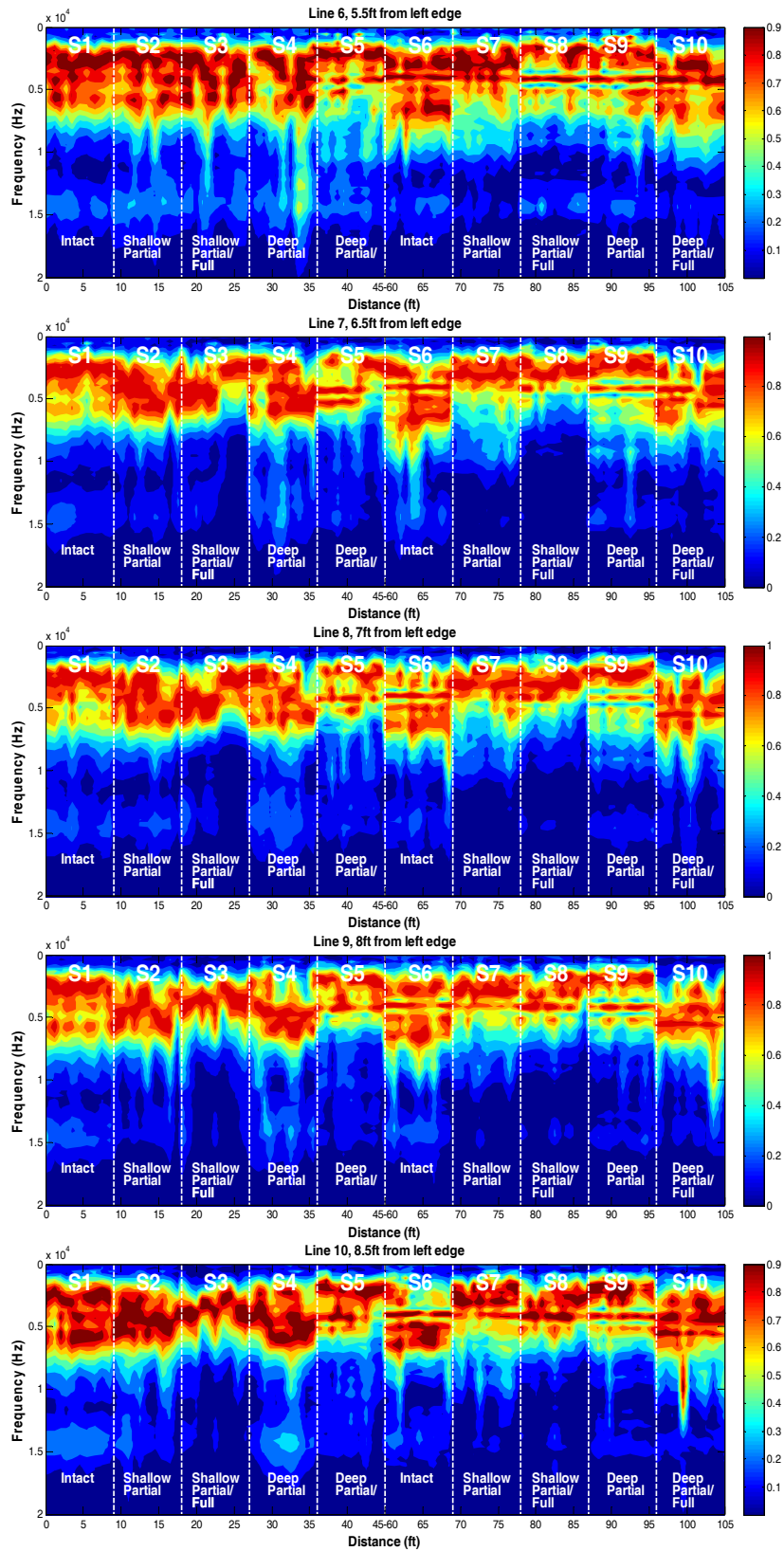


Figure E.5 Contd. – IE Results with PSPA on Extended Tests of Small Scale Study (Hot Weather)

Table E.9 – FFT Ratios of Impulse Response on Small Scale Study. Fine Mix and Transition (Cool Weather)

Section	Point	Impulse Response FFT Ratios (Load/Geophone)									
		Line 1	Line 2	Line 3	Line 4	Line 5	Line 6	Line 7	Line 8	Line 9	Line 10
S10, Deep and Full Debonding	10	3.05	3.31	3.06	2.85	2.85	2.82	2.35	2.20	1.74	1.41
	9	3.25	3.30	3.00	2.82	2.42	2.54	2.44	2.20	1.63	1.43
	8	3.13	3.45	2.84	3.16	2.83	2.71	2.40	2.21	1.33	1.13
	7	3.12	2.78	3.06	3.03	3.02	2.54	2.19	2.06	1.15	0.89
	6	2.23	2.87	3.22	2.96	2.92	2.54	1.85	2.13	1.31	0.90
	5	1.86	2.72	2.88	3.04	3.02	2.70	1.76	1.49	1.29	1.02
	4	1.96	2.63	3.13	2.93	2.85	2.64	1.72	1.50	1.03	1.08
	3	2.06	2.46	2.93	2.74	2.51	2.64	1.69	1.48	1.25	1.18
	2	2.07	2.69	2.89	2.84	2.58	2.76	1.78	1.46	1.46	1.19
	1	2.59	2.80	3.02	2.74	2.82	2.89	2.50	1.54	1.64	1.26
S9, Deep and Partial Debonding	10	2.47	2.87	2.19	1.93	2.67	2.69	2.03	1.81	1.62	1.47
	9	2.14	2.00	2.32	1.74	2.03	2.38	2.31	1.90	1.60	1.51
	8	2.15	2.89	1.92	1.71	2.01	1.87	2.44	1.88	1.60	1.40
	7	2.68	2.85	2.88	2.58	2.66	2.38	2.45	2.06	1.78	1.37
	6	2.03	2.74	2.46	2.05	2.06	2.23	2.43	1.96	1.65	1.36
	5	2.18	2.39	2.30	1.88	2.07	2.01	1.97	1.91	1.62	1.41
	4	1.63	2.56	2.12	1.98	1.76	2.08	1.97	1.98	1.68	1.39
	3	2.13	2.42	2.28	1.97	2.19	2.23	2.05	1.89	1.79	1.68
	2	2.39	2.47	1.88	2.17	2.30	2.06	2.30	2.00	1.80	1.42
	1	2.43	2.92	2.57	2.12	2.55	2.43	1.99	1.88	1.61	1.37
S8, Shallow and Full Debonding	10	2.25	2.45	1.75	1.66	1.97	2.21	1.43	1.24	1.05	1.27
	9	2.56	2.04	1.34	1.27	1.45	2.01	1.46	1.15	1.23	1.17
	8	2.34	2.20	1.33	1.40	1.71	2.06	1.39	1.06	1.20	1.21
	7	2.38	2.20	2.21	2.31	2.26	2.32	1.51	1.35	1.38	1.22
	6	2.18	2.59	2.64	2.40	2.49	2.38	1.86	1.70	1.45	1.48
	5	2.39	2.44	2.82	2.55	2.62	2.40	1.98	1.59	1.39	1.49
	4	2.63	2.62	2.77	2.54	2.48	2.39	1.83	1.44	1.41	1.26
	3	2.39	2.29	2.45	2.30	2.33	2.28	1.82	1.62	1.32	1.50
	2	2.41	2.32	2.52	2.32	2.31	2.42	1.87	1.79	1.47	1.63
	1	2.12	2.27	2.39	2.28	2.36	2.35	2.26	1.94	1.78	1.69
S7, Shallow and Partial Debonding	10	2.54	2.36	2.21	2.17	2.18	2.51	2.47	2.36	2.18	2.06
	9	2.56	2.24	1.98	2.13	2.04	2.56	2.27	2.25	2.24	2.02
	8	2.77	2.45	2.32	2.25	2.23	2.46	2.42	2.34	2.30	2.06
	7	2.65	2.58	2.16	2.44	2.20	2.36	2.52	2.35	2.32	2.08
	6	2.61	2.35	2.38	2.40	2.35	2.32	2.41	2.31	2.34	2.10
	5	2.41	2.43	2.21	2.45	2.09	2.33	2.21	2.12	2.23	2.00
	4	2.42	2.48	2.57	2.36	2.32	2.31	2.08	2.17	1.96	2.02
	3	2.46	2.67	2.50	2.31	2.23	2.29	2.10	2.04	1.89	2.08
	2	2.48	2.47	2.35	2.39	2.19	2.32	2.03	2.02	1.97	1.94
	1	2.32	2.63	2.60	2.40	2.30	2.40	2.12	2.10	2.17	2.00
S6, Intact	10	2.30	2.13	1.99	1.99	2.04	1.83	1.96	2.06	2.02	2.00
	9	2.18	2.10	1.98	1.94	1.99	1.93	1.86	2.09	2.13	1.89
	8	2.13	2.00	1.92	1.88	1.88	1.84	2.05	2.01	1.93	1.64
	7	1.82	1.92	1.87	1.92	1.95	1.82	2.00	1.81	1.90	1.71
	6	1.91	2.07	1.97	1.95	2.08	1.85	1.72	1.79	1.54	1.75
	5	1.97	1.89	1.99	1.92	1.96	1.89	1.75	1.89	1.88	1.81
	4	2.00	2.08	1.94	2.03	2.07	1.93	1.77	1.89	1.98	1.80
	3	2.22	2.28	2.09	2.15	2.07	1.94	1.79	1.83	1.78	1.90
	2	2.12	2.22	2.14	2.22	2.19	1.99	1.87	1.98	1.77	1.89
	1	2.12	2.18	2.07	2.14	2.15	1.97	1.76	2.11	1.95	1.79

Table E.9 Contd. – FFT Ratios of Impulse Response on Small Scale Study. Fine Mix and Transition (Cool Weather)

TRANSITION	15	1.85	1.96	1.65	2.00	2.17	2.35	2.17	2.26	1.99	1.77
	14	1.87	1.94	1.84	2.21	2.22	2.33	2.08	2.22	2.05	1.78
	13	1.91	1.90	2.06	2.19	2.07	2.11	2.07	2.01	2.00	1.75
	12	1.77	1.85	1.84	2.04	2.04	2.16	2.07	2.14	1.97	1.65
	11	1.66	1.80	1.86	1.80	2.01	2.14	1.96	2.13	1.94	1.69
	10	1.58	1.72	1.61	1.80	2.00	2.05	2.00	2.07	1.84	1.67
	9	1.53	1.83	1.72	2.03	2.07	1.98	1.95	1.89	1.83	1.63
	8	1.60	2.01	2.03	1.95	1.82	1.37	1.24	1.34	1.40	1.16
	7	1.91	2.18	2.01	1.90	1.45	0.46	0.55	0.88	1.25	0.77
	6	1.96	2.13	1.96	1.81	1.44	0.36	0.52	0.72	0.85	0.81
	5	2.14	2.26	2.12	1.91	1.49	0.68	0.85	0.83	0.94	1.44
	4	2.23	2.40	2.05	2.00	1.86	1.67	1.67	1.71	1.70	1.50
	3	2.26	2.42	2.33	2.36	2.50	2.44	2.39	2.40	2.15	1.81
	2	2.15	2.33	2.23	2.52	2.39	2.81	2.82	2.79	2.23	1.89
	1	2.01	2.37	2.33	2.33	2.30	2.93	2.90	2.85	2.22	1.95

Table E.10 – FFT Ratios of Impulse Response on Small Scale Study. Coarse Mix (Cool Weather)

Section	Point	Impulse Response FFT Ratios (Load/geophone)									
		Line 1	Line 2	Line 3	Line 4	Line 5	Line 6	Line 7	Line 8	Line 9	Line 10
S5, Deep and Full Debonding	10	1.90	2.02	2.09	2.02	2.19	2.54	2.45	2.21	1.70	1.65
	9	1.82	1.99	1.93	1.72	1.96	2.35	2.28	1.98	1.43	1.61
	8	1.90	1.98	2.03	1.54	1.84	2.37	2.22	1.83	1.68	1.80
	7	1.99	2.06	2.27	2.03	2.15	2.47	2.38	2.37	1.90	1.87
	6	2.08	2.16	2.43	2.31	2.45	2.56	2.34	2.23	1.95	2.07
	5	2.17	2.40	2.69	2.50	2.52	2.45	2.30	2.21	1.70	2.01
	4	2.21	2.55	2.86	2.52	2.66	2.48	2.21	1.99	1.26	1.66
	3	2.30	2.42	2.96	2.74	2.73	2.86	2.15	2.01	1.52	1.34
	2	2.32	2.48	2.88	2.76	2.68	2.70	2.21	1.88	1.49	1.61
	1	2.37	2.62	3.02	2.94	2.93	2.74	2.44	2.13	1.78	1.78
S4, Deep and Partial Debonding	10	2.37	2.81	2.59	2.53	2.76	2.79	2.48	2.37	2.16	2.05
	9	2.34	2.67	2.58	2.44	2.51	2.43	2.43	2.27	2.05	2.14
	8	2.32	2.59	2.32	2.13	2.43	2.32	2.11	2.19	2.10	2.05
	7	2.24	2.24	2.12	2.04	2.27	2.06	2.06	2.05	2.12	1.93
	6	2.05	2.12	1.95	1.97	2.04	1.97	2.00	2.08	1.91	1.73
	5	1.85	1.99	1.92	2.00	2.08	2.02	1.98	1.98	1.78	1.64
	4	1.93	1.96	2.01	2.07	2.08	1.99	2.01	2.00	1.57	1.38
	3	1.94	2.15	2.11	2.16	2.22	2.01	1.90	1.82	1.31	1.23
	2	1.95	2.30	2.32	2.29	2.36	2.06	1.83	1.73	1.44	1.22
	1	2.02	2.36	2.46	2.48	2.42	2.02	1.76	1.77	1.33	1.16
S3, Shallow and Full Debonding	10	2.22	2.47	2.20	1.98	2.27	1.99	1.53	1.35	1.54	1.35
	9	2.23	2.30	2.08	1.87	2.20	1.91	1.38	1.19	1.52	1.43
	8	2.25	2.40	2.30	2.02	2.37	2.01	1.36	1.27	1.59	1.44
	7	2.09	2.37	2.05	2.17	2.34	2.20	1.38	1.27	1.66	1.44
	6	2.01	2.21	2.04	2.17	2.30	2.29	1.75	1.64	1.67	1.52
	5	2.04	2.19	2.20	2.21	2.50	2.30	1.84	1.72	1.72	1.50
	4	1.94	2.19	2.28	2.38	2.53	2.23	1.73	1.69	1.58	1.51
	3	2.02	2.29	2.50	2.49	2.57	2.23	1.70	1.65	1.61	1.49
	2	1.99	2.40	2.53	2.63	2.66	2.18	1.73	1.78	1.71	1.51
	1	2.08	2.46	2.72	2.73	2.75	2.24	1.91	1.83	1.77	1.61
S2, Shallow and Partial Debonding	10	2.00	2.33	2.65	2.82	2.79	2.27	2.17	2.03	1.89	1.63
	9	2.08	2.32	2.27	2.41	2.45	2.53	2.35	2.28	1.93	1.77
	8	2.28	2.27	2.30	2.48	2.26	2.54	2.39	2.32	2.03	1.77
	7	2.32	2.56	2.58	2.37	2.58	2.20	2.31	2.32	2.07	1.84
	6	2.10	2.15	2.50	2.56	2.56	2.68	2.35	2.35	2.13	2.00
	5	1.99	2.13	2.40	2.55	2.24	2.65	2.30	2.31	2.16	1.89
	4	1.93	2.25	2.82	2.84	2.83	2.63	2.27	2.26	2.16	1.95
	3	1.87	2.21	2.85	2.82	2.85	2.76	2.35	2.12	2.01	1.89
	2	2.02	2.40	2.76	2.96	2.93	2.61	2.26	2.16	2.11	2.00
	1	0.89	2.53	3.05	3.08	3.02	2.64	2.28	2.02	2.32	2.06
S1, Intact	10	2.47	2.48	2.38	2.18	2.23	1.98	2.10	2.18	2.29	2.02
	9	2.33	2.85	2.62	2.33	2.32	2.26	2.06	2.10	2.27	1.98
	8	2.60	3.19	2.78	2.70	2.53	2.06	1.91	2.00	2.16	1.99
	7	2.80	3.27	3.20	2.94	2.75	2.14	1.83	1.83	2.18	2.01
	6	2.56	3.17	2.96	2.61	2.52	2.06	1.80	1.97	2.20	2.04
	5	2.31	2.76	2.59	2.09	2.32	2.12	1.92	2.10	2.19	2.08
	4	2.20	2.78	2.66	2.19	2.27	2.17	1.99	1.96	2.13	1.96
	3	2.19	2.55	2.74	2.06	2.15	2.13	2.05	1.84	2.13	1.90
	2	1.96	2.54	2.35	2.25	2.26	1.99	2.09	1.91	2.01	1.92
	1	1.94	2.63	2.19	2.21	2.34	1.81	1.95	1.98	2.05	1.99

Table E.11 – FFT Ratios of Impulse Response on Small Scale Study. Fine Mix and Transition (Hot Weather)

Section	Point	Impulse Response FFT Ratios (Load/Geophone)									
		Line 1	Line 2	Line 3	Line 4	Line 5	Line 6	Line 7	Line 8	Line 9	Line 10
S10, Deep and Full Debonding	10	3.34	3.48	3.22	2.87	2.73	2.57	2.35	1.81	1.57	1.35
	9	3.42	3.12	3.18	3.03	2.87	2.71	2.24	1.69	1.15	1.08
	8	3.56	3.39	3.29	3.14	2.73	2.50	2.23	1.75	1.19	1.03
	7	3.51	3.61	3.59	3.25	2.89	2.64	2.23	1.99	1.40	1.11
	6	3.13	3.24	3.30	3.25	3.03	2.64	2.29	2.22	1.47	1.18
	5	2.34	3.07	3.39	3.16	2.99	2.74	2.11	1.77	1.23	1.29
	4	2.47	3.06	3.32	3.19	2.91	2.83	2.09	1.47	1.05	1.16
	3	2.47	3.03	3.31	2.96	2.92	2.68	1.71	1.28	0.92	1.07
	2	2.63	2.84	2.90	2.94	2.62	2.51	1.71	1.39	1.13	1.03
	1	2.50	2.99	2.92	2.92	2.69	2.89	2.28	1.63	1.29	1.17
S9, Deep and Partial Debonding	10	3.32	3.35	3.43	3.50	3.86	4.01	3.01	2.16	1.56	1.55
	9	3.59	3.16	3.37	2.71	3.16	3.49	2.26	1.85	1.42	1.35
	8	3.53	3.63	3.55	3.08	3.19	3.33	2.52	2.07	1.37	1.39
	7	4.31	4.00	3.83	3.83	3.70	3.84	3.35	2.54	1.68	1.45
	6	3.44	3.45	3.24	2.69	2.86	3.10	3.04	2.20	1.57	1.78
	5	2.86	3.19	3.03	2.73	2.66	2.74	2.76	2.15	2.08	1.73
	4	2.78	3.30	3.12	2.83	2.81	2.88	2.40	1.87	1.78	1.80
	3	2.63	3.18	2.76	2.74	3.00	2.93	2.24	1.76	1.70	1.77
	2	2.82	3.08	3.13	3.03	3.32	2.99	2.56	1.97	1.95	1.91
	1	2.95	3.28	3.07	3.13	3.31	3.26	2.66	2.18	2.10	1.82
S8, Shallow and Full Debonding	10	3.14	3.16	2.25	2.14	2.22	2.56	1.76	1.75	1.37	1.54
	9	2.98	2.61	1.82	1.74	1.74	2.30	1.60	1.16	1.05	1.31
	8	2.72	2.68	2.02	1.83	2.10	2.59	1.69	1.29	1.21	1.21
	7	2.66	2.61	2.67	2.62	2.61	2.80	2.00	1.68	1.56	1.69
	6	2.51	2.67	2.81	2.83	2.90	2.96	2.70	2.43	2.44	2.47
	5	2.57	2.73	2.83	2.89	3.16	3.01	2.74	2.77	2.43	2.44
	4	2.71	2.72	2.90	2.73	2.90	3.13	2.75	2.15	1.83	2.07
	3	2.59	2.66	2.65	2.70	2.72	2.78	2.22	1.68	1.58	1.75
	2	2.68	2.76	2.67	2.77	2.58	3.03	2.55	2.27	2.06	2.28
	1	2.92	2.88	2.83	2.88	2.83	3.03	2.72	2.61	2.88	2.78
S7, Shallow and Partial Debonding	10	2.30	2.41	2.46	2.58	2.54	2.72	2.48	2.77	3.02	3.35
	9	2.58	2.46	2.49	2.36	2.61	2.70	2.54	2.60	2.60	2.91
	8	2.64	2.59	2.43	2.56	2.57	2.65	2.61	2.75	2.34	2.95
	7	2.64	2.59	2.69	2.55	2.76	2.72	2.66	2.83	2.77	3.23
	6	2.38	2.59	2.60	2.58	2.70	2.64	2.51	2.70	2.94	3.03
	5	2.41	2.31	2.49	2.61	2.53	2.61	2.37	2.59	2.73	3.03
	4	2.45	2.26	2.39	2.47	2.57	2.46	2.36	2.45	2.56	3.00
	3	2.48	2.49	2.26	2.43	2.36	2.43	2.40	2.16	2.17	2.60
	2	2.39	2.36	2.20	2.36	2.26	2.31	2.35	2.33	2.39	2.72
	1	2.10	2.32	2.26	2.19	2.25	2.40	2.64	2.66	2.99	3.04
S6, Intact	10	2.79	2.38	2.28	2.30	2.30	2.64	2.74	3.33	3.83	3.99
	9	2.54	2.31	2.22	2.32	2.49	2.81	2.61	3.27	3.62	4.11
	8	2.45	2.32	2.31	2.44	2.74	3.05	2.73	3.07	3.32	3.71
	7	2.21	2.36	2.38	2.58	2.97	3.01	2.64	3.04	3.40	3.48
	6	2.40	2.37	2.56	2.66	2.99	3.03	3.24	3.30	3.22	3.40
	5	2.69	2.65	2.66	2.68	2.89	3.26	2.89	3.41	3.32	3.37
	4	2.92	2.83	2.60	2.78	2.87	2.83	2.96	2.81	3.29	3.21
	3	2.92	2.97	2.85	2.79	2.88	3.07	2.62	2.84	2.99	3.15
	2	2.63	2.82	2.76	2.66	2.90	3.00	3.08	3.28	3.27	3.68
	1	2.33	2.61	2.86	2.81	2.71	2.91	3.05	3.71	4.02	4.12

Table E.11 Contd. – FFT Ratios of Impulse Response on Small Scale Study. Fine Mix and Transition (Hot Weather)

TRANSITION	15	2.02	2.31	2.33	2.32	2.32	2.44	2.61	2.99	3.22	3.16
	14	1.90	2.18	2.14	2.36	2.23	2.25	2.51	2.80	3.37	3.37
	13	1.87	2.04	2.06	2.10	2.27	2.20	2.44	2.80	3.26	3.16
	12	2.00	2.00	2.08	2.09	2.19	2.31	2.45	2.74	3.02	3.16
	11	1.95	1.92	1.93	1.99	2.06	2.09	2.22	2.50	3.03	2.91
	10	1.91	1.88	1.87	1.93	1.98	2.11	2.24	2.50	2.94	2.88
	9	1.79	1.88	2.03	2.05	2.01	2.09	2.31	2.40	2.82	3.02
	8	1.78	2.12	2.19	2.10	1.91	1.50	1.46	1.32	1.89	1.61
	7	2.03	2.23	2.40	2.16	1.74	0.95	0.72	1.02	1.45	1.47
	6	2.30	2.47	2.39	2.12	1.63	0.73	0.77	1.09	1.47	1.50
	5	2.55	2.71	2.57	2.28	1.79	1.07	0.84	0.74	1.04	1.28
	4	2.66	3.08	2.86	2.54	2.38	2.02	2.46	2.65	2.46	2.75
	3	2.78	3.27	3.15	3.00	2.93	3.24	3.66	3.86	3.75	3.43
	2	2.56	3.11	3.20	3.24	3.19	3.41	3.97	3.89	3.68	3.26
1	2.58	3.20	3.18	2.99	3.07	3.57	3.86	4.24	3.80	3.10	

Table E.12 – FFT Ratios of Impulse Response on Small Scale Study. Coarse Mix (Hot Weather)

Section	Point	Impulse Response FFT Ratios (Load/geophone)									
		Line 1	Line 2	Line 3	Line 4	Line 5	Line 6	Line 7	Line 8	Line 9	Line 10
S5, Deep and Full Debonding	10	2.02	2.31	2.33	2.32	2.32	2.44	2.61	2.99	3.22	3.16
	9	1.90	2.18	2.14	2.36	2.23	2.25	2.51	2.80	3.37	3.37
	8	1.87	2.04	2.06	2.10	2.27	2.20	2.44	2.80	3.26	3.16
	7	2.00	2.00	2.08	2.09	2.19	2.31	2.45	2.74	3.02	3.16
	6	1.95	1.92	1.93	1.99	2.06	2.09	2.22	2.50	3.03	2.91
	5	1.91	1.88	1.87	1.93	1.98	2.11	2.24	2.50	2.94	2.88
	4	1.79	1.88	2.03	2.05	2.01	2.09	2.31	2.40	2.82	3.02
	3	1.78	2.12	2.19	2.10	1.91	1.50	1.46	1.32	1.89	1.61
	2	2.03	2.23	2.40	2.16	1.74	0.95	0.72	1.02	1.45	1.47
	1	2.30	2.47	2.39	2.12	1.63	0.73	0.77	1.09	1.47	1.50
S4, Deep and Partial Debonding	10	2.55	2.71	2.57	2.28	1.79	1.07	0.84	0.74	1.04	1.28
	9	2.66	3.08	2.86	2.54	2.38	2.02	2.46	2.65	2.46	2.75
	8	2.78	3.27	3.15	3.00	2.93	3.24	3.66	3.86	3.75	3.43
	7	2.56	3.11	3.20	3.24	3.19	3.41	3.97	3.89	3.68	3.26
	6	2.58	3.20	3.18	2.99	3.07	3.57	3.86	4.24	3.80	3.10
	5	2.02	2.31	2.33	2.32	2.32	2.44	2.61	2.99	3.22	3.16
	4	1.90	2.18	2.14	2.36	2.23	2.25	2.51	2.80	3.37	3.37
	3	1.87	2.04	2.06	2.10	2.27	2.20	2.44	2.80	3.26	3.16
	2	2.00	2.00	2.08	2.09	2.19	2.31	2.45	2.74	3.02	3.16
	1	1.95	1.92	1.93	1.99	2.06	2.09	2.22	2.50	3.03	2.91
S3, Shallow and Full Debonding	10	1.91	1.88	1.87	1.93	1.98	2.11	2.24	2.50	2.94	2.88
	9	1.79	1.88	2.03	2.05	2.01	2.09	2.31	2.40	2.82	3.02
	8	1.78	2.12	2.19	2.10	1.91	1.50	1.46	1.32	1.89	1.61
	7	2.03	2.23	2.40	2.16	1.74	0.95	0.72	1.02	1.45	1.47
	6	2.30	2.47	2.39	2.12	1.63	0.73	0.77	1.09	1.47	1.50
	5	2.55	2.71	2.57	2.28	1.79	1.07	0.84	0.74	1.04	1.28
	4	2.66	3.08	2.86	2.54	2.38	2.02	2.46	2.65	2.46	2.75
	3	2.78	3.27	3.15	3.00	2.93	3.24	3.66	3.86	3.75	3.43
	2	2.56	3.11	3.20	3.24	3.19	3.41	3.97	3.89	3.68	3.26
	1	2.58	3.20	3.18	2.99	3.07	3.57	3.86	4.24	3.80	3.10
S2, Shallow and Partial Debonding	10	2.02	2.31	2.33	2.32	2.32	2.44	2.61	2.99	3.22	3.16
	9	1.90	2.18	2.14	2.36	2.23	2.25	2.51	2.80	3.37	3.37
	8	1.87	2.04	2.06	2.10	2.27	2.20	2.44	2.80	3.26	3.16
	7	2.00	2.00	2.08	2.09	2.19	2.31	2.45	2.74	3.02	3.16
	6	1.95	1.92	1.93	1.99	2.06	2.09	2.22	2.50	3.03	2.91
	5	1.91	1.88	1.87	1.93	1.98	2.11	2.24	2.50	2.94	2.88
	4	1.79	1.88	2.03	2.05	2.01	2.09	2.31	2.40	2.82	3.02
	3	1.78	2.12	2.19	2.10	1.91	1.50	1.46	1.32	1.89	1.61
	2	2.03	2.23	2.40	2.16	1.74	0.95	0.72	1.02	1.45	1.47
	1	2.30	2.47	2.39	2.12	1.63	0.73	0.77	1.09	1.47	1.50
S1, Intact	10	2.55	2.71	2.57	2.28	1.79	1.07	0.84	0.74	1.04	1.28
	9	2.66	3.08	2.86	2.54	2.38	2.02	2.46	2.65	2.46	2.75
	8	2.78	3.27	3.15	3.00	2.93	3.24	3.66	3.86	3.75	3.43
	7	2.56	3.11	3.20	3.24	3.19	3.41	3.97	3.89	3.68	3.26
	6	2.58	3.20	3.18	2.99	3.07	3.57	3.86	4.24	3.80	3.10
	5	2.02	2.31	2.33	2.32	2.32	2.44	2.61	2.99	3.22	3.16
	4	1.90	2.18	2.14	2.36	2.23	2.25	2.51	2.80	3.37	3.37
	3	1.87	2.04	2.06	2.10	2.27	2.20	2.44	2.80	3.26	3.16
	2	2.00	2.00	2.08	2.09	2.19	2.31	2.45	2.74	3.02	3.16
	1	1.95	1.92	1.93	1.99	2.06	2.09	2.22	2.50	3.03	2.91

APPENDIX F – ADDITIONAL NDT RESULTS ON PORTLAND AND BOSTON
INTERNATIONAL AIRPORTS

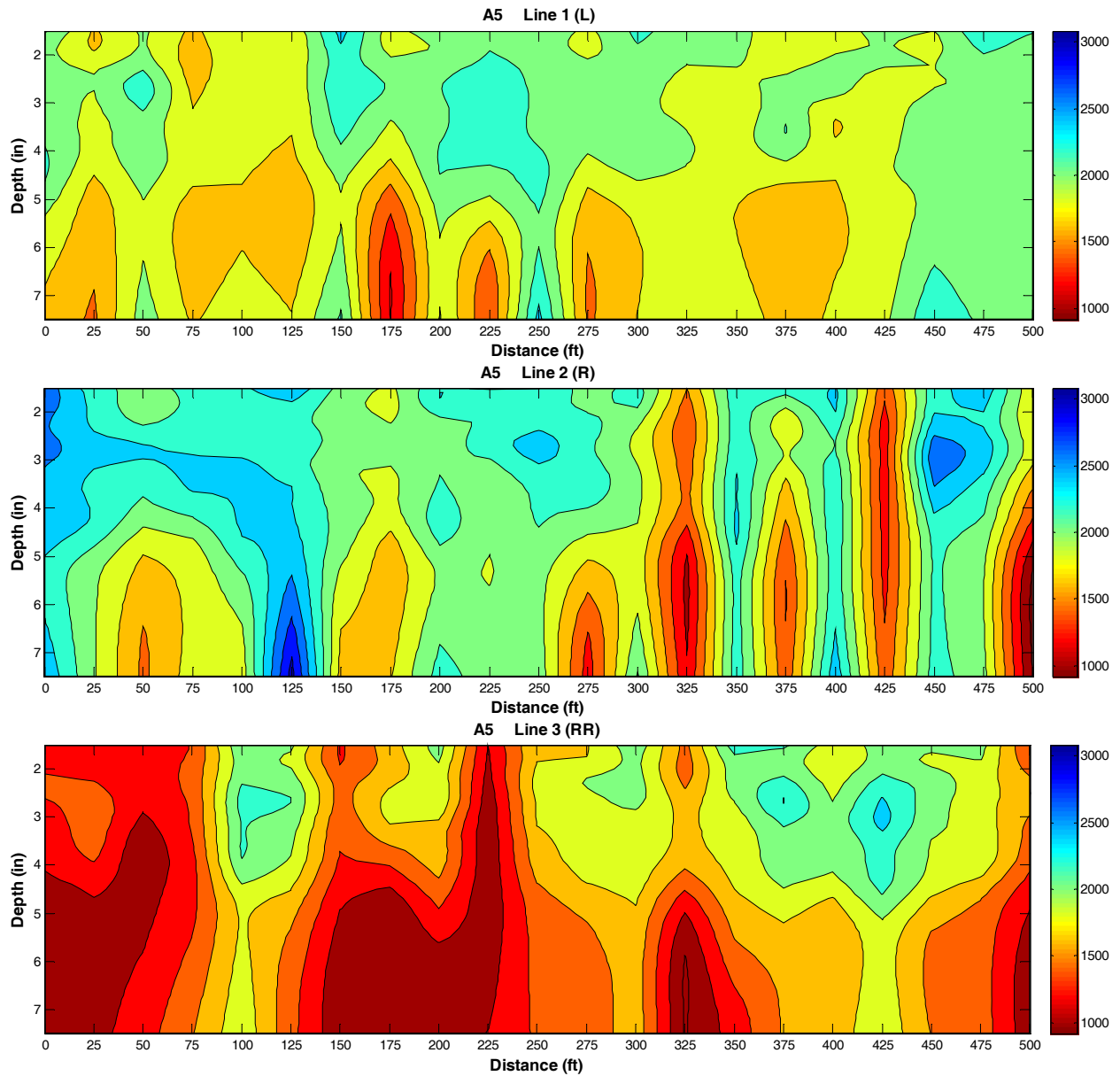
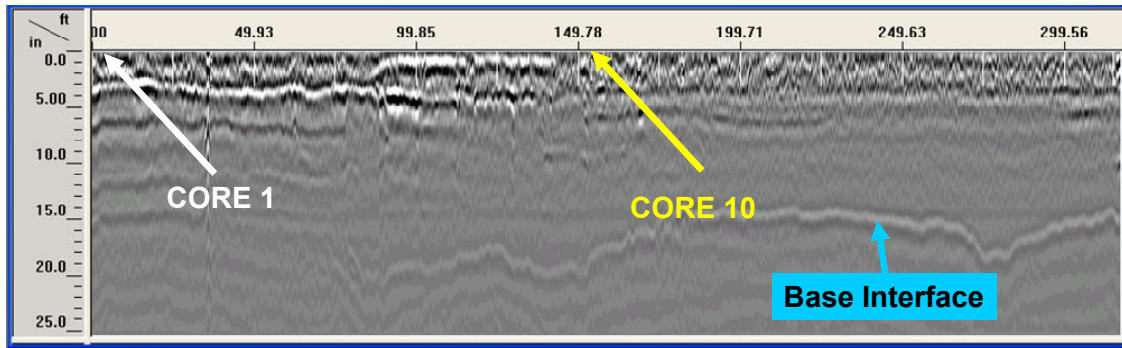
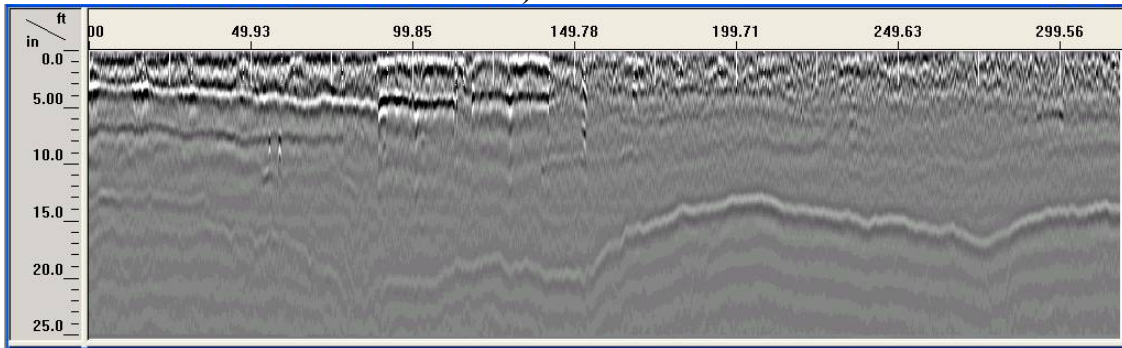


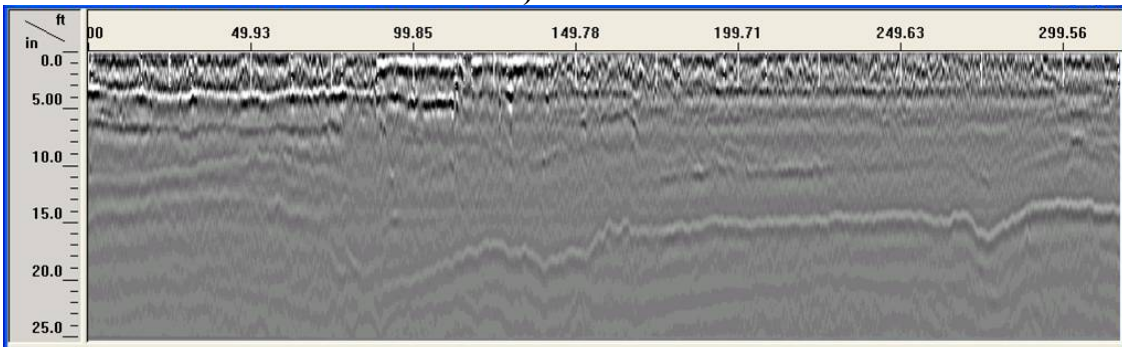
Figure F.1 – Dispersion Curves for Section A5



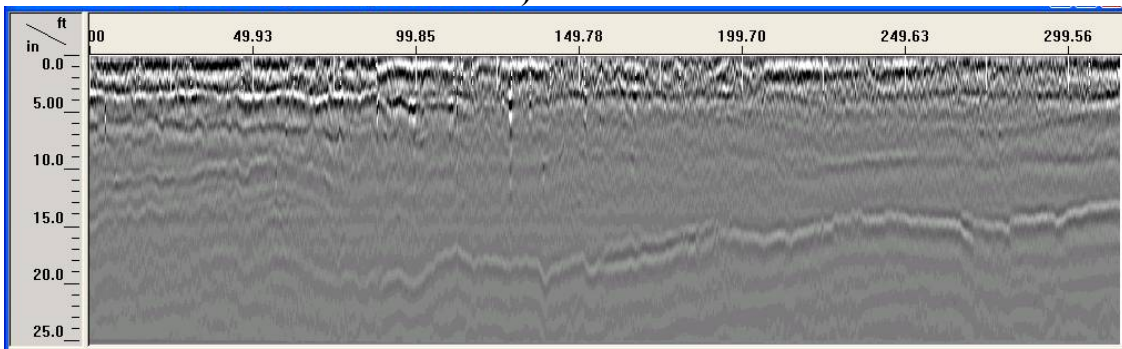
a) Line 1



b) Line 2



c) Line 3



d) Line 4

Figure F.2 – Post-processed GPR Linescans on Section C6

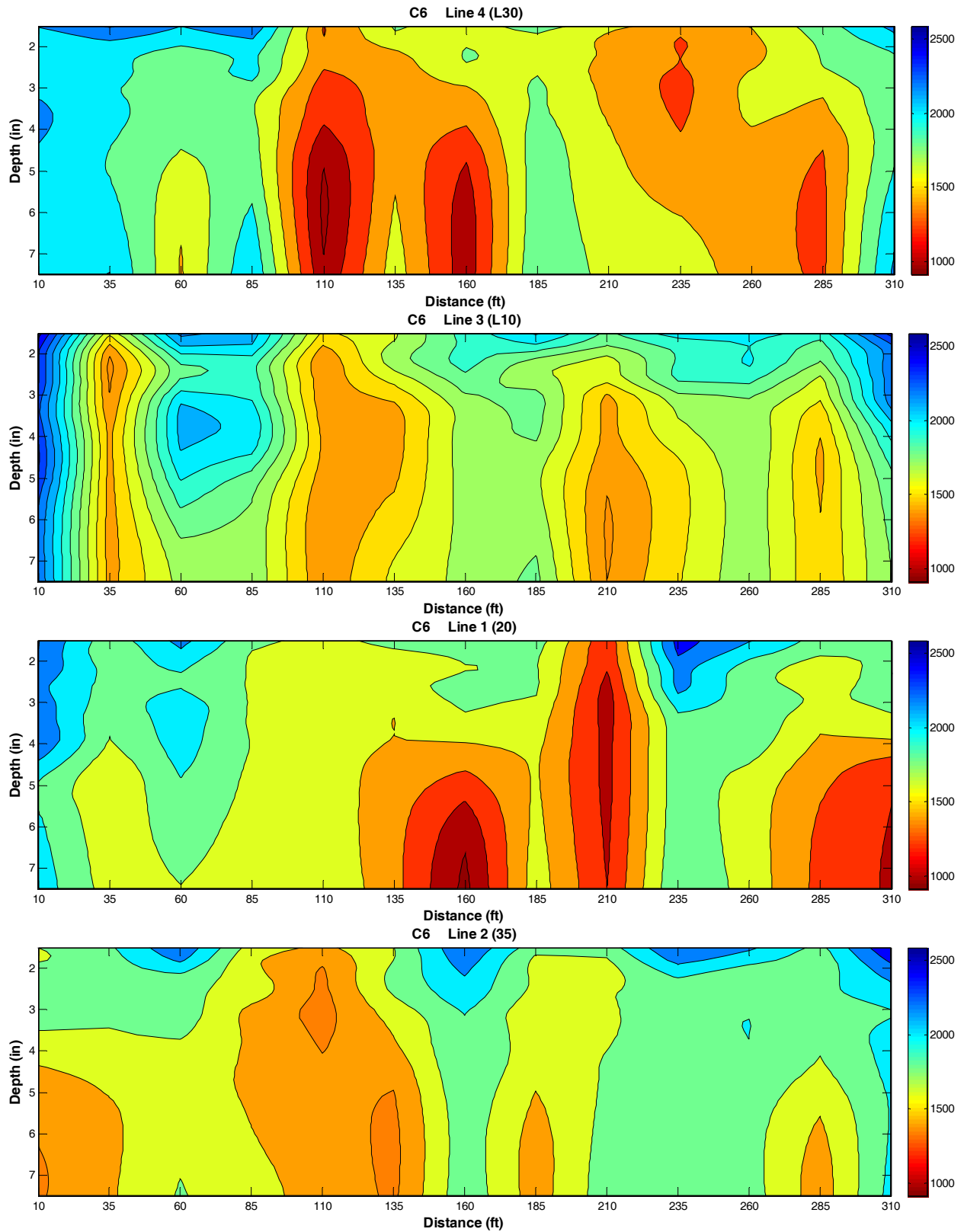
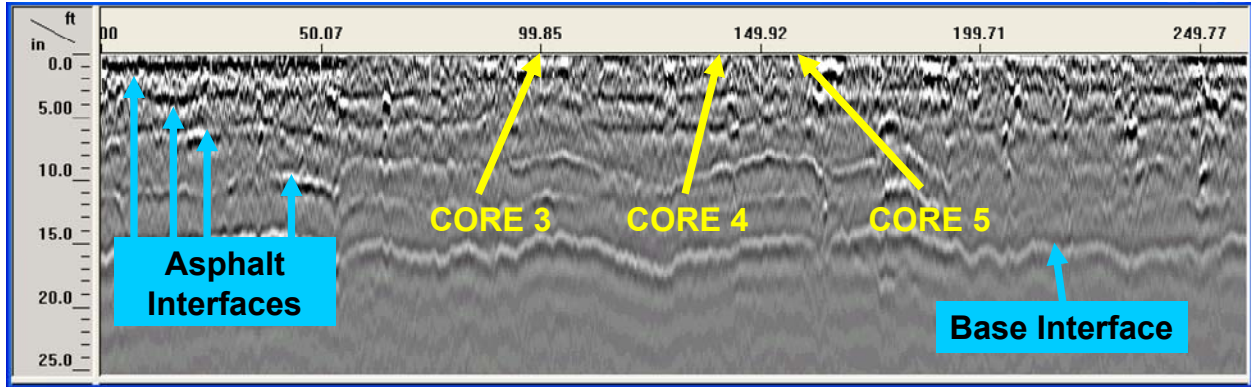
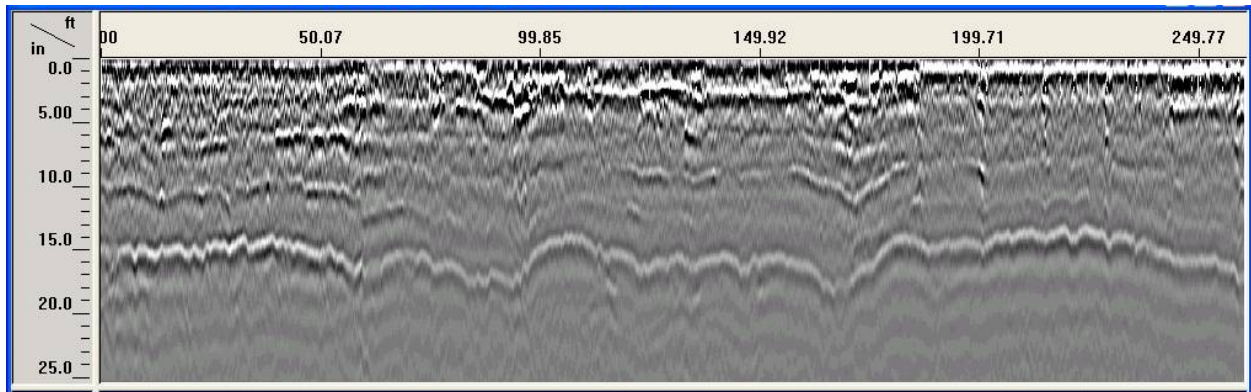


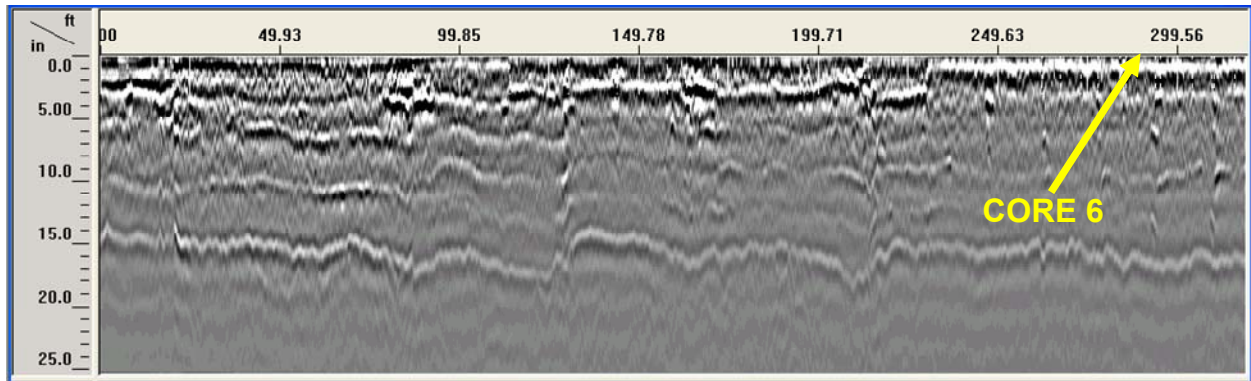
Figure F.3 – Dispersion Curves for Section C6



a) Line 1



b) Line 2



c) Line 3

Figure F.4 – Post-processed GPR Linescans on South Ramp Section

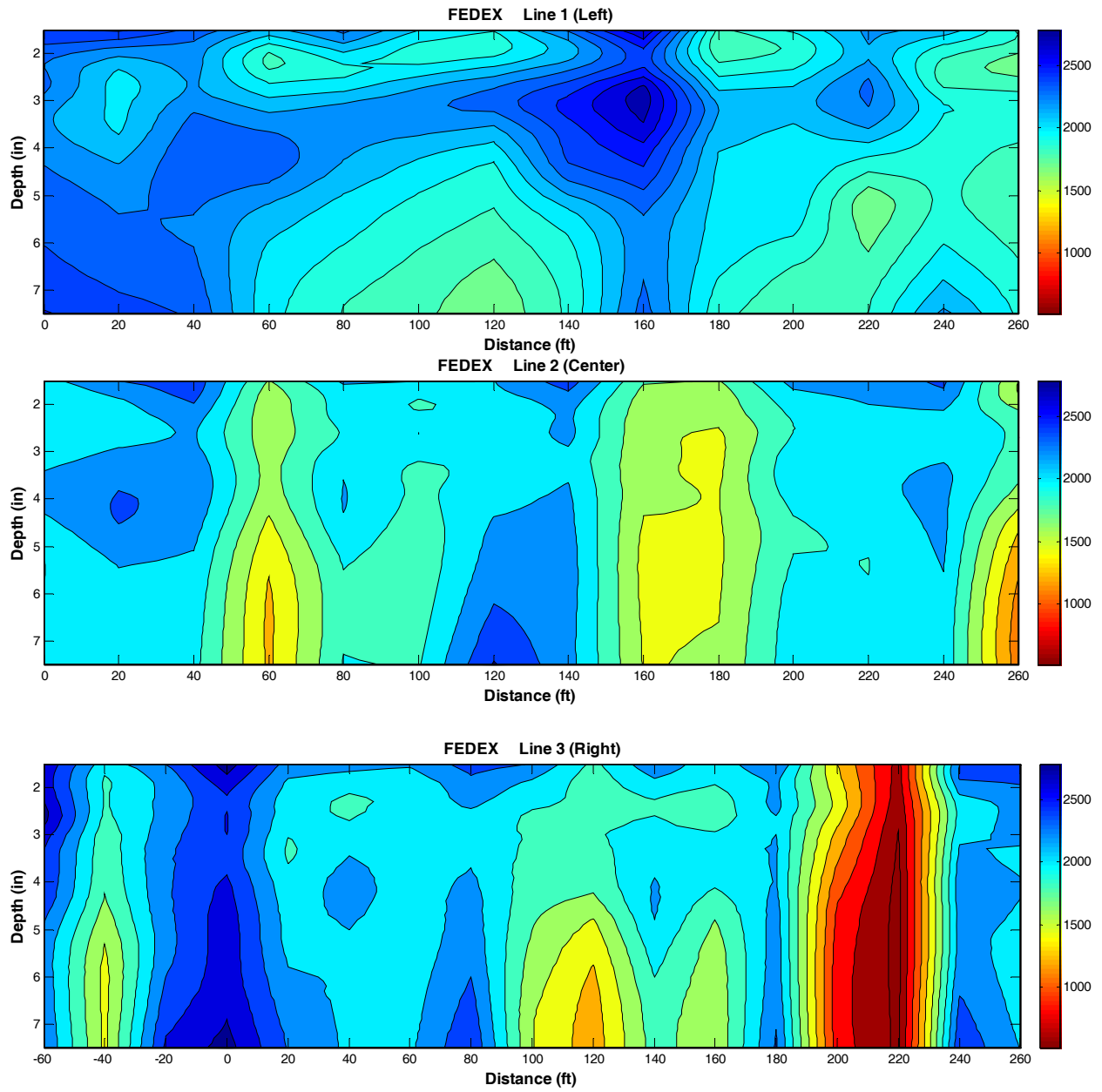
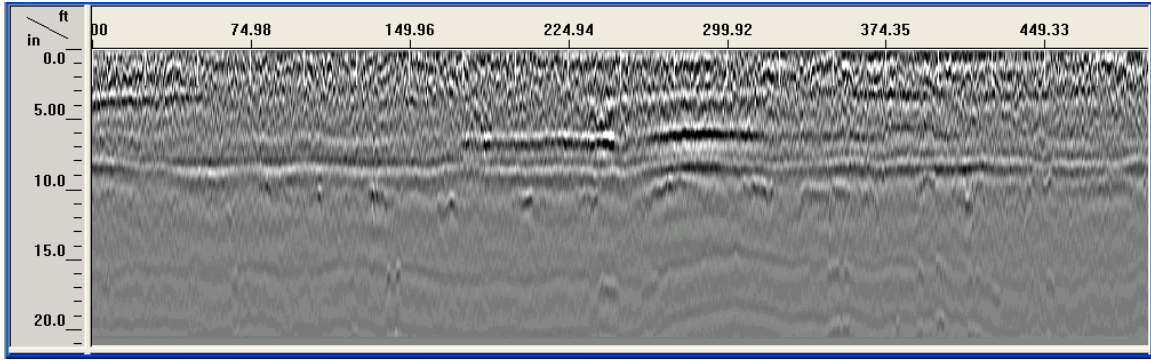
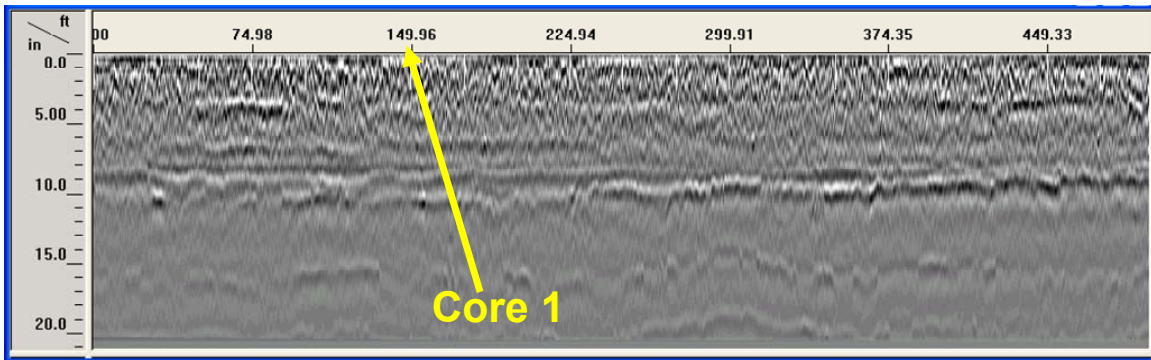


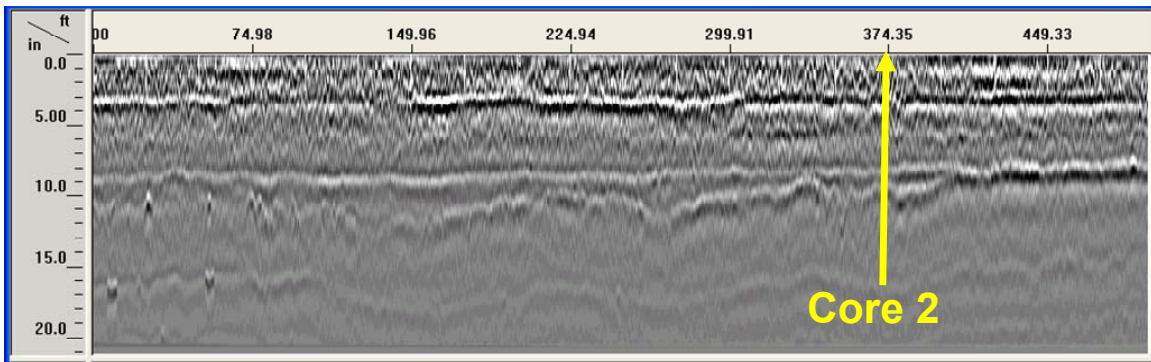
Figure F.5 – Dispersion Curves for South Ramp Section



a) Line 1

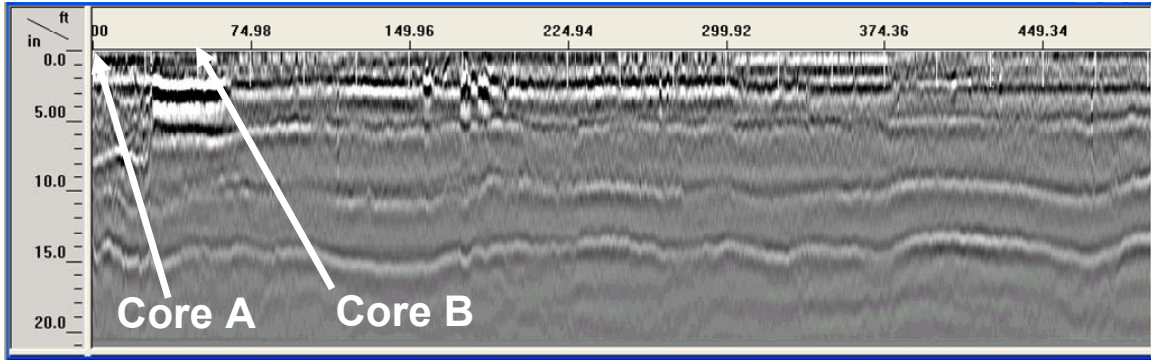


b) Line 2

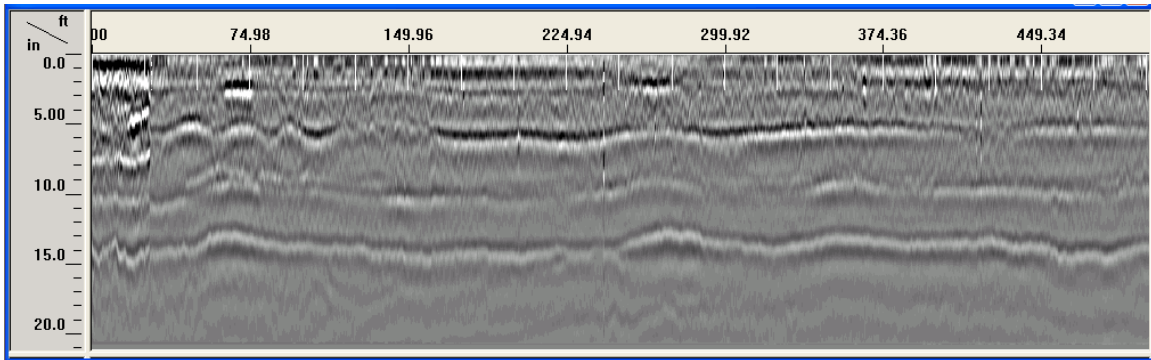


c) Line 3

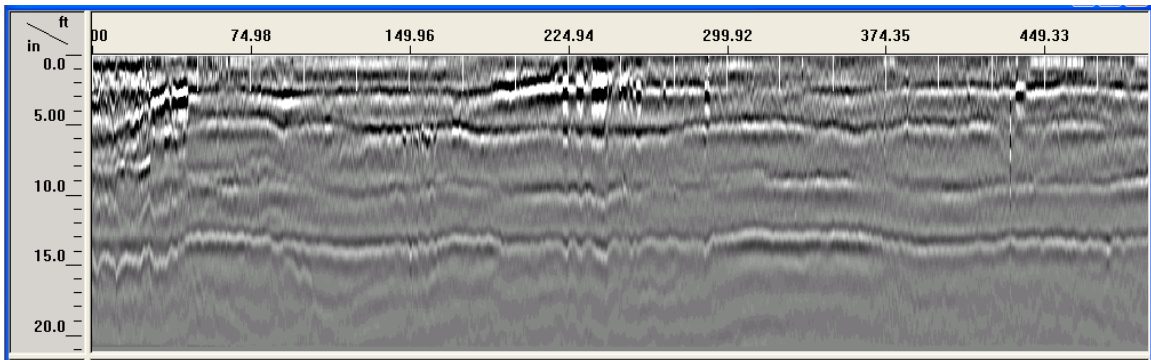
Figure F.6 – Post-processed GPR Linescans on Section 1 of E4



a) Line 1



b) Line 2



c) Line 3

Figure F.7 – Post-processed GPR Linescans on Section 2 of E4

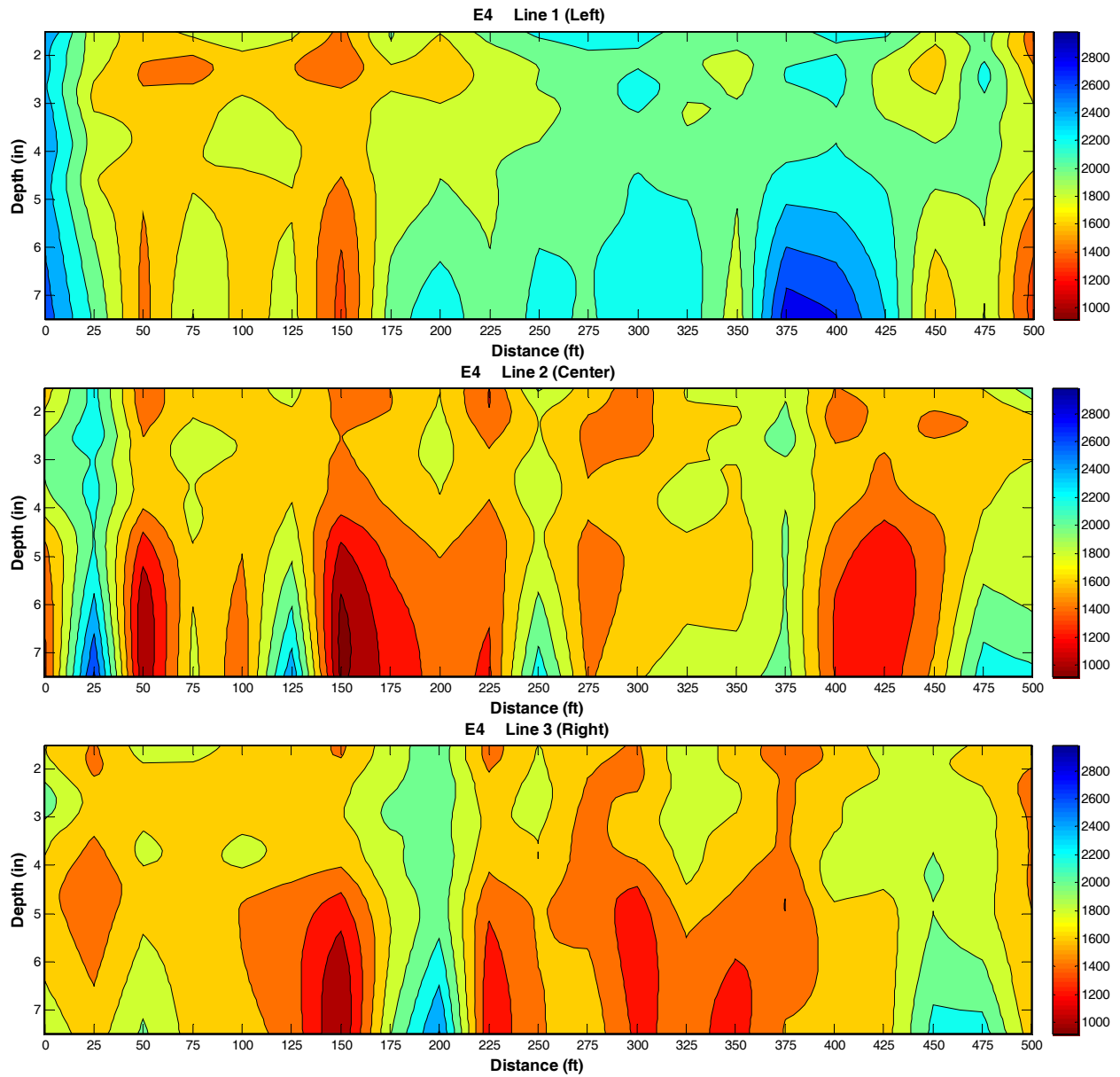


Figure F.8 – Dispersion Curves for Section 1 of E4

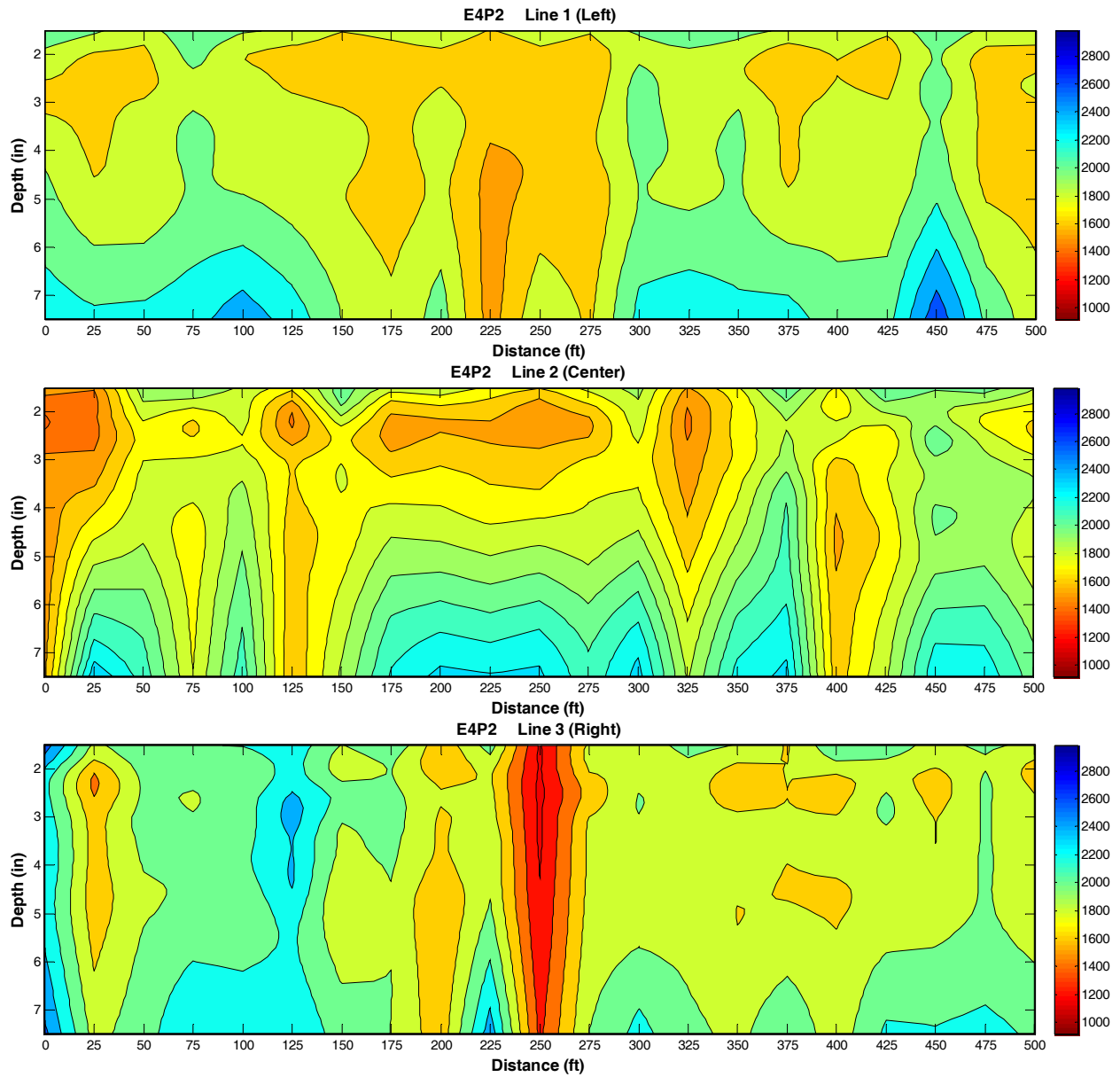


Figure F.9 – Dispersion Curves for Section 2 of E4

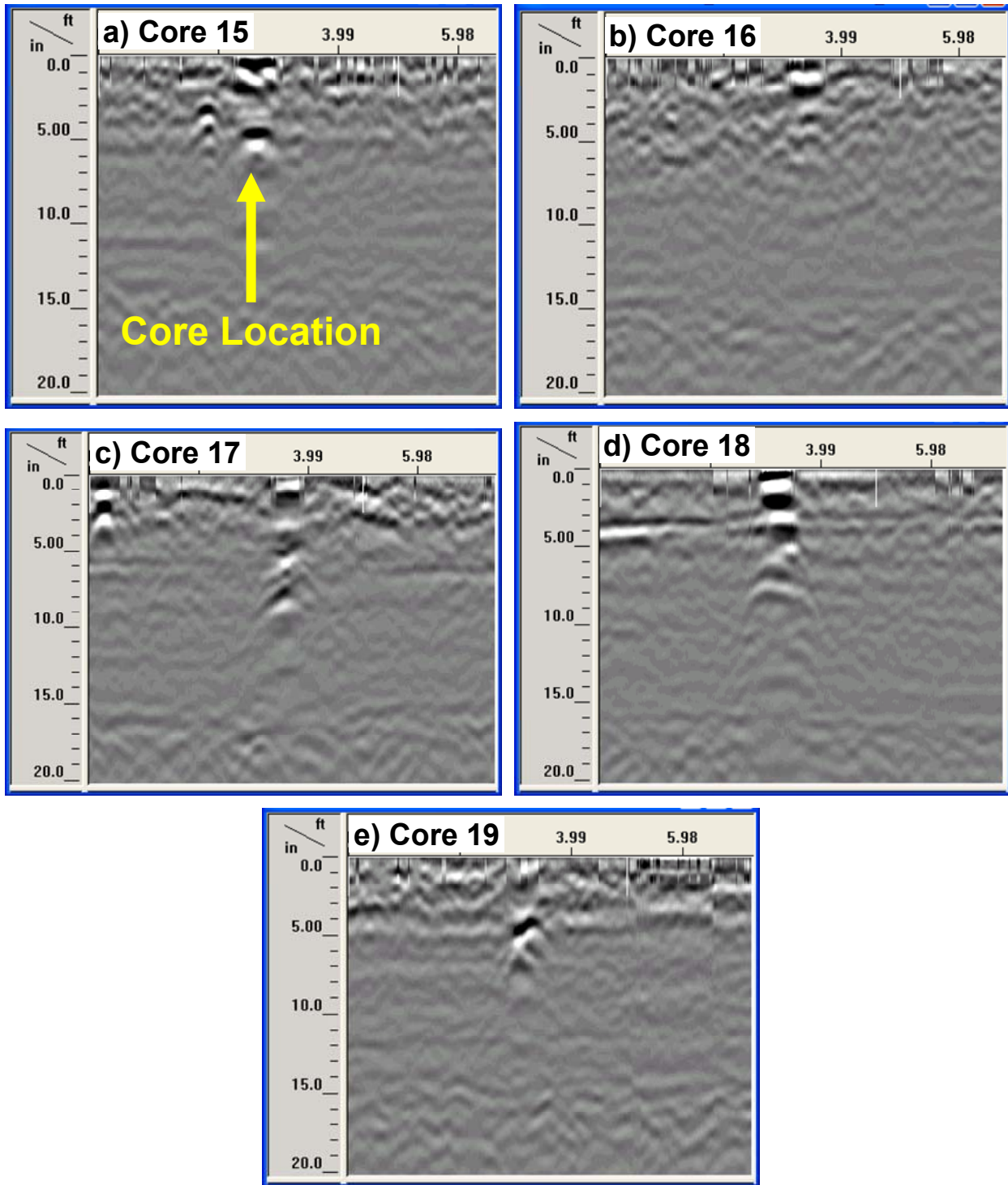


Figure F.10 – Post-processed GPR Linescans on Selected Cores of Section 1

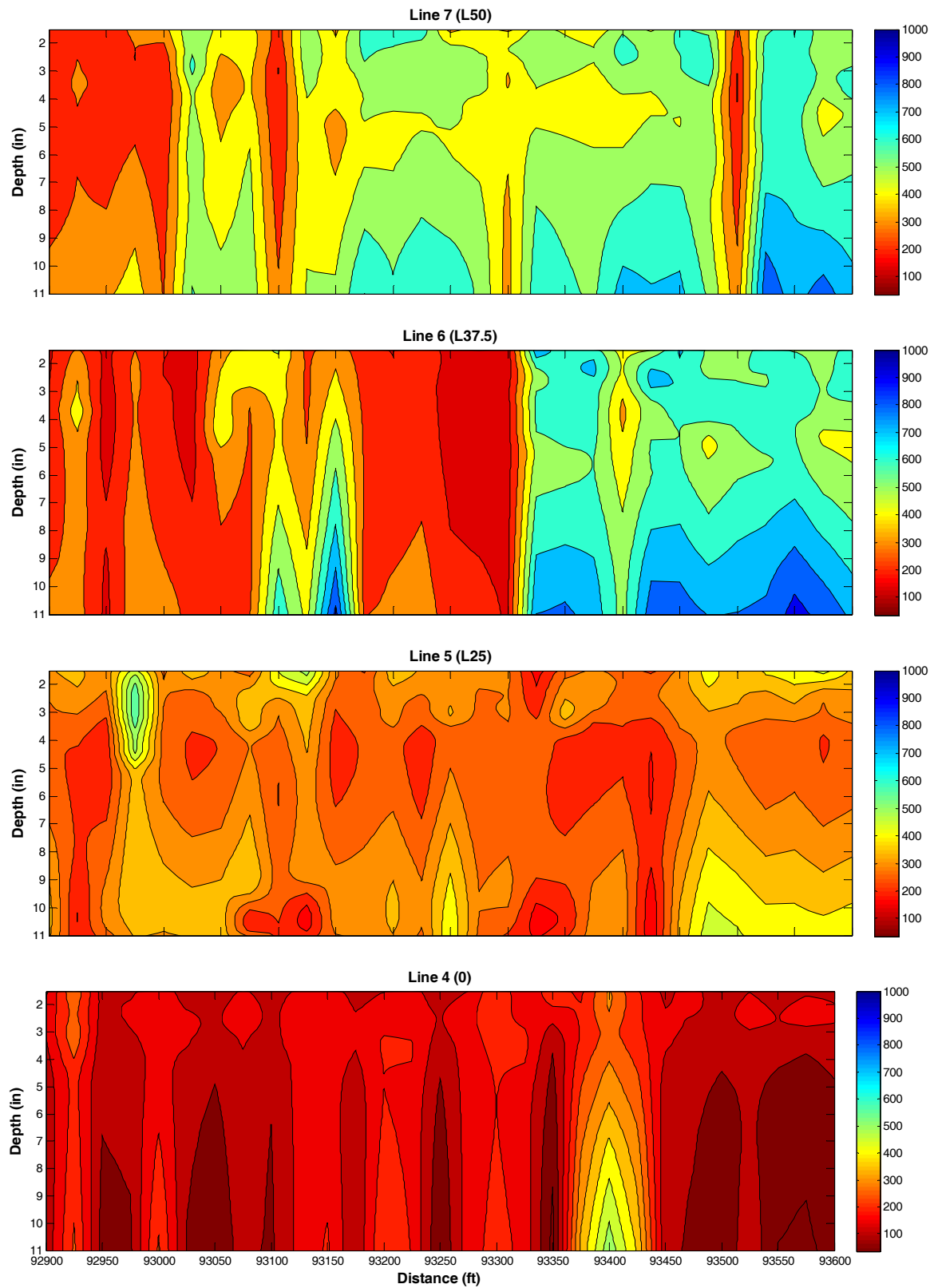


Figure F.11 – Dispersion Curves for Section 1

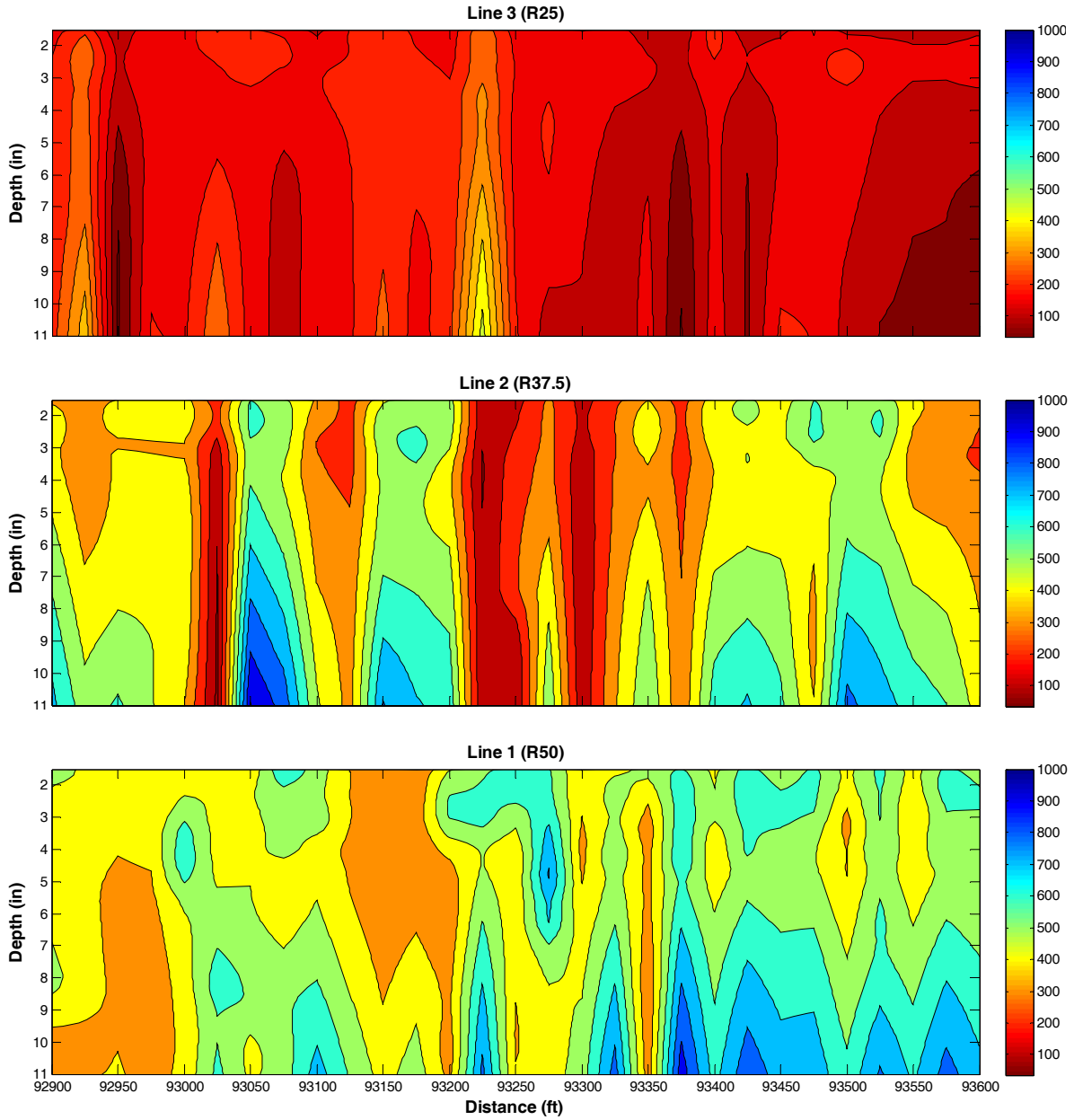


Figure F.11 Contd. – Dispersion Curves for Section 1

APPENDIX G – COMPLETE NDT RESULTS FOR DETECTABILITY STUDY

Table G.1 – Probability of Success of NDT Methods to Detect Different Levels and Sizes of Delamination

NDT Device	HMA Type	Area Size (ft)	Cool Weather				Hot Weather			
			Debonding Depth and Type				Debonding Depth and Type			
			Deep (5 in.)		Shallow (2.5 in.)		Deep (5 in.)		Shallow (2.5 in.)	
			Full	Partial	Full	Partial	Full	Partial	Full	Partial
PSPA	Fine Mix	4 by 9	43%	60%	88%	58%	48%	28%	93%	27%
		2 by 2	0%	17%	67%	33%	8%	33%	67%	33%
		1 by 1	0%	50%	0%	0%	0%	0%	0%	0%
		0.5 by 0.5	0%	0%	50%	0%	0%	50%	25%	0%
	Coarse Mix	4 by 9	18%	37%	90%	65%	3%	18%	98%	72%
		2 by 2	8%	17%	67%	0%	0%	33%	83%	33%
		1 by 1	25%	100%	50%	50%	0%	0%	75%	0%
		0.5 by 0.5	0%	100%	0%	0%	0%	0%	0%	0%
IR	Fine Mix	4 by 9	50%	72%	95%	30%	80%	85%	78%	20%
		2 by 2	0%	33%	92%	0%	0%	0%	83%	0%
		1 by 1	0%	0%	0%	0%	0%	0%	0%	0%
		0.5 by 0.5	0%	50%	0%	0%	0%	0%	0%	50%
	Coarse Mix	4 by 9	40%	52%	100%	48%	10%	42%	100%	40%
		2 by 2	58%	0%	8%	0%	92%	17%	50%	0%
		1 by 1	0%	50%	0%	0%	0%	50%	0%	0%
		0.5 by 0.5	0%	0%	0%	0%	0%	0%	0%	0%
FWD (Deflections)	Fine Mix	4 by 9	0%	13%	100%	72%	75%	59%	100%	0%
		2 by 2	0%	0%	0%	0%	0%	100%	100%	0%
		1 by 1	0%	0%	0%	0%	0%	100%	100%	100%
		0.5 by 0.5								
	Coarse Mix	4 by 9	0%	19%	100%	66%	0%	19%	100%	31%
		2 by 2	0%	0%	0%	0%	0%	0%	100%	0%
		1 by 1	0%	0%	0%	0%	0%	0%	100%	0%
		0.5 by 0.5								
FWD (Modulus)	Fine Mix	4 by 9	75%	41%	100%	38%	75%	59%	67%	0%
		2 by 2	0%	100%	50%	0%	0%	0%	0%	0%
		1 by 1	50%	0%	0%	0%	0%	0%	0%	100%
		0.5 by 0.5								
	Coarse Mix	4 by 9	17%	41%	100%	59%	0%	19%	100%	31%
		2 by 2	100%	100%	0%	100%	0%	0%	100%	0%
		1 by 1	0%	0%	50%	0%	0%	0%	100%	0%
		0.5 by 0.5								
GPR	Fine Mix	4 by 9					42%	36%	44%	34%
		2 by 2					0%	67%	92%	75%
		1 by 1					75%	0%	100%	50%
		0.5 by 0.5					50%	0%	50%	0%
	Coarse Mix	4 by 9					6%	9%	72%	23%
		2 by 2					33%	8%	8%	17%
		1 by 1					50%	0%	50%	0%
		0.5 by 0.5					25%	50%	25%	0%

CURRICULUM VITAE

Manuel Celaya was born on November 3, 1973 in Madrid, Spain. The second son of Manuel Celaya Yllana and Pilar Palomar Sanchez, he graduated from San Isidro High School, Madrid, Spain, in the spring of 1991 and entered Universidad Politecnica de Madrid in the fall of the same year. He received his bachelor's degree in Civil Engineering from Universidad Politecnica de Madrid in 2000. While pursuing his bachelor's degree he joined the Spanish army for one year, as a mandatory fulfillment (1998). In the fall of 2000, he entered the graduate program of the Civil Engineering at The University of Texas at El Paso. He received the Cotton Memorial Scholarship in the spring of 2001 for his academic achievements.

Upon graduation he joined the Center for Transportation Infrastructure Systems (CTIS) at UTEP as a Research Engineer. He started working on nondestructive methods and their application to pavements. He has been working at CTIS for over eight years. He is currently a Research Specialist at the CTIS. During these years, he has obtained broad experience related to design and management of pavement structures and material characterization using nondestructive technologies. As the Co-PI and lead researcher on several research projects, his efforts have contributed to developing better nondestructive methods to improve pavement management and to use them as better tools for forensic investigations. He has over 30 publications and research related reports and have presented at several national and international conferences.

Permanent address: Camino Viejo de Leganes 79. Apt. 7B.

Madrid 28019 (Spain)

This dissertation was typed by Manuel Celaya.